MODELING BASED CHARACTERIZATION OF GLACIERS AND GLACIAL LAKE OUTBURST FLOODS (GLOF) USING EARTH OBSERVATION TECHNIQUES

Ph.D. THESIS

by

ASHIM SATTAR

**DEPARTMENT OF EARTH SCIENCES
INDIAN INSTITUTE OF TECHNOLOGY ROORKEE
ROORKEE – 247 667 (INDIA)
JUNE, 2019**

MODELING BASED CHARACTERIZATION OF GLACIERS AND GLACIAL LAKE OUTBURST FLOODS (GLOF) USING EARTH OBSERVATION TECHNIQUES

A THESIS

Submitted in partial fulfilment of the requirements for the award of the degree

of

DOCTOR OF PHILOSOPHY

in

EARTH SCIENCES

by

ASHIM SATTAR

DEPARTMENT OF EARTH SCIENCES
INDIAN INSTITUTE OF TECHNOLOGY ROORKEE
ROORKEE – 247 667 (INDIA)
JUNE, 2019

INDIAN INSTITUTE OF TECHNOLOGY ROORKEE
ROORKEE

<u>CANDIDATE'S DECLARATION</u>

I hereby certify that the work which is being presented in the thesis entitled **"MODELING BASED CHARACTERIZATION OF GLACIERS AND GLACIAL LAKE OUTBURST FLOODS (GLOF) USING EARTH OBSERVATION TECHNIQUES"** in partial fulfilment of the requirements for the award of the Degree of Doctor of Philosophy and submitted in the Department of Earth Sciences of the Indian Institute of Technology Roorkee, Roorkee is an authentic record of my own work carried out during a period from July, 2015 to June, 2019 under the supervision of Dr. Ajanta Goswami, Assistant Professor, Department of Earth Sciences, Indian Institute of Technology Roorkee, Roorkee and Dr. A.V.Kulkarni, Divecha Centre for Climate Change , Indian Institute of Science Bangalore.
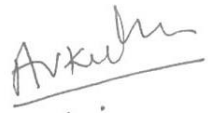
The matter presented in the thesis has not been submitted by me for the award of any other degree of this or any other Institute.

(ASHIM SATTAR)

This is to certify that the above statement made by the candidate is correct to the best of our knowledge.

Date: (Ajanta Goswami)   (A. V. Kulkarni)
                                  Supervisor   Supervisor

ABSTRACT

The Himalayan belt is known for its ice cover over the high-altitude regions, consisting of a total of more than 12000 glaciers. It has been observed that the sensitivity and vulnerability of the glaciers to climate change have led to its significant recession. Thinning and retreat of the glaciers have led to the formation of numerous high-altitude lakes in the Himalaya, most often dammed by glacial deposits. Several pieces of evidence have shown the growth of the existing lakes associated with the retreat of the parent glacier. The increase in the volume of these lakes can affect the integrity of the damming material, thereby increasing the chances of its failure. The growth of these lakes at higher elevations, therefore, increases the risk of the low-lying areas to catastrophic glacial lake outburst flood (GLOF) events. GLOF events are associated with the sudden discharge of a large volume of water along steep and narrow channels, with potential flow energy that can cause great damage to humans and infrastructure in the downstream region. GLOF events have mostly been reported extremely catastrophic in the Himalaya and are one of the primary concerns of the mountain communities due to the threat it imposes on them.

This thesis is aimed at providing a synoptic view of the potential GLOF's in the central Indian Himalaya (Uttarakhand and Sikkim). This is achieved by field and modeling based analysis of the potentially critical lakes in the region. Also, the integration of remote-sensing and hydrodynamic modeling enabled hazard assessment of the inaccessible lakes located at higher elevation. The preliminary data required for the analysis of GLOF hazard is a glacial lake inventory. The study presents a new updated glacial lake inventory for the central Himalaya. A series of hydrodynamic simulations were performed to model different moraine-breach scenarios based on different modes of failure (overtopping & piping) and breach parameters (breach width and failure time). The study performs dynamic routing of GLOF hydrographs along the main channels to evaluate the potential impact in the downstream region. This is achieved by characterizing the potential GLOF events in term of its hydraulic properties like flow velocity (ms^{-1}), flow depth (m), inundation area (m^2), peak discharge (m^3s^{-1}) and time of peak (in min).

The growth of an existing proglacial lake and the formation of new lakes depends on the topography of the glacier bed. Accurate mapping of the glacier-bed topography enables evaluation of the potential lake formation sites in the future. The present study is aimed to evaluate the future GLOF potential of the existing proglacial lakes by mapping its maximum

extent. This is achieved by spatially distributed glacier ice-thickness modeling, which in turn is employed to map depressions present on the glacier bed. The future hazard assessment of the lakes is performed by dynamic modeling considering the future volume of the proglacial lakes.

Overall, this thesis is an attempt to characterize different potential extreme GLOF events (present and future) and to understand the complex flow hydraulics during its propagation along a given flow channel. It involves identification of critical glacial lakes in Uttarakhand and Sikkim Himalaya and the detailed risk assessments of four potentially critical lakes to evaluate its impact in the downstream region. The sensitivity of the hydrodynamic model is analyzed by performing a series of GLOF-scenario modeling on a potentially hazardous lake.

The present study includes five different case studies of potential GLOF assessment considering four potentially critical lakes spread across the state of Uttarakhand and Sikkim. Based on the accessibility, the integration of field- and modeling assessment of the Satopanth lake located in the Alaknanda basin, Uttarakhand is undertaken. Field mapping of the lake and its associated moraine was performed using accurate DGPS points. Here, a potential GLOF event is coupled with a 100-year return period flood to evaluate a combined impact on a hydropower dam site located downstream. The potential flood event resulted in a peak discharge of 2612 m^3s^{-1} that arrived at the dam site 38 minutes after the initiation of the breach event.

The study also undertakes a bathymetry-based hydrodynamic study of the South Lhonak lake located in the Teesta basin, Sikkim. The lake is one of the largest lakes in the state of Sikkim which has shown exponential growth in the past decade. A detailed potential-GLOF assessment of the lake is performed based on the lake bottom topography. Different moraine-failure mechanism (overtopping and piping) is modeled for scenario evaluation. Further, one- and two-dimensional hydrodynamic routing is performed to evaluate the impact of a potential GLOF along the given flow channel till it reaches a hydropower dam site at Chungthang town located 62.3 km downstream of the lake. An overtopping failure of the lake resulted in a peak flood of 3828.08 m^3s^{-1} calculated at the Chungthang town, which has a potential to inundate a total area of 55,000 m^2 of the existing settlements where flow depth and velocity reach up to 8 m and 9 ms^{-1} respectively.

The potential future-GLOF assessment was carried out on two lakes namely the Dhauliganga lake and the South Lhonak lake. The Dhauliganga lake is the largest and the highest proglacial lake located in the Dhauliganga basin, Uttarakhand. The maximum extent of the lake is mapped using an ice-thickness based approach. The future volume of the lake is calculated to evaluate a

potential future-GLOF event of the lake. The potential impact on a hydropower dam site located 72 km downstream is assessed using one-dimensional hydraulic routing. At the dam site, a maximum discharge of 1686 m^3s^{-1} is calculated where the peak discharge is reached within 98 min (1.6 hr) after the initiation of the moraine-breach event. Peak discharge of 1595 m^3s^{-1} (T_f= 0.50 hr) and 1489 m^3s^{-1} (T_f= 0.75 hr) is recorded at the dam site with a time of peak recorded at 103 min (1.7 hr) and 111 min (1.8 hr) respectively. Similar, evaluation is performed on the South Lhonak lake, Sikkim to examine the future potential of the lake. Three different potential moraine-breach scenarios based on varied time of moraine failure (T_f=1 hr, 2hr, and 3hr) is evaluated. The GLOF hydrograph T_f =1.0 hr produced the maximum peak discharge of 8021 m^3s^{-1}. The peak discharge decreases to 7076 m^3s^{-1} and 6462 m^3s^{-1} for T_f=2.0 hr and T_f=3.0 hr respectively. At the hydropower dam (Chungthang town) a maximum discharge of 4801 m^3s^{-1} is calculated where the peak discharge is reached within 124 min (2.06 hr) after the initiation of the moraine-breach event. Peak discharge of 4677 m^3s^{-1} (T_f= 2.0 hr) and 4653 m^3s^{-1} (T_f= 3.0 hr) is recorded at the dam site with a time of peak of 142 min (2.4 hr) and 156 min (2.6 hr) respectively.

The sensitivity of the hydrodynamic model to the input parameters and channel characteristics is evaluated by performing a series of hydrodynamic simulations of potential GLOF on the Safed lake located in the Goriganga basin, in the state of Uttarakhand. The lake have grown double its size in a span of 48 years from 1968 to 2016. The potential GLOF of the lake is evaluated by a modeling a moraine-breach event in which breach parameters (breach width and formation time) were calculated using empirical relations. For sensitivity analysis, a series of hydrodynamic GLOF routing is performed for the same lake for varied Manning's N, breach width and formation time to evaluate the sensitivity of the model. The sensitivity of the model results to channel properties like slope and top-width is evaluated along the flow channel. The breach hydrograph is most sensitive to the breach formation time (T_f) when compared to the width of the breach (B_w). It is observed that the flow velocity is more sensitive to Manning's N as compared to flow depth. Also, flow velocities have shown a linear increase as the slope of the channel increases (R^2=0.78). Flow depth and velocity vary with the top-width of the channel. The flow velocity vs. top width has shown a correlation coefficient of 0.83 and that of depth vs. top width is 0.93.

ACKNOWLEDGEMENT

TABLE OF CONTENTS

LIST OF FIGURES

LIST OF TABLES

number of overdeepening sites (N_{ovr}), elevation range of glacier (ΔE), elevation range of overdeepening sites (ΔE_{ovr}), and total area of the overdeepenings (S_{ovr})

CHAPTER 1: INTRODUCTION

1.1 GENERAL

The cryospheric components of the globe can be categorized into glaciers, ice caps, ice shelves and ice sheets (Lemke et al., 2007; IPCC 2007) which contains 75% of the world's total freshwater (Anthwal et al., 2006). There would be a rise of 65 m in the global sea level if all the glaciers in the globe melt (Zemp and van Woerden, 2008). The ice sheets (Antarctic and Greenland) account for 87.2% of the total ice-covered area in the globe constituting 97% of the total ice volume. The glaciers account for 0.45% of the total ice volume occupying 3.36% of the global ice-covered area (IPCC, 2007). Figure 1.1 shows the regional distribution of the cryospheric components in the globe. There is a total of 198,000 glaciers worldwide with a total area of 726,000 km^2 (Pfeffer et al., 2014). The glaciers are distributed over North America, central and north Asia, South America, Central Europe, Scandinavia, New Zealand, Africa and New Guinea (Dyurgerov and Meier, 2005). The central Asia has the largest glacier extent in the globe of which the Himalayan-Karakoram region has the maximum. The region extends from Pakistan in the west to China in the east, spanning along Nepal and the northern belt of India.

1.2 GLACIER AND ITS IMPORTANCE IN THE HIMALAYA

The Himalayan arc extends for 2,400 km from west-northwest to east-southeast containing over 50,000 glaciers with a total area of approximately 40,000-60,000 km^2 (Kulkarni and Karyakarte, 2014; Bajracharya and Shreshta, 2011; Bolch et al., 2012). Himalayan glaciers are a storehouse of fresh water and play a significant role in influencing the runoff through numerous perennial rivers flowing over the Indo-Gangetic plains, providing freshwater to the second largest populated country in the world. The Himalayan-Karakoram region accounts for the maximum glacier cover outside the polar regions. It has gained widespread interest owing to the accelerated rate of glacier mass loss that affects processes like runoff of glacier-fed rivers and global sea level rise (Dyurgerov and Meier, 1997; 2005; Huss et al., 2008; Radic´ and Hock, 2011). Equally noteworthy is the socio-economic impact it has on the regions along the foothills of the Himalaya, for which glaciers serve as a constant source of fresh water (Kaser et al., 2010). The perennial nature of the major river systems in the Himalayan foothills (Indus, Ganga, and the Brahmaputra) is attributable to the snow and glacier melt runoff, which contribute to about 20-32% of the total annual discharge (SAC, 2016). Moreover, reviews based on glacier extent and mass balance suggests that there has been an increase in mass loss of the Himalayan glaciers (Miller et al.,

2012; Bolch et al., 2012, Bandyopadhyay et al., 2018b), the meltwater of which is eventually discharged to these major river systems. The total annual discharge contributed by snow and glacier melt runoff to the Indus, Ganga and Brahmaputra rivers are 60%, 8.7%, and 19% respectively (Immerzeel et al., 2010). These values do not remain constant but may vary with time and space depending on the climatic conditions across the region. The availability of freshwater runoff not only has an influence on the livelihood of a large global population (~50%) (Barnett et al., 2005) but also has an influence on other factors like power generation, as most of the hydropower stations are constructed along theses Himalayan rivers. Owing to the importance of glaciers in the Himalaya, it is necessary to access its sustainability on a regular basis.

The glacier inventories available for the Himalaya provides the preliminary information on the attributes of individual glaciers such as the location and total area, which can be further employed for its sustainability analysis. The most widely used glacier inventory is the Randolph Glacier Inventory (RGI) of which the RGI version 6.0 (2017) is the latest (RGI Consortium, 2017). The RGI is an additional product of the Global Land Ice Measurements from Space initiative (GLIMS) which was released for the estimation of glacier ice volumes and mass changes at a global scale (Bishop et al., 2014). The data is freely available to the end users in the form of glacial outlines with relevant geographical information. Figure 1.2 shows the Himalayan arc with the glacier outlines obtained from the Randolph Glacier inventory (RGI 6.0). There are several other glacier inventories for the Himalaya which have been made available by different agencies. The International Centre for Integrated Mountain Development (ICIMOD) and Glacier Area Mapping for Discharge from the Asian Mountains (GAMDAM) are other inventories available for the Himalayan glaciers. Such inventories are based on different mapping strategies and the data used to create it (Nuimura et al., 2015).

The effect of climate change on glaciers has been observed worldwide (Haeberli et al., 1999; Dyurgerov and Meier, 2000; Hoelzle et al., 2003; Paul et al., 2004; Bolch et al., 2012; Bandyopadhyay and Singh, 2018). In the Himalayan cryosphere, it is evident in terms of glacier shrinkages and varied river runoff (Akhtar et al., 2008; Immerzeel et al., 2010; Bolch et al., 2012; Kaab et al., 2012; Bandyopadhyay et al., 2018a), except for the Karakoram where glacier expansion has been reported (Hewitt, 2005). The formation of lakes in the high-altitude regions are other consequences of climate change in the Himalaya (Zemp et al., 2005). Moraine-dammed lakes are formed when glacier meltwater is trapped between the end moraine and the glacier snout (Westoby et al., 2014). The meltwater from the parent glacier is held by the depressions present in the glacier bed (Zemp et al., 2005). The catastrophic failure of these lakes may cause great damage to the low-lying communities and infrastructure (Lliboutry et al., 1977; Haeberli,
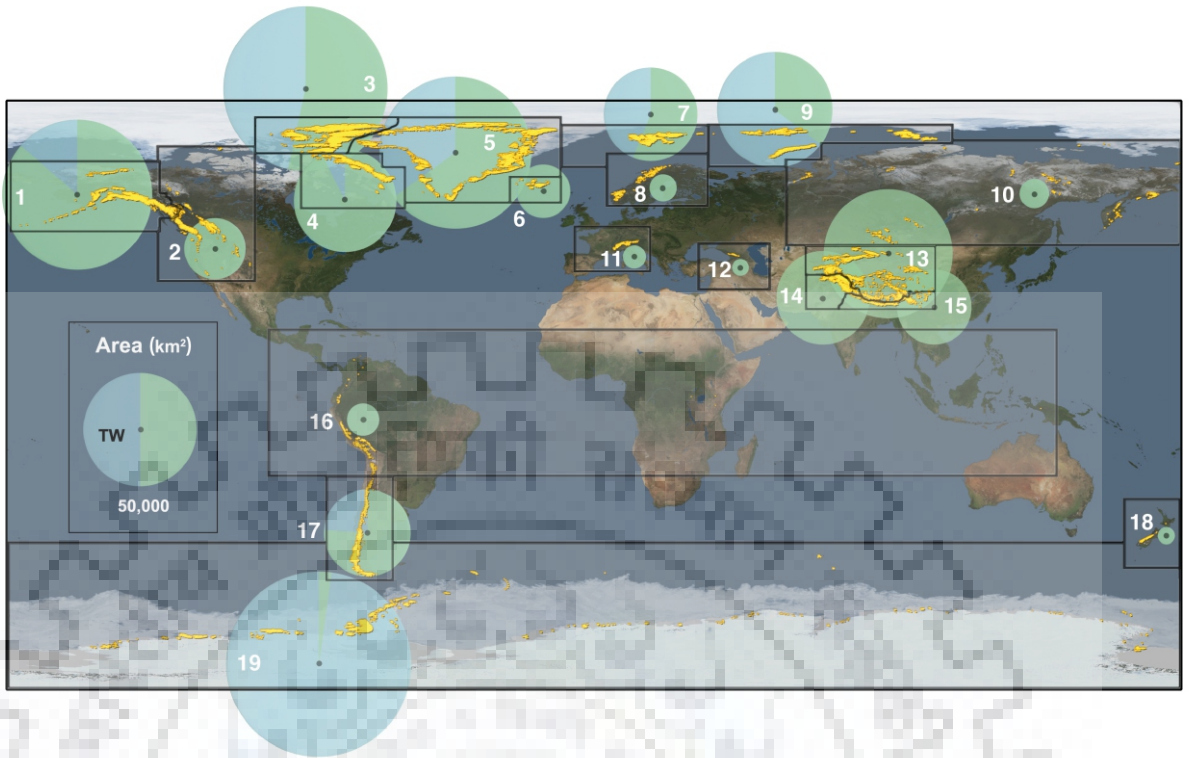
Figure 1.1. Regional distribution of the cryosphere components (glaciers and ice caps) in the globe; the area of the circles indicates the total glaciated area in the region; the regions are numbered based on the Randolph Glacier Inventory (RGI) (Davies, 2017)
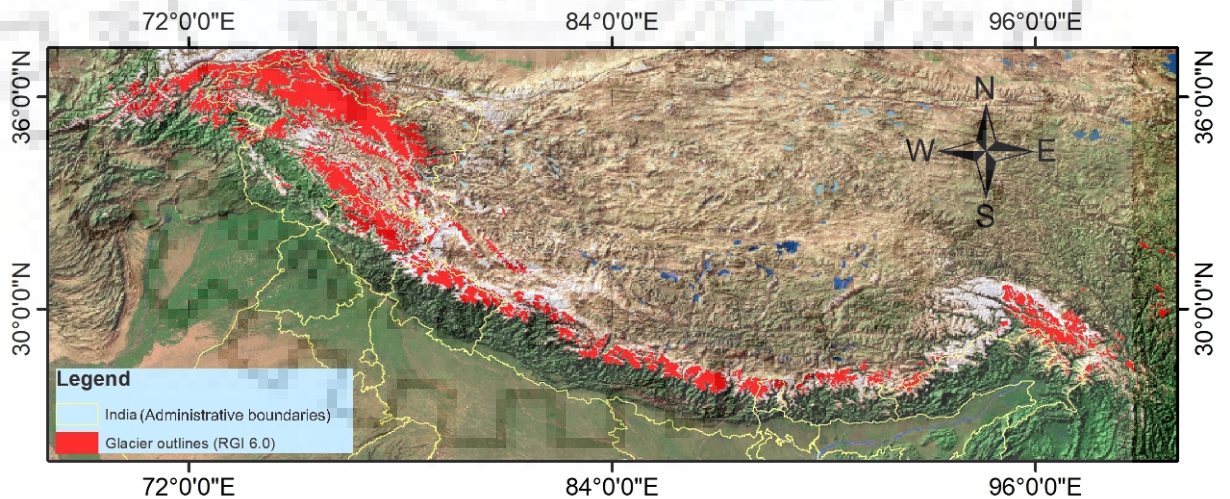
Figure 1.2 The Himalayan arc showing the distribution of the glaciers; the glacier outlines were obtained from the Randolph Glacier Inventory (RGI v 6.0)

1983; Carey, 2005; Mergili and Scheider, 2011; Stoffel and Huggel, 2012; Sattar et al., 2019). Over the past decade, high altitude lakes in the Himalaya have been showing significant growth in their size and number, and with this the ever threatening hazard of glacial lake outburst flood (GLOF) is increasing manifold (Richardson and Reynolds, 2000; Ageta et al., 2000; Mool et al., 2001; Quincey et al., 2007; Ives et al., 2010; Gardelle et al., 2011; Nie et al., 2013; Wang et al., 2015). These changes occur due to a general trend of glacier recession, remarkably observed in the Hindu Kush Himalaya (Kulkarni et al., 2007; Bolch et al., 2012).

In today's era of climate change, the assessment of the Himalayan glaciers in terms of its sustainability becomes a much necessary concern. Moreover, the presence of high-altitude lakes in the Himalaya makes it a potential hazard, as it presents a risk of high magnitude floods to the low-lying areas. The monitoring of the glaciers and the associated lakes can be achieved using simple mapping techniques to complex modeling approaches. Glacier characterization in terms of its ice-thickness facilitates extraction of information on glacier bed topography. The holistic monitoring of glaciers and its related hazards demands a regional assessment, for which remote sensing techniques serve as a major tool (Bishop et al., 2000; Kaab et al., 2002; Kaab et al., 2003; Kargel et al., 2014). Also, due to the harsh climatic conditions and inaccessible terrain in the Himalaya, in-situ experiments become difficult. Therefore, earth-observation techniques can be employed to remotely serve the purpose.

1.3 GLACIAL LAKES AND ITS ASSOCIATED HAZARDS IN THE HIMALAYA

The Himalayan belt is known for its ice cover over the high-altitude regions, consisting of a total of >50,000 glaciers (Kulkarni and Karyakarte, 2014; Bolch et al., 2012). It has been observed that the sensitivity and vulnerability of the glaciers to climate change have led to its significant recession (Richardson and Reynolds, 2000; Dyurgerov and Meier, 2000; Hoelzle et al., 2003; Scherler et al., 2011; Stocker et al, 2013). Thinning and retreat of the glaciers may lead to the formation of glacial lakes, dammed by glacial deposits (Costa and Schuster, 1988; Kargel et al., 2011; Emmer, 2017; Harrison et al., 2018; Mergili et al., 2018; Kumar et al., 2018) thereby increasing the exposure of the low-lying areas to glacial lake hazards like outburst floods (Haritashya et al., 2018). There is a total of over 25,500 glacial lakes spread across the Hindu-Kush Himalaya covering a total area of over 1444 km^2 (Maharjan et al., 2018). The distribution of the glacial lakes spread across the major Himalayan basins is shown in Figure 1.3. The growth of these lakes at higher elevation increases the risk of catastrophic glacial lake outburst flood (GLOF) events. These flood events are mostly associated with processes like dam breach formation and subsequent failure of the damming moraine (Richardson and Reynolds, 2000; Clague and Evans, 2000; Benn et al., 2012; Emmer and Vilímek, 2013; Emmer and Cochachin, 2013; Worni et al., 2014; Bajracharya et al., 2008). Figure 1.4 shows an example of a growing proglacial lake in the Alaknanda basin from 1994 to
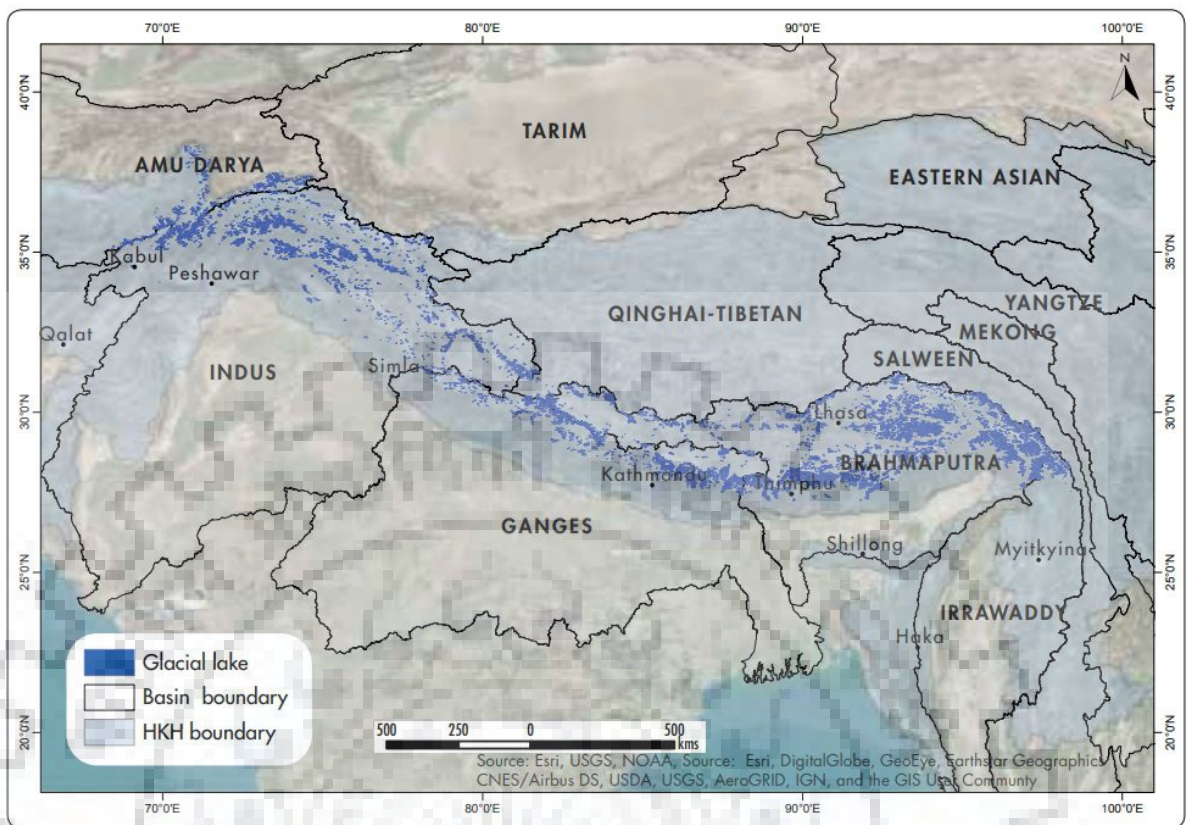
Figure 1.3 Glacial lake distribution in the Hindu Kush Himalaya (Maharjan et al., 2018-ICIMOD); a total of over 25000 glacial lakes has been identified spread across the major Himalayan river basins.
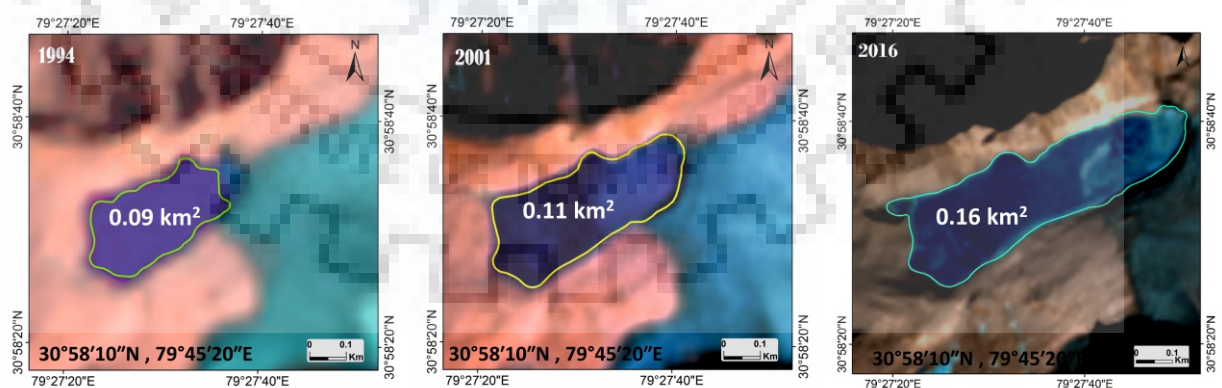
Figure 1.4 Satellite imageries showing the growth of a proglacial lake in the Alaknanda basin from 1994 to 2016; the area of the lake increased from 0.09 km^2 to 0.16 km^2 over the years.

2016 using remote sensing data. GLOF events have mostly been reported extremely catastrophic in the Himalayan terrain, due to its steep slopes and narrow flow channels (Mool, 1995; Yamada, 1998; Reynolds, 1998; Richardson and Reynolds, 2000; Iwata, 2002; Worni et al., 2012). Sudden discharge of a large volume of water along steep narrow channels amplifies the flow energy, which manifolds its potential to cause substantial damage along the flow channel (Costa and Schuster, 1988; Evans and Clague, 1994; Watanbe and Rothacher, 1996; Carey, 2005; Mergili and Schneider, 2011). Over the past decades, significant growth of the existing glacial lakes in the Himalaya has considerably increased the risk levels due to GLOF hazard (Watanabe et al., 1994; Komori, 2007; Gardelle et al., 2011; Raj et al., 2013). Also, the formation of new glacial lakes leads to the emergence of new susceptible low-lying areas, most likely to be at risk of high magnitude outburst floods in the near future (Anacona et al., 2014). In such context, the study of GLOF hazard becomes more significant, as the Himalaya caters many life-line and major infrastructures like hydropower plants, bridges, and highways, which are vital to the economy and welfare of the country (Richardson and Reynolds, 2000; Bajracharya et al., 2007; Thakur et al., 2016; Jha and Khare, 2016). The Himalayan terrain is known for its hydropower potential attributable to the perennial nature of the river systems (Pandit and Grumbine, 2012). Apart from the in-situ risk involved in and around the hydropower dams due to mass wasting, climate forcing, and greenhouse gases (Keunza et al., 2004; Barros et al., 2011; Kumar and Sharma, 2016a, Kumar and Sharma, 2016b, Kumar and Sharma, 2016c; Kumar et al., 2018; Kumar et al., 2019), GLOF events may pose greater risk to the hydropower plants because of its potential to cause great damage.

Over the past few decades, numerous GLOF events have been reported in the Himalaya (Richardson and Reynolds, 2000; Ives et al., 2010; Ray et al., 2016). GLOF events carry great damage potential thereby presenting a massive risk to the downstream regions. A total of forty-seven GLOFs has been documented so far (Emmer, 2018). The Kedarnath disaster that occurred on 16th-17th June 2013 in the state of Uttarakhand, can be taken as a recent example to show the extent of fatality of these events in the Himalaya. This event occurred due to a cloudburst and the failure of Chorabari lake that led to over 6000 human fatalities and caused great damage to the downstream infrastructure (Dobhal et al., 2013; Das et al., 2015; Ray et al., 2016). Figure 1.5 shows the pre- and post-flood images of the Kedarnath village, which was severely affected during the 2013 event (Das et al., 2015). The Dig Tsho GLOF (Nepal Himalaya) 1985 and Lugge Tso GLOF (Bhutan Himalaya) 1994, are events recorded in history, which caused severe damage to the downstream regions (Mool, 1995; Watanbe and Rothacher, 1996). The water load released in such events may travel tens or hundreds of kilometers downstream at a speed of 14 to 18 kmh[-1]. Moreover, GLOF-induced debris flow speeds may be much higher thereby presenting a great
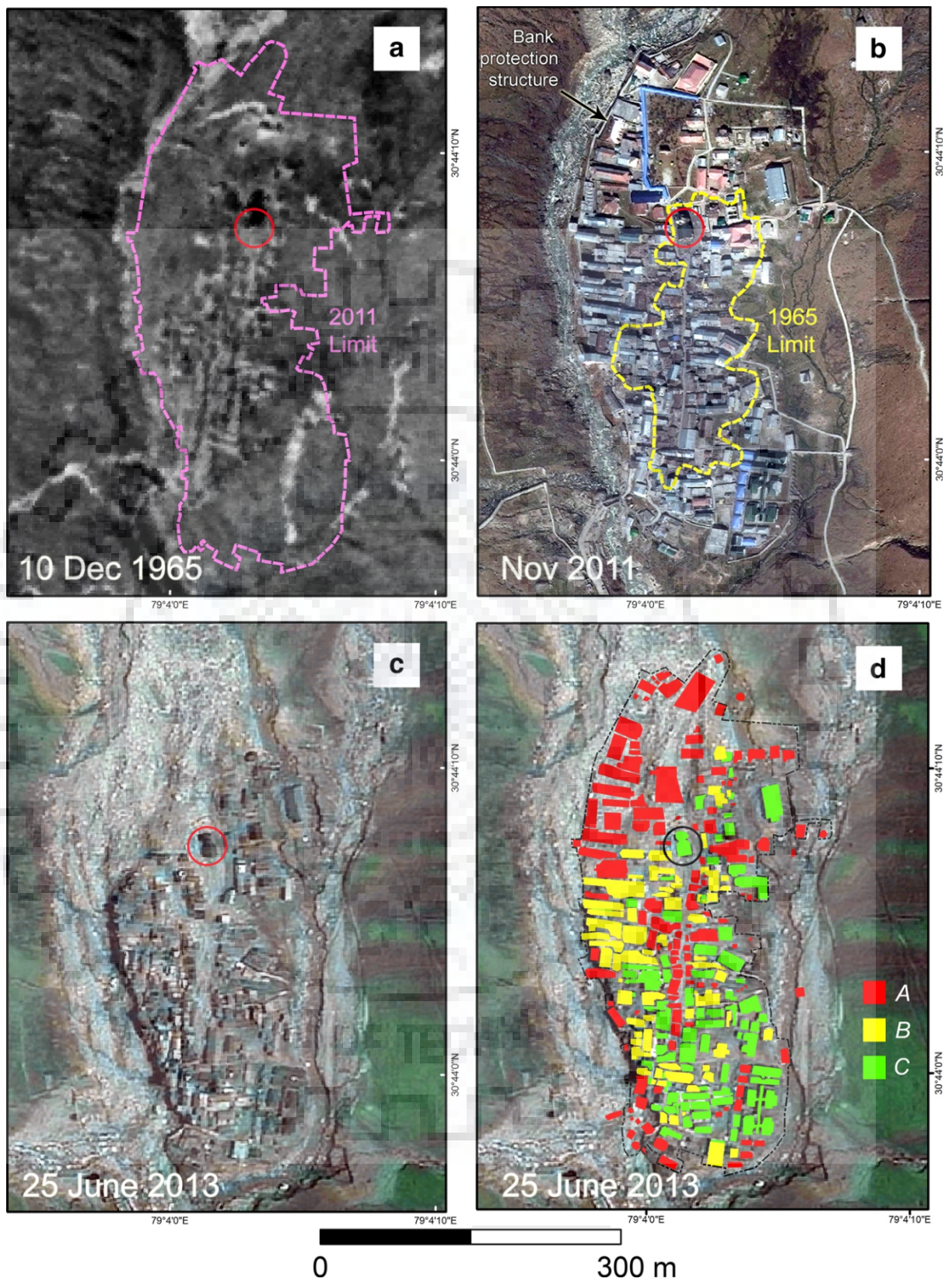
Figure 1.5 Pre- and post-images of the Kedarnath Village; (a,b) shows the settlements for the year 1965 and 2011 respectively; (c,d) the post-flood images showing the intensity of damage to the existing structures - completely damaged (A), moderately or partly damaged (B) and with minimal damage (C) (Das et al., 2015).

threat to the low-lying areas (O'Connor et al., 2001; Emmer and Vilimek, 2013). It is recognized that GLOF hazards are one of the primary concerns of the mountain communities, due to the threat it imposes on them. Thus, evaluation of these mountain hazards is a vital prerequisite for risk assessment of the low-lying areas in the Himalaya. In the Hindu-Kush Himalaya, only 142 scientific studies were carried out that includes the hazard assessment of the potentially dangerous lakes (Emmer, 2018). Therefore, it is elementary to expand the knowledge of glacial lake hazard and its potential risks over the Himalaya.

1.4 THEMATIC AND SCIENTIFIC BACKGROUND

1.4.1 Glacial lake outburst floods (GLOF)

Glacial lake outburst floods are characterized by a sudden release of huge volume of water, due to catastrophic failure of the damming moraine (Worni et al., 2013; Westoby et al., 2014; Björnsson 1992). The amount of water released in a failure event depends on factors such as the dam failure mechanism, breach width, and triggering mechanism (Clague and Evans, 2000; Richardson and Reynolds, 2000). In addition, the water discharge in a GLOF event may vary with the breach formation time. The less is the breach formation time, sooner is the peak discharge at a point downstream of the lake site. The discharge in a GLOF event may produce a dynamic and highly unstable flood wave which tends to make its way along a given flow channel downstream of the lake. The hydraulic behavior of GLOFs are complex and are associated with a chain of processes. It initiates with an external trigger like snow or rock avalanche, landslides, glacier calving, and seismic activity (Björnsson and Einarsson, 1990; Björnsson 2009; Haritashya et al., 2006). This triggering process results in the generation of an impulse wave which leads to the eventual breaching of the damming moraine. The schematic diagram of a glacial lake system showing the different GLOF triggering sources is represented in Figure 1.6. In any particular GLOF event, a moraine-breach may occur by either of the two failure mechanisms – (a) overtopping or (b) piping, the schematic of which is shown in Figure 1.7. In an overtopping failure, the breach is initiated when water traverse the crest-width of the moraine, caused by the displacement of the water column of the lake (Costa and Schuster, 1988; Clague and Evans, 2000; Richardson and Reynolds, 2000). In such event, an external force or impact is most often responsible for displacement of the water column thereby initiating erosion at the dam crest. In a piping failure, breaching may initiate at any point on the moraine due to internal failure thereby affecting the integrity of the damming material and eventually leading to the development of the breach (Lliboutry et al., 1977; Costa and Schuster, 1988).

The phenomenon of GLOFs can be evaluated with the help of different modeling approaches. The methods used to model GLOFs can be broadly categorized into empirical, analytical, and
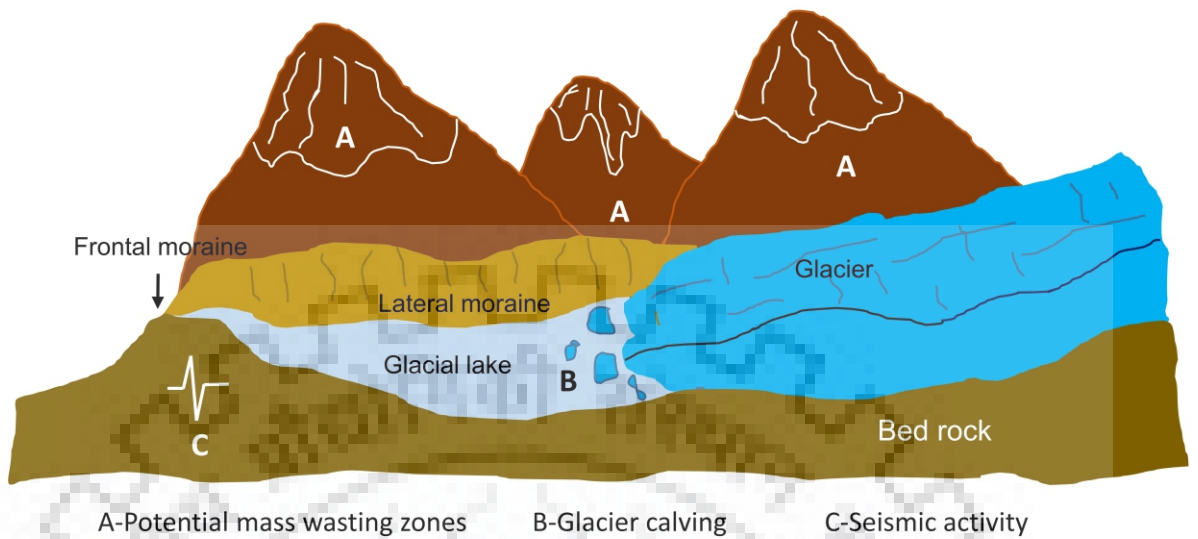
Figure 1.6 Schematic diagram showing the GLOF triggering sources in a glacial lake system; mass wasting zones includes the zones of landslides, snow avalanche, and rock falls
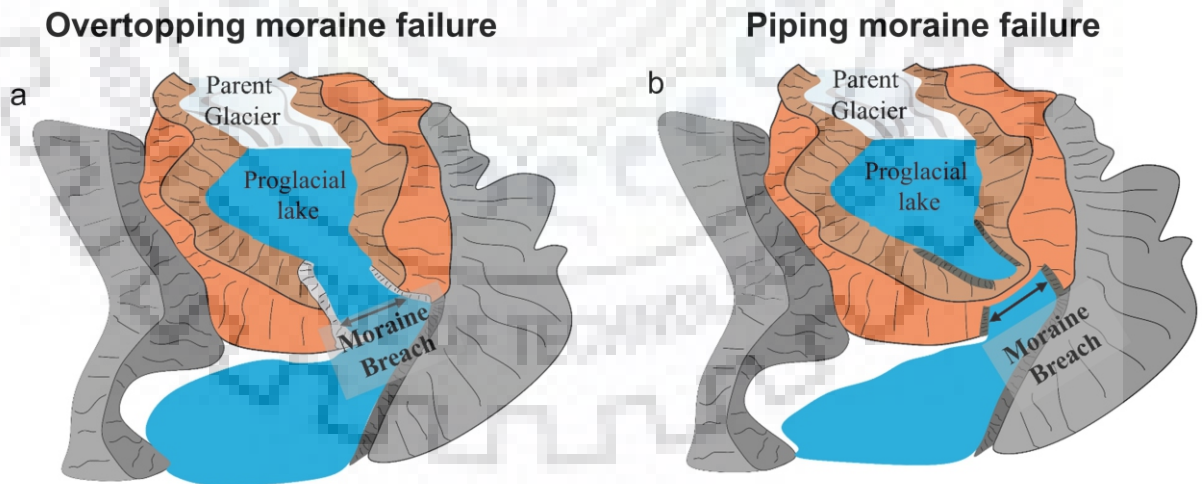
Figure 1.7 Schematic showing the different moraine failure modes of a glacial lake; (a) Overtopping- the water column flows over the moraine; (b) Piping- breach initiates at any point on the moraine.

physical-numerical. Empirical models are based on regression relationships derived using the data available from past events (Costa and Schuster, 1988; Froehlich, 1995; Evans 1986). The relationships developed can be employed to compute discharge, time of peak and volume of the lake in a GLOF event (Froehlich, 1995, Huggel et al., 2002). The empirical models provide an approximation of the actual GLOF properties as the actual processes like dam breach and hydraulic routing is neglected. Analytical models are partial physically-based, employed to analyze the physical process of GLOF and its associated processes (Morris et al., 2009). These models neglect the actual representation of the breaching process and assume it to be time-dependent (Westoby et al., 2014). Numerical models are entirely physical-based and can be employed to understand the complex phenomenon of moraine breach and its related flow hydraulics. Several hydrodynamic models are available to study the various hydraulic process of GLOFs. This includes both one- and two-dimensional models which are either freely or commercially available. The list of popular models used in the GLOF studies is presented in table 1.1. The models are based on conservation of mass and conservation of momentum which is given by the St-Venant equations (Barré de St-Venant, 1871) as:

$$\frac{\partial Q}{\partial x} + \frac{\partial A}{\partial t} = 0 \qquad \text{eq.1}$$

$$\frac{1}{A}\frac{\partial Q}{\partial t} + \frac{1}{A}\frac{\partial}{\partial x}\left(\frac{Q^2}{A}\right) + g\frac{\partial h}{\partial x} - g(S_0 - S_f) = 0 \qquad \text{eq. 2}$$

Where equation (1) and equation (2) are the conservation of mass and conservation of momentum equations respectively where, Q is the discharge, A the cross-sectional area, t is time, g is acceleration due to gravity (9.81 ms^{-1}), h is the average water depth, S_0 is the longitudinal bed slope, and S_f is the friction slope.

Table 1.1 A summary of well-established models and its required inputs for glacial lake outburst flood modeling; abbreviations are defined at the bottom of the table.

Sl. no.	Models	Approach	Purpose and required inputs
1	**HEC RAS-1D**	UNSTD and DMB	One-dimensional steady and unsteady flow (Brunner, 2002) **Inputs:** Terrain cross-sections, LULC, PMF, lake storage volume, Manning's roughness coefficient, moraine dimensions
2	**HEC RAS-2D**	UNSTD and DMB	Two-dimensional steady and unsteady flow (Brunner, 2002)

			Inputs: Terrain (DEM), LULC, PMF, lake storage volume, Manning's roughness coefficient, moraine dimensions
3	**FLO-2D**	UNSTD	Two-dimensional hydraulic flood-routing model for channel and unconfined overland flow (O'Brien, 2001). **Inputs:** Terrain (DEM), LULC, PMF, lake storage volume, flow rheological parameters, sediment concentration
4	**HEC-HMS**	STD	Hydrological modeling of watershed systems. (USACHE-HEC, 2006) **Inputs**: DEM, Soil information, topographic data, land use, daily precipitation, and daily observed runoff data
5	**MIKE 11**	UNSTD and DMB	One-dimensional steady and unsteady flow (DHI, 1995) **Inputs:** Terrain cross-sections, LULC, PMF, lake storage volume, moraine dimensions
6	**MIKE 21**	UNSTD and DMB	Two-dimensional steady and unsteady flow (DHI, 1996) **Inputs:** Terrain (DEM), LULC, PMF, lake storage volume, Manning's roughness coefficient, moraine dimensions
7	**MIKE HYDRO-RIVER**	UNSTD	One-dimensional steady and unsteady flow (DHI, 2015) **Inputs:** Terrain cross-sections, LULC, PMF, lake storage volume, moraine dimension
8	**BASEMENT**	SDFLW and DMB	Two-dimensional water-sediment flow propagation (Faeh et al., 2012). **Inputs:** Breach Discharge Hydrograph, sediment input, Terrain (DEM), LULC,
9	**RAMMS**	DFLW	Two-dimensional rapid mass movements (Christen et al., 2010) **Inputs:** Cross-sectional area (A), LULC, PMF, lake storage volume, sediment, and debris load
10	**LAHARZ**	DFLW	Two-dimensional debris flow propagation (lahars) (Iverson et al., 1998)

			Inputs: Cross-sectional area (A), LULC, PMF, lake storage volume, Debris load

*UNSTD: Unsteady flow routing; **STD:** Steady flow routing; **SDFLW:** Sediment flow; **DFLW: Debris Flow; DMB:** Dam Breach*

1.4.2 Characterization of glaciers and glacier beds

Glacier characterization in terms of its ice thickness can be achieved by numerical modeling based on glacier surface velocity, slope and basal shear stress (Gantayat et al., 2014). Shear-stress based methods to reconstruct glacier ice thickness is dependent on the relationship between basal stress, slope of the glacier, and its thickness (Linsbauer et al., 2012). The relationship can be given as:

$$\tau_b = f \rho g H \sin \alpha \qquad \text{eq. 3}$$

Where τ_b is the basal stress, H is the ice thickness, $sin\ (\alpha)$ is the slope, ρ is the ice density, g is the acceleration due to gravity (9.8 ms^{-1}), f is the shape factor, which is defined as the ratio between the driving stress and basal stress along a glacier (Haeberli and Hoelzle, 1995) and has a range of 0.6 to 1.0.

Also, glacier ice thickness is related to its surface velocity based on the relationship between surface velocity, surface slope, basal velocity, and ice thickness. The relation is given by:

$$U_s = U_b + \frac{2A}{n+1}(\tau_b)^n H \qquad \text{eq. 4}$$

Where U_s is the surface velocity (ms^{-1}), U_b is the basal velocity which is assumed to be 25% of U_s (Swaroop et al., 2003; Gantayat et al., 2014), A is the creep parameter which is assigned a constant value of 3.24×10^{-24} Pa^{-3}s^{-1} for temperate glaciers (Cuffey and Paterson., 2010), n is Glen's flow constant with a value assumed to be 3, τ_b is the basal stress, and H is the ice thickness (in m).

Combining equation (3) and (4), the equation derived to calculate ice thickness can be given as:

$$H = \sqrt[4]{\frac{1.5\ Us}{A\ (f\rho g sin\alpha)^3}} \qquad \text{eq. 5}$$

The spatially distributed ice-thickness calculated using equation (5) can be exploited to extract information of the glacier bed. This is achieved by an arithmetic operation between glacier surface elevation and ice thickness:

$$B_E = S_E - H \qquad \text{eq. 6}$$

Where B_E is the spatially distributed glacier-bed elevation (m a.s.l.), S_E is the distributed glacier-surface elevation (m a.s.l.) and H is the ice thickness (m). This principle can be adopted to map the glacier bed using ice thickness estimates. The accurate mapping of glacier bed can expose the depressions present on the bed (overdeepenings), which are the potential lake formation sites in the future (Linsbauer et al., 2016; Remya et al., 2019). In case of an existing lake, the future extent of the lake can be predicted by mapping the glacier bed underneath the present terminus of the glacier. Figure 1.8 is a schematic showing the future expansion of a proglacial lake. The future hazard potential of the existing proglacial lakes can thus be evaluated.

1.5 STUDY AREA

In this thesis, we have analyzed and modeled different potential-present and potential-future GLOF events, the study sites of which are spread over the central Himalaya. The study is confined to only the Indian part of the central Himalaya that includes the state of Uttarakhand and Sikkim. Figure 1.9 shows the location of the study area and specific sites presented in the thesis. The study sites are described briefly in the following:

1.5.1 Lake inventory- Central Indian Himalaya

a. Uttarakhand

The state of Uttarakhand is located between the latitudes 28°43′-31°27′ N and longitudes 77°34′-81°02′ E with a total area of 53,484 km². The area above 3500 m a.s.l. is mostly snow and glacier covered. Most of the rivers in the state are glacier-fed and are a good source of freshwater to the downstream regions. The temperature remains at the sub-zero level at high-lying areas above 3500 above m a.s.l.

b. Sikkim

The state of Sikkim lies between 27°04′ to 28°07′ N latitude and 80°00′ to 88°55′ E longitude with a total area of 7,096 km². The major part (>90%) of Sikkim falls under the Teesta river basin. The state is surrounded by Bhutan in the east, Nepal in the west, China (Tibet) in the north and West Bengal in the south.

The existence of numerous high-altitude lakes of glacier origin within the state boundaries makes it relevant for the study. The present study generates a glacial lake inventory and performs a remote sensing based temporal growth assessment of the glacial lakes present within the state boundary.

1.5.2 Study sites for detailed risk assessment

a. Satopanth lake (Alaknanda Basin, Uttarakhand Himalaya)

The Satopanth lake (30°44'36.44" N, 79°21'25.69" E) is located in the northern part of the Alaknanda valley, in the state of Uttarakhand, Central Himalaya. It has an elevation of 4350 m a.s.l. The presence of a hydroelectric powerplant (HEP) located downstream of the lake at Vishnuprayag, Uttarakhand, Central Himalaya, make the study site important for detailed risk assessment.

b. Dhauliganga lake (Dhauliganga Basin, Uttarakhand Himalaya)

The Dhauliganga basin is a major basin located in the state of Uttarakhand, Central Himalaya. The lower and upper bounds of the basin lie between latitudes 29°58' N to 30°31' N and longitudes 80°21' E to 80°34' E encompassing a total area of 1667 km^2. Over 85 percent of the basin is covered with seasonal snow. Moreover, the area above 5000 m a.s.l. is restricted to permanent ice and snow. The primary importance of the study site lies in the fact that the largest proglacial lake (30°26'44.44"N and 80°23'14.00"E) lies adjacent to the mainstream of a hydropower dam located 72 km downstream of the lake at Gargua in Pithoragarh district.

c. Safed lake (Goriganga basin, Uttarakhand Himalaya)

The Safed lake (30°33′46.55″ N and 80°10′19.15″ E) is located in the northern part of the Goriganga basin in the state of Uttarakhand, Central Himalaya. The basin is drained mostly by the Goriganga river, originating from the Milam glacier. The lake has an elevation of 4882 m a.s.l. It is the largest proglacial lake in the basin with a total area of 0.023 km^2. A village "Milam" is located at a distance of 16.2 km downstream of the lake. It is a small village in the Pithoragarh district with a population of only 135. The primary importance of the study site lies in the fact that a part of the settlement of the village falls at the confluence of the Gonka (originating from the lake) and the Gori rivers.

d. South Lhonak lake (Teesta Basin, Sikkim Himalaya)

The South Lhonak Lake (27°54'43.70"N and 88°11'58.60"E) is located in the north-eastern part of the Teesta Basin, in Sikkim, Central Himalaya. The lake has an elevation of 5200 m a.s.l. It is a proglacial lake formed due to retreat of the South Lhonak glacier. At 62.35 km downstream of the lake, a major town called the "Chungthang" is located. Other minor townships along the valley are Lachen, Latong, and Yuigang. Also, the presence of a hydropower dam site located at the confluence of the Lachen and the Lachung rivers justifies the selection of the study site.

PRESENT

Glacier surface

Ice thickness

Glacial lake

Bed rock

Frontal moraine

a

FUTURE

Retreat of the parent glacier

Glacier thinning

A grown glacial lake

Newly exposed bed rock

Frontal moraine

b
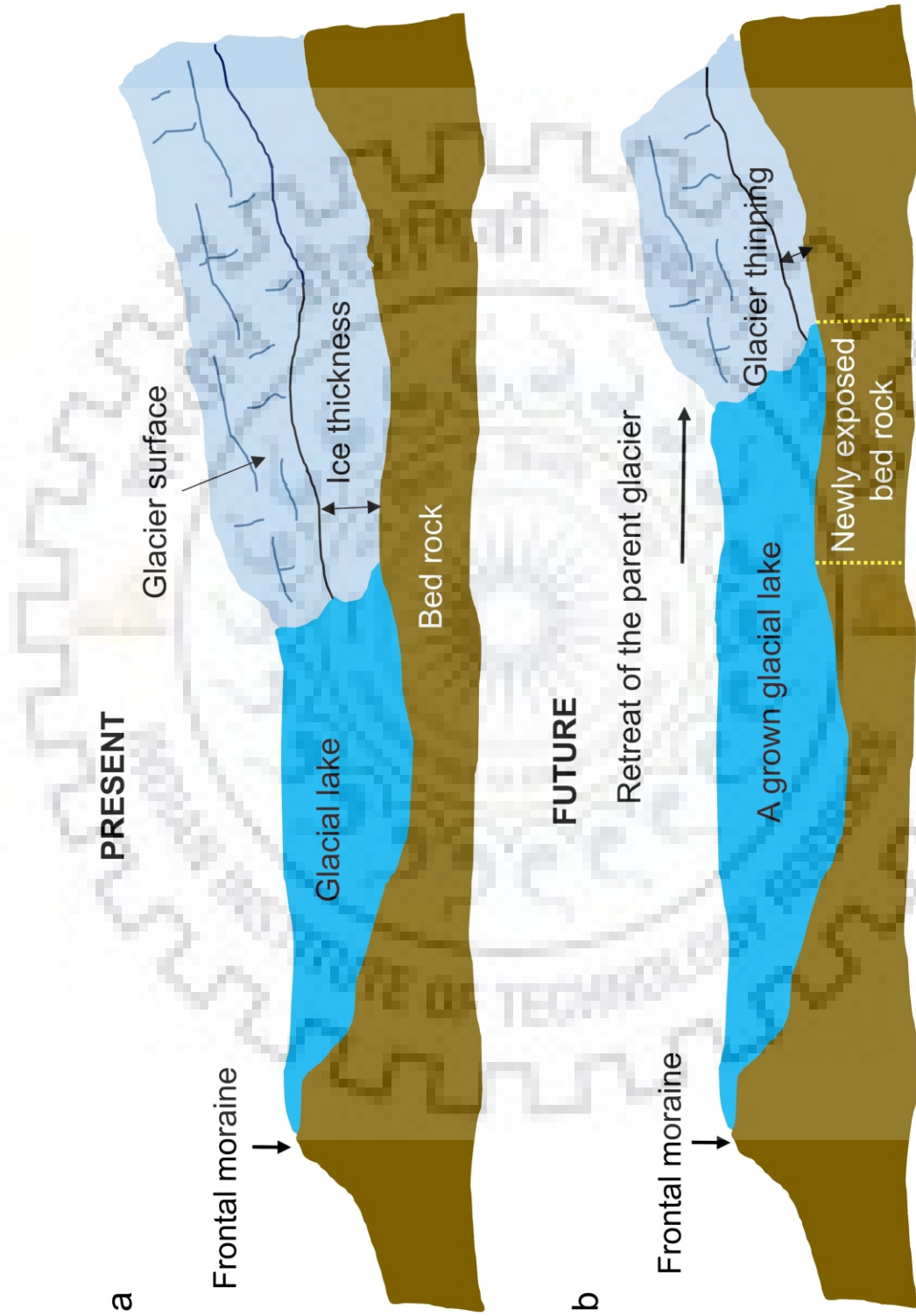
Figure 1.8 Schematic diagram showing the future expansion of a proglacial lake; (a) a proglacial lake system at present; (b) lake grows as the glacier bed is exposed in the future

1.6 ORGANIZATION OF THE THESIS

The present thesis is divided into seven chapters, the content in each chapter is briefly explained in the following:

Chapter 2 "Inventory of glacial lakes and temporal growth assessment"

In this chapter, an updated glacial lake inventory is prepared using satellite images and Digital Elevation Models (DEM). A growth assessment of the glacial lakes is performed by temporally mapping lake surfaces using historical remote sensing data. The inventory data created in this chapter is employed in the following chapter to evaluate the growth assessment of the individual lakes.

Chapter 3 "Field-based 1D and 2D hydrodynamic modeling of potential GLOF"

In this chapter, the integration of field data and modeling is adopted to evaluate the GLOF hazard of a potentially critical lake (Satopanth lake) in the state of Uttarakhand. The chapter demonstrates the field procedures for lake and moraine mapping. The impact of a potential GLOF event on a hydropower dam located downstream is evaluated using one- and two-dimensional dynamic modeling.

Chapter 4 "Bathymetry-based potential GLOF hazard assessment"

In this chapter, bathymetry-based dynamic modeling of GLOF is performed for the South Lhonak lake, Sikkim. Here, different moraine-breach mechanisms (overtopping and piping) is modeled to characterize potential GLOF events. The impact on the downstream region is evaluated using one- and two- dimensional hydraulic routing of the GLOF wave.

Chapter 5 "Ice-thickness based mapping of maximum lake extent - Impact analysis of potential future GLOF"

In this chapter, a glacier surface-velocity based ice thickness model is used to map the glacier bed in the Dhauliganga basin. The study identifies the overdeepenings in the glacier bed, which are potential lake formation sites in the future. The future extent of a proglacial lake (Dhauliganga lake) in the basin is mapped and its dynamic GLOF modeling is carried out considering the future volume of the lake. Its potential impact on a hydropower station located at a distance of 72 km downstream is evaluated. The study was extended to the South Lhonak lake Sikkim to evaluate the future GLOF potential. This is the first time that hydrodynamic modeling is employed to evaluate the future GLOF potential of existing proglacial lakes.

Figure 1.9 The Himalayan arc showing the study area in Uttrakhand and Sikkim Himalaya; the individual study sites are marked using different location points

Chapter 6 "Sensitivity analysis in hydrodynamic modeling of GLOF"

In this chapter, the sensitivity of the hydrodynamic model to Manning's N, breach width (B_w) and breach formation time (T_f) is evaluated. In addition, a sensitivity analysis of the model results (flow velocity and flow depth) to various channel characteristics like slope and top-width of the flow channel is evaluated by performing a series of hydrodynamic simulations. The study is performed on the Safed lake system, located in the Goriganga basin, in the state of Uttarakhand. The impact of the potential GLOF on the nearest settlement "Milam" located at a distance of 16.2 km is thereby analyzed.

Chapter 7 "Summary and conclusions"

This chapter summarizes the major findings of the overall work done on the glacial lake hazard assessment in the Central Himalaya and lists the recommendations based on the study.

PUBLICATIONS

REFERENCES

CHAPTER 2: INVENTORY OF GLACIAL LAKES AND ITS TEMPORAL GROWTH ASSESSMENT

2.1 INTRODUCTION

The formation of glacial lakes is a direct indication of glacier changes, as these lakes form when glaciers retreat (Gardelle et al., 2011). In the Himalaya, glacier retreat is reported in most of the regions except for the Karakoram, where glacier mass gain is observed (Bolch et al., 2012). The existence of the high-altitude lakes in the Himalaya makes it a potential hazard, as it imposes a risk of glacial lake outburst flood (GLOF) to the downstream regions (Richardson and Reynolds, 2000; Mool et al., 2001; Mool and Bajracharya, 2003; Worni et al., 2012). GLOF events have claimed thousands of human lives and caused severe damage to the low-lying areas in the Himalaya (Vuichard and Zimmermann, 1986; Tashi, 1994; Bhargava, 1995; Osti and Egashira, 2009; Dobhal et al., 2013; Das et al., 2015; Ray et al., 2016).

In the Himalaya, considering the risk of GLOF that it presents to the downstream regions, it is important to assess the locations of the glacial lakes, its growth, and outburst probability from time to time. A glacial lake inventory is a preliminary component for GLOF studies. Many studies in the past mapped glacial lakes over different regions on the Hindu Kush Himalaya (HKH) (Hewitt, 1982; Yamada and Sharma, 1993). Previous inventories of glacial lakes covered parts of Bhutan, Nepal, Tibet and India (Yamada and Sharma, 1993; Fujita et al., 2008; Komori, 2008; Raj et al., 2013; Wang et al., 2013). ICIMOD (2010) presented the first broad inventory of glacial lakes in different regions spanning over the HKH. The inventory reported a total of 8790 glacial lakes spread over Bhutan, Nepal, Pakistan, Tibet, and India. The glacial lakes were identified and mapped using topographic maps and satellite data (Landsat TM, LISS 3, SPOT) (Ives et al., 2010). Of the identified glacial lakes, 203 lakes were categorized as potentially dangerous based on their temporal growth assessment and the geomorphic setting of its associated moraines and surroundings. Worni et al. (2013) presented the glacial lake inventory covering the entire Indian Himalaya. The lakes were mapped using Landsat ETM+ from 2000 to 2002 and google earth imageries. A total of 251 glacial lakes with an area > 0.01 km^2 were identified of which 12 lakes were critical and 93 were potentially critical based on a lake outburst probability analysis. A detailed hazard assessment of 4 out of 12 critical lakes was performed using sophisticated hydrodynamic models (Worni et al., 2013).

In the context of central Indian Himalaya that includes the state of Sikkim and Uttarakhand, several glacial lake inventories are available in the previous literature. For the state of Sikkim, the maximum number of glacial lake inventories are available till date, of which the first glacial lake inventory was presented by Mool and Bajracharya. (ICIMOD, 2003), where 266 lakes were mapped with a total area of 20.2 km^2 in which 14 lake were identified to be potential critical. In 2013 (Banerjee, 2013, Thesis-IIRS) mapped a total of 270 lakes in the state of Sikkim, of which 73% of the lakes were located in the elevation band of 4800 m-5600 m. Satellite data of Landsat MSS, TM and ETM+ was employed to create the inventory. The third glacial lake inventory for Sikkim was presented by Raj et al. (2013) in which satellite data of Resourcesat-1 and LISS 3, from 2005 to 2010 were used to generate the database. A total of 320 lakes were identified and mapped for the year 2010. A total of 85 new lakes has been reported to have formed from 2003 (ICIMOD) to 2010 (Raj et al., 2013). Another glacial lake inventory for the state of Sikkim was presented by Haakeem et al. (2018) where a total of 644 lakes (> 0.001 km^2) were mapped for the year 2014 covering a total area of 29.7 km^2. Remote sensing images of Resourcesat 2, LISS IV and Landsat ETM were used to create the inventory. Later, Aggarwal et al. (2017) presented an inventory of glacial lakes using Resourcesat 2 and LISS IV imageries, reporting a total of 472 lakes (> 0.01 km^2) till 2015, of which 21 lake were identified as potentially critical. A latest glacial lake inventory was presented by Shukla et al. (2018). A total of 466 lakes were mapped (> 0.003 km^2) using Hexagon, Landsat TM, ETM, OLI, and Sentinel 2 datasets till 2017.

For Uttarakhand Himalaya, the database for glacial lake inventory is very limited. Worni et al. (2013) identified 27 lakes (>1.01 km^2) of which 52% were reported as potentially critical. The data used to create the inventory was Landsat ETM+ imageries from the year 2000 to 2002. Figure 2.1 presents the glacial lake outburst probability assessment performed to create a database of critical and potentially critical glacial lakes based on dam type, dam geometry, freeboard, and potential lake impacts (modified after Worni et al., 2013). The latest glacial lake inventory of Uttarakhand was presented by Raj and Kumar (2016). They mapped glacial lakes in the entire state using high-resolution Corona, Hexagon and LISS IV satellite imageries. A total of 362 lakes were identified in the entire state which included supraglacial, proglacial, erosional, and blocked lakes. Temporal growth assessment of selected lakes was carried out from 1962 to 2013.

In this chapter, inventory and growth assessment of the glacial lakes in the state of Sikkim and Uttarakhand (central Indian Himalaya) is presented. In Uttarakhand, as no growth assessment of the glacial lakes in terms of number and area has been performed after 2013, there lies a research gap to further evaluate the glacial lake dynamics in the state. Here, an updated glacial lake

Lake outburst susceptibility	Low	Medium	High
Dam Type	No dam , Rock dam	Ice dam	Moraine dam
Dam geometry — Width-height ratio	> 0.5	0.2-0.5	0.1-0.2
Moraine crest width	> 60 m	-	< 60 m
Slope of the downstream face of the moraine	< 20 degrees	-	> 20 degrees
Moraine freeboard	> 15 m	5-15 m	< 5 m
Potential for lake impact — Ice / snow avalanches	No	-	Yes
Debris flow / rock fall	No	-	Yes

Figure 2.1 Lake outburst probability analysis to identify potentially critical glacial lakes (modified after Worni et al., 2013)
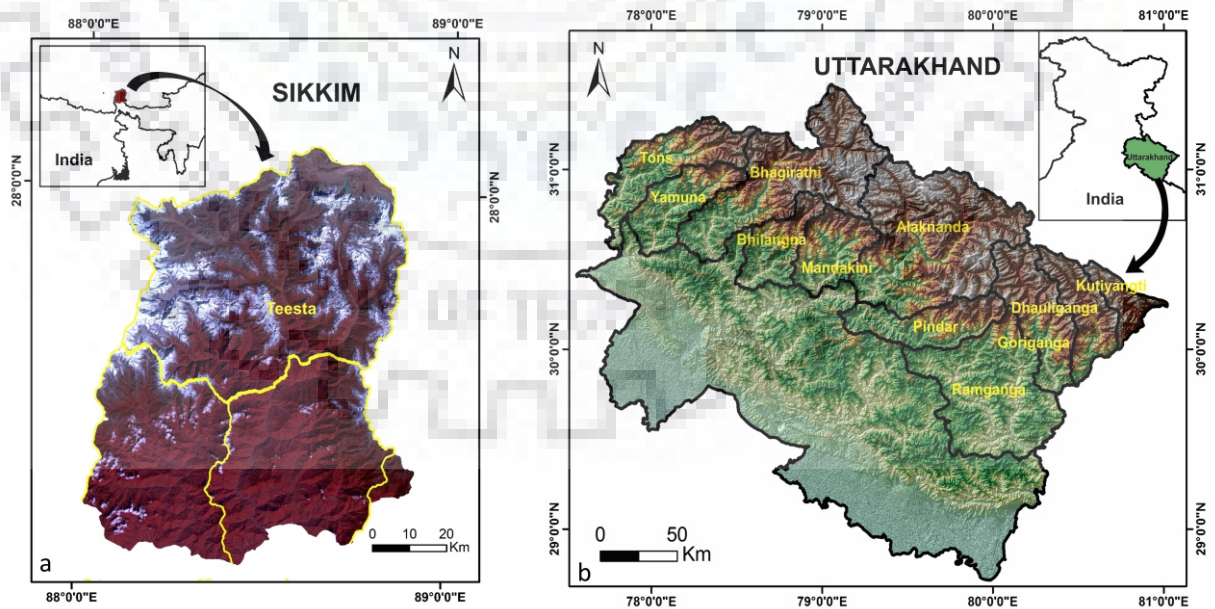
Figure 2.2 The state of (a) Sikkim and (b) Uttarakhand showing the major river basins

inventory of glacial lakes for the state of Uttarakhand is presented. A temporal assessment was performed to evaluate the change in the number and area of the glacial lakes in in the state. For, Sikkim Himalaya a total of six glacial lake inventories were previously available (Mool and Bajracharya, 2003; Banerjee, 2013; Raj et al., 2013; Haakeem et al., 2018; Aggarwal et al., 2017; Shukla et al., 2018). To avoid redundancy of data, the study is restricted to the growth evaluation of the larger lakes which are identified as critical and potentially critical in the state.

2.2 STUDY AREA

The present study is carried out in the central Indian Himalaya (Uttarakhand and Sikkim). Since lakes of glacier origin lie in the high-altitude regions of Himalaya, the study is restricted to elevation above 3500 m a.s.l. The state of Uttarakhand lies between the latitudes 28°43′–31°27′N and longitudes 77°34′–81°02′E encompassing a total area of 53,484 km^2. It lies within the elevation band of 210 to 7800 ma.s.l. The state of Uttarakhand is divided into 11 river basins namely Alaknanda, Bhagirathi, Dhauliganga, Ramganga, Goriganga, Kutiyangti, Tons, Mandakini, Bhilangna, Pindar, and Yamuna.

The state of Sikkim lies between 27°04′N to 28°07′N latitude and 80°00′E to 88°55′E longitude with a total area of 7,096 km^2. The major part (>90%) of Sikkim falls under the Teesta river basin. The state is surrounded by Bhutan in the east, Nepal in the west, China (Tibet) in the north and West Bengal in the south. Figure 2.2 shows the central Himalayan states of Sikkim (A) and Uttarakhand (B) and their major river basins.

2.3 DATA USED

The study employs time series data acquired by different satellite sensors. Optical remote sensing images of Landsat TM, ETM+, OLI of 30 m resolution were used to map the glacial lakes. The Advanced Spaceborne Thermal Emission and Reflection Radiometer (ASTER) global digital elevation model (DEM) (v2) was used to extract topographic information. ASTER GDEM (v2) is a latest version of publicly available elevation model (https://earthexplorer.usgs.gov/) that provides elevation information between 83°N and 83°S with a spatial resolution of 30 m and a vertical accuracy of ~10-20 m for hilly terrains (Fujita et al., 2008; Tachikawa et al., 2011). The historical extent of the lakes was mapped using cloud-free declassified aerial photographs of Corona KH-4 (7.5 m). The Corona database is a collection of very high-resolution aerial images acquired from 1960 to 1972 during a space reconnaissance programme, operated jointly by the Central Intelligence Agency (CIA) and the US Air Force (USAF) (Dashora et al., 2007). The Landsat and Corona data used in the study are freely downloaded from https://earthexplorer.usgs.gov/. The acquisition dates and sensor information for the Corona, Landsat TM, ETM+, and OLI are given in Table 2.1 to 2.4 respectively.
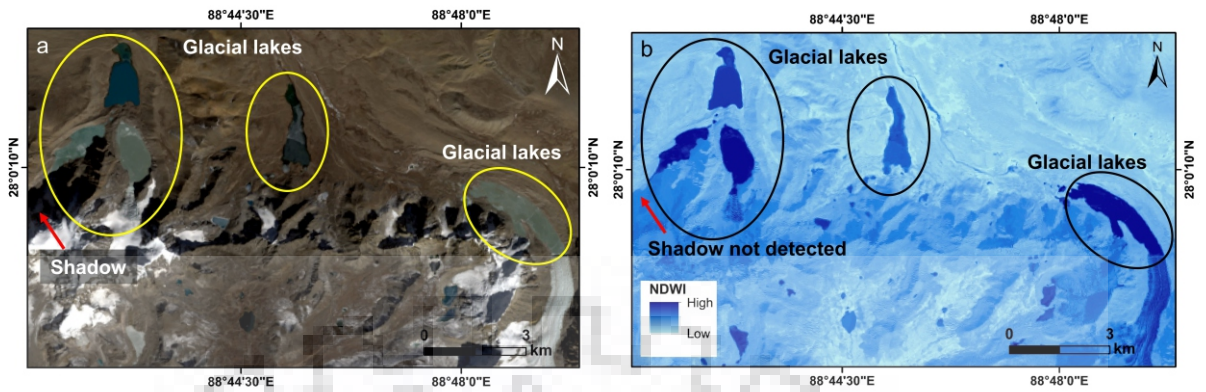
Figure 2.3 Glacial lakes identification using (a) optical remote sensing data, (b) Normalized Differential Water Index (NDWI)
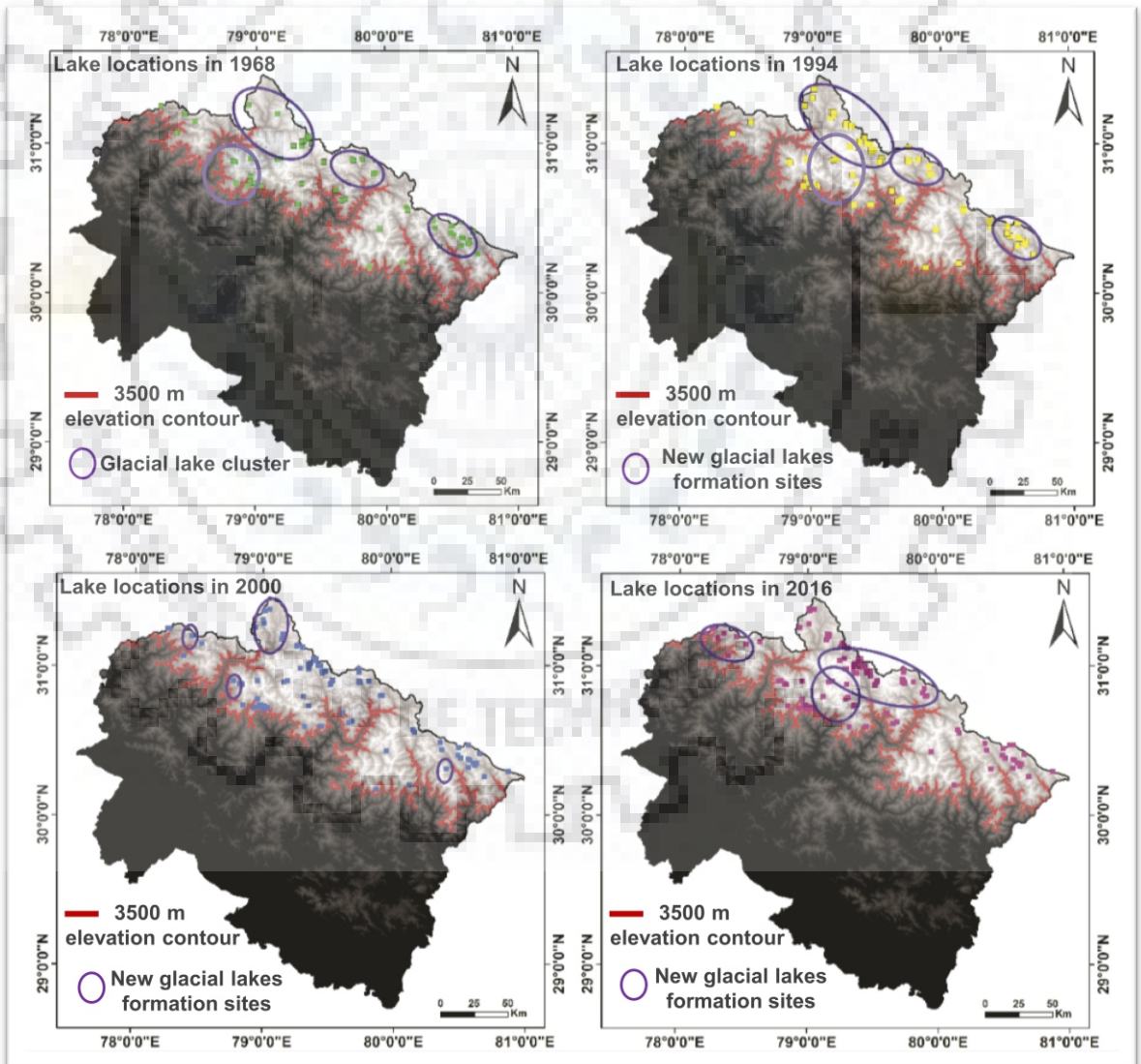
Figure 2.4 Location of glacial lakes (> 0.01 km^2) and the new lake formation sites for the year 1968, 1994, 2000, and 2016 in the state of Uttarakhand, central Himalaya

Table 2.1 Specifications of CORONA data

Sl. No.	Data	Date of acquisition	Sensor	Area of interest
1	DS1024-1023DF118	24-09-1965		
2	DS1024-1023DA121	24-09-1965		
3	DS1024-1023DA123	24-09-1965		
4	DS1048-1134DA108	27-09-1968	KH4/CORONA	Uttarakhand Himalaya
5	DS1048-1134DA109	27-09-1968		
6	DS1048-1134DA110	27-09-1968		
7	DS1048-1134DA111	27-09-1968		
8	DS1048-1134DA112	27-09-1968		

Table 2.2 Specifications of LANDSAT TM data

Sl. No.	Data	Date of acquisition	Sensor	Area of interest
1	LT05_L1TP_145039_19941025_20170111_01_T1	25-10-1994		
2	LT05_L1TP_144039_19941018_20170111_01_T1	15-11-1994		
3	LT05_L1TP_146038_19940930_20170112_01_T1	30-09-1994	LANDSAT TM	Uttarakhand Himalaya
4	LT05_L1TP_146039_19941016_20170111_01_T1	16-10-1994		
5	LT05_L1TP_139041_19901223_20170129	23-12-1990	LANDSAT TM	Sikkim Himalaya

Table 2.3 Specifications of LANDSAT ETM+ data

Sl. No	Data	Date of acquisition	Sensor	Area of interest
1	LT05_L1TP_139041_20001031_20161213	03-10-2000	LANDSAT ETM+	Sikkim Himalaya
2	LT05_L1TP_139041_20101214_20161011	14-12-2010		
3	LE71450392001293SGS00	20-10-2001		
4	LE71440392001286SGS00	13-10-2001		
5	LE71470382001291SGS00	18-10-2001	LANDSAT ETM+	Uttarakhand Himalaya
6	LE71450382001293SGS00	20-10-2001		
7	LE71460382000282SGS00	07-10-2002		

Table 2.4 Specifications of LANDSAT OLI/TIRS data

Sl. No.	Data	Date of acquisition	Sensor	Area of interest
1	LC08_L1TP_146039_20161028_20170319_01_T1	28-10-2016		
2	LC08_L1TP_145039_20161021_20180524_01_T1	21-10-2016		
3	LC08_L1TP_144039_20161014_20170319_01_T1	14-10-2016	LANDSAT OLI/TIRS	Uttarakhand Himalaya
5	LC08_L1TP_146038_20161028_20170319_01_T1	28-10-2016		
6	LC08_L1TP_145039_20161021_20180524_01_T1	21-10-2016		
7	LC08_L1TP_139041_20181220_20181227_01_T1	20-12-2018	LANDSAT OLI/TIRS	Sikkim Himalaya

Table 2.5 Specifications of ASTER DEM

Sl. No.	Data	Scene ID	Area of interest
1		ASTGDEMV2_0N29E077	
2		ASTGDEMV2_0N29E078	
3		ASTGDEMV2_0N29E079	
4		ASTGDEMV2_0N29E080	
5	ASTER GDEM	ASTGDEMV2_0N30E077	Uttarakhand Himalaya
6		ASTGDEMV2_0N30E078	
7		ASTGDEMV2_0N30E079	
8		ASTGDEMV2_0N30E080	
9		ASTGDEMV2_0N31E078	
10		ASTGDEMV2_0N31E079	
11		ASTGDEMV2_0N27E087	
12	ASTER GDEM	ASTGDEMV2_0N27E088	Sikkim Himalaya
13		ASTGDEMV2_0N28E088	

2.4 METHODOLOGY

The study is conducted in the high-altitude regions of the central Indian Himalaya. ASTER GDEM is employed to demarcate the elevation contour of 3500 m a.s.l. The mapping of glacial lakes is restricted to the region above 3500 m elevation contour and to the lake with a total surface area >0.01 km^2. The Normalized Difference Water Index (NDWI) method is employed to identify and map the existing glacial lakes. NDWI is a band rationing method that utilizes the two regions of the electromagnetic spectrum -blue (0.63-0.69 µm) and the near infrared region (0.76-0.90 µm). The low reflectance property of water in the NIR band and high reflectance in the green band is exploited to map the water surfaces of the existing glacial lakes (Huggel et al., 2002; Bulley et al., 2013). The formula for NDWI is given as:

$$NDWI = \frac{Green - NIR}{Green + NIR} \qquad \text{eq. 1}$$

The NDWI method proved to be efficient in detecting larger lake surfaces throughout the study region (Uttarakhand and Sikkim). However, due to similar reflectance properties of shadows, smaller lake surfaces sometimes remain undetected by this automated approach. Also, lakes in the semi-frozen state are often misclassified. Therefore, visual interpretation of the glacial lakes with the help of high-resolution google-earth imageries is adopted. A temporal growth assessment of the glacial lakes is performed by mapping lake surfaces using time series data. The historical high-resolution google-earth data is exploited to evaluate the past extent of the lakes. Figure 2.3 shows the detection of the glacial lakes using the NDWI method.

2.5 RESULTS AND DISCUSSION

2.5.1 Glacial lake inventory and temporal growth assessment in Uttarakhand Himalaya

Glacial lake inventories were prepared for the year 1968, 1994, 2000-02, and 2016. The study was confined to 3500 m a.s.l. in the entire state of Uttarakhand. A temporal growth assessment of the glacial lakes (>0.01 km^2) was carried out using temporally separated optical satellite imageries, the details of which are given in section 2.3. A total of 61 glacial lakes were identified and mapped in 1968 using historical Corona datasets. The number of lakes increased to 90, 105, and 130 for the year 1994, 2000- 02, and 2016 respectively (Figure 2.5). Figure 2.4 shows the locations of glacial lakes (>0.01 km^2) and the sites of new lake formation for the year 1968, 1994, 2000-02, and 2016. The lakes were mapped based on NDWI (Section 2.4) and visual interpretation. The area of individual lakes was calculated using GIS-based tools. The total area of all the mapped glacial lakes in the state has increased from 1.90 km^2 to 4.90 km^2 in a period of 48 years from 1968 to 2016. Figure 2.6 shows the increase in the total surface area of the glacial lakes over the years.

The state of Uttarakhand was subdivided into eleven river basins (Figure 2.2b), of which glacial lakes exist in nine basins. The basin-wise distribution of glacial lakes in the state of Uttarakhand is given in Table 2.6. The Alaknanda basin has the maximum number of glacial lakes with a total of 56 lakes (Figure 2.7). A total of 33 new lakes formed in the basin within a span of 48 years from 1968 to 2016. The Bhagirathi basin has the second largest number of glacial lakes next to Alaknanda. It has a total of 28 lakes (2016) which increased from 10 lakes in the year 1968.

ASTER GDEM is employed to create contour bands of 500 m covering the entire state of Uttarakhand. A total of six elevation bands are created within the total elevation range of 3500 to 6000 m a.s.l. The distribution of the lakes within each elevation band was evaluated using GIS-based overlay operations. It is evident that the maximum number of lakes in the state occur in the elevation band of 4000 m-4500 m. Moreover, this elevation band shows the maximum increase in the total number of lakes over the years (1968 to 2016). The second maximum number of lakes exists in the elevation band of 5000 m-5500 m. The elevation band of 3500 m-4000 m contains the least number of glacial lakes. Figure 2.8 shows the elevation-wise distribution of glacial lakes in the state of Uttarakhand from 1968 to 2016.
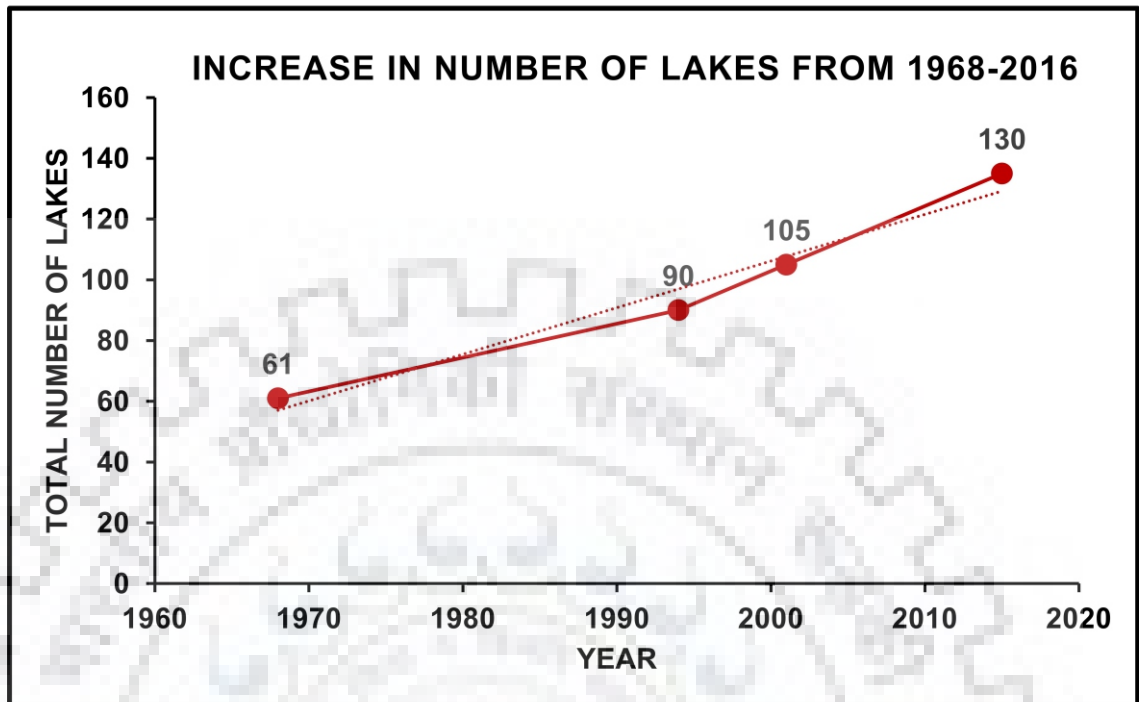
Figure 2.5 Increase in the total number of glacial lakes in the state of Uttarakhand from 1968 to 2016; the total number of lakes increased from 61 to 130
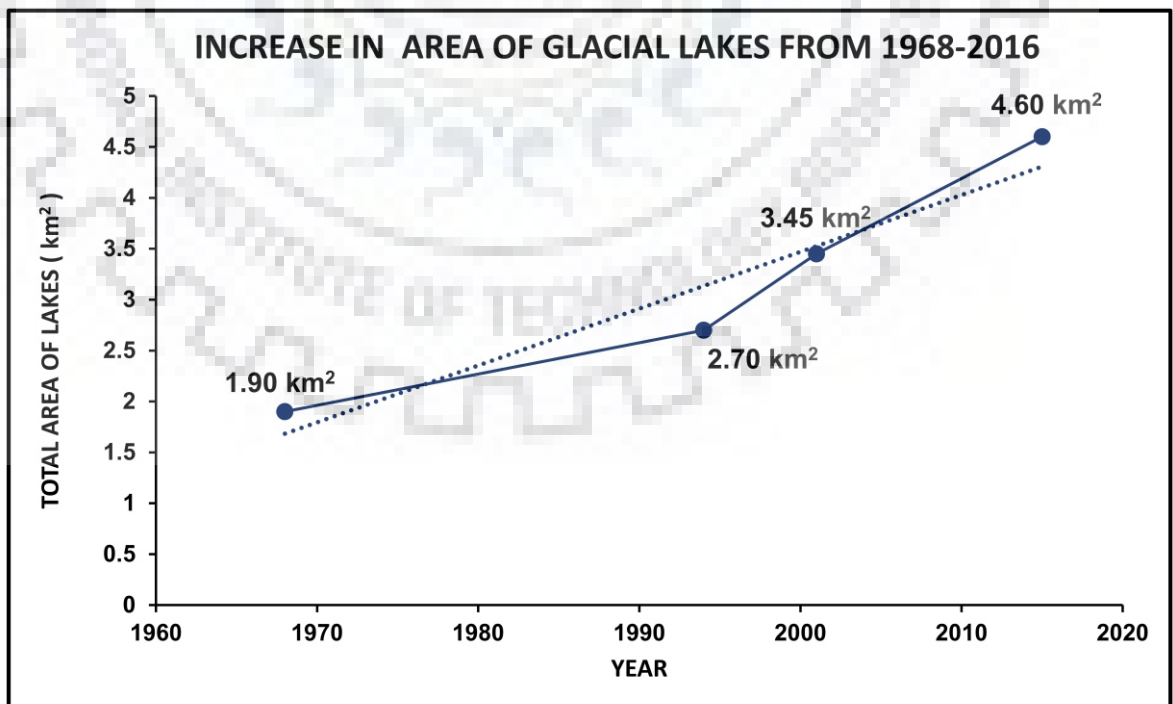
Figure 2.6 Increase in the total surface area (in km^2) of the glacial lakes in the state of Uttarakhand from 1968 to 2016; the total lake area increased from $1.9\,km^2$ to $4.60\,km^2$
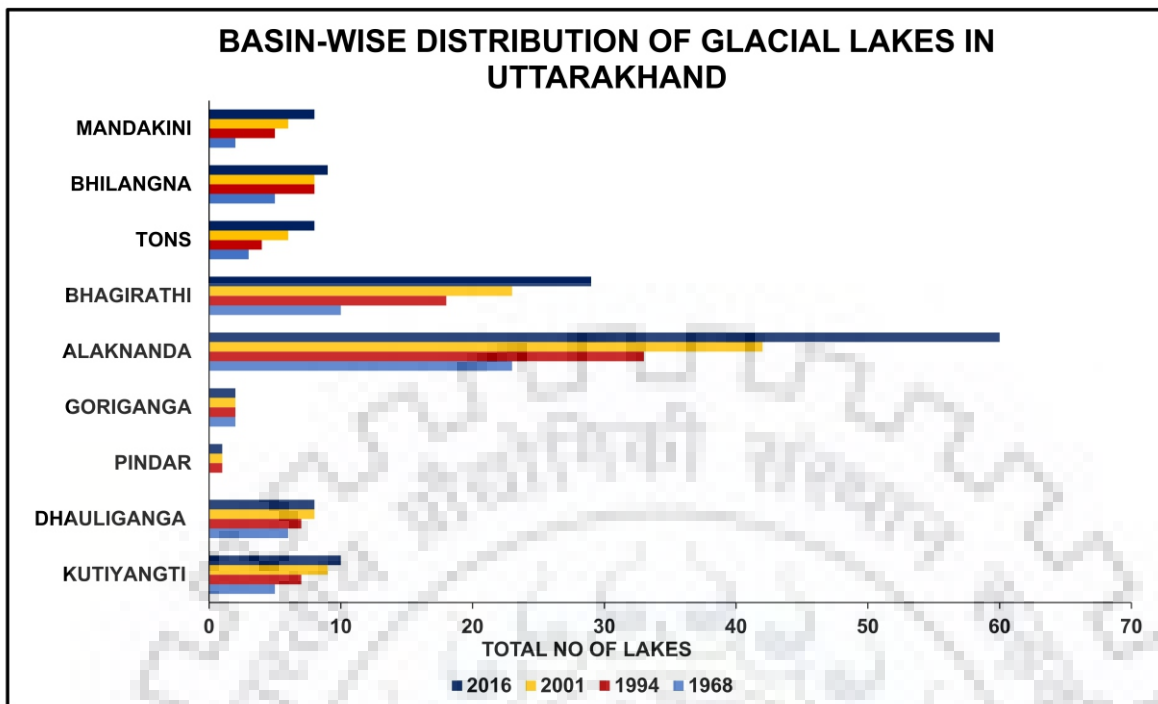
Figure 2.7 Basin-wise distribution of glacial lakes in the state of Uttarakhand for the years 1968, 1994, 2001, and 2016
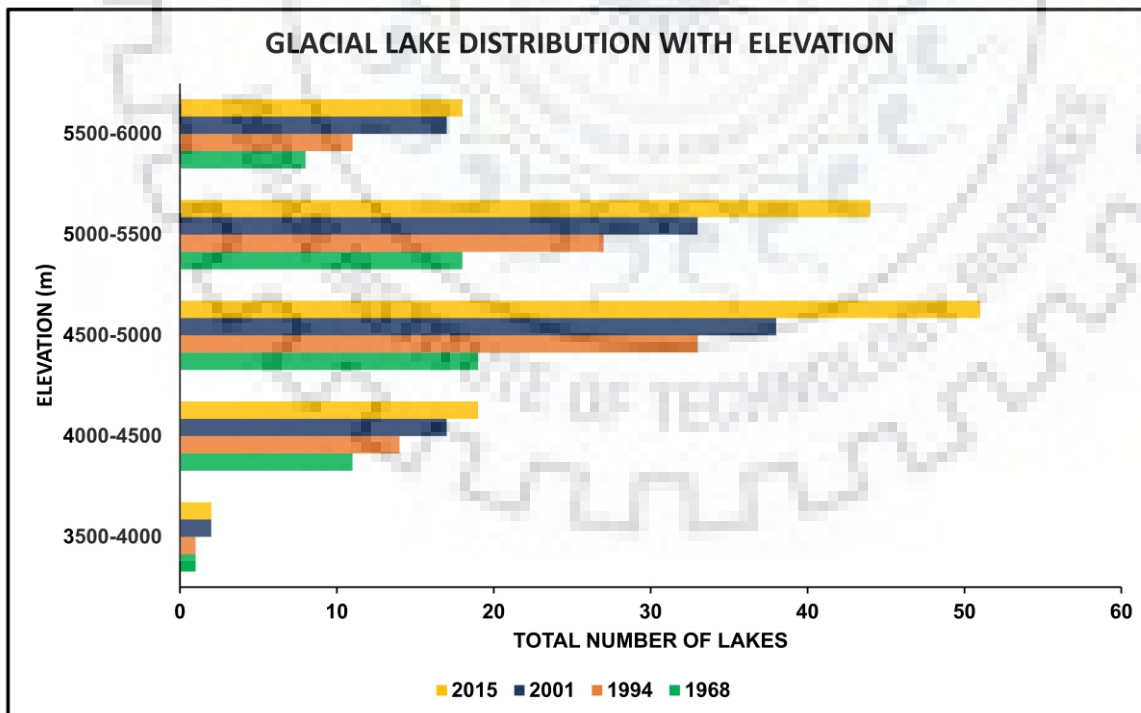
Figure 2.8 Elevation-wise distribution of glacial lakes in the state of Uttarakhand for the years 1968, 1994, 2001, and 2016
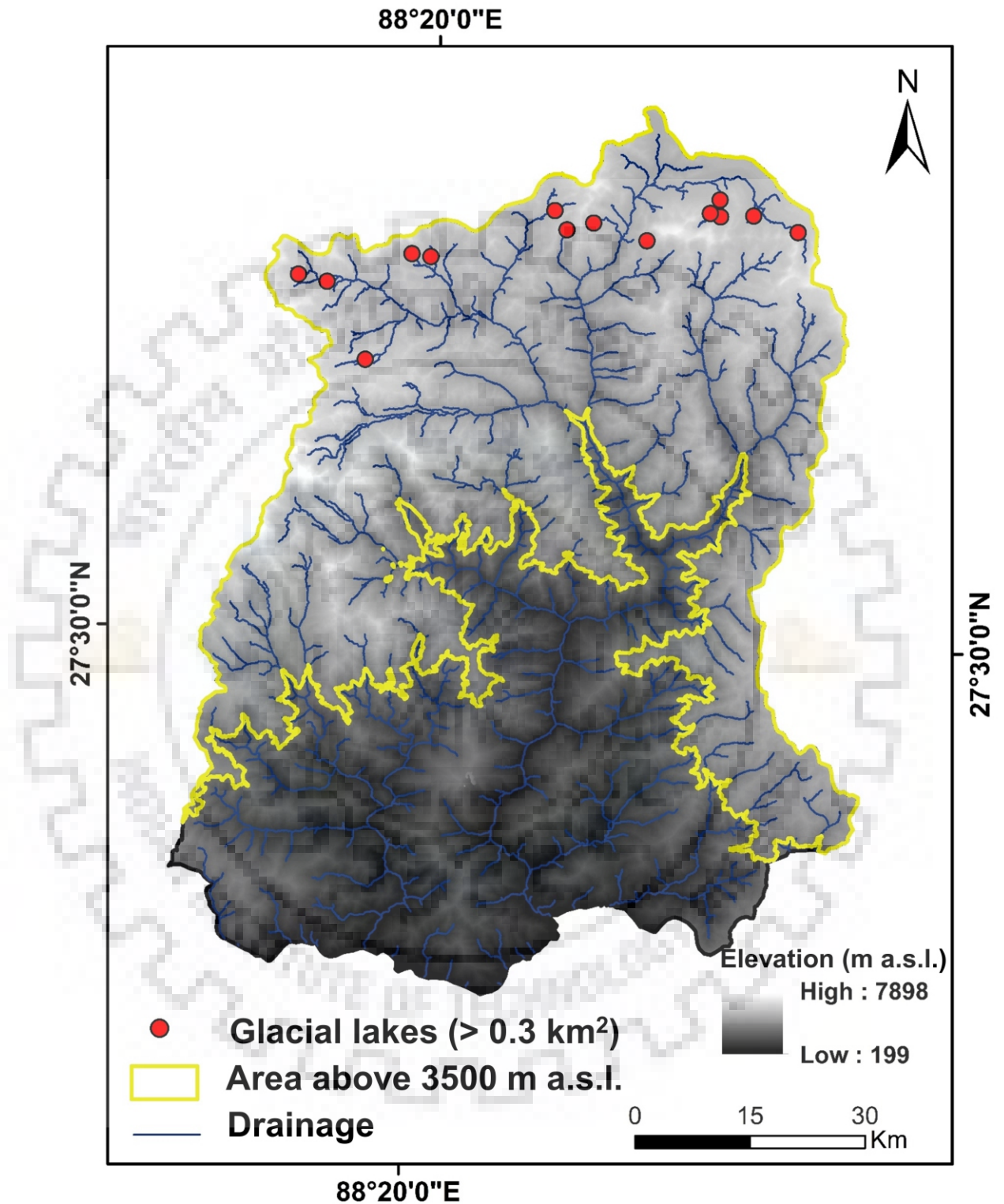
Figure 2.9 Map showing the locations of larger glacial lakes in the state of Sikkim (> 0.3 km^2)

Table 2.6 Basin-wise distribution of glacial lakes in the state of Uttarakhand

Year	KYG	DHG	PND	GRG	ALK	BHR	TON	BHG	MDK	Total
1968	5	6	0	2	23	10	3	5	2	56
1994	7	7	1	2	33	18	4	8	5	85
2001	9	8	1	2	42	23	6	8	6	105
2016	10	8	1	2	56	28	8	9	8	130

KYG:Kutiyangti; DHG:Dhauliganga; PND:Pindar; GRG:Goriganga; ALK:Alaknanda; BHR: Bhagirathi; TON: Tons; BHG:Bhilangna; MDK:Mandakini

2.5.2 Glacial lake inventory and temporal growth assessment in Sikkim Himalaya

As several glacial lake inventories are already available for the state of Sikkim from the previous literature (Section 2.1). Also, previous hazard assessments of the glacial lakes in the state of Sikkim (Mool and Bajracharya 2003; Worni et al., 3013; Raj et al., 2013; Aggarwal et al., 2017) shows that the larger lakes (> 0.3 km ^{2}) in Sikkim are critical or potentially critical (Table 2.7). To avoid redundancy of data, the present study is therefore restricted only to identify and map the larger lakes (> 0.3 km^2) in the state. The larger glacial lakes were mapped for the year 1990, 2000, 2010, and 2018. The study is confined to 3500 m a.s.l in the entire state of Sikkim. Figure 2.9 shows the state of Sikkim and the location of the larger glacial lakes in the state. A growth assessment of the glacial lakes (> 0.3 km^2) was carried out using temporally separated optical satellite imageries, the details of which are given in section 2.3. A total of 14 glacial lakes were identified with a present lake surface area of > 0.3 km^2. The distribution of these lakes with respect to elevation is evaluated using contours (500 m) extracted from DEM. It is evident that all the larger lake in the state lies in the elevation band of 5000 m-5500 m. Figure 2.10 shows the location of glacial lakes plotted over elevation contours.

The lakes were mapped based on NDWI (Section 2.4) and visual interpretation to calculate the area of individual lakes. The total area of the larger lakes (> 0.3 km^2) in the state is calculated to be 11.6 km^2 for the year 2018. The total area of the lakes increased by 3.5 km^2 over a period of 28 years from 1990 to 2018. The growth assessment of the individual lakes is carried out by mapping the lake surfaces for different years. Figure 2.11 shows the outlines of the individual lake for the year 2018.

Of the 14 identified larger glacial lakes in the state, "Lake 14" is the largest with a total area of 1.77 km^2. It is followed by "Lake 2" which has a total area of 1.31 km^2. The area of the individual lakes for the years 1990, 2000, 2010, and 2018 is given in Figure 2.12. It is evident that "Lake 3" has shown the maximum change over the years from 1990 to 2018 (Figure 2.13). It shows a total percentage increase of 98.8% in its area. It is followed by "Lake 7" which showed a
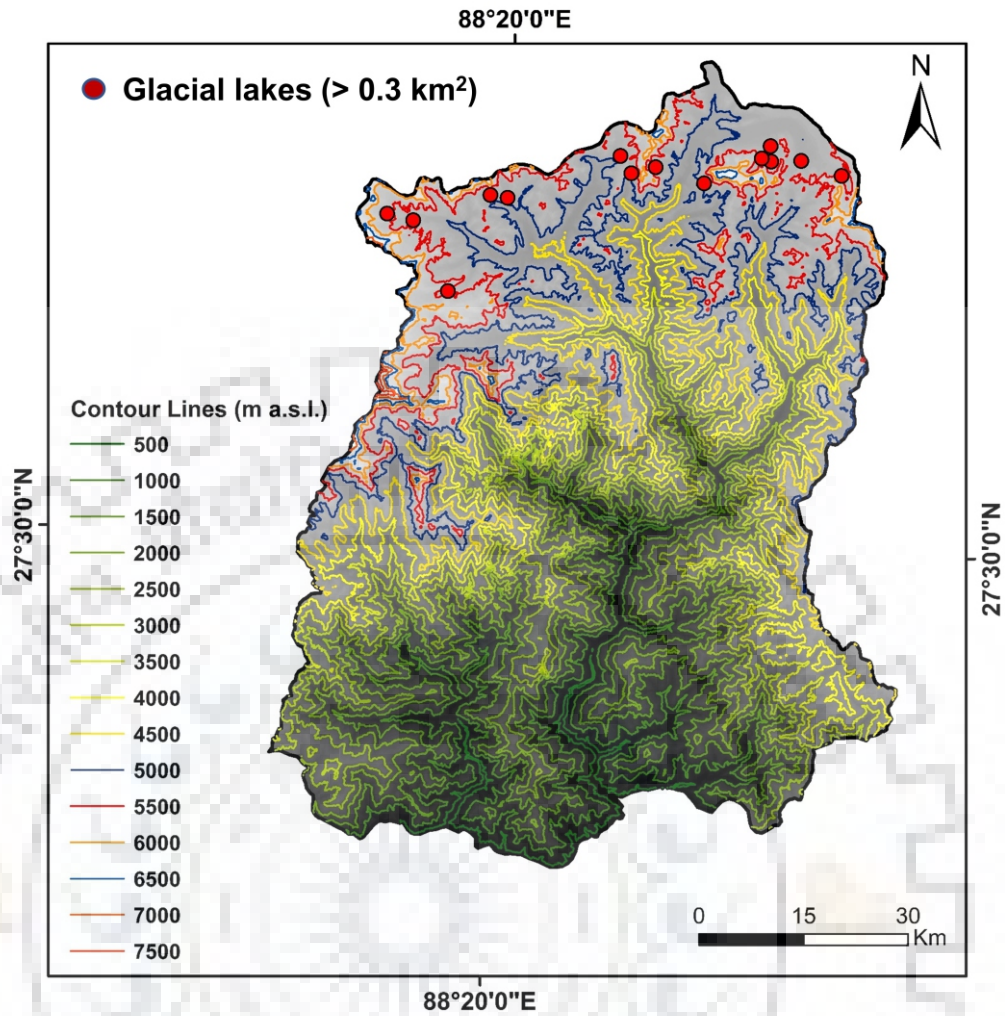
Figure 2.10 The state of Sikkim showing the lake locations and elevation contours at an interval of 500 m; the larger lakes in the state lies in the elevation band of 5000 m-5500 m a.s.l.
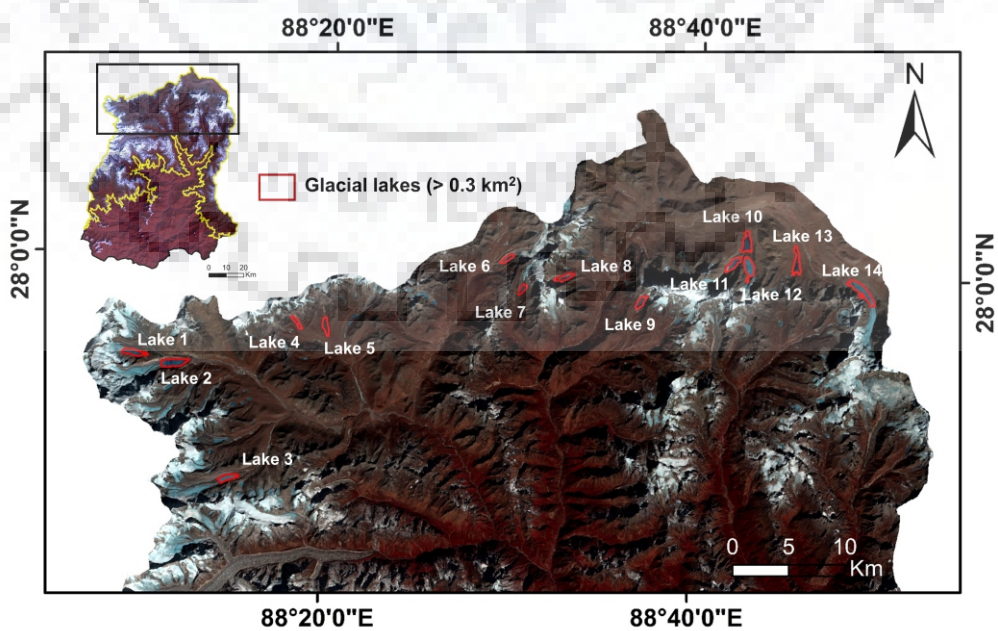
Figure 2.11 Glacial lake outlines (2018) of the larger lakes (> 0.3 km^2) in the state of Sikkim; the lakes are numbered as 1 to 14 from left to right
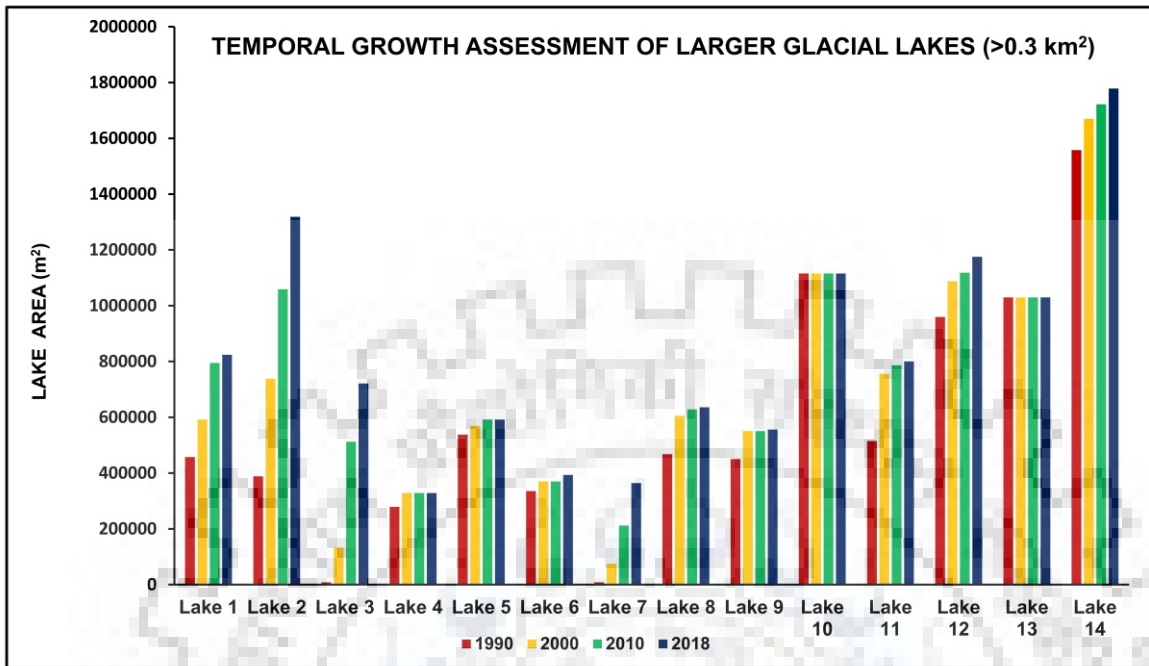
Figure 2.12 Lake-wise area for the years 1990, 2000, 2010, and 2018; the lake numbers correspond to Figure 2.11
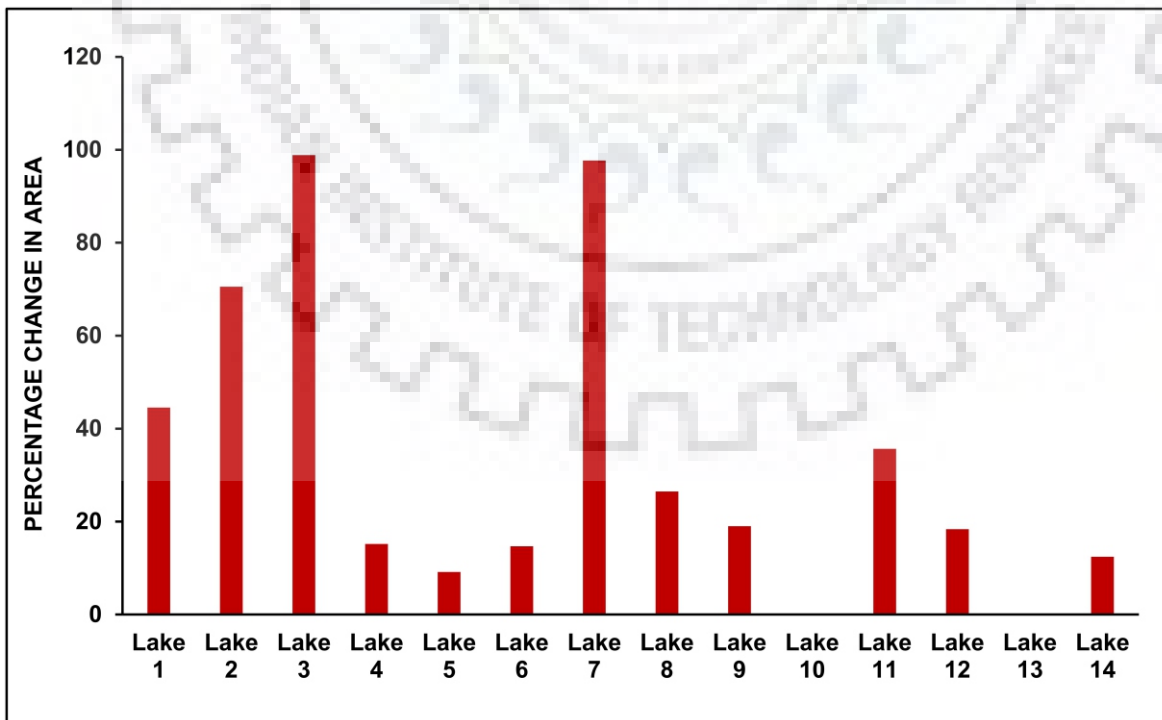
Figure 2.13 Lake-wise percentage change in the total surface area from 1990 to 2018; the lake numbers correspond to Figure 2.11

percentage increase in its total area by 97.6% within a period of 28 years. "Lake 2" shows a percentage change of 70.53%, as the size of the lake increases from 0.38 km^2 (1990) to 1.31 km^2 (2018). The remaining lakes showed an average percentage increase of 17.8% in their total area.

A comparison of the previous hazard assessments- (i) Mool and Bajracharya. (ICIMOD 2003), (ii) Worni et al. (2013), and (iii) Aggarwal et al. (2017) of the selected larger glacial lakes in the state is compared. Table 2.12 shows the comparison of the outburst probability and GLOF susceptibility of the 14 lakes identified in the present study. Based on the comparison, Lake 2 (South Lhonak lake), was reported to have high outburst probability (ICIMOD, 2003; Worni et al., 2013) and high GLOF susceptibility (Aggarwal et al., 2017). In addition, Lake 11 and 12 (twin lakes of Kangchengyao) were also identified as potentially critical.

Table 2.7 Outburst probability and GLOF susceptibility for the larger lakes in Sikkim reported in the previous literature; the lake numbers correspond to Figure 2.11; lake 2 was reported to be potentially dangerous, critical and with high GLOF susceptibility in all previous studies (highlighted in dark grey)

Lake No.	Outburst probability ICIMOD (2003); Raj et al. (2013)	Outburst probability (Worni et al., 2013)	GLOF susceptibility (Aggarwal et al., 2017)
1	Potentially dangerous	Potentially critical	Medium
2	Potentially dangerous	Potentially critical	High
3	Potentially dangerous	Potentially critical	Low
4	Not dangerous	Potentially critical	Medium
5	Not dangerous	Potentially critical	Medium
6	Potentially dangerous	Potentially critical	Medium
7	Not dangerous	Potentially critical	Medium
8	Not dangerous	Critical	Medium
9	Not dangerous	Critical	Medium
10	Potentially dangerous	Potentially critical	Low
11	Potentially dangerous	Critical	Medium
12	Not dangerous	Critical	High
13	Not dangerous	Potentially critical	Low
14	Potentially dangerous	Potentially critical	Low

Basis: ICIMOD (2003), Raj et al. (2013)- past GLOF events, field observations, geomorphological and geo-technical properties, size and position with respect to the parent glacier; Worni et al. (2013)- Dam type, dam geometry, freeboard, and potential for lake impacts; Aggarwal et al. (2017)- Analytic Hierarchy Method and Weighted Index Overlay Analysis considering lake growth, freeboard, slope, distance from the glacier, lake type, activity of lake, physical surroundings and tectonic activity.

2.6 CONCLUSION

In this study, an updated glacial lake inventory for central Indian Himalaya is produced. The temporal growth assessment to the glacial lakes were carried out by mapping the past extents of lake surfaces using remote sensing datasets. The state of Uttarakhand has shown a linear growth in the number of glacial lakes from 1968 to 2016. The total number of lakes increased from 61 to 130 within a span of 48 years, with a maximum change occurring in the Alaknanda basin. The distribution of the lakes with respect to elevation shows the existence of maximum lakes in the elevation range of 4500-5000 m a.s.l.

In the state of Sikkim, a total of 14 large glacial lakes (> 0.3 km^2) were identified in the entire state, the surfaces of which were mapped for 1990, 2000, 2010, and 2018. It was evident that the total area of the lakes increased by 3.5 km^2 over a period of 28 years from 1990 to 2018. All the larger lakes lie in the elevation band of 5000 -5500 m a.s.l. Three of the fourteen lakes showed an average percentage increase of 89% in its total area over a period of 28 years.

The inventory data presented in the study is exploited in the following chapters (Chapters 3, 4, 5 and 6) where growth assessment of a selected potentially critical lakes is performed. Hazard assessment of the selected lakes is performed using complex hydraulic modeling to evaluate its GLOF potential. The lakes selected for detailed GLOF assessment were selected from the based on the present inventory and the GLOF susceptibility reported in the previous literature. In Sikkim the hazard assessment of the lakes in the previous literature shows the larger lakes to be potentially critical, it can be attributed to their larger volume and other determining factors (Table 2.7). Of all the larger lakes in Sikkim, Lake 2 (South Lhonak lake) was reported to have high outburst probability (ICIMOD, 2003; Worni et al., 2013) and high GLOF susceptibility (Aggarwal et al., 2017). The identified lake "Lake 2" is considered for detailed risk assessment in the following chapters (Chapter 4 and Chapter 5). In the Uttarakhand Himalaya, three potentially critical glacial lakes were selected based on their accessibility and availability of remote sensing data namely, the Satopanth lake, Dhauliganga lake, and the Safed lake. The detailed risk assessment of which is presented in the following chapters (Chapter 3, Chapter 5 and Chapter 6).

CHAPTER 3: FIELD-BASED 1D AND 2D HYDRODYNAMIC MODELING OF POTENTIAL GLOF

3.1 INTRODUCTION

Glacier retreat driven by climate change may often be associated with the formation of glacial lakes (Komori, 2008; Gardelle et al., 2011; Haritashya et al., 2009). The catastrophic failure of these lakes may cause great damage to the low-lying communities and infrastructure (Lliboutry et al., 1977; Haeberli, 1983; Carey, 2005; Mergili and Scheider, 2011; Stoffel and Huggel, 2012; Sattar et al., 2019). Over the past decade, high altitude lakes in the Himalaya have shown significant growth in their size and number, and with this the ever threatening hazard of glacial lake outburst flood (GLOF) is increasing manifold (Richardson and Reynolds, 2000; Ageta et al., 2000; Mool et al., 2001; Quincey et al., 2007; Ives et al., 2010; Gardelle et al., 2011; Nie et al., 2013; Wang et al., 2015). These changes occur due to a general trend of glacier recession, remarkably observed in the Hindu Kush Himalaya (Kulkarni et al., 2007; Bolch et al., 2012). Moraine-dammed lakes are formed when glacier meltwater is trapped between the end moraine and the glacier snout (Westoby et al., 2014). However, such lakes can also form when glacier- or snow-melt water is blocked by a lateral moraine. The lakes are most commonly called as blocked lakes (Raj and Kumar, 2016). The increase in the volume of these lakes can lead to percolation of the water into the moraine, thereby affecting the stability of the dam (Clague and Evans, 2000). In the Himalaya, intense rainfall events may cause water level in lakes to increase, which may exert pressure on the damming material and eventually lead to a failure event (Kargel et al., 2010; Worni et al., 2012). The severity of a GLOF depends on the volume of water released during the failure event and also the terrain characteristics (Westoby et al., 2014, Gudmundsson et al., 1997). These lake failure events are most often triggered by snow or rock avalanche, glacier calving or seismic activity (Richardson and Reynolds, 2000; Westoby et al., 2014).

India is a sub-tropical country, in which 80% annual precipitation is received in the monsoon season from June to September every year (Ghosh et al., 2009). Spatial distribution of the rainfall shows high rainfall along the Himalayan arc (Bookhagen and Burbank, 2006). Trend analysis of the annual occurrences of rainfall shows a significant increase in the 'high' to 'extremely high' rainfall occurrences, especially over Uttarakhand and Himachal Pradesh (Ghosh et al., 2009). It is also reported that rainfall over the northern part of India tend to migrate rapidly towards the high altitude regions due to excess moisture convergence into the low-pressure pockets (Pattanaik et al., 2015). These events can have a significant effect on the human community

(Nagabhatla et al., 2015). These rainfall events can also have a significant impact on the Himalayan cryosphere. Rain on snow accelerates the melting process and can cause downstream flooding (Heeswijk et al., 1996). The formation of new high altitude lakes and an increase in the volume of the existing lakes are other significant effects of rainfall over the high altitude regions in the Himalaya (Komori, 2008). The water accumulated during heavy rainfall, over an existing lake can significantly increase the pre-existing volume, thereby exerting additional pressure on the embankment and thus could affect the integrity of the moraine (Westoby et al., 2014). A sudden increase in the lake volume may initiate overtopping flows, leading to the formation of an eventual breach (Clague and Evans, 2000). Several GLOF events have been reported in the Himalaya (Richardson and Reynolds, 2000; Ives et al., 2010), of which forty-seven has been documented so far (Emmer, 2018). One such major event was the Kedarnath disaster, 16th-17th June 2013, in which a cloudburst event and the failure of Chorabari lake, led to over 6000 human fatalities and caused great damage to the downstream infrastructure (Dobhal et al., 2013; Ray et al., 2016). The Chorabari lake was a moderately small sized seasonal glacial lake blocked by the western lateral moraine of the Chorabari glacier, mostly fed by snowmelt and rainfall runoff. Following the 2013 event, Uttarakhand Space Application Centre (USAC) revealed satellite images showing the existence and growth of another lake called the Satopanth lake, located 26 km east of Chorabari glacier. The Satopanth lake has a very similar geological and geomorphologic setting as that of the Chorabari lake. Worni et al. (2012) performed a risk assessment of the glacial lakes in the Himalaya in which 93 glacial lakes including the Satopanth lake were considered potentially critical as it presented GLOF risk to the downstream regions. Following the flood event of 2013 that devastated parts of Uttarakhand, GLOF risk assessment became much necessary scrutiny for the state.

A large number of hydroelectric powerplants (HEP) were reported to have experienced great damage in the 2013 cloudburst and GLOF event (Das, 2013). The 400 MW Vishnuprayag HEP, located 28 km downstream of the Satopanth lake was one of the affected HEP during the 2013 cloudburst event. Due to the fact that a number of glacial lakes exist within the limits of the Vishnuprayag HEP catchment, GLOF risk assessment for this hydropower station becomes very vital. Assuming that extreme rainfall events may occur contemporaneously with catastrophic lake failures upstream of the Vishnuprayag dam (similar to the 2013 event), the present chapter evaluates the hazard potential of a lake outburst combined with an extreme precipitation event and assesses its impact on the HEP.

So far, one-dimensional hydrodynamic models have been used popularly to understand GLOF waves in the Himalaya (Jain et al., 2012; Thakur et al., 2016). Very few studies have employed

two-dimensional models to understand the hydraulic flow behavior of these events (Alho and Aaltonen, 2008; Worni et al., 2012). This chapter incorporates (i) growth assessment of the Satopanth lake using multi-temporal satellite imagery (ii) field investigation of the lake and the associated valley (iii) hydrodynamic modeling to assess the hazard potential of Satopanth lake on the nearest hydropower station based on one-, two-dimensional models and ground data (iv) analysis of the potential GLOF impact of the Satopanth lake coupled with a 100-year return period flood. Thus, the study is an integration of remote sensing and field methods to evaluate a hazard assessment of the Satopanth lake. The datasets employed in the study are presented in section 3.3.

3.2 STUDY AREA

The study presented in this chapter is carried out in the Alaknanda basin located in the state of Uttarakhand, Central Himalaya. The basin is mainly drained by two major glacier-fed rivers namely Alaknanda and the Bhagirathi. The upper and the lower bounds of the catchment lies between latitude $30°15'22''$N to $31°14'00''$N and longitude $79°11'00''$E to $80°28'00''$E with a total area of 6385.69 km^2. The Alaknanda river originates from the Satopanth and the Bhagirath Kharag glaciers and flows as Saraswati in the sub-watershed until it joins Dhauliganga tributary at Vishnuprayag. The presence of a potentially critical lake (Satopanth) (Worni et al., 2012) upstream of a hydroelectric powerplant (HEP) located over the Alaknanda mainstream at Vishnuprayag, Central Himalaya, make the area important to study the impact of a potential GLOF event on the HEP. The Satopanth lake ($30°44'36.44''$N, $79°21'25.69''$E) is located in the northern part of the basin, at an altitude of 4350 m a.s.l. Hydrodynamic simulations are made along the channel, from the Satopant lake to the HEP located at Lambagarh, Vishnuprayag. The distance from the lake to the HEP stretches for about 28 km along the main flow channel. The channel takes a turn towards south from Mana village and flows downstream for 11 km till it reaches the dam site. The channel is characterized by steep slopes and varied land use land cover. Figure 3.1 shows the study area, marked are the location of the lake and the hydropower dam.

3.3 DATA USED

3.3.1 Satellite Data

The present study exploits Landsat OLI/TIRS (30 m) of 22 May 2013 (LC08_L1TP_145039_20130522_20170504_01_T1) to map the lake extent prior to the cloudburst event that occurred on 16th-17th June 2013 (Ray et al., 2016). Since no cloud-free Landsat satellite scene was available immediately after the cloudburst event, the lake area has been mapped from Raj and Kumar (2016) for 21 June 2013. Terrain data for GLOF modeling

was obtained from Advanced Spaceborne Thermal Emission and Reflectance Radiometer (ASTER) global digital elevation model (GDEM). ASTER global DEM is a freely available model (https://earthexplorer.usgs.gov/) that provides elevation information between 83°N and 83° S with a spatial resolution of 30 m. A glacial lake inventory is prepared using Landsat OLI/TIRS (LC81450392015276LGN00) and cross verified using high-resolution geo-referenced CNES/Airbus imagery tiles of google earth. The land use land cover (LULC) classification, to determine Manning's roughness coefficient of the given terrain is obtained using GlobCover (v2). GlobCover is the global product of land cover maps created from the 300 m MERIS sensor onboard of the ENVISAT satellite. The LULC (GlobCover) for the study area is compared to the Landsat TM (LT05_L1TP_145039_20101106_20161012_01_T1) derived LULC map.

3.3.2 Field data

A total of over 1000 very high-resolution differential GPS (DGPS) points (model Leica GS 25) were collected to map the lake extent and moraine height. In addition to this, over 900 points collected along the given valley were used to validate the LULC derived from satellite data. The acquired DGPS points displayed positional accuracy of <1cm. The 100-year return period flood data was collected from the dam site during the field visit (September 2017). Several other relevant information like flood marks, approximate water discharge, the timing of flood at the dam site is obtained on site from Jaypee group (JP), a hydropower dam construction company based at Noida, Uttar Pradesh, India.

3.4 METHODS

3.4.1 Inventory of glacial lakes and hydropower stations and temporal growth assessment of the Satopanth lake, Alaknanda basin

To evaluate the vulnerability of the 400 MW Vishnuprayag hydropower dam to a potential failure event of an existing lake located in the Alakananda basin, an inventory of high-altitude lakes and hydropower dam is prepared. The proglacial, blocked and moraine-dammed lakes (Raj and Kumar, 2016) more than 0.01 km^2 were considered for the inventory. The lakes were identified and mapped using Landsat OLI derived Normalized Difference Water Index (NDWI). The formula used to derive NDWI (Huggel et al., 2002) is given in equation 1, where band 3 and band 5 are green and NIR channels respectively. The locations and the extent of the lakes have been verified using high resolution google earth images. A total of 25 such lakes has been identified in the basin.

$$NDWI = \frac{Band\ 3 - Band\ 5}{Band\ 3 + Band\ 5} \qquad \text{eq. 1}$$
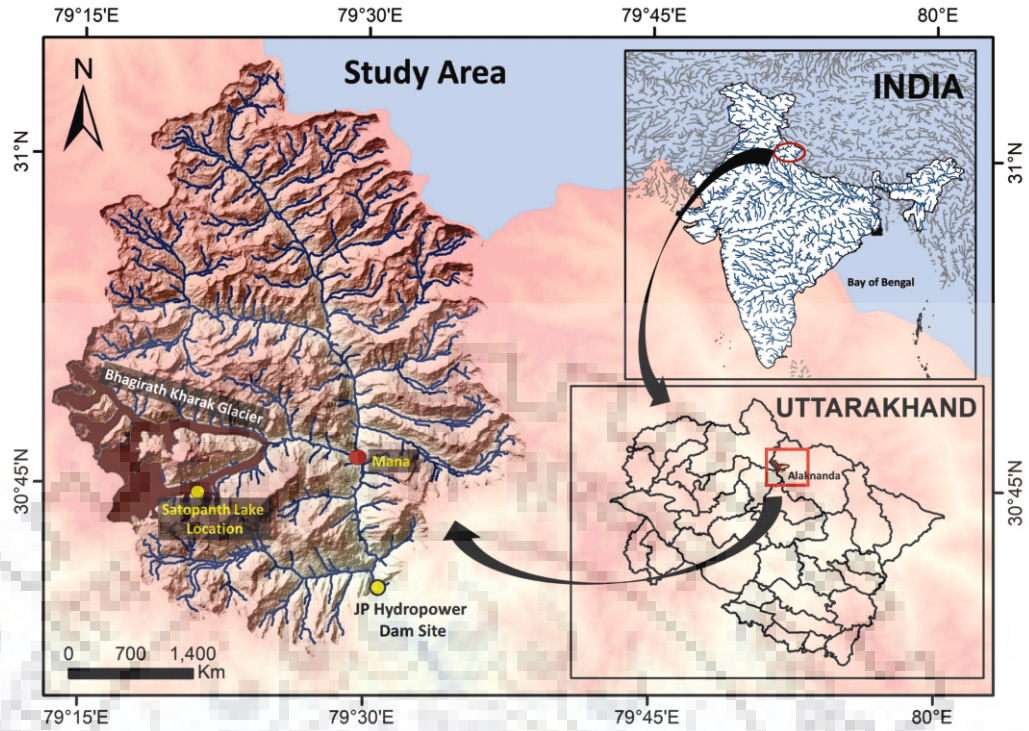
Figure 3.1 Map showing the location of the Alaknanda basin in the state of Uttarakhand, Central Himalaya; the location of the Satopanth lake, the Mana village and the hydropower dam site is shown in the given catchment
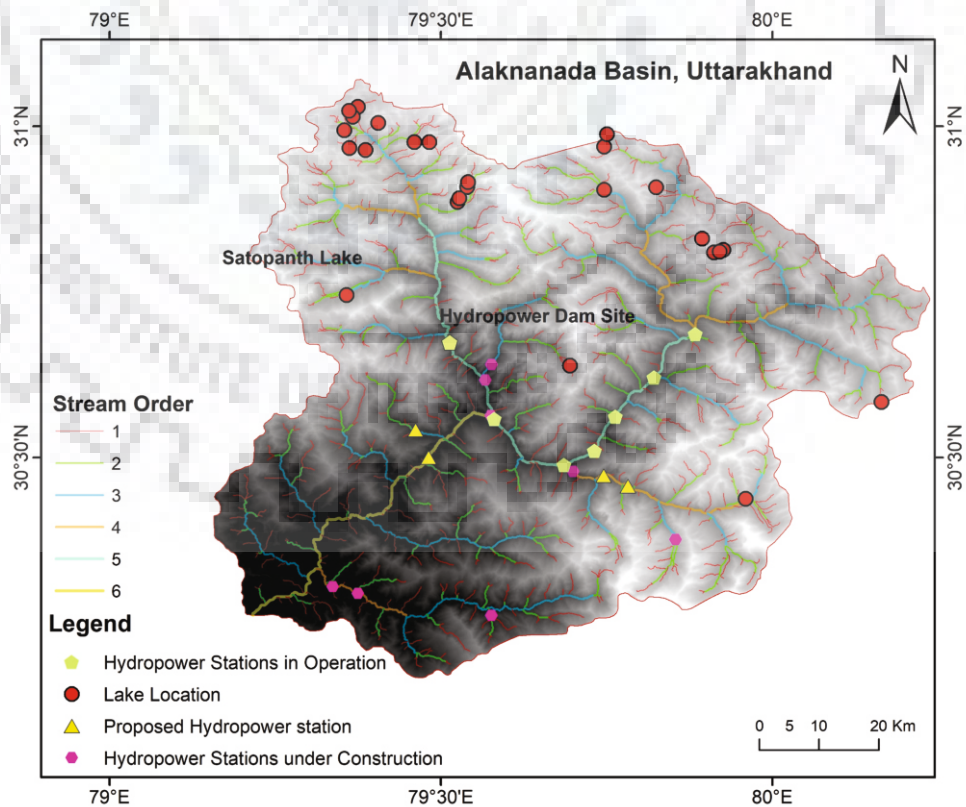
Figure 3.2 The Alaknanda basin showing the locations of the glacial lakes and the hydropower stations (in operation, under construction and proposed); the drainage of the basin is divided into six stream orders

Based on the data provided by the Alternate Hydro Energy Centre (AHEC) for the different hydropower stations in the given basin, a GIS-based inventory is prepared. The stations are divided into 3 categories as: (i) stations in operation, (ii) under construction and (iii) proposed stations.

A stream ordering of the basin is performed by employing the standard Arc-hydro tools on ASTER GDEM (Maidment, 2002). The drainage of the basin is categorized into stream orders of six based on Strahler's method of stream ordering (Shreve, 1966). A GIS-based overlay operation reveals that all the HEP (in operation) are situated over the two main fifth order streams namely the Alaknanda and the Dhauliganga. Figure 3.2 shows the locations of the lakes, the hydropower stations and the drainage of the given basin. A proximity analysis indicated that the nearest lake to the 400 MW Vishnuprayag HEP is the Satopanth lake, which is located at a distance of 28 km upstream of the lake. As the Satopanth lake has been reported to be potentially hazardous (Worni et al., 2012), a growth assessment of the lake is performed using remote sensing imageries. The lake extent is mapped using satellite images of 22 May 2013 (pre cloudburst) and 21 June (post cloudburst) (Raj and Kumar, 2016). The assessment reveals a significant increase in the size of the lake immediately after the cloudburst event. Figure 3.3 shows the pre- and post-cloudburst images of Satopanth lake. The total area of the lake before the cloudburst event was calculated to be 23834.8 m^2 as on 22 May 2013, which increased to 42245.8 m^2 after the event (Figure 3.3a). A grown Satopanth lake mapped immediately after the cloudburst event is shown in figure 3.3b.

3.4.2 Field Methods

The field methods in the present study involved (i) mapping of the Satopanth lake and the associated moraines (ii) collection of very high-resolution DGPS points along the given valley (iii) geotagging field photographs for validation of LULC.

The DGPS points were collected using a Leica GS-25 receiver, equipped with an inbuilt radio-modem for higher accuracy. The points were collected using RTK (Real Time Kinematics) survey mode. The ability to measure a larger number of points in limited time is a major advantage of RTK surveys. In order to check the precision of the collected points, 10 pilot ground points are selected, where measurements were repeated thirty times for each point location. The DGPS repetitions over the given points revealed that the average horizontal accuracy of 1-3 cm and vertical of 2-5 cm remains constant for the first ten, twenty, thirty points and it also remains constant for even a single point. A total of over 1000 points covering an altitude range from 2242 m to 4321 m a.s.l has been collected.
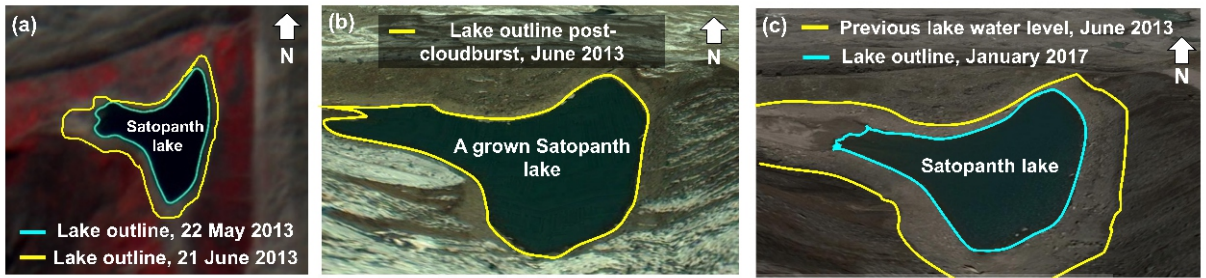
Figure 3.3 (a) Outline of the Satopanth lake mapped on May 2013 (pre cloudburst) and June 2013 (post cloudburst) (Raj and Kumar 2016); (b) a grown Satopanth lake after the cloudburst event, June 2013; (c) lake outlines mapped for the year 2017; the previous lake water level is marked in yellow
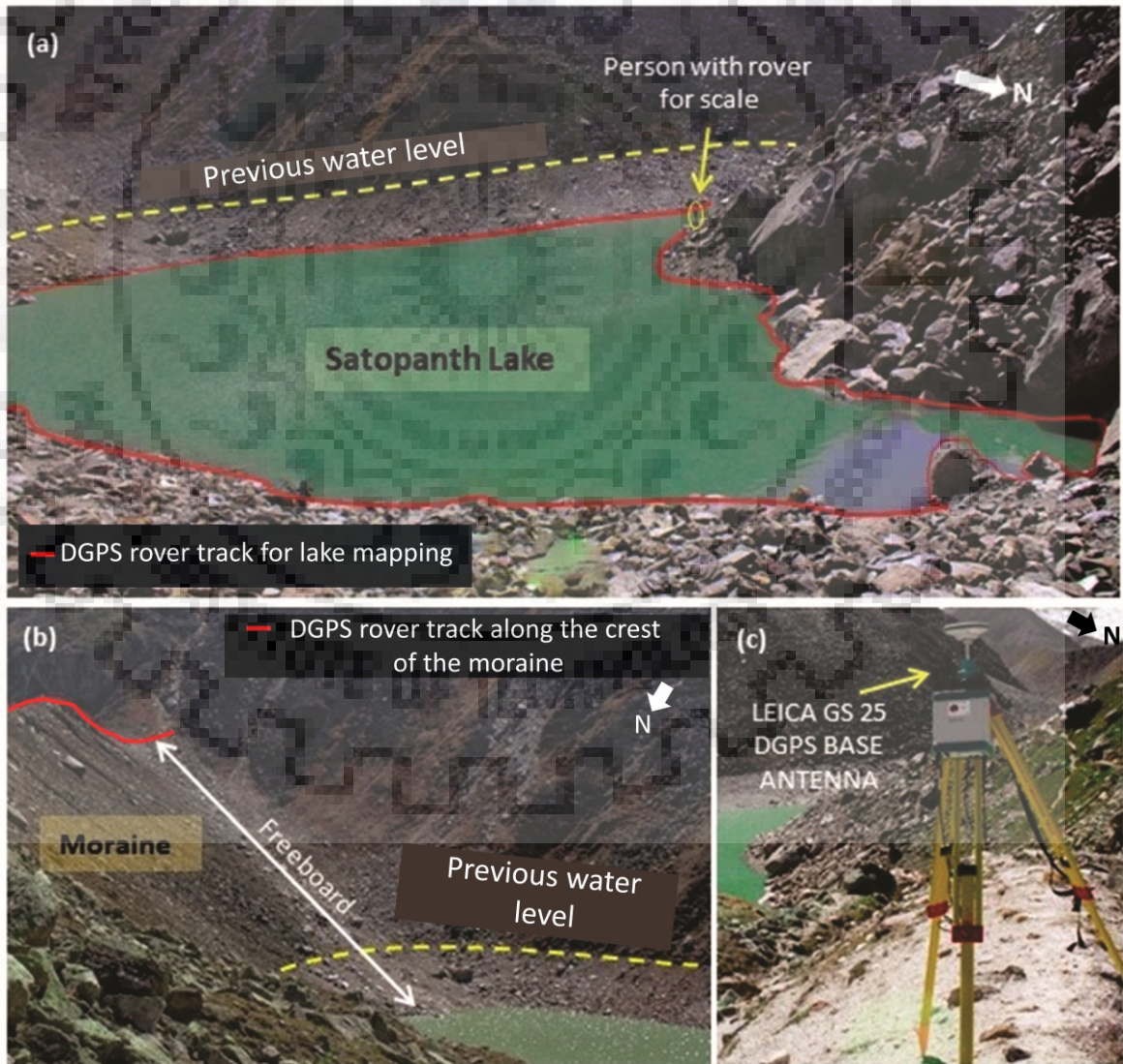
Figure 3.4 (a) Satopanth lake showing the DGPS rover track (person with rover for scale); (b) rover track along the crest of the moraine; (c) location of the DGPS base station set at a relatively higher elevation

a. Lake and moraine mapping

A total of over 1000 points with an accuracy of <1 cm was collected along the Satopanth lake boundary and the associated moraine. A DGPS base station is set at an elevated ground (moraine) as shown in figure 3.4c. A GPS receiver (rover) is used to measure point locations along the lake boundary and the moraine. Figure 3.4a shows the DGPS rover track along which the lake and the associated moraine were mapped. The freeboard of the lake is calculated using the difference in elevation points along the lake boundary and the crest of the associated moraine (Figure 3.4b).

b. LULC classification and validation

The land use land cover (LULC) map for the study region was first generated using multi-spectral Landsat TM (30 m). The satellite dataset chosen for the purpose was such that (i) it covers the entire valley of interest, from the Satopanth lake to the HEP; (ii) and has <10% cloud cover. The Gaussian maximum likelihood (GML) algorithm is applied to the satellite data for classification. The GML is a robust method of classification (Chen et al., 2004) which efficiently classifies the given image by considering mean, variances and covariance of the training samples. The classification resulted in a total of six LULC categories. The Landsat LULC is compared to the Envisat Meris derived ESA GlobCover LULC (version 2.3) (Bontemps et al., 2011). It is evident that GlobCover is a more reliable source to obtain LULC classified data for the given region, as it categorizes the region into a total of eleven classes. The LULC (GlobCover) is extracted for a buffer zone of 250 m along the main flow channel, in a way that it also covers the flood plains. In order to validate the derived LULC (GlobCover), a set of high-resolution DGPS sample points were collected in the field at different locations over different LULC classes. To validate the same for the inaccessible areas, geotagged field photographs were taken at different locations along the main flow channel. Figure 3.5 shows the spatial distribution of LULC along the buffer zone of the main flow channel and the DGPS point locations for LULC validation.

The Manning's roughness coefficient defines the frictional resistance of a terrain exerted on given flow (Coon, 1997). The values of Manning's roughness coefficient (Manning's N) are assigned based on the ground conditions that exist at the time of a particular flow event (Carter et al., 1963; Arcement and Schneider, 1989). In the present study, the Manning's N is derived along the flow channel from the Satopanth lake to the HEP using the extracted LULC. It is assumed that the LULC of the given area has not changed much over the years. Table 3.1 shows the LULC classes of the study area with their respective Manning's roughness coefficient and ground validation points. It is evident that more than 90% of the flow area has LULC classes with Manning's N ranging from 0.034 to 0.06. A Manning's N in the range of 0.04 to 0.06 has mostly been used for hydrodynamic simulation for Himalayan rivers (Worni et al., 2012; Jain et al., 2012; Thakur et al., 2016). In the present study, an average of all the Manning's roughness coefficient values (N=0.045) along the given channel is considered. Figure 3.6 shows field
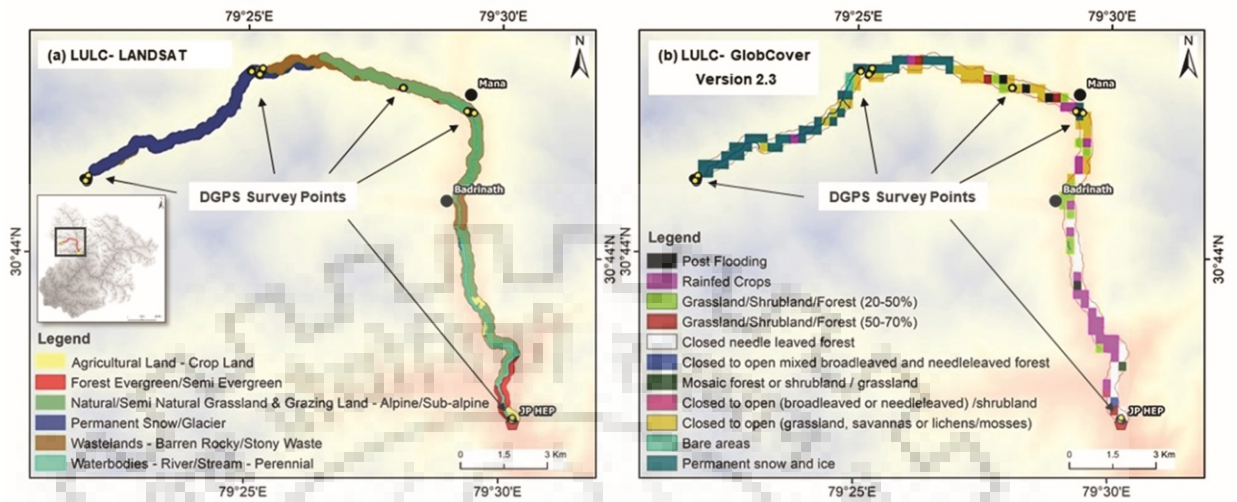
Figure 3.5 LULC along the main flow-channel derived using (a) Landsat TM; (b) LULC GlobCover (Version 2.3); yellow dots show the DGPS points for validation
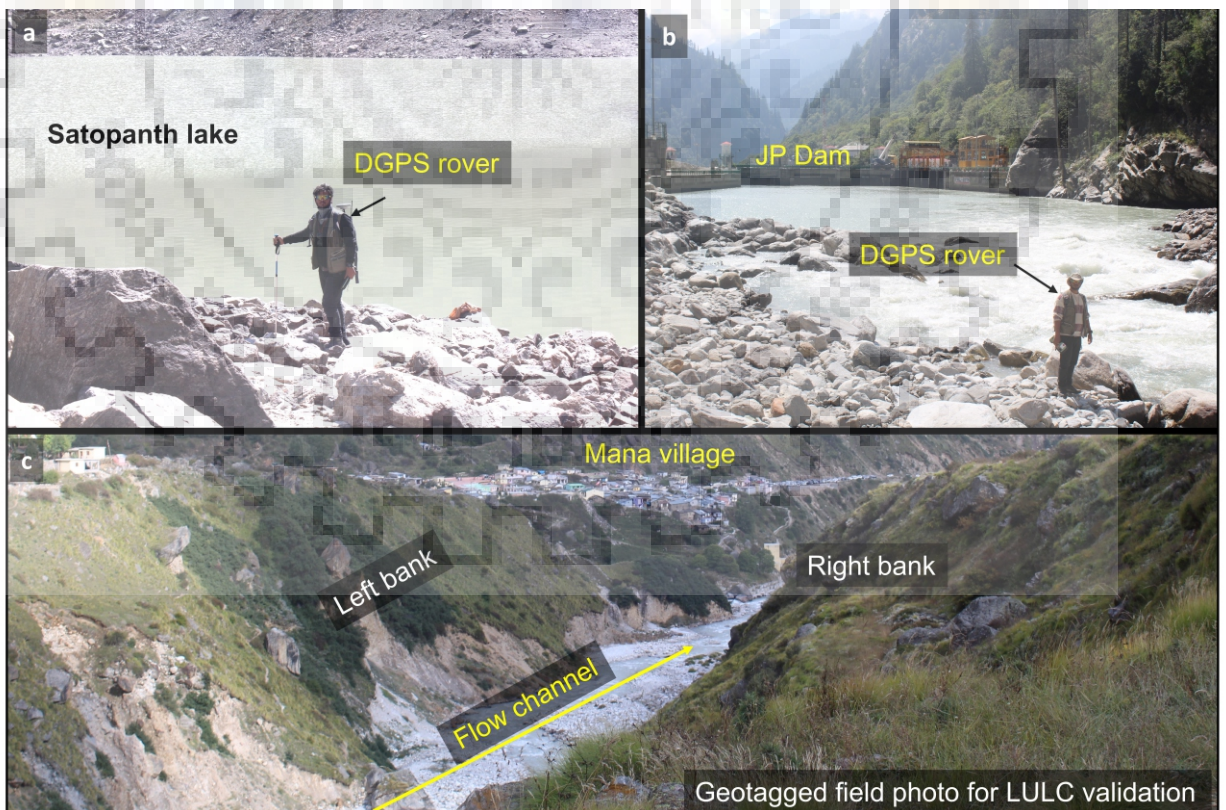
Figure 3.6 Field photographs showing DGPS survey at (a) the Satopanth lake; (b) the dam site; (c) geotagged photograph of the flow channel showing the left and the right bank at Mana village

photographs of DGPS survey at the Satopanth lake, the dam site, and geotagged photograph of the flow channel showing the left and the right bank at Mana village.

Table. 3.1 LULC classes of the study area with their respective Manning's roughness coefficient and DGPS point locations for validation

LULC class	Manning's N	Validation location (Lat/Long)	DGPS/Geotagged field photos (GFP)
Permanent snow and ice	0.04	30°44'44.39"N 79°21'46.40"E	DGPS and GFP
Bare areas	0.035	-	-
Closed to open (grassland, savannas or lichens/mosses)	0.034	30°47'00.78"N 79°26'51.11"E	DGPS and GFP
Closed to open (broadleaved or needle leaved forest) /shrub land	0.05	30°43'13.69"N 79°29'44.90"E	GFP
Mosaic forest or shrub land / grassland	0.034	-	-
Closed to open mixed broadleaved and needle-leaved forest	0.035	-	-
Closed needle-leaved forest	0.11	30°41'48.58"N 79°30'36.13"E	GFP
Grassland/Shrub land/Forest (50-70%)	0.034	30°46'39.26"N 79°28'15.93"E	DGPS and GFP
Grassland/Shrub land/Forest (20-50%)	0.035	30°46'39.77"N 79°28'24.63"E	GFP
Rainfed Crops	0.06	-	-
Post Flooding	0.03	30°46'37.60"N 79°28'22.39"E	DGPS and GFP

3.4.3 GLOF modeling and flood routing coupled with a 100-year return period flood event
In the present study, both one- and two-dimensional computation of the flow hydraulics is performed for a potential GLOF event of the Satopanth lake combined with a 100-year return period flood. The one-dimensional hydrodynamic models are based on the St-Venants or shallow water equations (SWE) where conservation of mass and momentum is taken into consideration along a single direction (Brunner, 2002). On the other hand, two-dimensional models solve SWE, to produce depth-averaged and spatially-distributed hydraulic characteristics of a given flow (Chanson, 2004).

The total volume of water released during a GLOF event is one of the prime inputs for hydrodynamic models in order to simulate a moraine-breach event (Westoby et al., 2014). Since no ground estimate of the total water volume of the lake is available, an empirical relation by Huggel et al. (2002) is used to calculate the total volume of the Satopanth lake. The equation is given as:

$$V=0.104\ A^{1.42}$$ eq. 2

Where V is the total volume of the lake and A is the area of the lake. The aerial extent of the lake, immediately after the 2013 cloudburst event is used to calculate the volume. The total area of the Satopanth lake as on 21 June 2013 was calculated to be 42245.81 m^2 (Raj and Kumar, 2016). The volume thus calculated using equation 2 is 3.85×10^5 m^3. Other model input parameters include Manning's roughness coefficient, river reach, channel bank lines, valley cross-sections, and breach formation time. The river reach, channel bank lines, and valley cross-sections are derived using GIS-based operations on ASTER GDEM and high resolution google earth images.

a. Distribution of 100-year return period flood

A 100-year return period flood is a flood event that has a 1% probability of occurring in any given year (Chow et al., 1988). Thus, it very crucial to analyze severe combinations of GLOF events, and these critical meteorological conditions affecting a given region. In the present study, the 100-year return period flood distribution in the given basin is evaluated. Further, the 100-year flood discharge is combined with the potential GLOF discharge to evaluate its effect on the hydraulic properties of the potential flood wave. The 100-year return period flood data was collected from the dam authorities during field visit which has a value of 2000 m^3s^{-1} at the dam site.

In order to distribute the 100-year flood discharge at a sub-catchment level, ASTER DEM is employed to delineate the major and the minor watersheds. The Arc Hydro tools (Arc Map 10.3) is exploited to perform necessary hydrological operations (Chandana and Aggarwal, 2001). The major watershed is delineated by taking an outlet discharge point at the JP HEP dam site. This is further divided into six sub-catchments using different discharge points along the main flow channel, as shown in figure 3.7. The 100-year flood is distributed based on the total area of the sub-watersheds using Dickens formula, 1865 (Alexander, 1972). It is given by the equation:

$$Q_p = C_D A^{\frac{3}{4}}$$ eq. 3

Where Q_p is the maximum flood discharge in m^3s^{-1}, A is the catchment area in km^2 and C_D is Dickens constant which has a value of 11 to 14 for northern Indian hilly regions. In the present study, C_D is calculated to be 11. 1 based on the total area of the major catchment. The entire area of the major catchment is calculated to be 1020.11 km^2. The 100-year return period flood

discharge at Mana village is calculated to be 1708 m^3s^{-1} (Equation 3). In the present study, the potential GLOF discharge of the Satopanth lake is coupled with the 100-year return flood discharge at Mana village and the combined effect of the flood event is analyzed till it reaches the dam site located further downstream.

b. One-dimensional GLOF modeling and flood routing combined with 100-return period flood

In the present study, the HEC-RAS 1D hydrodynamic model is employed to simulate a moraine-breach event of the Satopanth lake. The HEC-RAS model is one of the most popular open source models used for glacial hazard studies (Alho et al., 2005; Alho and Aaltonen, 2008; Carling et al., 2010). Here, a potential moraine failure event is modeled that releases the total volume of the lake. It is assumed that the total width of the moraine (dimensions derived from DEM) fails to release the stored volume of the lake. A set of different moraine-failure time (0.5, 0.7 and 1.0 hours) has been used to calculate the initial breach hydrograph. The hydrograph that produced the maximum peak flood (worst-case scenario) is routed along the main flow channel until it reaches the HEP dam site. The cross-sections of the main flow channel were derived (ASTER DEM) for every 500 m along the full length of the channel in a way that they cover the entire floodplain. Figure 3.8 shows the plot of the DEM-derived cross-sections along the main flow channel. The central axis of the main flow channel (flow path) and the maximum flood extent (bank-lines) are delineated using high resolution google earth images.

In the routing process, breach hydrograph and the frictional slope between the last two cross-sections are taken as the upstream and downstream boundary condition respectively (Brunner 2010). The flood hydrographs were evaluated at different locations along the flow channel to determine the amount and the time of peak discharge. The resultant hydrograph is then coupled with the calculated 100-year flood discharge (section 3.4.3.a) at Mana village and further routed until it reaches the hydropower dam site. An average Manning's roughness coefficient of 0.045 as calculated in section 3.4.2.b has been considered.

c. Two-dimensional GLOF modeling and flood routing combined with a 100-year return period flood

A two-dimensional unsteady flow modeling of a potential Satopanth lake GLOF event is performed using the latest version of HEC-RAS (v 5.0.5), which delivers an effective solution for Saint-Venant equations in a 2D array. The two-dimensional modeling routes the initial breach hydrograph over a raster-based terrain. In the present study, the terrain is divided into a mesh with equal grid dimensions of 30×30. Each cell is defined with a set of terrain properties like Manning's roughness coefficient and elevation. The projection system of UTM- 44 has been defined based on the location of the present study. A 2D flow area is defined within the limits of the terrain model containing the lake and the HEP. A Manning's N of 0.045 (Section 3.4.2.b) is
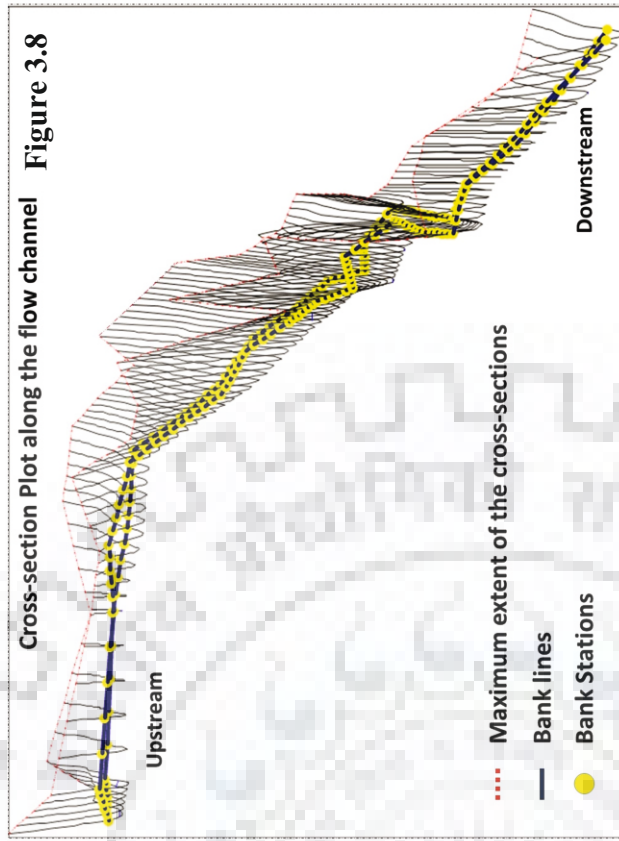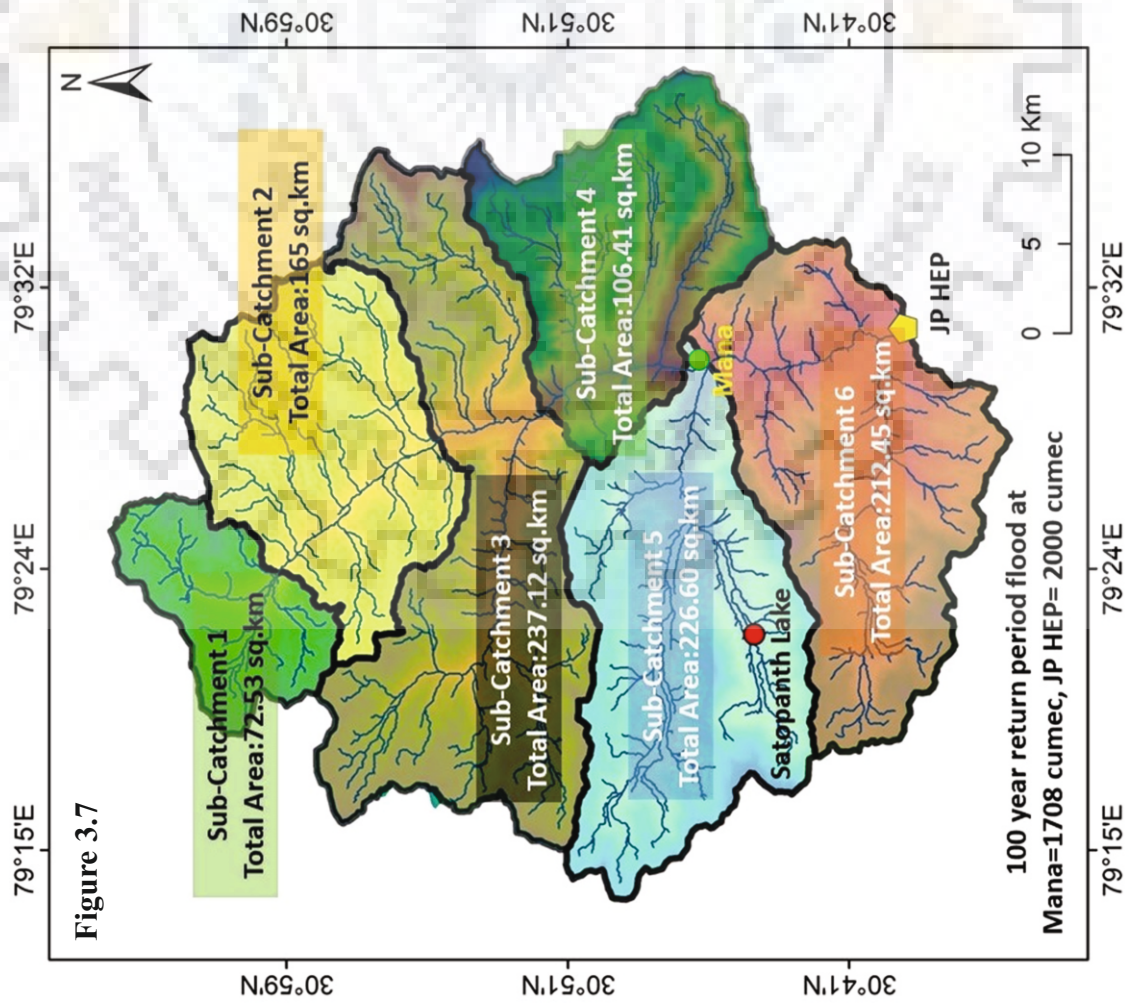
Figure 3.7 Total catchment of the JP HEP divided into six sub-catchments based on different discharge points along the main flow channel; the 100-year return period flood at Mana village is calculated to be $1708 \, m^3 \, s^{-1}$

Figure 3.8 Plot of the DEM-derived cross-sections along the main flow channel; the maximum mapped extent and the bank-stations along the given channel are shown in red and yellow respectively

assigned to each cell within the 2D flow area. A breach event of a lateral structure, in the form of a glacial moraine with dimensions similar to that used in Section 3.4.3.b is modeled. The upstream and downstream boundary conditions are the same as one-dimensional modeling. Unsteady hydraulic routing of the breach hydrograph is performed for a distance of 28 km from the lake until it reaches the HEP. In the hydraulic routing process, the calculated 100-year flood discharge (Section 3.4.3.a) is combined with the potential GLOF discharge at Mana village to study its effect on the hydraulic properties of the potential flood wave. A temporal assessment of the spatially distributed outputs of water depth, velocity, and inundation of a GLOF event coupled with a 100-year return period flood of the catchment is performed at the dam site. In addition, 2D hydraulic computation of stream power is performed for the potential flood wave. The stream power is the product of the average velocity and the average shear stress. The shear stress is given by the equation:

$$\tau = \delta g \ dS \qquad\qquad \text{eq. 4}$$

Where τ is the shear stress in Nm^{-2}, ρ is the specific density of water in kgm^{-3}, g is acceleration due to gravity in ms^{-1} and S is the energy gradient calculated from the channel slope. Temporal evaluation of the 2D hydraulic properties of the potential flood wave at the dam site is performed. The 2D outputs of the modeled flood event were mapped at two different time steps- first, when the flood wave arrives at the dam site and second, at the initiation of the dam overflow. Figure 3.8 shows the overall methodology of the present study.

3.5 RESULTS AND DISCUSSION

The Satopanth lake is identified as one of the potentially critical lakes located in the Alaknanda basin, Central Himalaya (Worni et al., 2012). Here, one- and two-dimensional hydraulic modeling of potential GLOF of the lake is performed to evaluate its impact on a HEP located downstream. A moraine-breach modeling releasing the total volume of the lake was performed for different failure time of 0.5, 0.7, and 1.0 hour. The total lake volume calculated immediately after the 2013 cloudburst event is 3.8×10^5 m^3. Figure 3.10a shows the modeled GLOF hydrographs for different failure time. In order to simulate the worst-case flood scenario, one-dimensional hydraulic routing of the GLOF hydrograph with a peak discharge of 870 m^{3}s^{-1} (breach formation time of 0.5 hours) is performed. The routing was carried out for a distance of 28 km along the main flow channel from the Satopanth lake to the dam site. The discharge hydrographs at different locations were evaluated along the flow channel to determine the peak flood and the time of peak. A hydrograph with a peak discharge of 315 m^{3}s^{-1} is obtained at Mana village which is located at a distance of 16.5 km downstream of the lake (Figure 3.10b). The flood was further routed until it reaches the dam site coupled with the discharge of a 100-year return period flood discharge of 1708 m^{3}s^{-1} at Mana village (Section 3.4.3.a). The average Manning's N of 0.045 based on the LULC has been considered in the present study (Section 3.4.2.b). A sensitivity analysis of the model to the average Manning's N for the study area shows
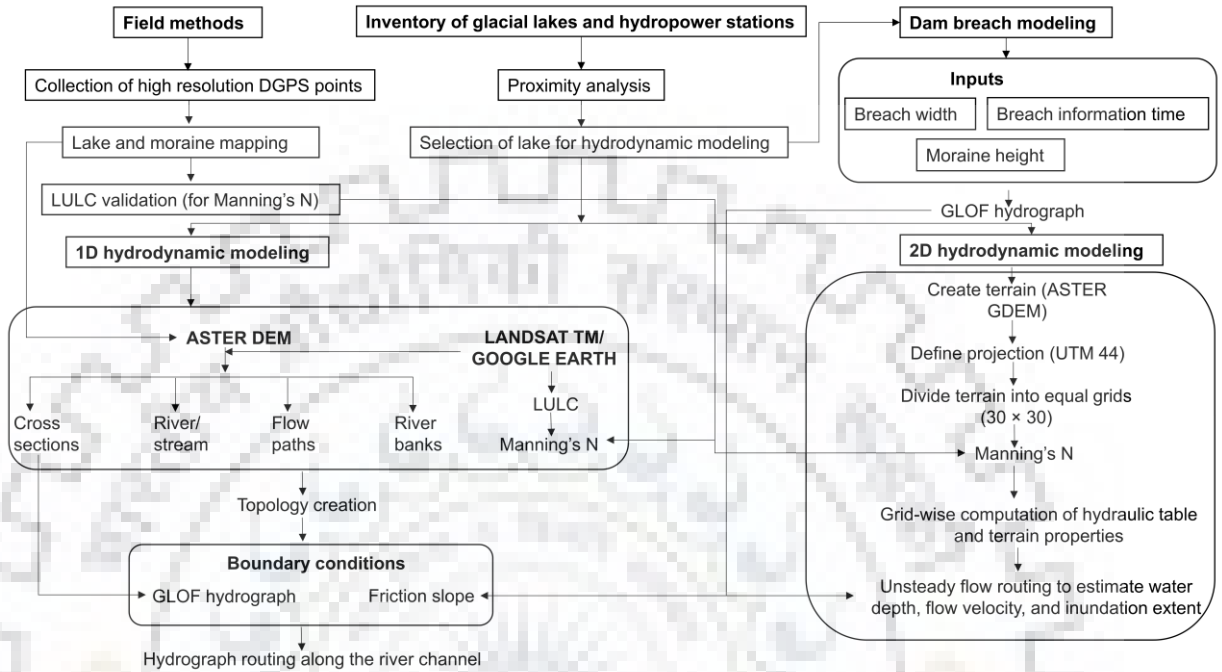
Figure 3.9 Flowchart showing the methodology of one- and two-dimensional GLOF modeling for Satopanth lake, Alaknanda Basin, central Himalaya
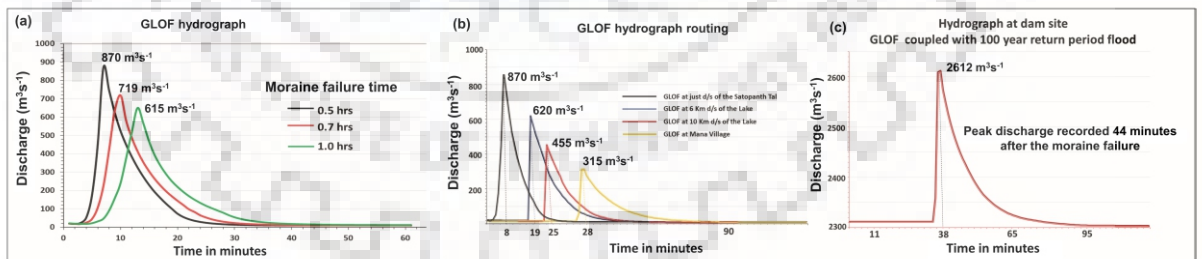
Figure 3.10 (a) Breach hydrographs for different moraine failure time of 0.5, 0.7, and 1.0 hour; (b) GLOF hydrograph at different locations along the flow channel; (c) GLOF hydrograph coupled with a 100-year flood at the dam site

a variation of 5 to 6 percent in the peak discharge when δn is 0.01. The flood wave arrives at the HEP dam site 38 minutes after the initiation of the failure event, producing a flood with a peak discharge of 2612 m^3s^{-1}. Figure 3.10c shows the routed flood hydrograph at the dam site produced during the combination of GLOF and the 100-year flood discharge.

Two-dimensional GLOF modeling and hydraulic routing were carried out using the same set of input parameters as in the one-dimensional model. Flow simulations to analyze the hydraulic behavior of a potential GLOF wave were performed over a 2D gridded terrain. The routed GLOF discharge is combined with the 100-year flood discharge at Mana village. The study assumes the lowermost cross-section of the study as the dam structure and that the control gates of the dam remain closed. The Satopanth GLOF coupled with 100-year flood resulted in a potential flood wave that arrives the dam site at a maximum flow velocity of 7.6 ms^{-1}. A maximum inundation depth of 7.2 m is reached at the dam site immediately after the flood wave arrival. The stream power is calculated taking into consideration the shear stress as given in section 3.4.3.c. The stream power being a function of flow velocity, a gradual decrease in the stream power at the dam site is evident as the flow velocity decreases. Figure 3.11 (a) and (b) shows the spatially-distributed plots of flow velocity, stream power, inundation depth, and extent derived using 2D hydraulic routing.

The data of dam height and crest length were obtained during the field visit, which are 17 m and 63 m respectively. The temporal evaluation of the 2D modeled hydraulic outputs at the dam site shows a rapid increase in the water depth at an average rate of 4.5 meters per minute. At this rate, the maximum height of the dam is reached within 4 minutes after the initial flood wave arrival, leading to a dam overflow. In addition, flood inundation extent is mapped at the time of dam overflow i.e. 4 minutes after the initial flood wave arrival. The modeled flood inundation width of the potential flood obtained at the dam site is 136 m, which is 73 m more than the dam crest length. This implies that the flood water would inundate the area surrounding the dam.

The results produced in the present study can be compared to the 2013 cloudburst event (Dobhal et al., 2013; Ray et al., 2016) that impacted this dam located at Vishnuprayag, leading to overflow and causing great damage to the dam infrastructure and also in the downslope regions. A discharge of approximately 2200 m^3s^{-1} was recorded at the dam site during the 2013 event (data from the dam authorities). Figure 3.12a shows a photograph of the dam site during the 2013 flood. A field photograph taken during field visit (September 2017) shows the previous flood marks at a distance of 100m upstream of the dam site (Figure 3.12b). The results of the presen study reveal that with a potential discharge of 2612 m^3s^{-1} at the dam site, which is 412 m^3s^{-1} in excess than what was caused in 2013 would lead to a more severe flood situation. Therefore,
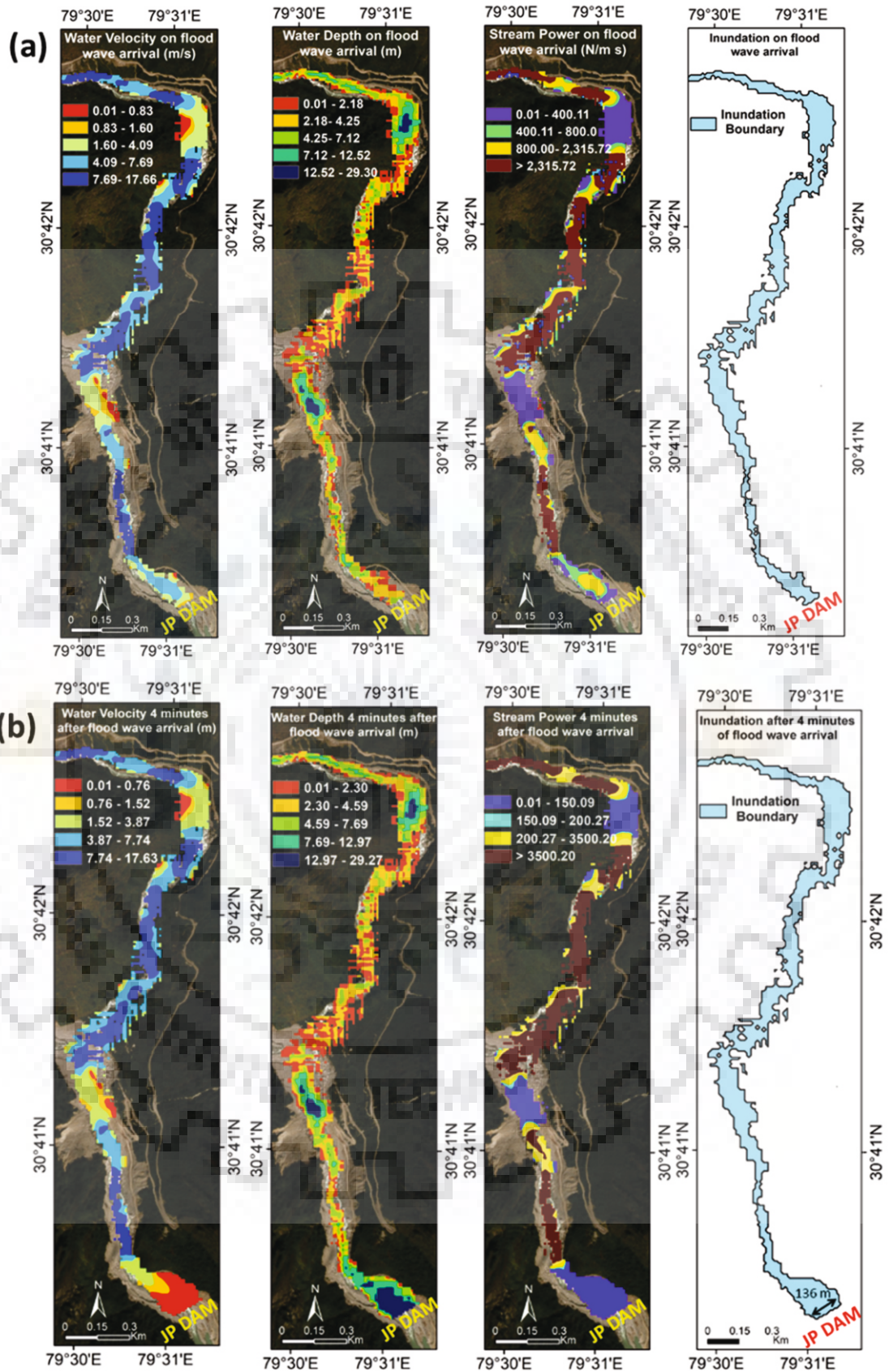
Figure 3.11 (a) Spatially distributed plots of flow velocity, water depth, stream power and inundation extent immediately after the flood wave arrival. (b) 2D plots of flow velocity, water depth, stream power and inundation extent, 4 minutes after the flood wave arrival
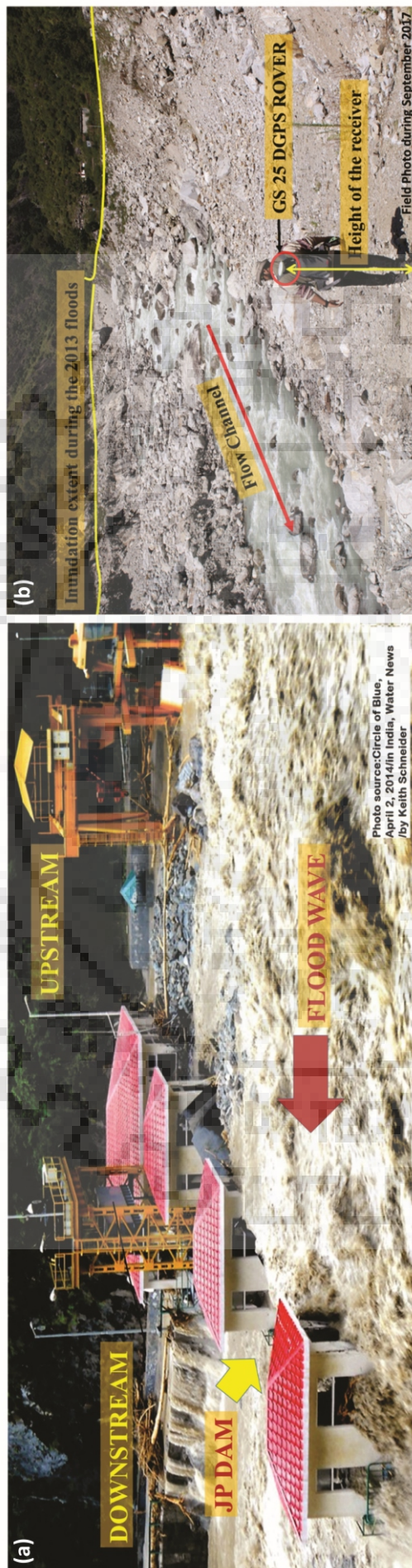
Figure 3.12 (a) JP dam site during the 2013 floods with the discharge of ~2000 m^{3}s^{-1} , (b) Field photograph at 100 m upstream of the dam site showing the 2013 flood inundation marks along the flow channel

considering glacial lake outburst flood assessment of the Satopanth lake was crucial to evaluate the vulnerability of the JP HEP to the severe flood situation, a sudden discharge from the high altitude lakes can amplify an existing flood situation.

3.6 CONCLUSION

The Satopanth lake is not only reported to be one of the potentially critical lakes in the available literature (Worni et al., 2012) but also has past evidence of lake level changes due to cloudburst events in the higher reaches of the basin. The present study evaluates the hazard potential of the Satopanth lake when combined with a 100-year return period flood event. Here, different scenarios of a moraine-breach event of the Satopanth lake were modeled based on different moraine failure parameters (failure time-0.5 hrs, 0.75 hrs, and 1.0 hrs), to calculate the discharge. Further, its impact on a HEP located at a distance of 28 km downstream is evaluated using 1D and 2D hydrodynamic routing along the main flow channel.

One-dimensional GLOF modeling coupled with a 100-year return period flood resulted in a peak discharge of 2612 m^3s^{-1} at the dam site. The potential GLOF wave arrived at the dam site 38 minutes after the initiation of the moraine-breach event. Two-dimensional routing of the GLOF hydrograph was performed from the lake to the dam site to evaluate the spatially distributed hydraulic properties (flow velocity, flow depth, and inundation area) of the potential flood wave. The potential GLOF wave when combined with the 100-year return period discharge at Mana village, resulted in a flood that arrived at the dam site with a maximum velocity of 7.6 ms^{-1}. Assuming that the control gates of the dam remain closed, the water depth at the dam site increases at a rate of 4.5 m per minute. The dam overflows in approximately 4 minutes after the initial arrival of the flood wave. The unavailability of high-resolution terrain data limits the degree of accuracy in the computation of the hydraulic properties of the potential flood. The study presented in this chapter recommends regular monitoring of the Satopanth lake especially during and post-monsoon season, due to the potential risk it imposes on the downstream region when combined with high-intensity precipitation events.

CHAPTER 4: BATHYMETRY-BASED POTENTIAL GLOF HAZARD ASSESSMENT

4.1 INTRODUCTION

Several studies have been taken up in the past to assess the glacial lake distribution in the Hindu Kush Himalaya covering the states of Nepal, Tibet, Bhutan and the Indian Himalaya (Komori, 2007; Fujita et al., 2009; Ives et al., 2010; Wang et al., 2013; Raj et al., 2013; Nie et al., 2017; Rounce et al., 2017; Nagai et al., 2017; Haritashya et al., 2018). However, the hazard potential of these lakes in the high-altitude region of the Himalaya remains unclear. Accurate risk assessment of these lakes demands complex modeling based on field observations and high-resolution satellite data. So far, a limited number of studies have been carried in the Himalaya to understand the hydrodynamic behavior of GLOF events using one-dimensional dynamic models (Jain et al., 2012; Worni et al., 2012; Thakur et al., 2016; Jha et al., 2016). Also, only a few studies have been taken up to study these potential extreme floods using sophisticated two-dimensional hydrodynamic models. In addition to this, the unavailability of bathymetric data limits the applicability of these models to produce more accurate real-time results. Thus, it is important to carry out a comprehensive study on the high-altitude lakes in the Himalaya to characterize the potential extreme flood events with the help of precise simulation techniques and available bathymetric data.

Considering the Sikkim Himalaya, a limited number of studies have been carried out to understand the hazard potential of the high-altitude lakes (Raj et al., 2013; Aggarwal et al., 2017; Shukla et al., 2018). Haakeem et al. (2018) presented a remote sensing-based inventory of glacial lakes in the Teesta basin in Sikkim. Worni et al. (2012), categorized the high-altitude lakes in Himalaya based on its outburst probability and damage potential, of which thirty lakes in the Sikkim Himalaya were identified as potentially critical. Of the identified potentially critical lakes, the South Lhonak lake is one of the largest lakes in Sikkim. It is reported to have substantial GLOF potential to cause damage in the low-lying areas (Worni et al., 2012; Raj et al., 2013; Aggarwal et al., 2017; Sharma et al., 2018). In this chapter, a detailed hazard assessment of the South Lhonak lake is performed.

For the sustainable development of high mountain areas GLOF risk management is a prime concern worldwide (Richardson, 2010; Vilímek et al., 2014). Several remediations of GLOF related hazard were implemented for effective management of such hazards (Ives, 1986; Reynolds et al., 1998; Reynolds, 1999; Rana et al., 2000; Kattelmann, 2003; Richardson, 2010;

Emmer et al., 2018). Two-dimensional hydraulic modeling of high magnitude floods allows temporal assessment of flood parameters like flow velocity, inundation depth, and area. To assess the hazard associated with such flood events, it is necessary to pinpoint locations of potential damage along a given flow channel. Spatially distributed results obtained as outputs in 2D flood simulations can be used to identify the areas susceptible to the damage in a potential flash flood event. This chapter also proposes a potential flood remediation measure based on the 2D hydrodynamic results of the potential GLOF of the South Lhonak lake, Sikkim.

Overall the chapter presents, the evaluation of the South Lhonak lake for its GLOF potential, and its flow behavior is assessed using hydrodynamic models. The study incorporates (i) construction of a realistic bathymetric model to depict different GLOF scenarios, (ii) one and two-dimensional hydrodynamic modeling to assess the hazard potential of the South Lhonak lake, (iii) a detailed investigation of a topographic flow-barrier and its impact on the flow hydraulics of potential GLOF wave from South Lhonak lake, and (iv) modeling of a framework to propose a potential flood remediation measure. In GLOF studies, the failure mechanism (overtopping and piping) has a significant influence on the flood produced in the downstream region. In an overtopping failure, water traverses over the damming material and causes failure when the flow shear-stress exceeds the strength of the damming material (Korup and Tweed, 2007). Whereas in a piping failure, the seepage may initiate at any point of the dam, from where it progresses, thereby reducing the overall physical strength of the dam and eventually leading to a breach event (Clague and Evans, 2000). Thus, the present study evaluates a potential GLOF event of the South Lhonak lake by modeling different failure modes to determine the initial dam breach hydrograph.

4.2 STUDY AREA

The South Lhonak lake (27°54'43"N and 88°12'7"E) is located in the northern part of the Teesta Basin, in Sikkim, Central Himalaya. The basin is drained mostly by glacier-fed rivers, the prominent being the Teesta river originating from the Pahunri glacier. The lake has an elevation of 5200 m above mean sea level (amsl). It is a proglacial lake located at the snout of the South Lhonak glacier, formed due to its retreat (Raj et al., 2013). Sharma et al. (2018) carried out a field survey to measure the lake bathymetry and dimensions of the frontal moraine. The lake has a frontal moraine with a height of 16.3 m and a height to width ratio of 0.031. The lake has a maximum depth of 120 m and stores 65.81×10^9 L of water (Sharma et al., 2018). Temporal analysis using remote sensing images has shown a rapid growth of the lake from 0.10 km^2 to 1.37 km^2, over the past four decades (Chapter 1). The study covers a stretch of 62.35 km along the flow channel from the South Lhonak lake to the Chungthang town. Hydrodynamic simulations to study the GLOF wave characteristics are made along the flow channel, to evaluate its impact on the major townships located along the
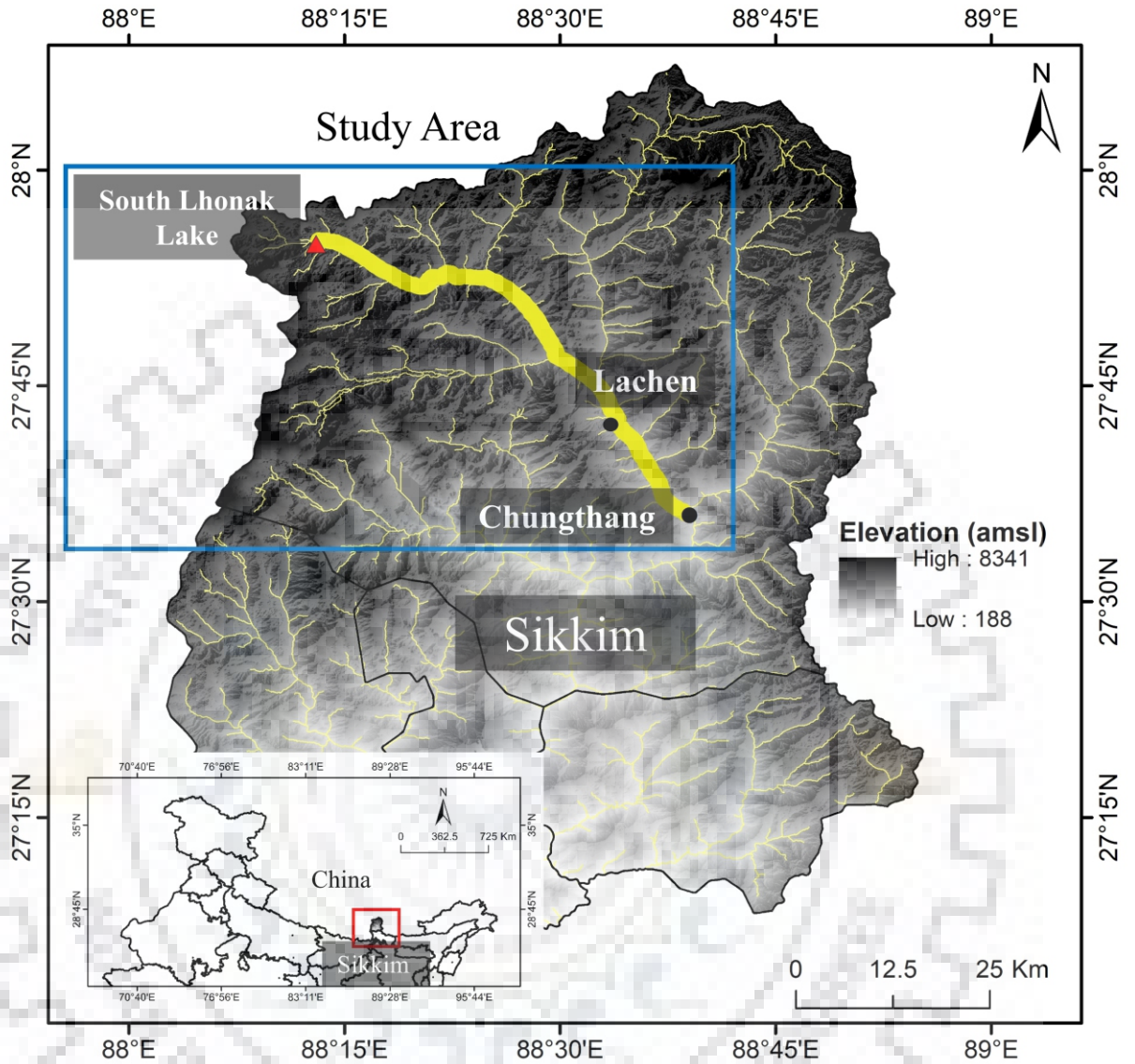
Figure 4.1 Map showing the location of the South Lhonak lake, Sikkim and its flow channel up to the town 'Chungthang'
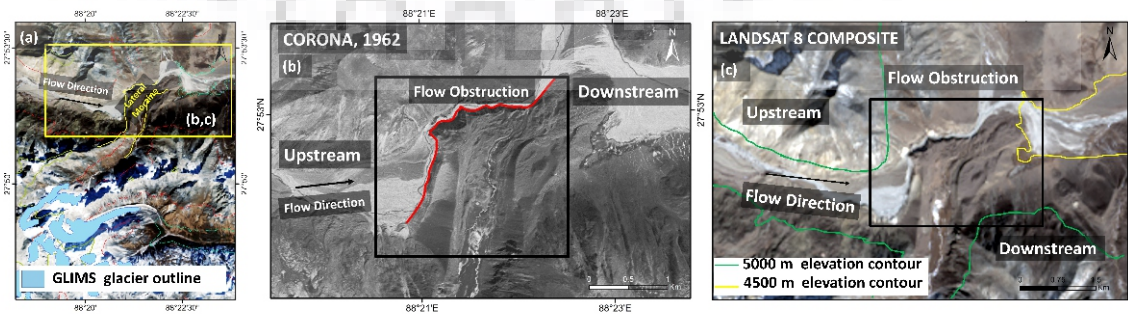
Figure 4.2 Lateral moraine cross-cutting the main flow channel. Subsets 'b' and 'c' shows the flow obstruction mapped on Corona and Landsat 8 respectively

valley (Lachen, Latong, Yuigang, and Chungthang), until it reaches the hydropower reservoir site located at the confluence of the Lachen and the Lachung rivers. Figure 4.1 shows the study area, marked are the flow channel, location of the south Lhonak lake and the locations of the settlements.

4.2.1 Description of the flow channel

The term "Chu" is referred to as 'little river' in Sikkim. The flow channel originates as Goma Chu from the South Lhonak lake and flows SSE for a distance of 22.8 km, from where it flows as Langbo Chu, Lhonak Chu, and Zemu Chu till it joins the Teesta River at Hema. The channel is characterized by steep side slopes and varied land use land cover. It has a complex terrain with a paleo-glaciomorphic feature cross-cutting the flow channel. In the present study, historical high-resolution declassified data and optical satellite imagery are employed to visually interpret and detect the major flow obstructions along the main flow channel. A surface depositional landform in the form of lateral moraines could be identified, cross-cutting the main flow channel of the Goma Chu at a distance of 15.5 km downstream from the South Lhonak lake. It is located between elevation contours of 4500 m and 5000 m amsl. The investigation of such surface features is crucial in studies concerning dynamic modeling of extreme floods, as these may act as topographic barriers to the flow, substantially minimizing the impact of a flood wave. Figure 4.2 shows the lateral obstruction that cross-cuts the main flow channel of Goma Chu.

4.3 DATA USED

CORONA (7.5 m) and LANDSAT ETM+ (30 m) have been used to study the flow channel of the South Lhonak valley. The images acquired in the years 1962 and 2018 were used to visually interpret the flow obstruction over the main flow channel. Terrain data for dynamic modeling of the GLOF wave was obtained using radiometric terrain corrected ALOS PALSAR DEM with a spatial resolution of 12.5 m. The terrain corrected ALOS PALSAR elevation data was released globally from October 2014 and has a global coverage except for Antarctica, Greenland and north Eurasia (Alaskan Satellite facility). The land use land cover (LULC) data used for the retrieval of Manning's roughness coefficient along the flow area was obtained from GlobCover (V2.3). GlobCover is a reliable open-source global LULC dataset derived from ENVISAT MERIS (Sophie et al., 2010).

4.4 METHODS

4.4.1 Lake Bathymetry and dam breach modeling

One of the most important inputs in the dynamic modeling of GLOFs includes lake bathymetric data (Westoby et al., 2014). Accurate information of the lake-bottom topography and the dimensions of the associated moraine is essential to evaluate the actual mechanism of a glacial lake
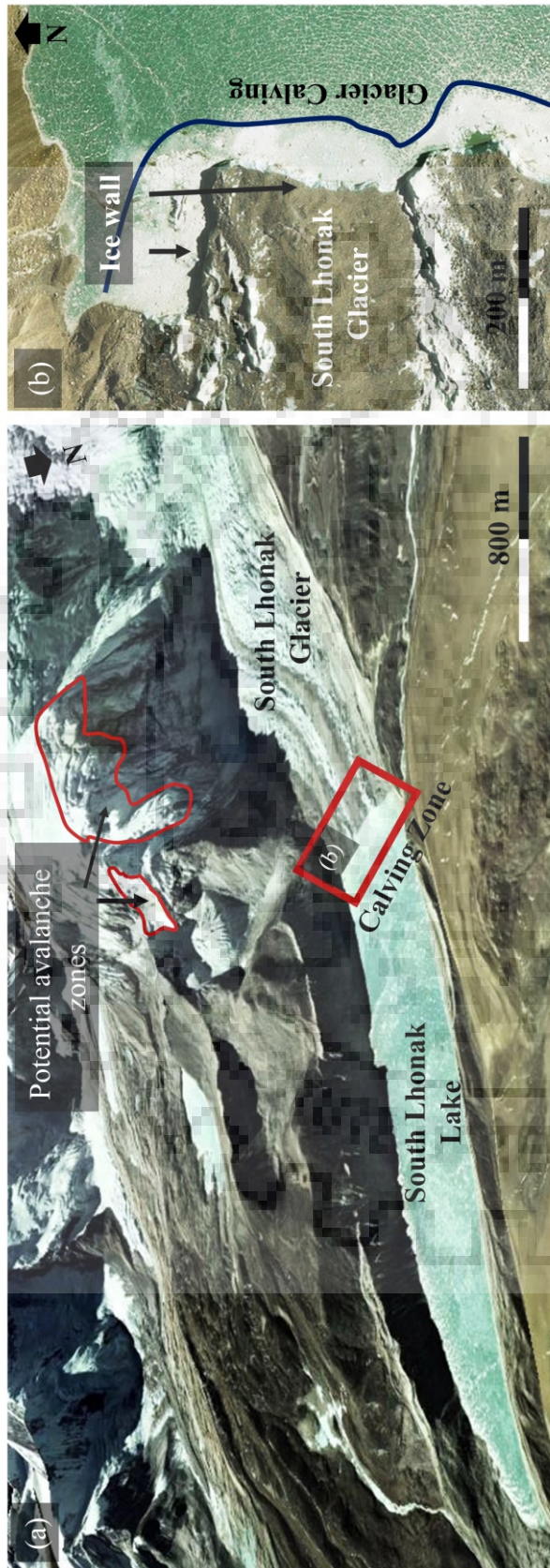
Figure **4.3** a. South Lhonak lake showing the potential sources of mass to reach the lake.; b. zone of calving in front of the glacier snout
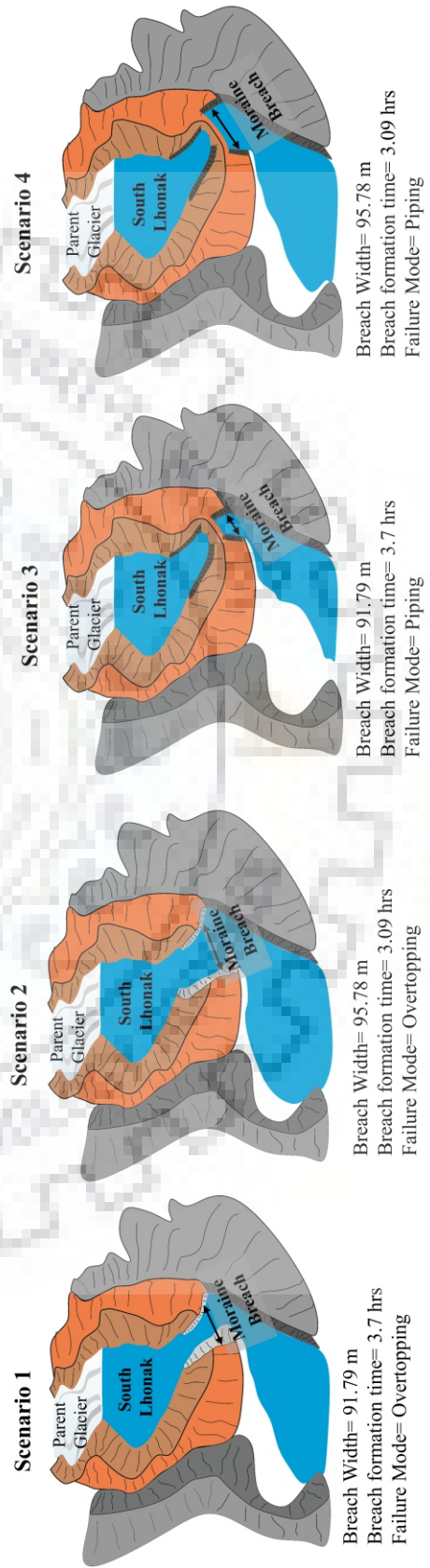
Figure 4.4 Schematic diagram of the South Lhonak lake, showing the different mechanism of moraine failure with varied breach width and failure time

outburst, thereby defining the actual total volume of water that will potentially be released in a failure event (Westoby et al., 2014). It also determines the initial wave generation at the failure site and further routing of the wave enables characterization of the flood wave along a given flow channel. Till date, glacial lake bathymetry is known only for a very few lakes in the Himalaya. This restricts accurate modeling of GLOFs, as the total volume of the lake remains unknown and the dam failure mechanism becomes independent of the lake bottom topography. Area-based scaling is one of the widely used methods to calculate the total volume of an existing glacial lake where ground data is not available (Huggel et al., 2004). Sharma et al. (2018) carried out bathymetric surveys on the South Lhonak lake in the year 2016 to map the lake bottom surface. In the present study the bathymetry of the South Lhonak lake is reconstructed from Sharma et al. (2018). The HEC-RAS model (Version 5.0.5) is used to construct the 3D-model of the lake and the frontal moraine based on the dimensions reported by Sharma et al. (2018). The 3D model is further used to simulate the different failure mechanism and to determine the actual volume of water that would be released during a moraine failure event of the South Lhonak lake. Figure 4.6 shows the reconstructed 3-D lake model based on the bathymetry of the South Lhonak lake. The lake has a maximum depth of 130 m at a distance of 1.8 km from the frontal moraine.

HEC-RAS is one of the most popular open source models used for glacial hazard studies (Alho et al., 2005; Alho and Aaltonen, 2008; Carling et al., 2010; Klimeš et al., 2014). Its user-friendly interface and capability of performing complex dynamic simulations (Brunner, 2002) makes it a reliable model to study the hydraulic behavior of unsteady flows. A 3-D geometric model of the South Lhonak lake was created based on the available spatially distributed bathymetric measurements of the lake. An inline structure depicting the frontal moraine is entered at the lower end of the lake, in accordance to the dimension measured in the field (Sharma et al., 2018). The failure event is modeled by breaching the inline structure, where the downstream boundary condition is considered as the normal depth, calculated based on the slope.

In a lake outburst probability assessment carried by Worni et al. (2012) in the state of Sikkim, categorized the South Lhonak lake as a potentially critical lake based on triggering factors like ice/snow avalanches and debris low/rock fall. In addition to this Kumar and Prabhu (2012) stated earthquakes as a triggering factor for a GLOF event of the lake. Also, avalanche and rock fall may possibly trigger such overtopping failure. Field evidences reported frequent calving processes near the snout of the South Lhonak glacier (Sharma et al., 2018). Calving processes may generate impulse waves capable of initiating an overtopping failure of the frontal moraine (Westoby et al., 2014). Figure 4.3 shows high-resolution google-earth imagery (Digital Globe and Navinfo) of the South Lhonak lake and the potential sources of mass to reach the lake. An overtopping flow may initiate erosion of the frontal moraine and further progression into deeper
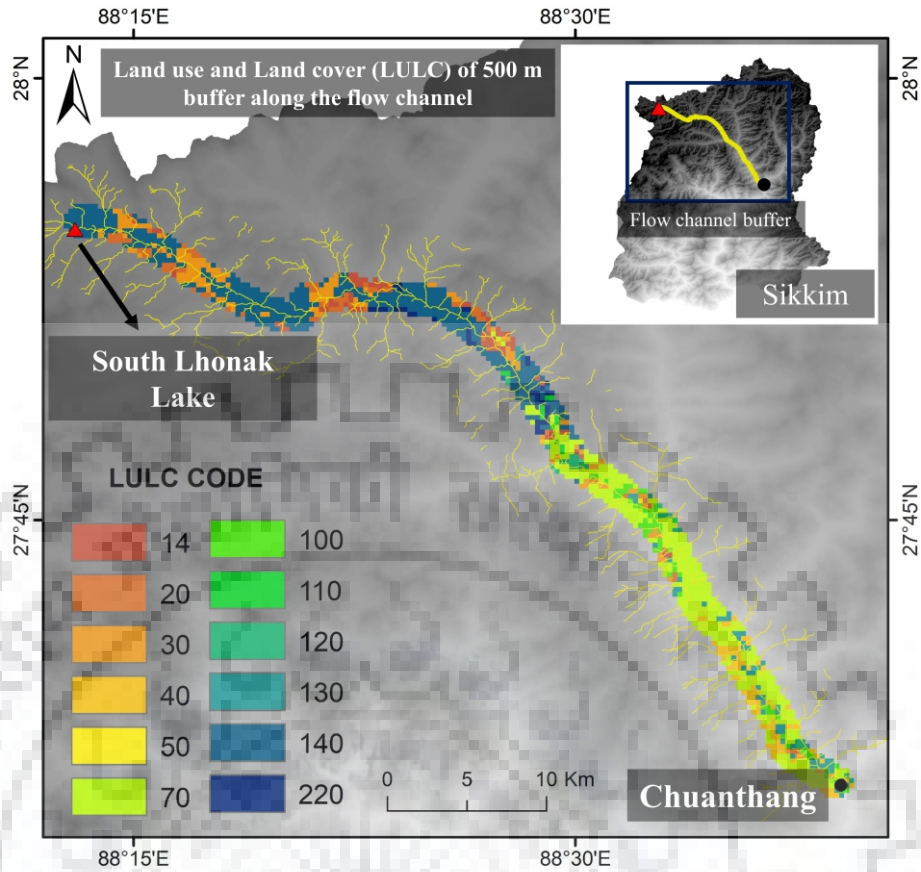
Figure 4.5 LULC along the buffer zone of the main channel from the South Lhonak lake up to Chungthang town; LULC code is given as per table 4.2
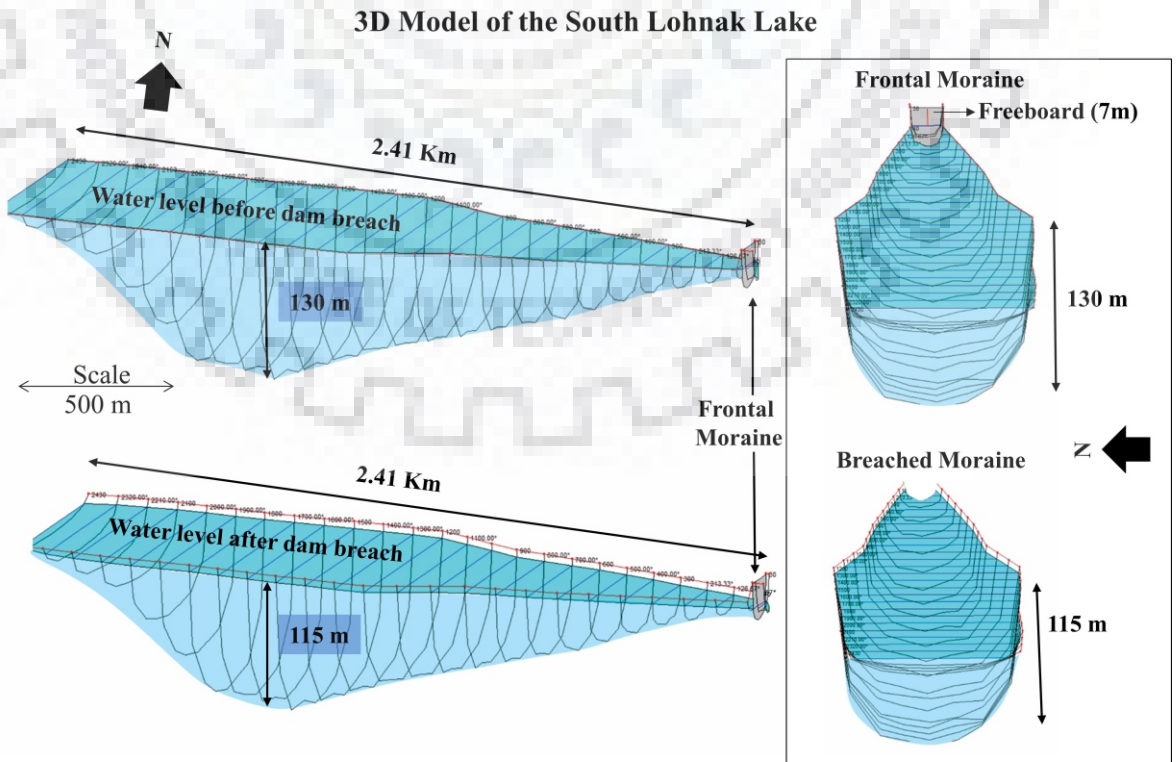
Figure 4.6 3-D model of the South Lhonak lake (reconstructed from Sharma et al., 2018) showing water levels before and after the breach event (Scenario-2)

levels creates a runway incision until it reaches the base of the moraine (Westoby et al., 2014). In the present study, four different dam breach scenarios based on varied breach width, failure time and breach mechanism are modeled for the South Lhonak lake. The breach scenarios are modeled for two different failure mechanism- overtopping and piping. The average breach width and failure time were calculated using the empirical relations given by Froehlich (1995). Equation 1 shows the relation of total breach width (B_w) as a function of the total volume of water upstream (V_w) and the height of the breach (h_b). The relation for determining the time of failure (T_f) based on the same parameters, is given in equation 2. Here, an unsteady flow simulation is performed, where the breach width is reached within the calculated time of failure, releasing a definite volume of water stored in the lake. Figure 4.4 shows a schematic diagram of the South Lhonak lake and the different mechanism of moraine failure with varied breach width and failure time. To evaluate a potential worst-case GLOF event of the lake, the scenario producing the maximum peak flood (Q_{max}) is considered for further routing along the flow channel until it reaches the Chungthang town.

$$B_w = 0.1803 K_o (V_w)^{0.32} (h_b)^{0.19} \qquad eq. \ 1$$

$$(T_f) \ in \ h = 0.00254 \ (V_w)^{0.53} (h_b)^{-0.9} \qquad eq. \ 2$$

The study models two different overtopping failure scenarios of the South Lhonak frontal moraine. In addition, piping failure was modeled to evaluate two additional scenarios, where the moraine failure initiates at a point of the lake water level. The total breach depths of 12 m and 15 m were considered based on the longitudinal depth profile of the lake and the freeboard of the frontal moraine (Sharma et al., 2018). It is assumed that triggers like ice/snow avalanches, debris low/rock fall or calving processes may generate impulse waves capable of initiating an overtopping failure eventually leading to a GLOF event with breach depth reaching up to a maximum of 15 m. Two different breach width of 91.79 m and 95.78 m, calculated based on the final breach depths (eq. 1), were used to model both overtopping and piping failure mechanisms to calculate the initial GLOF hydrograph. The empirically calculated failure time using the breach invert levels of 12 m and 15 m are 3.70 hrs and 3.09 hrs respectively (eq. 2). Table 4.1 gives details of breach parameters like breach width (m), time of failure (hrs), and breach invert level (m) for the different scenarios. The peak discharge ($m^3 s^{-1}$) and the total discharge volume (m^3) is reported in each case.

Table 4.1 Details of breach parameters like breach width (m), time of breach formation (hrs), breach invert level (m) for the different GLOF scenarios; Modeled discharge volume (m^3) and the peak flood (m^{3}s^{-1}) of the breach hydrograph are listed.

	Failure Mode			
	Overtopping		Piping	
	Scenario 1	Scenario 2	Scenario 3	Scenario 4
Breach Width (B$_w$) (m)	91.79	95.78	91.79	95.78
Time of failure (T$_f$) (hrs)	3.7	3.09	3.7	3.09
Breach invert level (m)	12	15	12	15
Discharge Volume (m^3)	25.5 x 10^6	25.7 x 10^6	25.5 x 10^6	25.7x 10^6
Percentage Volume of water released	38.74 %	39.05%	38.74 %	39.05 %
Peak discharge (Q$_{max}$)(m^{3}s^{-1})	5082.8	6064.6	4572.8	5126.2

4.4.2 LULC and Manning's N

Manning's roughness coefficient (Manning's N) determines the friction presented by a flow surface to a given flow (Coon, 1997). It is dependent on the land use and land cover (LULC) of a given terrain. In the present study, Manning's N is obtained for the flow area from the GlobCover LULC product (V2.3). A buffer zone of 500 m is constructed around the main channel and LULC is extracted for the defined buffer area using GIS-based tools. A total of twelve LULC classes is identified within the flow area, of which 8 classes have a Manning's N value of less than 0.06 (Table 4.2). Westoby et al. (2015) stated the value of 0.05 as a global Manning's roughness coefficient for a flood plain setting consisting of pebbles, cobbles, and boulders. The average Manning's N value for the given flow area is calculated to be 0.059. The sensitivity of the model to Manning's N for the given flow area is evaluated by changing its value by ±0.01 and ±0.02. A variation of 2% and 3% in the peak flood, is evident when δn was considered to be 0.01 and 0.02 respectively. Thus, in the present study, a uniform Manning's N of 0.059 is considered as model input for the hydraulic GLOF routing of the South Lhonak lake. Figure 4.5 shows the LULC along the buffer zone from the South Lhonak lake up to the 'Chungthang' town.

Table 4.2 LULC classes along the flow area and its respective Manning's N

LULC CODE	Description	Manning's N
11	Post-flooding or irrigated croplands (or aquatic)	0.034
14	Rainfed croplands	0.06
20	Mosaic cropland (50-70%) / vegetation (grassland/shrubland/forest) (20-50%)	0.034
30	Mosaic vegetation (grassland/shrubland/forest) (50-70%) / cropland (20-50%)	0.034

50	Closed (>40%) broadleaved deciduous forest (>5m)	0.1
70	Closed (>40%) needle-leaved evergreen forest (>5m)	0.11
100	Closed to open (>15%) mixed broadleaved and needle-leaved forest (>5m)	0.11
110	Mosaic forest or shrubland (50-70%) / grassland (20-50%)	0.035
120	Mosaic grassland (50-70%) / forest or shrubland (20-50%)	0.035
130	Closed to open (>15%) (broadleaved or needle-leaved, evergreen or deciduous) shrubland (<5m)	0.07
140	Closed to open (>15%) herbaceous vegetation (grassland, savannas or lichens/mosses)	0.05
220	Permanent snow and ice	0.04

4.4.3 One-dimensional GLOF routing

The HEC-RAS 1D model was employed to simulate a potential GLOF event of the South Lhonak lake. The model provides the solutions of the full one-dimensional St. Venant equations for unsteady flows. In order to establish a functional setup of the model, HEC-RAS requires a series of inputs that includes terrain data, boundary conditions, and Manning's roughness coefficient. In one-dimensional dynamic routing, terrain data implies to the cross-sections along the flow channel, which is derived from ALOS PALSAR DEM (12.5 m) in the present study. Cross-sections were extracted for every 500 meters along the flow channel from the lake up to the Chungthang town. A left and a right bank are demarcated on every cross-section in a way that it covers the adjacent floodplains. The upper and the lower boundary conditions were defined as the breach hydrograph and normal depth respectively. A common projection of UTM-43 is considered for the study based on the geographic location of the area. The Manning's N value is assigned to each cross-section. An unsteady flow simulation with pre-defined settings of computational interval and hydrograph output interval is performed. The output hydrographs are analyzed at different point of interest along the flow channel to evaluate the peak flood (in m^3s^{-1}) and the time of flood wave arrival (in min).

4.4.4 Two-dimensional GLOF routing

The HEC-RAS 2D (Version 5.0.5) is used to rout the initial breach hydrograph along the flow area from the South Lhonak lake up to the Chungthang town. The primary input of the model includes terrain data and boundary conditions for simulating an unsteady hydraulic process. ALOS PALSAR DEM raster is used as a continuous pixel-based terrain input. A flow area is initially defined over the given terrain, containing the area of interest i.e. the lake to the Chungthang town. Thereafter, a 2D mesh is constructed within the given flow area, with an individual cell dimension of 30 × 30 m. Each cell is defined with a Manning's N value (same as 1D) and its respective terrain elevation (extracted from DEM). The two-dimensional dynamic
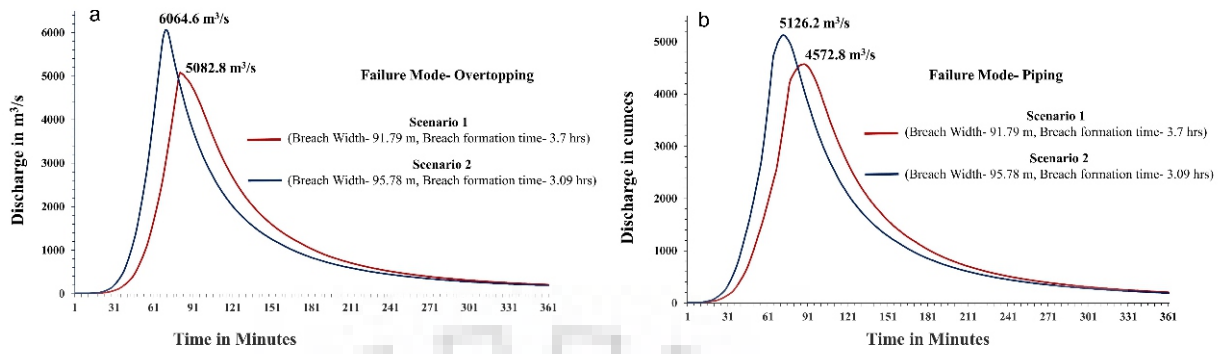
Figure 4.7 Moraine-breach outflow hydrographs showing peak discharge for two different scenarios – (a) overtopping failure mode; (b) piping failure mode
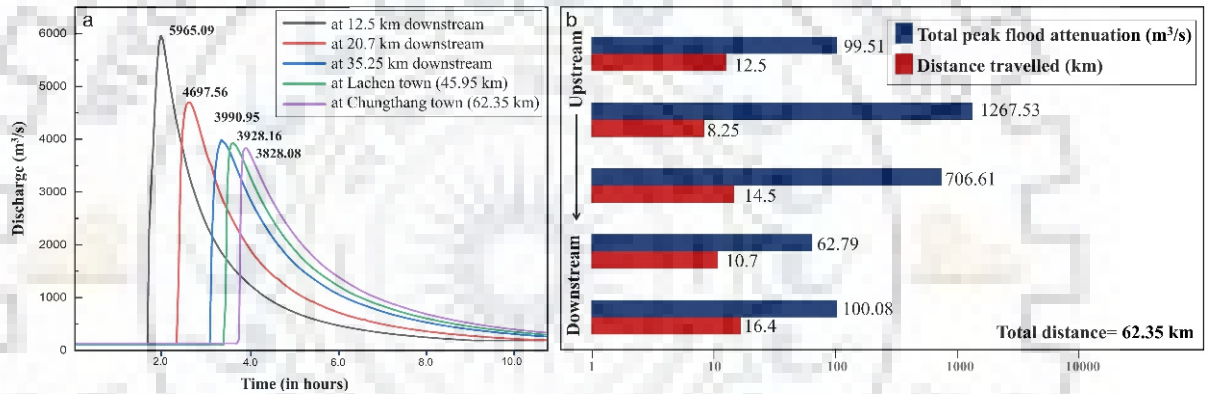
Figure 4.8 (a) Routed GLOF hydrographs at different locations along the flow channel; (b) total peak flood attenuation ($m^3 s^{-1}$) and its corresponding distance traveled (km) from upstream (South Lhonak lake) to downstream (Chungthang town)
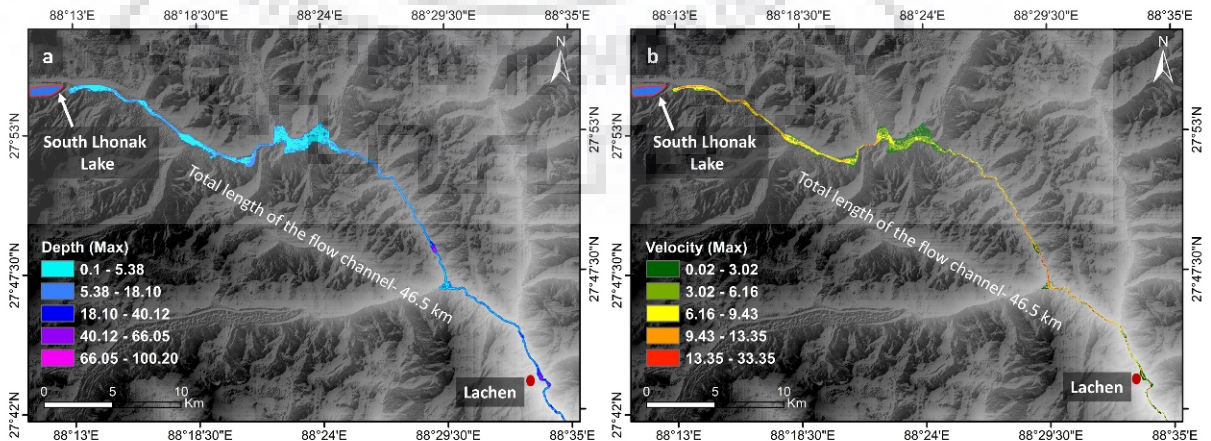
Figure 4.9 Spatial plots of (a) inundation depth and (b) flow velocity along the main channel from the South Lhonak lake to Lachen

modeling provides solutions based on depth-averaged shallow water equations (Hervouet, 2007). The multi-dimensional computation of hydraulic properties of the flood wave yields spatially distributed outputs of water depth, velocity, and inundation.

A potential GLOF impact of the South Lhonak lake is analyzed by spatial and temporal mapping the 2D model outputs. As GLOFs are associated with short-lived flood waves with high energy (Björnsson, 2003), its temporal characterization needs assessment in shorter time spans in the order of a few minutes to seconds. The presence of natural flow obstruction along the flow channel may interrupt the flow process, thereby affecting its overall impact due to the loss of energy and its transient nature. Thus, the present study attempts to evaluate the effect of a topographic barrier (as mentioned in section 4.2.1) on the hydraulic behavior of a potential GLOF wave of the South Lhonak lake. Two-dimensional simulation is performed to evaluate the flood wave hydraulics at points located upstream and downstream of the topographic barrier that cross-cuts the main channel of Goma Chu (Figure 4.12). Temporal assessment of the hydraulic properties like water depth and velocity have been carried out to understand the effect of such topographic barriers on the GLOF flow hydraulics.

4.4.5 Modeling potential flood remediation measure

The study aims in modeling a framework to propose a potential flood remediation measure of the South Lhonak lake GLOF by demonstrating the effect of a lateral inline structure along the flow channel, to check the flow of the potential flood wave. The HEC-RAS component that allows efficient modeling of inline structures to simulate complex flow and assess the effect of engineering structures on a particular flow is exploited here. The South Lhonak GLOF is simulated by adding a flow barrier in the form of an artificial broad-crested dam, to the model setup. The spatially distributed 2D GLOF results of the South Lhonak GLOF is evaluated to precisely identify the locations of potential damage along the flow channel. For this, raster layers of GLOF wave properties (depth, area, and velocity) are overlapped over high-resolution imageries using a GIS platform. The potential damage site that the generated flood-wave first encounters during its propagation is then identified. The dimension of the inline structure is based on the volume of water released in the GLOF event and maximum water depth at the location. The model input parameters are considered the same as that in section 4.4.4.

4.5 RESULTS AND DISCUSSION

The South Lhonak lake has shown exponential growth in its spatial extent over the past four decades (Sharma et al., 2018; Aggarwal et al., 2018). As identified to be one of the most hazardous lakes with a high outburst probability (Raj et al., 2013; Worni et al., 2014), a series of dam-break hydrodynamic simulations have been performed to evaluate a potential GLOF event
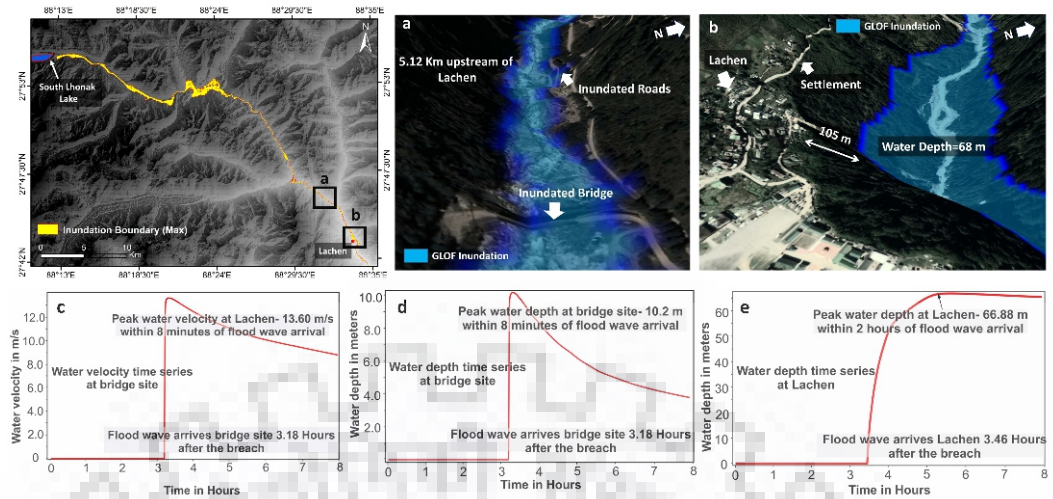
Figure **4.10** Spatial distribution plot of the inundation area along the main channel- Subset a and b shows the location of the bridge and town 'Lachen' respectively; (a) Inundation of bridges and roads at 5.12 km upstream of Lachen; and (b) inundation depth at Lachen; Plots showing (c) flow velocity vs. time at the bridge site; (d) inundation depth vs. time at the bridge site; (e) inundation depth vs. time at Lachen
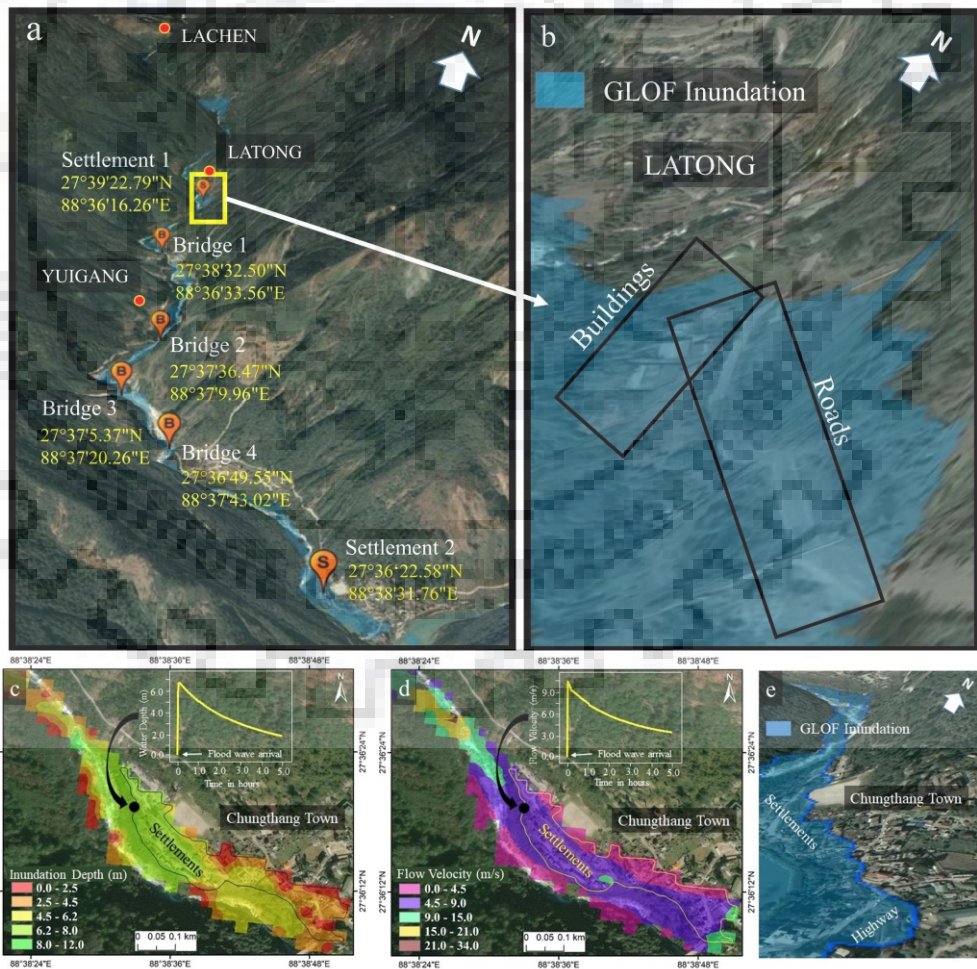
Figure 4.11 (a) Flowpath from Lachen to Chungthang showing the locations of the inundated bridges and settlements; (b) Inundated roads and buildings at Latong; Spatial plots showing (c) Flow depth, (d) Flow velocity, and (e) Flow inundation at Chungthang town

of the lake. One-dimensional hydraulic routing along the flow channel allowed calculation of the peak flood (in m^3s^{-1}) and the timing of flood (in minutes). In addition to this, two-dimensional routing of the breach hydrograph facilitated calculation of other significant flood wave parameters like water depth, inundation area, time of the flood, and flow velocity. The 1D and 2D results showed excellent comparability in terms of the flood wave arrival time and peak flood.

4.5.1 GLOF modeling

The South Lhonak moraine-breach was modeled to calculate the initial breach hydrograph, which is further routed along the given flow channel. In the present study, 'Scenario 2' with a calculated failure time of 3.09 hrs and a breach width of 95.78 m, produces the maximum peak flood of 6064.6 m^3s^{-1} releasing a total volume of 25.7 × 10^6 m^3 from the South Lhonak lake (Table 4.1). Thus, the breach hydrograph obtained in 'Scenario 2' is considered for one-dimensional and two-dimensional hydraulic routing along the main flow channel. Figure 4.6 shows the 3-D lake models with lake water levels, before and after the breach. Figure 4.7 shows the breach hydrographs obtained for two different failure mechanisms (overtopping and piping) based on the varied breach parameters as given in table 4.1.

4.5.2 Temporal hydraulics and flow phenomenon
a. One-dimensional hydraulic routing

One-dimensional unsteady flow routing of the breach hydrograph was performed from the lake up to the Chungthang town, located at a distance of 62.35 km downstream. This resulted in GLOF hydrographs revealing the peak flood and the time of flood wave arrival at different locations along the flow channel. The GLOF hydrographs are evaluated at five locations located at a distance of 12.5 km, 20.7 km, 35.25 km, 45.95 km (Lachen town) and 62.35 km (Chungthang town) downstream from the South Lhonak lake (Figure 4.8a). The assessment of the output hydrographs at different locations along the channel shows a maximum peak flood attenuation between 12.5 km and 20.7 km downstream from the lake. A 21% attenuation in the peak flood is evident as the GLOF propagates through this part of the flow channel (Figure 4.8b). This can be attributed to the decrease in the flood energy due to the presence of the flow obstruction (section 4.2.1) in the form of a lateral moraine, cross-cutting the main flow channel. Further routing along the channel reveals a GLOF hydrograph with a peak of 3928.16 m^3s^{-1} at Lachen town, located 42.95 km downstream from the lake. At Chungthang town, the modeled potential GLOF event results in a peak flood of 3828.08 m^3s^{-1} (Figure4.8a). The flood wave arrives the town 4 hours after the initial breach of the frontal moraine. The evaluation of the flow hydraulics shows minimal attenuation (2.6%) in the peak flood as the flood propagates the last 27.1 km until it reaches the Chungtang town (Figure 4.8b). The water volume is eventually discharged at the
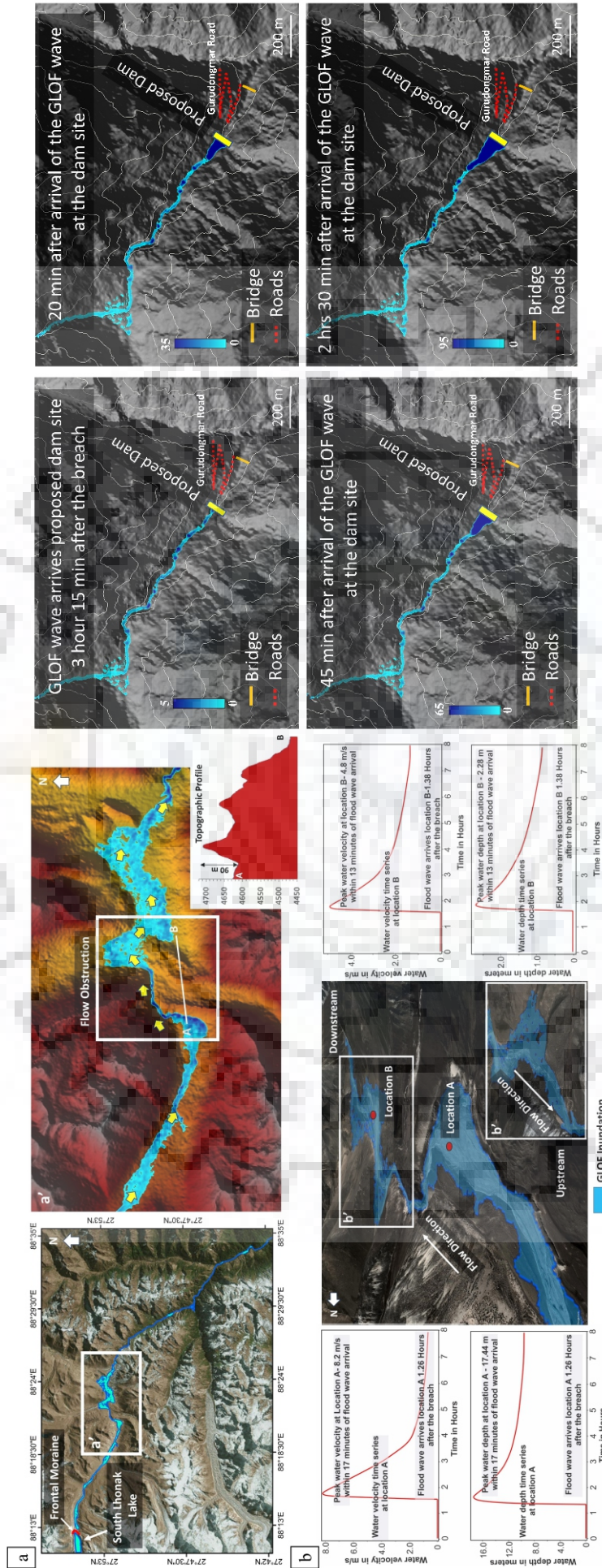
Figure 4.12 a. The South Lhonak lake, its frontal moraine, the location of the cross-cutting paleo-lateral moraines is shown in 'subset a''; (a') DEM showing the cross-cutting paleo lateral moraines cross-cutting the main channel, a cross-sectional plot (AB) showing the relief of the flow barrier; b. The main channel of the South Lhonak valley showing the location of the two points located upstream and downstream of the flow barrier (center); time series plots of inundation depth and flow velocity at location A (left) and location B (right)

Figure 4.13 Map showing the modeled dam structure and the downstream infrastructure (bridge, and roads); temporally mapped flood wave showing the spatial distribution of inundation depth at the proposed dam site

reservoir site of a dam located at Chungthang town. Table 4.3 gives the modeled GLOF peaks and the time of arrival at different locations along the flow channel.

Table 4.3 Peak flood and time of peak at different locations along the flow channel

Downstream distance from the lake	Peak Flood (m^3s^{-1})	Time of peak (in Hrs)
0 km	6064.6	1.0
12.5 km	5965.09	2.0
20.7 km	4697.56	2.75
32.25 km	3990.95	3.25
Lachen Town (45.95 km)	3928.16	3.40
Chungthang Town (62.35 km)	3828.08	4.0

b. Two-dimensional hydraulic routing

The potential impact of an extreme flow event that makes its onset from the South Lhonak lake is studied by evaluating the temporal and spatial two-dimensional hydraulic characteristics of the flood wave along the given channel. Due to the fact that high-magnitude flood events have a higher tendency to change its hydraulic properties with time, the present study evaluates the time series of the model outputs like inundation depth and flow velocity to understand its unsteady hydraulic behavior. Two-dimensional routing of the initial breach hydrograph is performed for a distance of 62.35 km along the main flow channel from the lake up to 'Chungthang' town through Lachen, Latong and Yuigang towns. The simulation resulted in a flood wave that reaches the nearest town 'Lachen' at 3 hours 38 minutes after the initiation of the lake-breach event. The maximum inundation area along the given valley is calculated to be 12.37 km^2. The mean water depth and flow velocity along the entire channel are recorded as 8.7 m and 11.25 ms^{-1} respectively. Figure 4.9 shows the spatial plots of water depth and flow velocity along the main channel from the South Lhonak lake to the nearest town 'Lachen'. The water depth at Lachen reaches up to 50 m within 20 minutes of the flood wave arrival (Figure 4.10e). The inundation depth further increases to 68 m within 2 hours from the time of flood wave arrival. However, the recorded maximum flow height remains 100 m below the elevation of the Lachen town (Figure 4.10b), which prevents inundation of the settlement. The flood wave makes its way to the Lachen, affecting infrastructure (roads and bridges) along the main flow channel. It inundates a major bridge and several roads constructed along the banks of the channel located 5.12 km upstream of Lachen (Figure 4.10a) where the flood wave arrives within 3 hours 24 minutes after the initial breach event. The flow velocities reach to a maximum of 13.6 ms^{-1} (Figure 4.10c) and water depth of 10.2 m (Figure4.10d) is recorded within 8 minutes of the flood wave arrival, potentially causing severe inundation of the bridge and roads.

In the present study, the GLOF wave is further routed for another 16.4 km to analyze its impact on one of the major townships in the valley called 'Chungthang'. The flood wave inundates

several manmade infrastructures like bridges and settlements as it propagates along the channel, however, the major inundation occurs at Chungthang town, where the flow channel opens into the confluence of the Lachen and the Lachung rivers. The flood wave encounters the first settlement at 'Latong' (27°39'22.79"N, 88°36'16.26"E) (Figure 4.11b) located 9 km upstream of Chungthang town, where flow velocities are recorded to a maximum of 8.9 ms^{-1} and flow depths up to 8m. The flood wave inundates four bridges, one downstream of Latong and three as the flood propagates from Yuigang to Chungthang (Figure 4.11a). At Chungthang the flood wave velocity reaches up to a maximum of 9 ms^{-1} and water depths reaching up to 12m (Figure 4.11c and d). The flood wave first encounters the settlements of Chungthang at location 27°36'22.58"N and 88°38'31.76"E. It inundates a total settlement area of 55,000 m2 along the banks of the flow channel (Figure 4.11e) at Chungthang where flow velocities reach up to a maximum of 9ms^{-1} and flow depths up to 8 m. The flood wave also inundates the north Sikkim highway-bridge, eventually discharging the entire volume to the hydropower reservoir at Chungthang.

4.5.3 Topographic controls over the main channel flow

Figure 4.12 shows the location of South Lhonak lake, its frontal moraine, and location of the cross-cutting paleo-lateral moraines. A 90 m tall barrier is clearly evident in its relief along profile AB over the cross-cutting paleo-lateral moraines (Figure 4.12a'). The dynamic simulation of the South Lhonak GLOF reveals a flood wave that strikes the cross-cutting lateral moraines after 1.26 hours of the initial breach event of the South Lhonak lake. The flood wave gets diverted towards the left as it strikes the flow-barrier and makes its way through a narrow passage and continues to flow downstream. A time series evaluation of the hydraulic properties of the flood wave is performed at two locations (upstream and downstream of the flow barrier), to understand the hydraulic behavior of the flood wave as it encounters the flow obstruction. Figure 4.12b shows the location of the two points on which time series evaluation of inundation depth and flow velocity was performed. An attenuation of the flood wave energy is clearly evident, as the flow velocity drops by 42.5% from 8 ms^{-1} to 4.6 ms^{-1} as the flow crosses the topographic barrier. The water depth at location 'A' reaches up to 17.44 m within 17 minutes of the initial flood wave arrival. It is gradually declined to a maximum depth of 2.28 m at location 'B' (Figure 4.12b).

4.5.4 Comparison with the empirical model

Hydrodynamic modeling is often associated with uncertainties, as not much information about the moraine characteristics and breach formation process are available. However, several empirical relations have been developed to estimate peak flows, as a function of the total discharge volume in a GLOF event (Costa and Schuster, 1988; Evans, 1986; Huggel et al., 2002).

This section is an assessment to compare the modeling outputs in the present study to empirically derived outputs. For that, the relation between peak flood discharge and volume of water given by Evans (1986) (Equation 3) is adopted to compare the peak discharge of the South Lhonak GLOF event.

$$Q^{max} = 0.72 \ V^{0.53} \hspace{2cm} \text{eq. 3}$$

Where Q^{max} is the peak GLOF discharge and V is the total volume of water released in the event.

In the present study, given as 'Scenario 2' (Table 4.1) produces a breach hydrograph with a peak flood of 6064.6 m^3s^{-1}. The peak flood is calculated using Evans, (1986) for the same discharge volume (25.7 × $10^6 \, m^3$) is 6089.7 m^3s^{-1}. A difference of 25.11 m^3s^{-1} accounts for 0.4% of the total modeled discharge. The difference in the peak flood between modeled discharge to that of Evans, (1986) for scenarios 1, 3 and 4 are 19.4%, 32%, and 18.7% respectively. Thus, it can be inferred that the different breach parameters considered to model 'Scenario 2' produced a hydrograph with a maximum peak discharge that is in line with that calculated using Evans (1986). And flood routing using the same breach hydrograph yields more realistic outputs of flow hydraulics of a potential GLOF along the South Lhonak valley.

4.5.5 Two-dimensional modeling to demonstrate the effect of a remedial lateral inline structure

In the present study, a modeling approach to construct a lateral structure along the flow path is adopted to propose a potential GLOF-remedial measure. Here, a lateral structure in the form of a broad-crested dam is modeled with a height and width of 110 m and 15 m respectively. An assessment is performed to evaluate the overall reduction in the susceptibility of the downstream infrastructure to a potential GLOF event of the South Lhonak lake in the presence of such an engineering structure. The volume capacity of the modeled remedial structure is calculated to be slightly greater than the total volume of water released in the potential worst-case GLOF event of the South Lhonak lake (25.7 × $10^6 \, m^3$). The site chosen to model the lateral structure is based on the 2-D hydrodynamic simulation outputs of a potential GLOF event of the lake. The chosen site is located 120 m upstream of the location where the potential GLOF wave encounters the first bridge located 5.12 km upstream of Lachen and potentially inundates it (Figure 4.10a). The study performs a two-dimensional simulation to understand the change in GLOF hydraulics due to flow-regime modification produced by the modeled lateral structure. The potential GLOF wave from the South Lhonak lake arrives the modeled dam site at 3 hrs 15 min after the initial breach event. The GLOF wave response, at the dam site, is evaluated by the temporal mapping of the inundation depth. Figure 4.13 shows the location of the modeled dam structure, location of bridge, roads and the temporally mapped water depth of flood wave at the dam site. The

simulation results reveal that the proposed dam structure can harness the water released during the GLOF event of the South Lhonak lake within 2 hours 30 min of the GLOF wave arrival. Thus, it may be inferred that the proposed lateral structure may be considered as an effective measure to check the flow of a potential GLOF event. In addition, facilitating a controlled flow through such a damming structure in its operational setting can significantly reduce its impact on immediate downstream regions in the given valley. Further downstream, such a measure would significantly reduce the impact of such high-water discharge on hydropower stations located along the flow channel of the South Lhonak lake. The construction of such flood remediation structures would require a detailed assessment that includes onsite investigation and evaluation of its cost-effectiveness. Also, construction of such remedial infrastructure requires detailed evaluation of the possible consequences from a multidisciplinary perspective. Thus, dam assessment modeling (Brown et al., 2008) may facilitate efficient planning for the construction of such flood-mitigation engineering structures.

4.6 CONCLUSION AND WIDER IMPLICATION

The South Lhonak lake has been gaining wide attention, due to the exponential increase in its size over the years. Being one of the largest lakes in the state of Sikkim, the government and the research community have been taking much interest in understanding its hazard potential. In the present study, a potential GLOF event of the South Lhonak lake is modeled taking into consideration an accurate bathymetric setup to model different breach failure mechanisms. The hazard assessment of the worst-case GLOF scenario which resulted from a 15 m breach in an overtopping failure was performed by the one-dimensional and two-dimensional routing of a potential dam breach hydrograph of the South Lhonak lake along the flow channel up to the town 'Chungthang', located 62.35 km downstream of the lake. The one-dimensional model outputs calculated the flood hydrographs to determine the peak flood (m^3s^{-1}) and the time of flood wave arrival (hrs) at different locations along the given flow channel. Whereas, two-dimensional routing of flood wave was employed to determine the areas, exposed to such a high magnitude GLOF event based on the spatially distributed model outputs of flow depth, velocity, and inundation. A more realistic modeling of the South Lhonak moraine-breach mechanism based on the available field measurements of the damming moraine, enabled us to estimate the actual volume of water that would be released in case of a dam-failure event of the lake. The flood routing was based on a uniform Manning's N value along the given flow channel. However, there is a scope to evaluate the temporal and spatial hydraulic variability of the flood wave to varied Manning's N along the given channel. In the present study, the worst-case GLOF scenario of the South Lhonak lake yielded an initial flood hydrograph with a peak discharge of 6064.6 m^3s^{-1}

releasing 39.05% of the total lake volume. The flood wave potentially inundates several infrastructures as it propagates through the Latong and Yuigang towns. A peak flood of 3828.08 m^3s^{-1}recorded at the Chungthang town, has a potential to inundate a total area of 55,000 m^2 of the existing settlements where flow depth and velocity reach up to 8 m and 9 ms^{-1} respectively. Based on the results, the most impacted area in a potential GLOF event of the South Lhonak lake can be identified as the Chungthang town where a major part of the settlement and infrastructure is affected. It may be noted that sudden discharge of such high volumes of water with a peak discharge reaching up to 3828.08 m^3s^{-1} is inferred to cause substantial damage to the hydropower dam site located at Chungthang, which needs further site-specific evaluation.

It is clearly evident from the study that the presence of a paleo-topographic feature cross-cutting the main flow channel significantly minimizes the energy of the South Lhonak GLOF wave. Despite being obstructed by such a topographic barrier, the resulting GLOF event can cause significant damage to the downstream regions. The investigation also involved the modeling of a framework to propose a potential flood remediation measure of the South Lhonak lake GLOF by demonstrating the effect of a lateral inline structure along the flow channel, to check the flow of the potential flood wave and thereby reducing the impact of the GLOF wave in the downstream regions. Facilitating the construction of such structures across the flow channel would help to manage the risk imposed by such extreme-flow events on the downstream regions. The proposed damage-reduction strategy prevents inundation of two settlements along the given flow area covering a total area of 5836 m^2, five major bridges, and several roads. In addition to this, the spatial and temporal results obtained in the present study revealing the flow hydraulic properties of a potential flood wave would help in the precise identification of sites, suitable for the installation of other mitigation infrastructures like check dams and early warning systems. Based on the results, an early warning, if broadcasted immediately after the initiation of the dam breach event would give a response period of 3.75 hours before the flood wave hits the first settlement in the Chungthang town where the peak flood is reached within 15 to 20 min of the flood wave arrival. An early warning system, if installed at 21 km downstream of the lake would facilitate early warnings that can provide an evacuation time of 1.25 hours at Chungthang town.

In further studies, investigation of the engineering properties and in-situ measurements of the geomorphic features along the flow channel and the associated moraine is recommended to better evaluate the failure mechanism of the lake. Furthermore, the application of very high-resolution terrain data can produce modeling outputs with a lower degree of uncertainty and thus is recommended for further studies.

CHAPTER 5: ICE-THICKNESS BASED MAPPING OF MAXIMUM LAKE EXTENT - IMPACT ANALYSIS OF POTENTIAL FUTURE GLOF

5.1 INTRODUCTION

The significance of calculating spatially distributed glacier ice-thickness could be realized from the fact that it can be exploited to extract information of the glacier bed (Ramshankaran et al., 2018; Remya et al.,2019). Glacier response to climate change can be related to individual glacier-properties like ice thickness and velocity near the terminus (Johannesson et al., 1989). Kulkarni et al. (2007) performed a retreat analysis for 466 glaciers located in three major basins in the Himalaya. The Himalayan glaciers have been showing an accelerated recessional behavior from the past decade (Kulkarni et al., 2006; Kulkarni et al., 2007; Bhambri et al., 2011). Moreover, their non-synchronous response is indicated by the wide-ranging rate of glacier fluctuation over different geographical and climatic zones in the Himalayan cryosphere (Bolch et al., 2012). The changes thus brought about are often reflected in a gradual reduction of the total glacier area thereby exposing the glacier bedrock beneath it. The presence of depressions in the glacier bed of a retreating glacier may allow storage of the glacier meltwater to form a glacial lake. Similarly, the growth of an existing proglacial lake depends on the glacier bed topography of the associated glacier. A proglacial lake will continue to grow if there is room for the glacier meltwater to be stored on the bedrock as the glacier retreats. These depressions in the glacier bed are called overdeepning (Remya et al., 2019; Sattar et al., 2019). In this chapter, the glacier bed is evaluated to map the overdeepening sites present underneath the glaciers. This is achieved by obtaining spatially distributed ice thickness which later can be employed with glacier surface elevation to map the glacier bed.

The knowledge about accurate glacier thickness in the Himalaya is very limited (Armstrong et al., 2010). Inaccessible and difficult terrain primarily account for the inadequacy of information on in-situ/ground ice thickness measurements. In one of the widely used methods, mean ice thickness of a particular glacier is derived from its total surface area (Bahr et al., 1997). The inability to determine the spatial distribution of ice thickness is a major drawback of such area-based scaling methods. Moreover, its application in different geographical regions needs adequate calibration using accurate ground measurements of ice thickness to fine-tune the scaling coefficients. Huss and Farinotti (2012) emphasized on the inapplicability of any single area-based relation for all glaciers present on the globe. Several models are available to calculate spatially

distributed glacier ice-thickness (Gantayat et al., 2014; Huss and Farinotti, 2012; McNabb et al., 2012; Clarke et al., 2013). Farinotti et al. (2019) presented the latest consensus estimate of ice thickness of the globe apart from the ice sheets.

Huss and Farinotti (2012) presented the first global comprehensive glacier thickness estimate, using a physically based dynamic modeling approach. A readily available updated database on glacier-ice thickness observations worldwide has been made accessible using a user interface called GlaThiDa (WGMS, 2016). Farinotti et al. (2019) presented the most recent ice thickness of all the glaciers apart from the Greenland and Antarctic ice sheets. The current study is an attempt to coalesce remote sensing data and numerical modeling techniques to calculate spatially distributed ice thickness. The study incorporates the modifications defined in the algorithm (Gantayat et al., 2014) by calculating ice thickness along multiple flowlines, and spatially interpolating between adjacent flowlines to obtain an ice thickness distribution (Gantatyat et al., 2017).

Farinotti et al. (2017) presented a comprehensive assessment of glacier-ice thickness model performances (ITMIX), concluding that the most reasonable ice thickness estimates can be obtained by averaging between the given models. However, with specific reference to Tasman glacier (valley glacier) and the ice caps, the model by Gantayat et al. (2014) was found to be efficient and a highly reliable method for estimating ice thickness. Moreover, its small model bias as compared to various other ice thickness models revealed its performance (Farinotti et al., 2017). Based on the average model performance of the various models, the model by Gantayat et al. (2014) has been ranked as the third best of the 17 participating models, when considering the ice thickness of glaciers, ice caps and synthetic glaciers together (Farinotti et al., 2017). In case of glaciers only, the small model bias of Gantayat-v2, makes it a comparatively reliable model to derive ice thickness for valley glaciers (Farinotti et al., 2017). The method was adopted in the study, primarily due to its simplicity and the fact that the inputs required (glacier-surface velocity and slope) are easily retrievable using remote sensing datasets. Despite being relatively undemanding, the model by Gantayat et al. (2014) produced as reliable outputs as those produced by models that take into consideration the glacial mass turnover and ice flow mechanics (Farinotti et al., 2017). However, complications may arise in deriving satellite-based glacier-surface velocities due to snow and cloud cover. The mass conservation approaches require glacier mass balance information to reconstruct ice thickness (Farinotti et al., 2009a; Farinotti et al., 2009b; Morlighem et al., 2011; Huss and Farinotti, 2012; Clarke et al., 2013; Brinkerhoff et al., 2016). In addition, shear stress models also involve mass balance inputs to calculate glacier volume (Clarke et al., 2013). Thus, the absence of mass balance data appears to be a major shortcoming for the application of these models over the Himalayan glaciers. Farinotti et al. (2017) reported

the HF-model (Huss and Farinotti, 2012) as the most efficient automated method which can handle large sample size. Due to very sparse glacier mass balance data for the Himalayan glaciers (Bolch et al., 2012), the approach adopted in the present study can be assumed reliable for ice thickness reconstruction, as it maintains the same order of accuracy as that of models taking into account the glacier mass balance like the HF-model (Huss et al., 2012; Farinotti et al., 2017).

The ice thickness model is calibrated over Chhota Shigri glacier, Western Himalaya, for which ground ice thickness estimates were available. A validation assessment is performed on the Satopanth glacier system, Central Himalaya. The present study uses previously published GPR measurements of ice thickness to calibrate and validate the model. For, inter-comparison of the obtained model output in the present study, distributed ice thickness obtained using a well-established model by Huss and Farinotti (2012) is exploited.

In this chapter, an investigation of the glacier bed topography is undertaken using empirically derived glacier-ice thickness for 15 larger glaciers in the Dhauliganga Basin. The study aims at the identification of overdeepening sites in the basin, which are likely the potential lake formation sites in the future (Bennett et al., 2012). Also, the study is aimed to map the maximum extent of the largest proglacial lake in the basin. Further, hydrodynamic modeling is performed to evaluate the future GLOF potential and its impact on hydropower dam sites located downstream. Similar, study to calculate the future GLOF potential is undertaken for the South Lhonak glacier, Sikkim, the present GLOF potential of which has been evaluated in Chapter 4.

5.2 STUDY AREA

The present study is carried out in the Dhauliganga basin, a major basin located in the state of Uttarakhand, Central Himalaya (Figure5.1). The basin is drained mostly by glacier-fed rivers, a premier being the Dhauliganga River, a major tributary of the Kali River. The enduring flow of the river is attributable to its steep slopes, intensive monsoon precipitation, and seasonal snowmelt, possessing great potential for hydropower generation. The lower and upper bounds of the basin lie between latitudes 29°58'N to 30°31'N and longitudes 80°21'E to 80°34'E encompassing a total area of 1667 km^2. Over 85 % of the basin is covered with seasonal snow. Moreover, the area above 5000 m a.s.l is restricted to permanent ice and snow. We pre-select 15 glaciers that are larger than 1 km^2. They cover a total surface area of 69 km^2 and lie in the elevation band between 3400 to 6445 m a.s.l. The majority of the selected glacier lies on the western flank of the basin that directly contributes its meltwater to the lesser Yanti river and the remaining in the eastern flank, to the Dhauliganga river. The primary importance of the study area lies in the fact that there is a direct contribution of glacier meltwater to the mainstream of a

hydropower dam (29°58′46″N, 80°34′05″E), located at the lowest point of the catchment, at Gargua in Pithoragarh district. Moreover, the largest proglacial lake in the basin is located immediately adjacent to the mainstream of the same hydropower dam. A potential failure of the lake would have a direct impact on the hydropower dam.

5.3 DATA USED

The present study exploits glacier outlines available in Randolph Glacier Inventory (RGI) which is an open-source database for the existing glaciers in the globe. The latest available version of glacier boundaries (RGI 6.0) is employed for calculating the total volume in the basin (RGI Consortium, 2017). The data can be freely downloaded from http://www.glims.org/RGI. A projection system of UTM-44 was defined to the glacier outlines based on the location of the study region. The Advanced Spaceborne Thermal Emission and Reflection Radiometer (ASTER) global digital elevation model (DEM) (v2) was used to extract topographic information. ASTER GDEM (v2) is a latest version of publicly available elevation model (https://earthexplorer.usgs.gov/) that provides elevation information between 83° N and 83° S with a spatial resolution of 30 m and a vertical accuracy of ~10-20 m for hilly terrains (Fujita et al., 2008; Tachikawa et al., 2011).

Landsat TM and OLI/TIRS (30 m) were used for glacier and lake mapping in the basin. Two Landsat-8 panchromatic bands (15 m) acquired for consecutive years were used for glacier velocity estimation in the basin, including the validation glaciers. The historical extent of the largest proglacial lake in the basin was mapped using cloud-free declassified aerial photographs of Corona KH-4 (7.5 m). The Corona database is a collection of very high-resolution aerial images acquired from 1960 to 1972 during a space reconnaissance programme, operated jointly by the Central Intelligence Agency (CIA) and the US Air Force (USAF) (Dashora et al., 2007). The Landsat and Corona data used in the study are freely downloaded from https://earthexplorer.usgs.gov/. The acquisition dates and sensor information for the remote sensing datasets are given in Table 5.1.

For the calibration and validation glaciers, available ground measurements of ice thickness were used to compare the model outputs. Ground penetrating radar (GPR) measurements along five transects with a positional accuracy of ± 0.1 m and overall uncertainty of ± 15 m in ice thickness were used for Chotta Shigri glacier system to calibrate the model inputs (Azam et al., 2012). Similarly, GPR measurements of ice thickness along two transects with a positional accuracy of 1 cm and 7 % uncertainty in ice thickness have been used to validate the model for Satopanth glacier system (Mishra et al., 2018). In addition to this, spatially distributed ice thickness of the
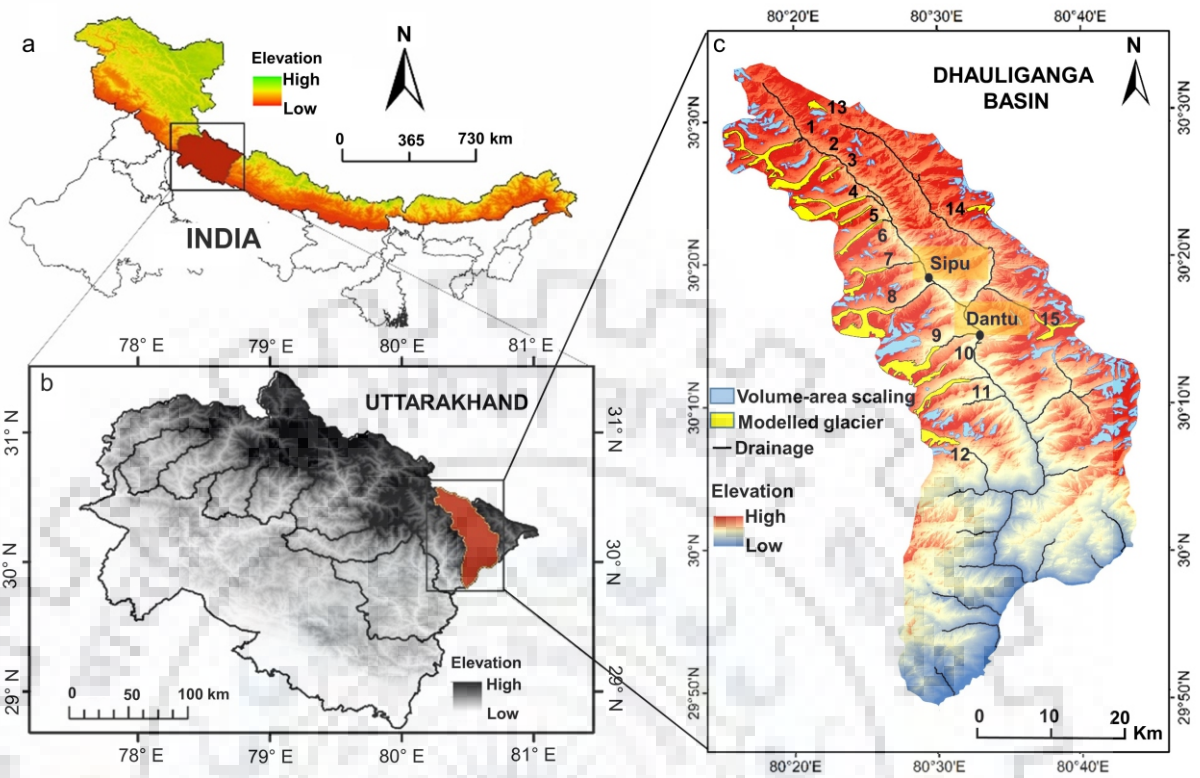
Figure 5.1 (a) Himalayan arch showing the state of Uttarakhand, Central Himalaya; (b) the location Dhauliganga Basin, North-east Uttarakhand; (c) Dhauliganga basin showing the glaciers selected for the study; the location of the largest proglacial lake and the hydropower dam is marked
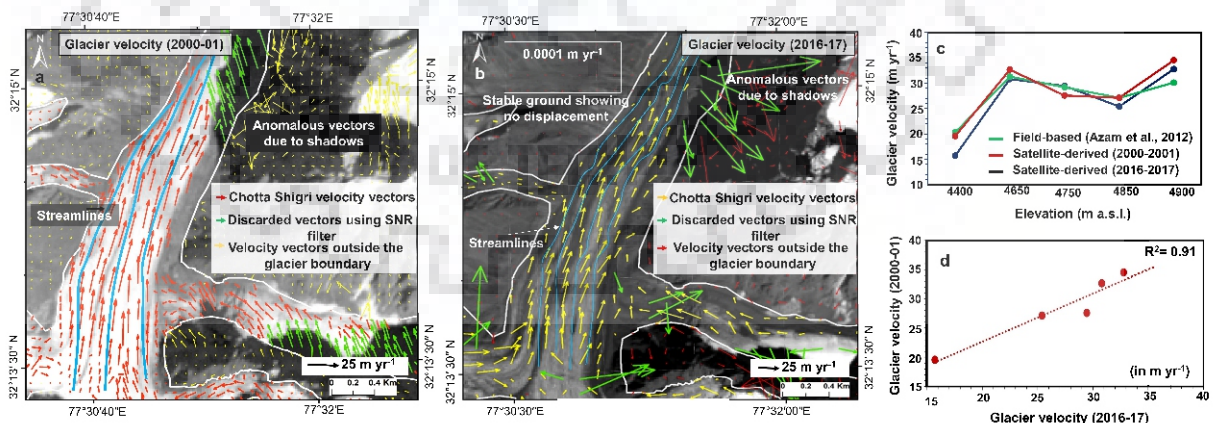
Figure 5.2 Satellite-derived velocity field of Chhota Shigri glacier for (a) 2000-01 and (b) 2016-17; displacement over stable ground is nearly zero; discarded vectors are based on signal to noise filtering; (c) Satellite-derived velocity (2000-01 and 2015-16) and field-based velocity (2003-04) (Azam et al., 2012) at different elevations; (d) Glacier velocity (2000-01) versus glacier velocity (2016-17)

HF-model by Huss and Farinotti (2012) were employed to compare the modeled ice thickness of the calibration and validation glaciers.

Table 5.1 Details of the satellite data used

Purpose	Satellite/Sensor	Date of Acquisition
Glacier and lake mapping; glacier-surface velocity (Dhauliganga)	**Landsat TM**	23 October 1990
	Corona (KH4)	27 September 1968
	Landsat OLI/TIRS	03 September 2015 03 September 2016
Basin delineation; slope estimation	**ASTER GDEM**	
Validation and Sensitivity		
(Chhota Shigri) Glacier-surface velocity	**Landsat TM**	15 October 2000 18 October 2001
	Landsat OLI/TIRS	03 October 2016 06 October 2017
(Satopanth Glacier) Glacier-surface velocity	**Landsat OLI/TIRS**	06 November 2016 24 October 2017
Slope	**ASTER GDEM**	

5.4 METHODOLOGY

In the first phase of the study, satellite imagery has been employed to modify the existing glacier outlines available in RGI (Version 6.0), by mapping the glaciers using a multiple-criteria decision algorithm (Paul et al., 2004). The glaciers chosen for the present study are based on the criteria given in section 5.4.1. The retreat analysis is performed for the glacier which contains the largest proglacial lake in the basin using multitemporal satellite data. The second phase of the investigation includes mapping of the overdeepening sites (section 5.6) using modeled ice-thickness distribution of the larger glaciers in the basin (section 5.4.3.b). The third phase of the study involves mapping of the maximum future extent of an existing proglacial lake, the future GLOF potential of which is analyzed to study its impact on a hydropower station. Further, the future GLOF potential of the South Lhonak lake, Sikkim is evaluated using modeled lake bathymetric data. The present GLOF potential of the South Lhonak lake has been evaluated in Chapter 4. The description of the methods adopted for the study is given in the following sections.

5.4.1 Glacier selection criteria

The 15 larger glaciers (>1 km^2) selected for the investigation of ice thickness and glacier bed, satisfy the following criteria: (i) the obtained velocity field of the glacier is directional with movements from higher to lower elevation, (ii) the glaciers lie entirely within the delineated basin boundary, (iii) the size of the glacier is large enough to map the total area lost using 15m pan corrected Landsat composite image. Most of the glaciers in the basin fulfill these criteria. The

glaciers with an area of less than 1 km^2 are not considered for thickness modeling due to an inappropriate yield of the velocity field.

5.4.2 Mapping

The remote sensing datasets selected for mapping of the 15 larger (>1 km^2) glacier outlines (for ice-thickness estimation) fulfil the following criteria: (i) acquired at the end of ablation season ensuring minimum snow cover, (ii) the presence of minimum cloud coverage in the satellite scene, and (iii) identifiable glacier terminus in both Landsat and Corona satellite imageries. Glacier outlines mapped using Landsat TM and OLI has been considered to estimate ice volume. Unsupervised classification to map glacier boundaries may lead to high level of uncertainties, as most of the glaciers are debris covered in the Himalaya (Tiwari et al., 2012; Kumar et al., 2017). Normalized difference snow index (NDSI) and band ratio method alone is inefficient to map debris-covered glaciers (Bhambri et al., 2011). Hence, the multiple-criteria decision analysis (MCDA) for mapping debris-covered glaciers by thresholding values of TM 4/TM 5, hue, and slope have been exploited (Paul et al., 2004). A band ratio of band 4 (TM 4) and band 5 (TM 5) is computed and a threshold value of 2.0 is applied to distinguish the glacier from its surrounding. Paul (2000) fully justified the accuracy of TM 4/TM 5 band ratio method for glacier mapping by comparing it with the outlines derived using high-resolution SPOT (Satellites Pour l'Observation de la Terre) imageries and thereby establishing an error of less than 1%. The vegetation is distinguished by thresholding the hue component to a value of 126 of an intensity hue-saturation color model developed from TM bands of red, near infra-red (NIR), and short wave infra-red (SWIR). Calculation of glacier slope has been achieved using ASTER GDEM (Abrams et al., 2015). As parts of the glaciers are debris covered a threshold value of <24° is applied to delineate glacier surfaces using slope (Paul et al., 2004). Lastly, an overlay operation of the thematic layers satisfying all the above-mentioned threshold criteria is used to classify glacier surfaces and to map glacier outline (Paul et al., 2004). The terminus of the glacier has been identified by the presence of indicators like a proglacial lake, glacial stream or minimum surface velocity at the snout.

5.4.3 Glacier-ice thickness and overdeepings in the modeled glacier bed
a. Glacier velocity estimation

Glacier-surface velocity is obtained by image-to-image correlation at a sub-pixel level using COSI-CORR (Co-registration of Optically Sensed Images and Correlation), a module in ENVI image-processing software. The technique performs co-registration and correlates optical satellite images to calculate the resultant displacement (Scherler et al., 2008). In the present

study, two Landsat 8 Pan bands, with a temporal interval of 1 year were used to derive the surface velocity of the glaciers in the Dhauliganga Basin. This method of velocity estimation yields an accuracy of 1/4 of a pixel (Heid et al., 2012). The approach produces N-S and E-W displacement components that are used to estimate the resultant surface movement. A signal to noise filter is finally applied to avoid the anomalous velocity values.

Inaccurate co-registration of the images most often transfer the error to the image matching process, leading to erroneous velocities. To justify the accuracy of the correlation technique, the RMSE of the displacement measurements obtained over the stable ground is investigated in the Dhauliganga basin. In the present study, ice-free ground within the basin is assumed to be stable. A total of 334 measurements well spread over the basin is considered, to reveal the shift over the stable ground. The RMSE for E-W component, N-S component, and the resultant displacement is calculated to be 1.4 m, 0.9 m, and 0.8 m respectively (Table 5.2). The displacement over the stable ground is negligible when compared to the mean resultant displacement of the glaciers in the basin that is measured to be 28 m.

Table 5.2 Root mean square error (RMSE) of displacement components obtained over 149 point locations on the stable ground (assumed to have zero displacements) over one year. The number of measurements is given by n. The total offset is calculated as sqrt(x^2+y^2).

Displacement component	RMSE (Stable ground) (in m)	n
E-W (x)	1.40	149
N-S (y)	0.96	149
Total offset	1.76	149

b. Ice thickness

The present study aims at calculating the glacier-ice thickness using a velocity-slope based modeling method. The ice thickness distribution of the selected glaciers is computed using equation 1 (Gantayat et al., 2014).

$$H = \sqrt[4]{\frac{1.5\,Us}{A\,(f\rho gsin\alpha)^3}}$$
<div align="right">eq. 1</div>

Where H is the ice thickness in meters, U_s is the surface velocity (derived using image to image correlation of optical satellite image), α is the slope estimated for every 100 m interval, ρ is the ice density, g is the acceleration due to gravity (9.8 ms^{-1}), f is the shape factor, which is defined as the ratio between the driving stress and basal stress along a glacier (Haeberli and Hoelzle, 1995) and has a range of 0.6 to 1.0, A is the creep parameter which is assigned a constant value of 3.24×10^{-24} Pa^{-3}s^{-1} for temperate glaciers (Cuffey and Paterson, 2010). Owing to the unavailability of ground ice thickness measurements in the Dhauliganga Basin, f is calibrated on Chhota Shigri glacier to constrain the value for shape factor (Section 5.5). The slope calculation

has been performed for each elevation distance of 100 m using ASTER GDEM. The ice thickness calculated using pixel-based velocity measurements for different elevation bands using equation 1. It is further mosaicked and converted to individual pixel-based ice thickness point-values using the raster to point GIS-conversion tool. The ice thickness values extracted along the manually digitized flowlines (Linsbauer et al., 2012; Gantayat et al., 2017) are interpolated to obtain a U-shaped ice thickness distribution over the entire glacier area, assuming zero ice thickness along the boundary.

c. Uncertainty analysis

The principal causes of the uncertainty in ice thickness calculation are (1) error in surface velocity, (2) uncertain shape factor, (3) glacier-ice density variation, and (4) slope calculation errors. The combined relative uncertainty in glacier-ice volume estimation is determined by the equation derived by taking the natural logarithm of both sides of equation (1) and differentiating:

$$\frac{dH}{H} = 0.25 \left[\frac{dUs}{Us} - \frac{dA}{A} - 3\frac{df}{f} - 3\frac{d\rho}{\rho} - 3\frac{d(\sin\alpha)}{(\sin\alpha)} \right] \qquad - eq.\ 2$$

The image-to-image orthorectification errors lead to uncertainty in surface velocity estimation. This, when combined with the error due to image-to-image georectification gives rise to a cumulative error that lies in the range of 3 to 9 m. The value of dU_s is the difference between the observed and correlated velocity measurements. Since no observed ground velocity measurements were available for the glaciers in the current basin, a value of 3.5 m per year is considered, that is the difference between the observed (Swaroop et al., 2003) and satellite-based glacier-surface velocity outputs as obtained by Gantayat et al. (2014). As f is assumed to be 0.8, which has a range of 0.6 to 1.0, thus the value of df is considered as ±0.2. The value for creep parameter (A) has been considered as 3.24×10^{-24} Pa^{-3} s^{-1} (Gantayat et al., 2014). A uniform ice density (ρ) of 900 kg m^{-3} throughout the glacier is considered due to unavailability of actual in-situ data. It is assumed the ice density may decrease up to 850 kg m^{-3}. An uncertainty of 5.5% is calculated when $d\rho$ is 50 kgm^{-3}. Also, the unavailability of ground elevation measurement for the study area to estimate the uncertainty in slope calculation bound us to consider 11m as vertical inaccuracy for ASTER DEM calculated for the Himalayan region (Fujita et al., 2008). The uncertainty due to inherent DEM error is given by $d(\sin\alpha)$ and is calculated to be 0.11 m.

5.5 CALIBRATION AND VALIDATION OF THE MODEL

The distributed ice thickness model adopted in the present study is calibrated on the Chhota Shigri glacier (Western Himalaya) and validated on the Satopanth glacier system (Central Himalaya). Ice thickness distribution was calculated for each glacier as in section 5.4.3.b. Glacier-surface velocity was calculated using the same approach as section 5.4.3.a.

For Chhota Shigri glacier, surface velocity is calculated for 2000-01 and 2016-17, revealing mean velocities of 20 m yr^{-1} and 21 m yr^{-1}, respectively. A near-zero displacement is evident over the ice free stable ground. The velocity vectors show a directional flow with surface velocities up to 25-28 m yr^{-1} at the central part of the glacier. It is in line with Nela et al. (2018) where the velocity of the glacier was estimated to be 26.59 m yr^{-1} for the year 2015. Figure 5.2a and 5.2b show the velocity-vector field calculated based on the correlation of remotely sensed images. The satellite-derived velocity measurements were validated using the available ground velocities given by Azam et al. (2012) (Figure 5.2c). The accuracy of the satellite-derived velocity was evaluated by direct comparison with the field-based velocity measurements obtained for the year 2000-01 and 2016-17 resulting in an RMSE of 2.2 m $yr^{-1}$and 2.5 m yr^{-1}, respectively. In addition, glacier velocity (2000-01) versus glacier velocity (2016-17) shows a high correlation with a linear correlation coefficient of 0.91 (Figure 5.2d). Thus, it can be assumed that the glacier-surface velocity does not change much over the given period of time and therefore the output velocities are assumed to be suitable for thickness reconstruction, despite their temporal separation. Ice thickness calculation was performed for two different shape factors (*f*) (0.6 and 0.8) to better constrain the value of *f*. The modeled ice thickness was validated using GPR bed profiles (Azam et al., 2012) along five cross-sections. The RMSE is calculated by taking the difference in the ice thickness at 10 uniformly distributed points along each cross-section. The value *f* =0.8 yielded ice thickness, highly comparable to the ground measurements with an RMSE of 12% to 23% and therefore seems reasonable to assume the applicability of the present approach and the given model parameters to other Himalayan glaciers. Moreover, the modeled glacier-bed profiles show a mean difference of ~15% when compared to the ones obtained using Huss and Farinotti (2012). Figure 5.3 shows the modeled ice thickness distribution plot and a comparison of the glacier bed profiles along the cross-sections.

A validation assessment is performed on the Satopanth glacier system which is located in the adjacent basin (Alaknanda) of the present study area in Central Himalaya. The glacier-ice thickness distribution is calculated using the same set of model inputs as that in the calibration setup. Since *f* was calibrated on the Chotta Shigri glacier to a value of 0.8, validation of the model is performed by directly comparing the modeled ice thickness (*f=0.8*) of Satopanth glacier to the GPR measurements available along two transects, one near the terminus and the other at 10 km upstream of the snout (Mishra et al., 2018). Figure 5.4 shows the glacier-surface velocity field, modeled ice thickness distribution and the modeled glacier-bed profiles (*f* =0.6 and *f* =0.8). The modeled glacier-bed profile is plotted against the GPR measurements along a transverse transect
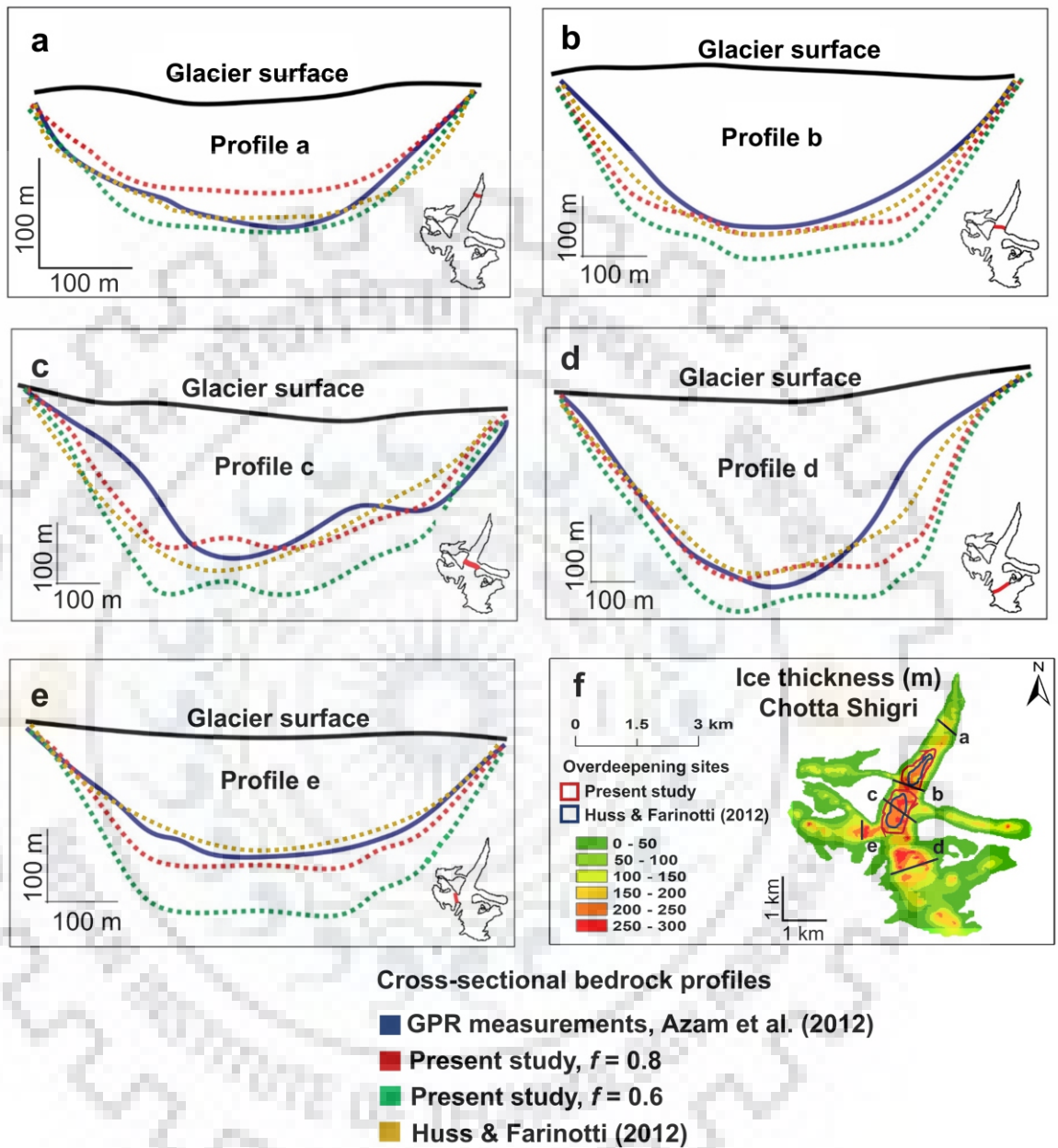
Figure 5.3 (a-e) Comparision of the model-derived glacier bed profiles of Chhota Shigri glacier (*f* =0.6 and *f* =0.8) with the GPR measurements and Huss and Farinotti (2012) and Azam et al. (2012); (f) Ice thickness distribution of Chhota Shigri glacier (Western Himalaya) showing the transects of the bed profiles; the outlines of the overdeepening sites have been marked by red (Present Study) and yellow (Huss and Farinotti, 2012)

near the terminus (Figure 5.4c) and also compared at a point location along a GPR transect in the upper part of the glacier (Figure 5.4d). The RMSE when f =0.8 is calculated to be 8.03 m. The results obtained using Huss and Farinotti (2012) is compared to the modeled ice thickness (f =0.8) along each transect (Figure 5.4c and d), resulting in an RMSE of 12.1 m.

5.6 IDENTIFICATION OF THE OVERDEEPENING SITES

The spatial distribution of glacier-ice thickness obtained using raster-based modeling technique can be used to extract information pertaining to glacier bed topography (Linsbauer et al., 2009). The overdeepening sites in the glacier bed are potential lake formation sites, as these depressions may hold water after the withdrawal of the overlying ice in the future (Linsbauer et al., 2012; Frey et al., 2014; Maanya et al., 2016). The bed topography of an individual glacier is determined by subtracting the ice thickness from the surface topography of the respective glaciers using GIS-based tools. The sinks in the glacier bed thus formed, are filled with the aid of arc-hydro tools for discrete identification of the overdeepening sites.

5.7 GROWTH ASSESSMENT OF THE LARGEST PROGLACIAL LAKE

The overall growth of the largest proglacial lake in the Dhauliganga basin is determined by calculating the difference in the spatial extent of the lake in 1968 and 2016, derived using Corona and Landsat imagery, respectively. Figure 5.5 shows the location of the largest glacial lake in the basin and its associated glacier. For retreat analysis of the glacier, a challenging task is to orthorectify Corona-KH4 imagery with the aid of ground control points (GCP) (Dashora et al., 2016). A Corona strip acquired on 27th September 1968 covering the study area with minimum snow and cloud cover has been employed to map glacier extent in the past. A two-dimensional curve fitting orthorectification technique has been adopted by selecting GCPs on high-resolution orthorectified base imagery. The spline curve fitting method, when applied to a larger spatial extent, may result in residual geometric distortions. Thus, rubber sheeting method for orthorectification is applied to the extracted subset of the Corona image for the given glacier (Bhambri et al., 2011). A total of 70 to 100 GCPs have been acquired for the Corona subset from Landsat pan-image and high-resolution geo-referenced CNES/Airbus imagery tiles of google-earth. The GCPs were evenly distributed following a gridded pattern to ensure accurate and even co-registration. However, additional GCPs have been collected in and around the glacier boundary to improve local accuracy. A root mean square error (RMSE) for geometric correction in the range of 11-18 m has been achieved. A manual approach to delineate historic glacier boundaries for the year 1968 is employed using the rectified Corona images. Figure 5.6 shows a loss in glacier area and lake growth of the highest lake in the Dhauliganga basin over a period of 48 years from 1968 and 2016. From the analysis, it is clearly evident that the proglacial lake
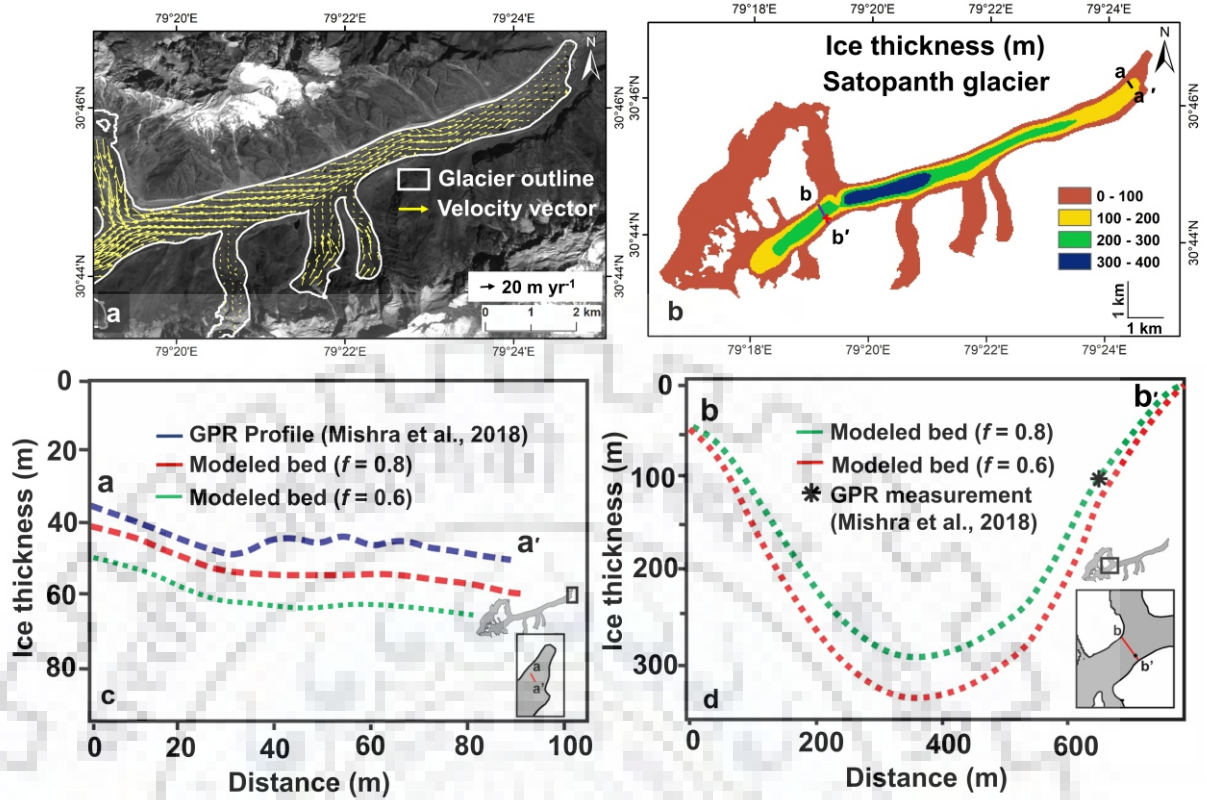
Figure 5.4 (a) Satellite-derived velocity vectors of Satopanth glacier (Western Himalaya); (b) Distributed ice thickness of the Satopanth glacier; (c and d) Comparison of the model-derived glacier bed profiles (*f* =0.6 and *f* =0.8) with the GPR measurements by Mishra et al. (2018) and Huss and Farinotti (2012)
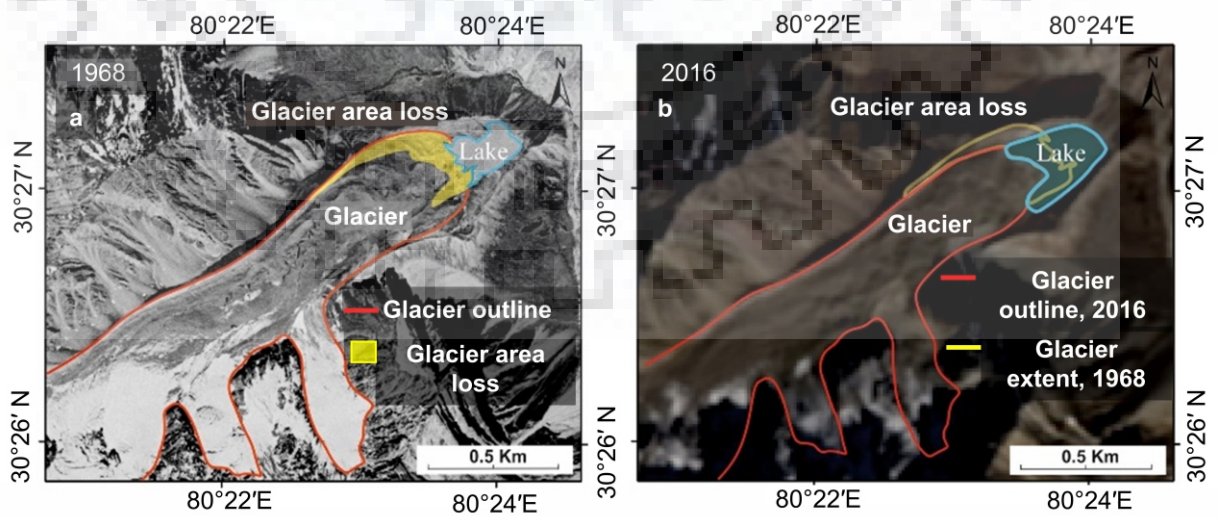
Figure 5.6 Change in the lake extent from 1968 to 2016 due to glacier area loss is shown over base imagery of (a) Corona- KH4 and (b) pan-corrected L8 composite image
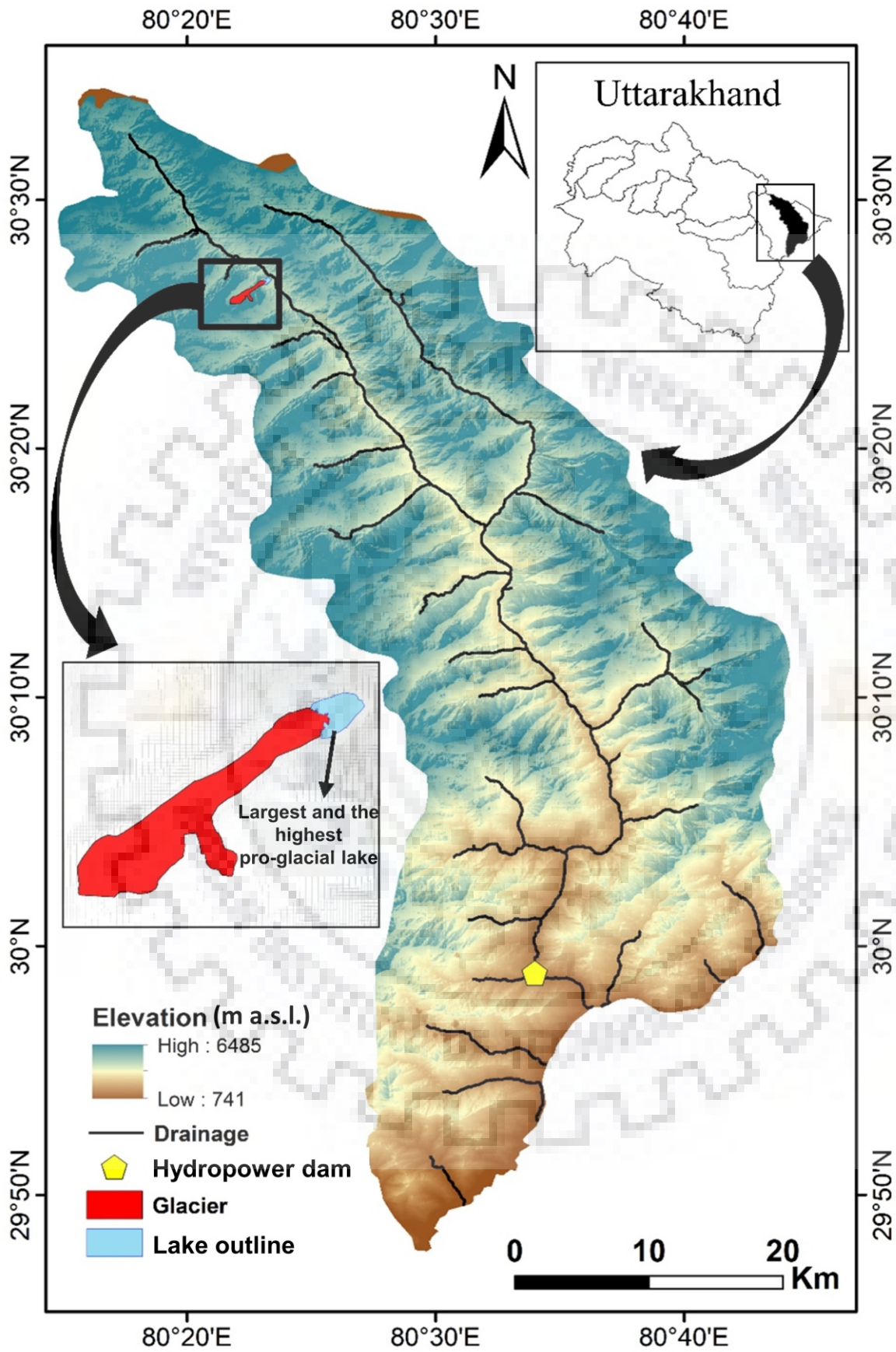
Figure 5.5 The Dhauliganga basin showing the location of the largest proglacial lake
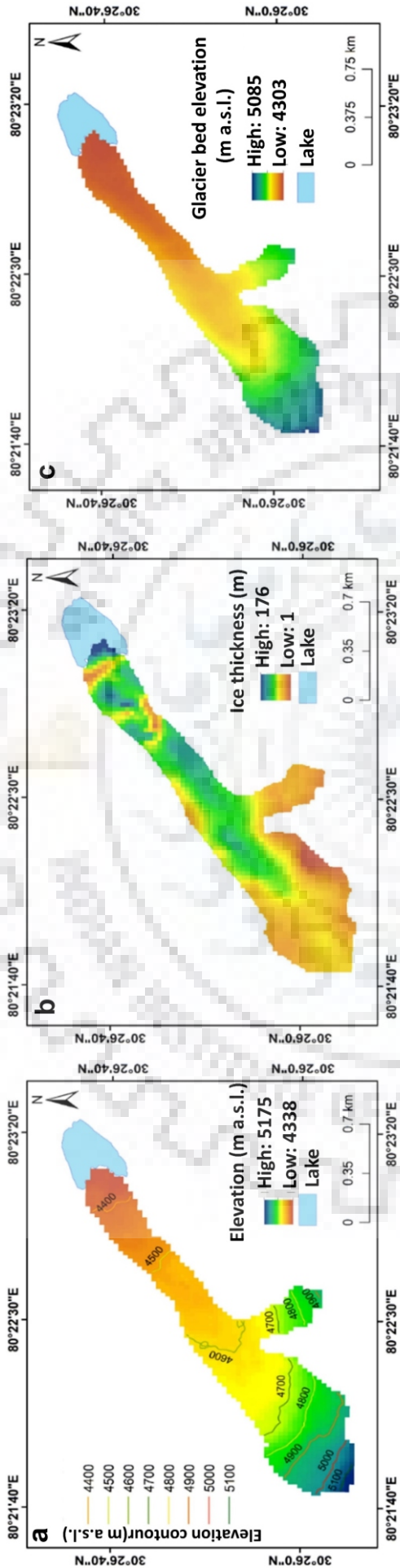
Figure 5.7 (a) DEM derived surface elevation of the glacier; (b) Modeled spatial ice-thickness distribution of the glacier; (c) Glacier bed elevation (ice thickness subtracted from glacier surface elevation)
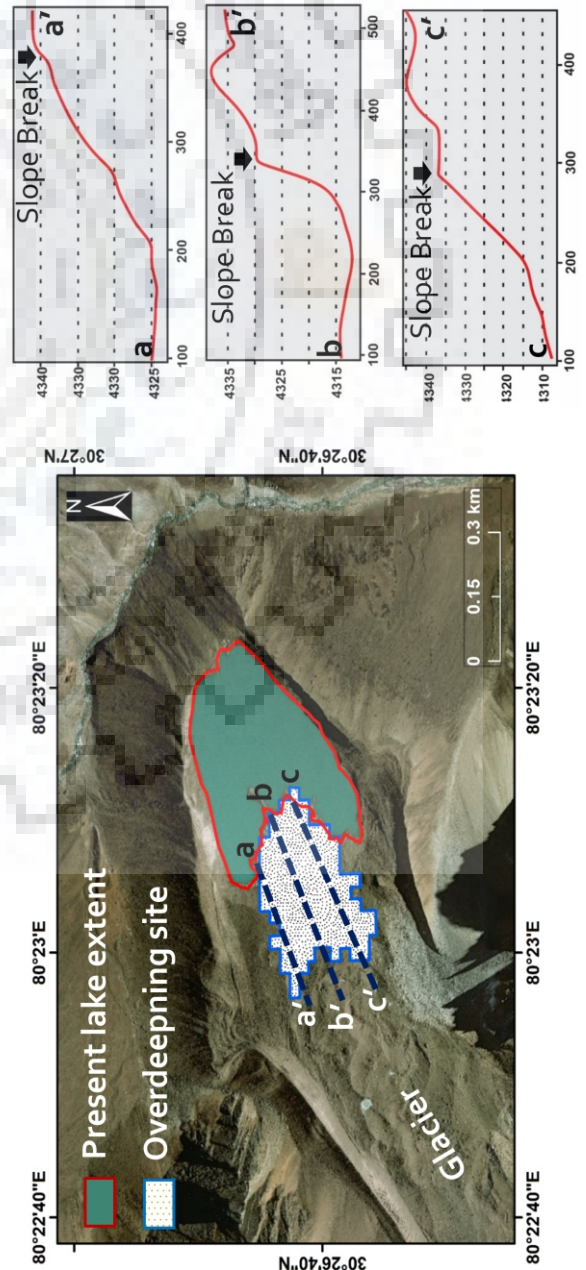
Figure 5.8 The present lake extent of the lake (red outline); overdeepening site adjacent to the lake (blue outline) is mapped using the spatially distributed glacier bed (Figure 5.7c); the subsets shows the glacier bed profiles along aa, bb, cc the slope-break marks the maximum extent of the lake in the future

located in the Dhauliganga basin has shown growth in its spatial extent. The area of the lake increased by 66258 m^2 from 46292 m^2 in 1968 to 132300 m^2 in 2016.

5.8 MAPPING THE MAXIMUM EXTENT OF PROGLACIAL LAKES

5.8.1. Largest proglacial lake in the Dhauliganga basin

In the previous section, it is clear that the largest proglacial lake in the Dhauliganga basin shows growth in its spatial extent from 1968 to 2016, associated with the retreat of the associated glacier. Jha et al., 2016 reported this lake as potentially hazardous in the Dhauliganga basin. The growth of proglacial lakes may also have an effect on the movement of the glacier (Haritashya et al., 2015). In this section, the glacier bed is investigated to map the overdeepening site adjacent to the existing proglacial lake. The maximum future extent of the proglacial lake is then calculated. GIS-based operations (Section 5.6) are performed using the glacier surface elevation (DEM) (Figure 5.7a) and glacier-velocity based spatially distributed modeled ice thickness (Section 5.4.3.b) (Figure 5.7b) to derive the glacier bed (Figure 5.7c). The sinks in the glacier bed thus formed, are filled with the aid of arc-hydro tools for discrete identification of the overdeepening sites. Figure 5.8 shows the overdeepening site adjacent to the largest proglacial lake in the Dhauliganga basin. A slope break is evident in the bed profiles along different sections as shown in the Figure. The total area of the overdeepening site is calculated to be 0.29 km^2. The maximum future extent of the lake is calculated by adding the present area of the lake and the area of the overdeepening site. The maximum extent of the lake is calculated to be 159686 m^2. The future volume of the lake is calculated using an area-based scaling method (Huggel et al., 2004), given by:

$$V=0.104 \times A^{1.42} \qquad \text{eq. 3}$$

The total future volume of the largest proglacial lake in the Dhauliganga basin is calculated to be 2.54×10^6 m^3. This calculated maximum volume is further considered for future GLOF modeling (Section 5.9).

5.8.2 South Lhonak lake, Sikkim

The south Lhonak lake is identified as one of the potentially hazardous lakes located in the Sikkim Himalaya (Worni et al., 2012). The detailed hazard assessment of the lake considering the present volume of the lake has been presented in Chapter 4. Here the future GLOF potential of the lake is evaluated by taking into consideration its future lake extent. Remya et al., 2019 adopted a surface velocity-based model to map the maximum extent of the South Lhonak lake (Figure 5.9). The future volume of which has been calculated to be 90×10^6 m^3. A future hazard analysis of the South Lhonak lake is performed considering the future volume of the lake.
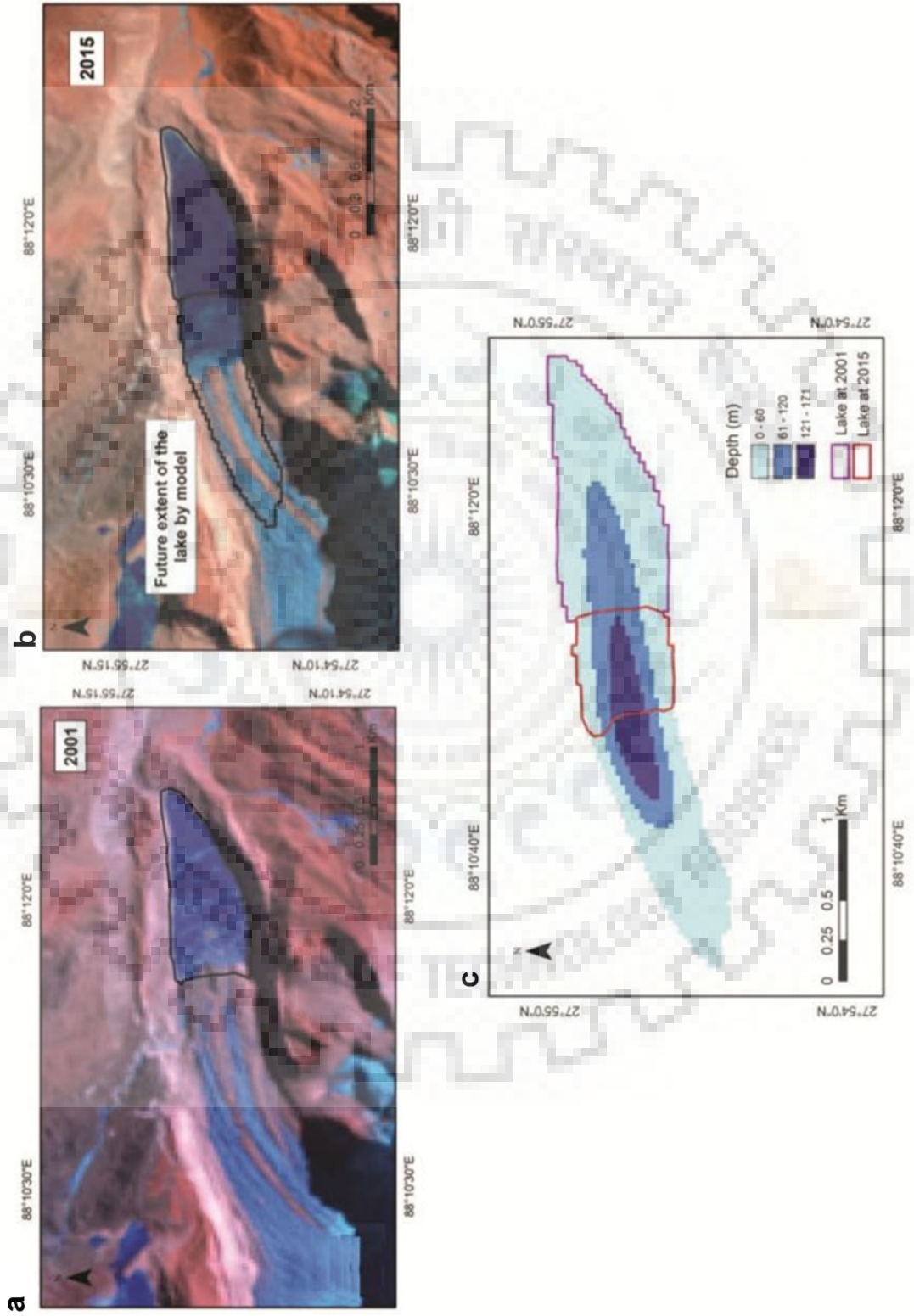
Figure 5.9 The extent of the South Lhonak lake, Sikkim for the year (a) 2001 (b) 2016; (c) modeled bathymetry of the future extent of the lake for which the volume is calculated (Remya et al., 2019); the total future volume of the South Lhonak lake was calculated to be $90 \times 10^6 \, \text{m}^3$

5.9 HYDRODYNAMIC MODELING TO EVALUATE FUTURE GLOF POTENTIAL

One dimensional hydrodynamic modeling is performed to assess the future GLOF potential of the two lakes (Dhauliganga lake and South Lhonak lake). The methodology adopted for hydraulic modeling is the same as that in chapter 3 (Satopant Lake) and 4 (South Lhonak lake). However, the breach parameters differ based on the calculated future volume of the lakes.

5.9.1 Dhauliganga Lake

One-dimensional hydrodynamic modeling is performed to evaluate the future GLOF potential of the largest proglacial lake in the Dhauliganga basin. Its impact on a hydropower dam (29°58′46″N, 80°34′05″E) located downstream is assessed by evaluating the flood hydrographs generated in the dam site. A potential future GLOF event is simulated by assuming that the entire future volume (as calculated in section 5.8.1) of the lake is drained in a dam breach event. One-dimensional moraine-breach modeling is carried out to calculate the initial breach hydrograph for different breach scenarios. Further, hydraulic routing of the breach hydrographs is carried out until it reached the hydropower dam site. A series of moraine-breach events were modeled with varied breach-formation time, in which a total breach width of 50 m is considered. A potential future GLOF event is evaluated considering three dam break scenario of different failure time ($T_{f=}$ 0.33 hr, 0.50 hr, and 0.75 hr). The breach hydrograph produced in all the three scenarios is routed along the main channel to evaluate its impact on the hydropower station located 72 km downstream (29°58′46″N, 80°34′05″E). Figure 5.10 shows the Dhauliganga basin, marked are the locations of the largest proglacial lake in the basin, the hydropower dam, and the main flow channel. The peak discharge (in m^3s^{-1}) and time of peak (in min) is computed for different flood scenario ($T_{f=}$ 0.33 hr, 0.50 hr, and 0.75 hr) along the channel and at the dam site. The hydraulic properties of the potential future GLOF wave are compared to the present (Jha et al., 2016). An average value of Manning's N along the main flow channel is considered for hydraulic flood routing. The LULC (GlobeCover v2.3) is extracted for a buffer of 500 m along the main flow channel, from the lake to the dam site. A total of 13 LULC classes exists along the buffer zone of the flow channel. The average value of the Manning's N is calculated to be 0.59, which is considered for hydraulic routing of the GLOF hydrographs along the main flow channel. Figure 5.11 shows the LULC distribution of LULC along the flow channel, the list of which along with the LULC code is given in table 5.3.
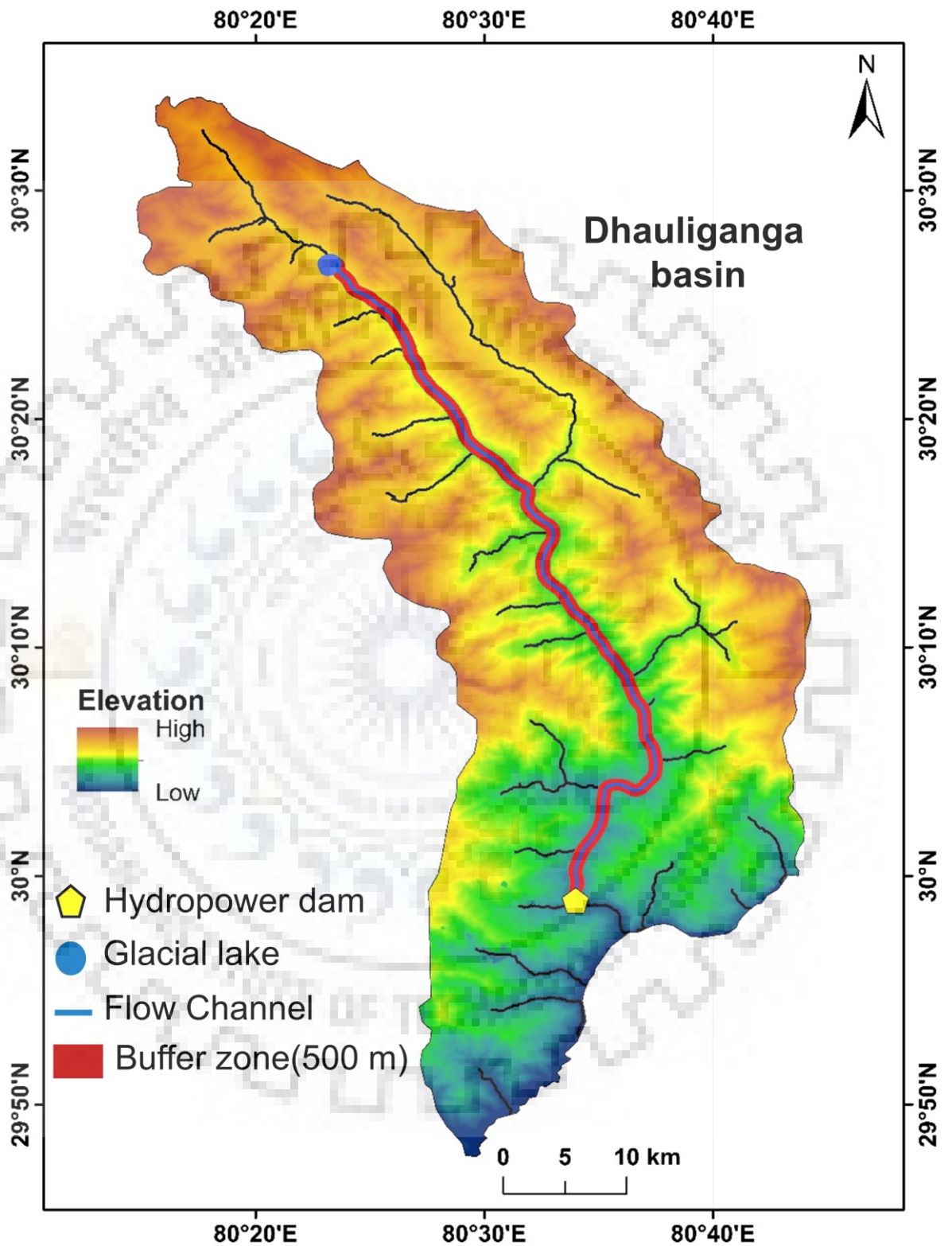
Figure 5.10 The Dhauliganga basin showing the location of the highest and the largest proglacial lake, its main flow channel and the location of the hydropower dam

Table 5.3 LULC classes along the flow area and its respective Manning's N.

LULC CODE	Description	Manning's N
11	Post-flooding or irrigated croplands (or aquatic)	0.034
14	Rainfed croplands	0.06
20	Mosaic cropland (50-70%) / vegetation (grassland/shrubland/forest) (20-50%)	0.034
30	Mosaic vegetation (grassland/shrubland/forest) (50-70%) / cropland (20-50%)	0.034
40	Closed to open (.5%) broadleaved evergreen and semideciduous forests (>5m)	0.1
50	Closed (>40%) broadleaved deciduous forest (>5m)	0.1
70	Closed (>40%) needle-leaved evergreen forest (>5m)	0.11
100	Closed to open (>15%) mixed broadleaved and needle-leaved forest (>5m)	0.11
110	Mosaic forest or shrubland (50-70%) / grassland (20-50%)	0.035
120	Mosaic grassland (50-70%) / forest or shrubland (20-50%)	0.035
130	Closed to open (>15%) (broadleaved or needle-leaved, evergreen or deciduous) shrubland (<5m)	0.07
140	Closed to open (>15%) herbaceous vegetation (grassland, savannas or lichens/mosses)	0.05
200	Bare areas	0.035
220	Permanent snow and ice	0.04

5.9.2 South Lhonak Lake

In this section a 3D bathymetric model is constructed of the south Lhonak lake, using the modeled future-lake bathymetry given by Remya et al. (2019) (Figure 5.9c). Figure 5.12 shows the 3D bathymetric model future South Lhonak lake. The total length of the lake increases from 2.41 km (present) to 3.9 km (modeled future). Here, a series of hydrodynamic simulations are performed to evaluate different moraine-breach scenarios. The moraine dimensions are based on field observations reported by Sharma et al. (2018) (Chapter 4). The breach width is calculated based on Froehlich, (1995) (Equation 4).

$$B_w = 0.1803K_o (V_w)^{0.32} (h_b)^{0.19} \qquad \text{eq. 4}$$

In the above equation, B_w is the breach width, V_w is the total volume of the lake, and h_b is the height of the breach. Since the future volume of the lake i.e 90×10^6 m^3 (Section 5.8.2) is considered, the breach width is calculated to be 141.7 m (eq 4). Three different moraine-breach scenarios based on varied breach formation time (T_f= 0.33 hr, 0.75 hr, and 1.0 hr) is modeled. One-dimensional hydraulic routing of the breach hydrograph along the flow channel is performed to evaluate its impact on the hydropower dam (Chungthang town) located at a distance of 62.3 km downstream of the lake. A Manning's N of 0.059 is considered for routing (Chapter 4). The results are compared with the present potential of the South Lhonak lake (Sattar et al., 2019).
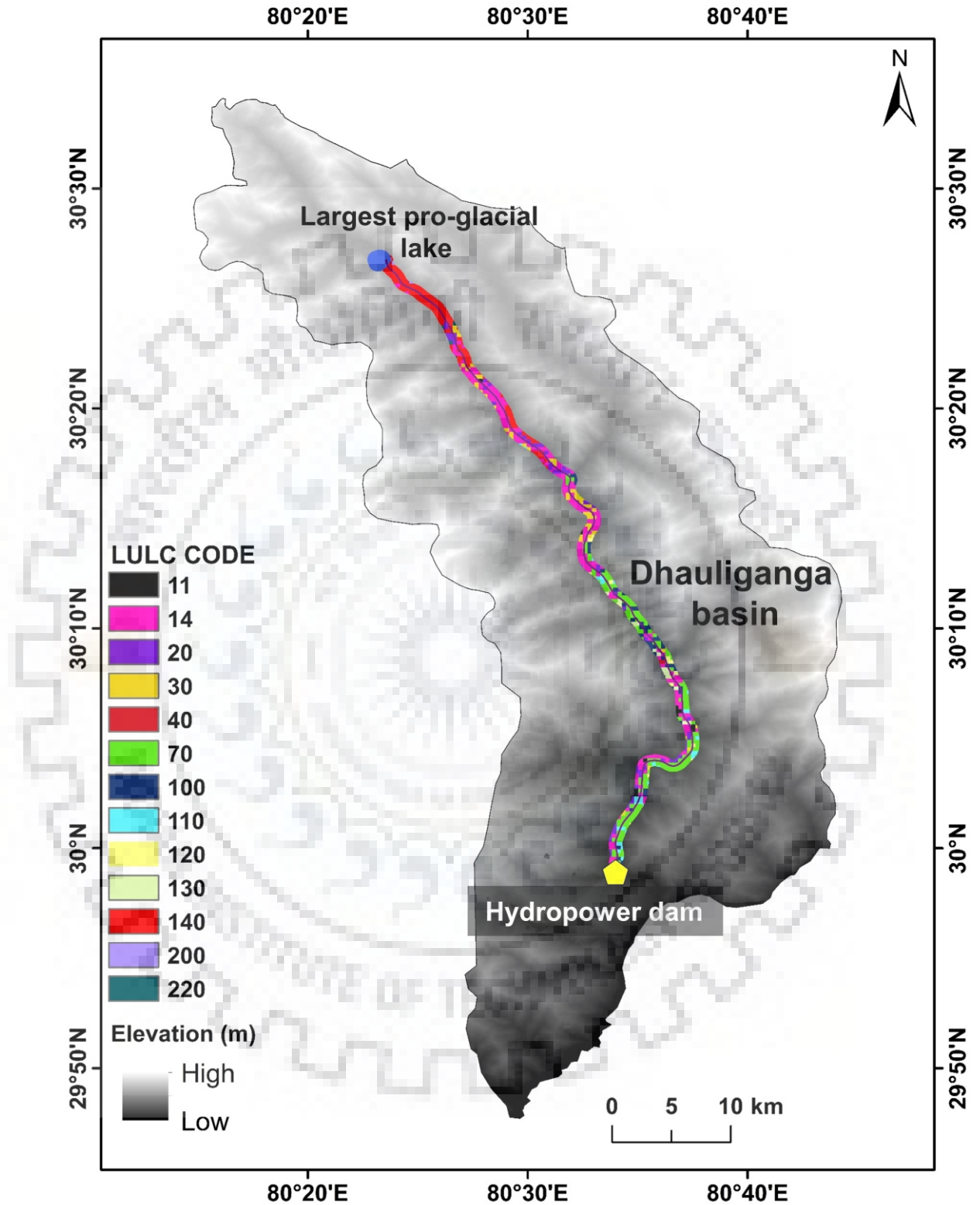
Figure 5.11 LULC along a buffer zone of 500 m along the main flow channel from the highest lake of the basin to the hydropower dam, derived using LULC GlobCover (Version 2.3); the description of the LULC codes is given in table 5.3

5.10 RESULTS

In the present study, glacier ice thickness was calculated for 15 larger (>1 km^2) glaciers to map the overdeepening sites in the Dhauliganga Basin, Central Himalaya. The study applies a glacier-surface velocity-based method to model the ice thickness distribution for the given glaciers. The method was first applied to Chotta Shigri and the Satopanth glacier for model calibration and validation, respectively.

Since field measurements of glacier-surface velocity are very sparse and involve rigorous fieldwork, a remote sensing based method to estimate glacier velocity was employed in the study. The satellite-based velocity measurements yielded a mean velocity of 27 m yr^{-1} for all the glaciers selected for the study. The maximum velocity of the glaciers occurs in the range of 50 to 70 m yr^{-1}. The glaciers exhibit highly directional flow with higher velocities in the upper part of the ablation zone, gradually decreasing towards the terminus of the glaciers.

The sparingly available ground ice thickness measurements for validation is a major limitation of the approach when applied over the Himalaya. A calibration and validation assessment on the Chotta Shigri and Satopanth glacier system (Section 5.5), has shown good agreement between GPR measurements and modeled ice thickness. The empirically derived ice thickness distribution of the calibration and the validation glaciers are compared to estimates calculated using Huss and Farinotti (2012) (Figure 6B).

The calibration of the model constrained the value of the valley shape factor (f) to 0.8. For Satopanth glacier, an overestimation of the total modeled glacier volume by 14.7% using the present approach was evident when f =0.6. A total uncertainty in the modeled ice thickness is estimated to be 18.4% (Section 5.4.3.c). The details of the glacier area, ice thickness, and volume are enlisted in Table 5.3.

The glacier-bed derived using ice-thickness is evaluated for discrete identification of topographic depressions on the glacier bed. The presence of these depressions at the frontal part of the glacier may lead to formations of proglacial lakes in the near future, as compared to those sites identified in the higher elevation ranges of the glaciers. A total of 54 overdeepening sites with a total area of 2.93 km^2 were identified, as enumerated in Table 5.3. The highest number of overdeepening sites are identified in the bed of Nipagal glacier (Glacier no. 10) covering an area of 0.84 km^2. The total overdeepening sites identified in the basin has a volume capacity to hold 15.1 $\times$ 10^7 m^3 of water.
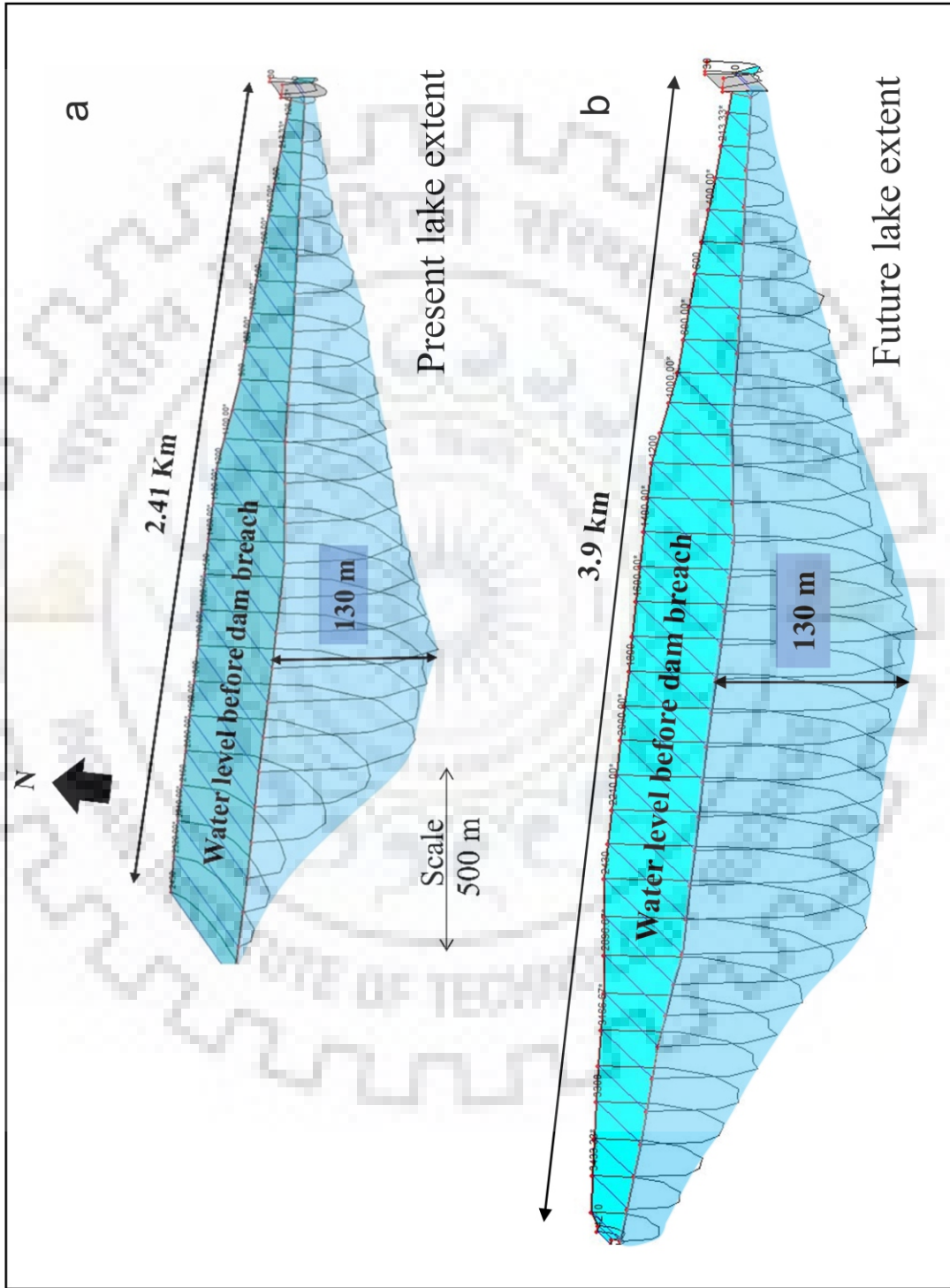
Figure 5.12 3D model of the (a) present lake extent (Sattar et al., 2019); (b) future lake extent of the South Lhonak lake, Sikkim

Table 5.4 Glacier volume derived from the calibrated volume-area scaling relation- Mean ice thickness (H_{mean}), total glacier area (S_{tot}), number of overdeepening sites (N_{ovr}), elevation range of glacier (ΔE), elevation range of overdeepening sites (ΔE_{ovr}), **and** total area of the overdeepenings (S_{ovr})

Glacier ID	Glacier name	H_{mean} (m)	S_{tot} (km²)	N_{ovr}	ΔE (m)	ΔE_{ovr} (m)	S_{ovr} (km²)
8	IN 5O103 04 015 (GSI ID)	63	11.54	5	2191	1349	0.22
9	Meola	36	9.22	2	2113	308	0.05
4	Damolija	59	8	5	838	536	0.13
1	IN 5O103 04 034 (GSI ID)	68	7.67	6	1665	327	0.38
2	Mabang	92	5.59	0	1792	-	0
12	IN 5O103 04 002 (GSI ID)	40	5.01	1	1060	270	0.02
11	Chipagal	62	4.13	7	1312	753	0.34
15	Rama Bhitar	57	3.51	2	1191	921	0.15
7	Nipchikang	63	3.39	3	1996	517	0.37
6	Jhulang	68	2.39	2	1926	576	0.16
10	Nipagal	29	2.11	13	2130	621	0.84
14	IN 5O103 04 075 (GSI ID)	32	1.61	4	1132	536	0.05
5	Ghugtan	65	1.34	3	754	291	0.12
13	IN 5O103 04 057 (GSI ID)	38	1.32	0	667	-	0
3	IN 5O103 04 030 (GSI ID)	17	1.16	1	1060	270	0.02

The largest proglacial lake is located at the snout of glacier 3 (Figure 5.5). Here, the maximum extent of the lake is calculated by mapping the overdeepening site adjacent to the lake (Section 5.8.1). The future area of the lake is calculated by adding the present area of the lake and the area of the adjacent overdeepening site. The total future extent of the lake is calculated to be 159686 m² (Section 5.8.1). The future volume of the lake is calculated using an area-based scaling method (Huggel et al., 2004). The total future volume of the largest glacial lake in the Dhauliganga basin is calculated to be 2.54×10^6 m³. This calculated maximum volume is further considered for future GLOF modeling (Section 5.9.1). A series of hydrodynamic simulations were performed to evaluate the future GLOF potential of the Dhauliganga lake. Three different GLOF scenarios with breach width of 50 m and varied failure time ($T_f = 0.33$ hr, 0.50 hr, and 75 hr) is considered for GLOF modeling. A peak flood of 5015 m³s^{-1} is obtained when $T_f = 0.33$ hr. There is a decrease

Figure 5.13 Future GLOF hydrograph of the Dhauliganga lake for different moraine-failure time (T_f); breach-width (B_w) is considered as 50 m

Figure 5.14 Routed hydrograph up to 25 km downstream of the lake for different moraine-failure time (T_f)
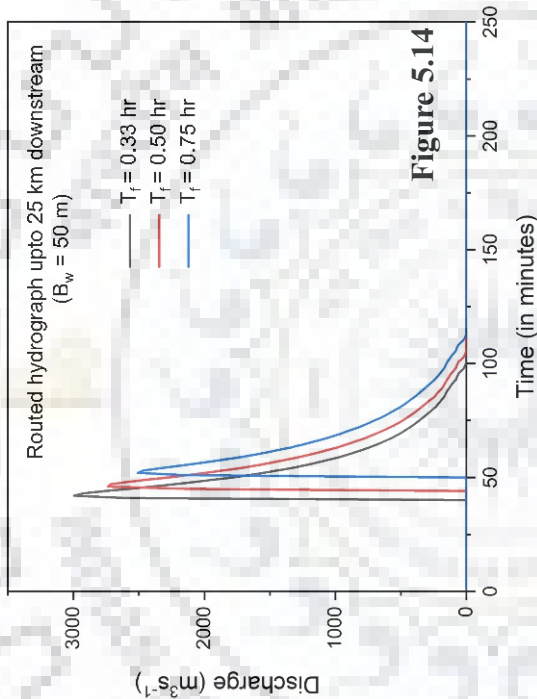
Figure 5.15 Routed hydrograph up to 50 km downstream of the lake for different moraine-failure time (T_f)
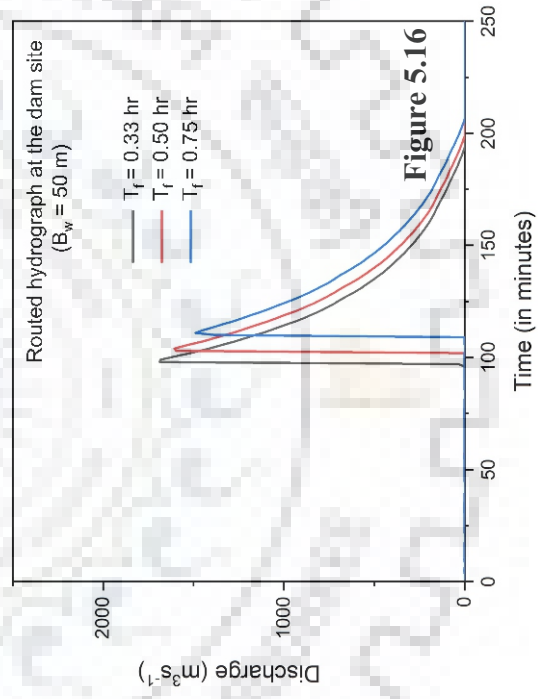
Figure 5.16 Routed hydrograph at the dam site (72 km downstream of the lake) for different moraine-failure time (T_f)
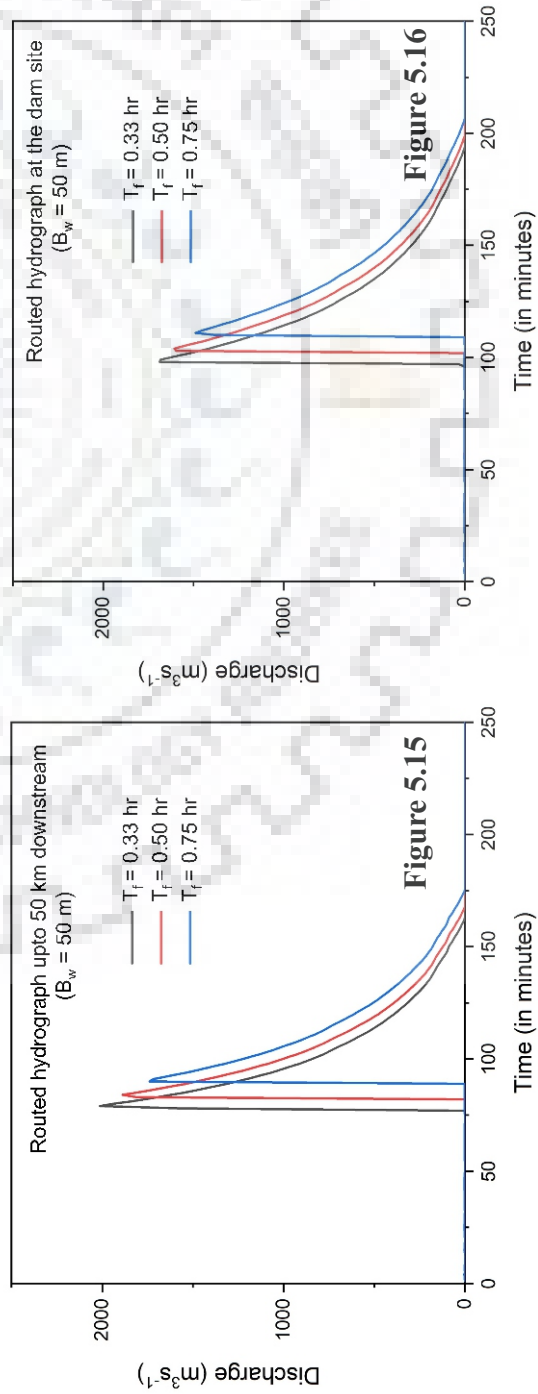
in the peak flood as the time of failure is increased. The future GLOF produces a peak of 4477 m^3s^{-1} and 3891 m^3s^{-1} for T_f= 0.50 hr and 0.75 hr respectively (Figure 5.13).

The breach hydrographs obtained for different moraine failure time is routed along the main flow channel for a distance of 72 km until it reached the dam site. The routed hydrographs at three different sites along the flow channel were evaluated i.e. at 25 km downstream of the lake, 50km downstream of the lake, and at the dam site. Figure 5.14-16 shows the routed hydrographs at different locations along the flow channel. At the dam site, a maximum discharge of 1686 m^3s^{-1} is calculated where the peak discharge is reached within 98 min (1.6 hr) after the initiation of the moraine-breach event. Peak discharge of 1595 m^3s^{-1} (T_f = 0.50 hr) and 1489 m^3s^{-1} (T_f = 0.75 hr) is recorded at the dam site with a time of peak of 103 min (1.7 hr) and 111 min (1.8 hr) respectively. The hydraulic properties of the potential future GLOF hydrograph are compared to the present GLOF (Jha et al., 2016). Table 5.5 and 5.6 show the comparison of the peak discharge (m^3s^{-1}) and time of peak (in min) for the future and the present GLOF hydrograph. The peak discharge of a potential future GLOF increases by 1267 m^3s^{-1} (T_f = 0.33 hr), 1786 m^3s^{-1} (T_f = 0.50 hr), 1997 m^3s^{-1} (T_f = 0.75 hr) and the time of peak discharge is achieved 4 minutes, 5 minutes and 7 minutes earlier respectively, when compared to the potential present GLOF. Figure 5.17 shows the comparison of a potential present and future GLOF of the Dhauliganga lake in terms of its peak discharge (m^3s^{-1}) and time of peak (in min).

Table 5.5 Peak discharge (in m^3s^{-1}) for a potential future and present GLOF of the highest glacial lake in the Dhauliganga lake

	Moraine-failure time (in hr)	**0.33**	**0.5**	**0.75**
Peak discharge of the breach hydrograph (m^3s^{-1})	Potential future GLOF (Present study)	5015	4477	3891
	GLOF potential at present (Jha et al., 2016)	3748	2691	1894

Table 5.6 Time of peak discharge (in min) for a potential future and present GLOF of the highest glacial lake in the Dhauliganga lake.

	Moraine-failure time (in hr)	**0.33**	**0.5**	**0.75**
Time of peak discharge of the breach hydrograph (in min)	Potential future GLOF (Present study)	10	14	20
	GLOF potential at present (Jha et al., 2016)	14	19	27

The study was further extended to the state of Sikkim, where the future GLOF potential of the South Lhonak lake is evaluated. The lake has been reported as potentially hazardous in the state of Sikkim (Worni et al., 2012; Sharma et al., 2018; Sattar et al., 2019). The details present hazard
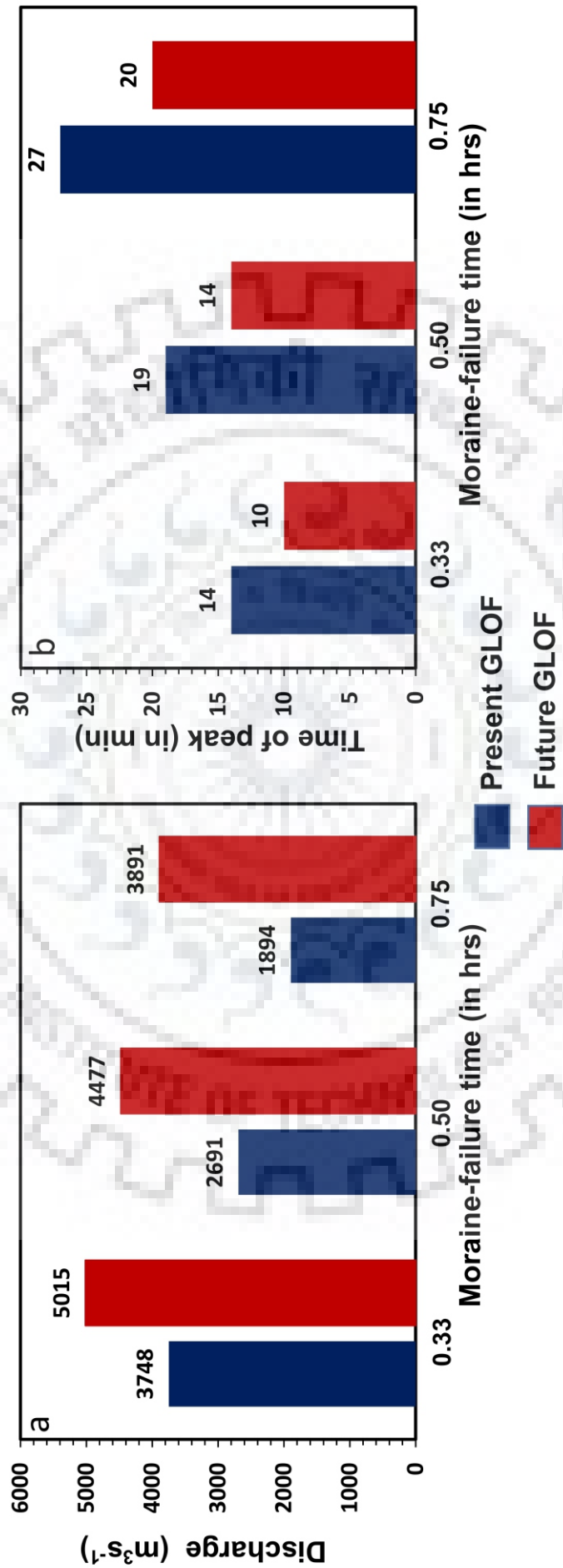
Figure 5.17 Comparison of a present GLOF hazard (Jha et al., 2016) and future GLOF hazard (present study) of the Dhauliganga lake in terms of (a) discharge, (b) time of peak discharge

potential of the South Lhonak lake is presented in Chapter 4. Here, the future GLOF potential is evaluated taking into consideration the future volume of the lake (Section 5.9.2). The future volume of the lake is calculated to be 90×10^6 m^3, based on the investigation of the overdeepening on the glacier bed adjacent to the lake (Remya et al., 2019). The ice thickness based modeled bathymetric data was used to construct a future 3D model of the lake (Section 5.9.2). A series of moraine-breach hydraulic simulations were performed to analyze the future GLOF potential of the South Lhonak lake. A breach width of 141 m was considered calculated based on the future lake volume using Froehlich equation (Section 5.9.2). Three different potential dam breach scenarios based on varied time of moraine failure (T_f =1 hr, 2hr, and 3hr) is evaluated. Figure 5.18 shows the future GLOF hydrographs for different failure time. The GLOF hydrograph $T_f = 1.0$ hr produced the maximum peak discharge of 8021 m^{3}s^{-1}. The peak discharge decreases to 7076 m^{3}s^{-1} and 6462 m^{3}s^{-1} for $T_f = 2.0$ hr and $T_f = 3.0$ hr respectively. The GLOF hydrograph obtained in all the three GLOF scenarios was further routed along the main flow channel for a distance of 62.3 km until it reaches the hydropower dam at Chungthang town. The routed hydrographs were evaluated at five different sites along the main flow channel i.e. at 12.5 km, 20.7 km, 35.4 km, 45.9 km downstream of the lake, and at the dam site. Figure 5.19-21 shows the routed hydrographs at different sites along the flow channel. At the hydropower dam (Chungthang town) a maximum discharge of 4801 m^{3}s^{-1} is calculated where the peak discharge is reached within 124 min (2.06 hr) after the initiation of the moraine-breach event. Peak discharge of 4677 m^{3}s^{-1} ($T_f = 2.0$ hr) and 4653 m^{3}s^{-1} ($T_f = 3.0$ hr) is recorded at the dam site with a time of peak of 142 min (2.4 hr) and 156 min (2.6 hr) respectively. The hydraulic properties of the potential future GLOF hydrograph are compared to the present GLOF (Sattar et al., 2019) (Figure 5.22). Table 5.7 and 5.8 shows the peak discharge (m^{3}s^{-1}) and time of peak (in min) for future GLOF hydrograph and the routed hydrograph at Chungthang town respectively. The results are compared to the present GLOF of the South Lhonak lake (Chapter 4). Table 5.9 shows the hydraulic properties of the present GLOF of the South Lhonak lake. Figure 5.1 shows the comparison of a potential present GLOF and future GLOF of the South Lhonak lake in terms of its peak discharge (m^{3}s^{-1}) and time of peak (in min). The peak discharge of a potential future GLOF increase by 398 m^{3}s^{-1} ($T_f = 3$ hr) and the time of peak discharge is achieved 4 minutes earlier when compared to the potential present GLOF ($T_f = 3.09$) (Chapter 4). At Chungthang town there is an increase in the future peak discharge by 825 m^{3}s^{-1} which is achieved at the town 84 min (1.4 min) earlier than a potential present GLOF.
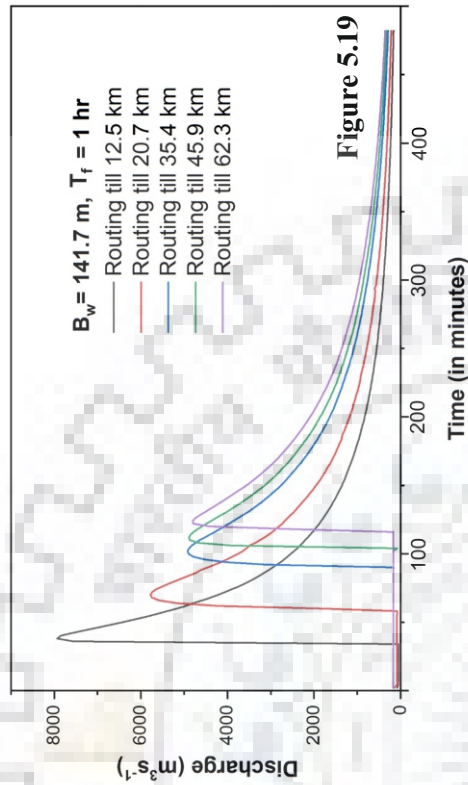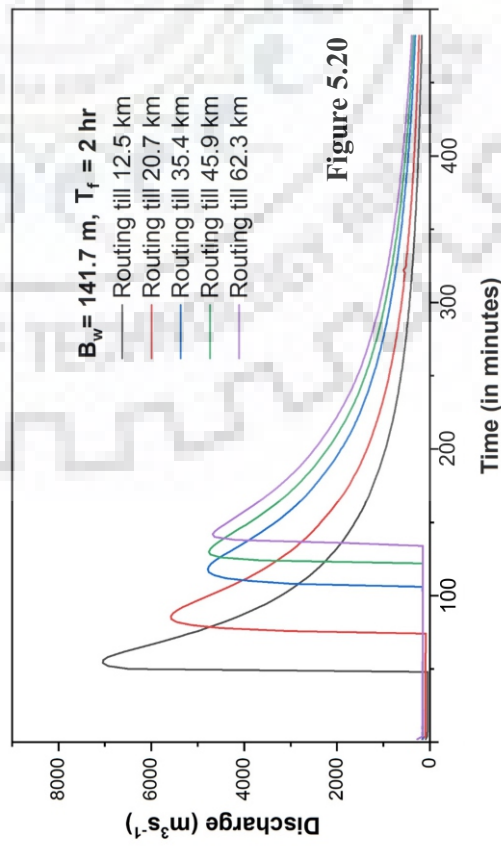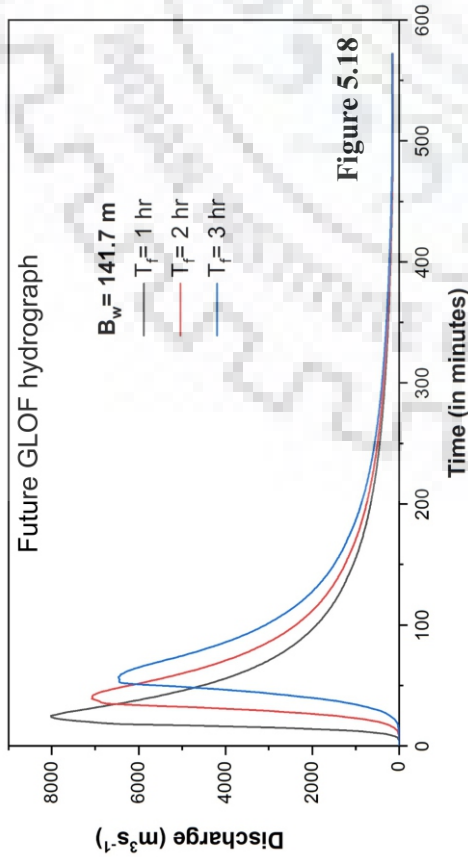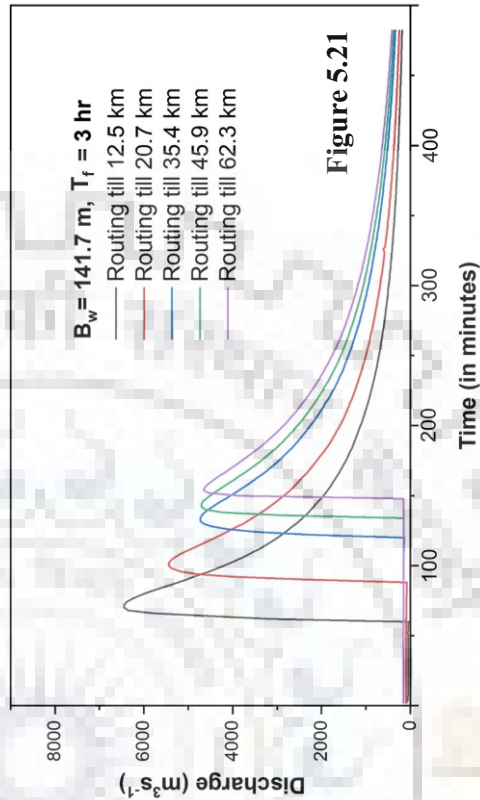
Figure 5.18 Future GLOF hydrograph of the South Lhonak lake for different moraine-failure time (T_f); breach-width (B_w) is considered as 50 m
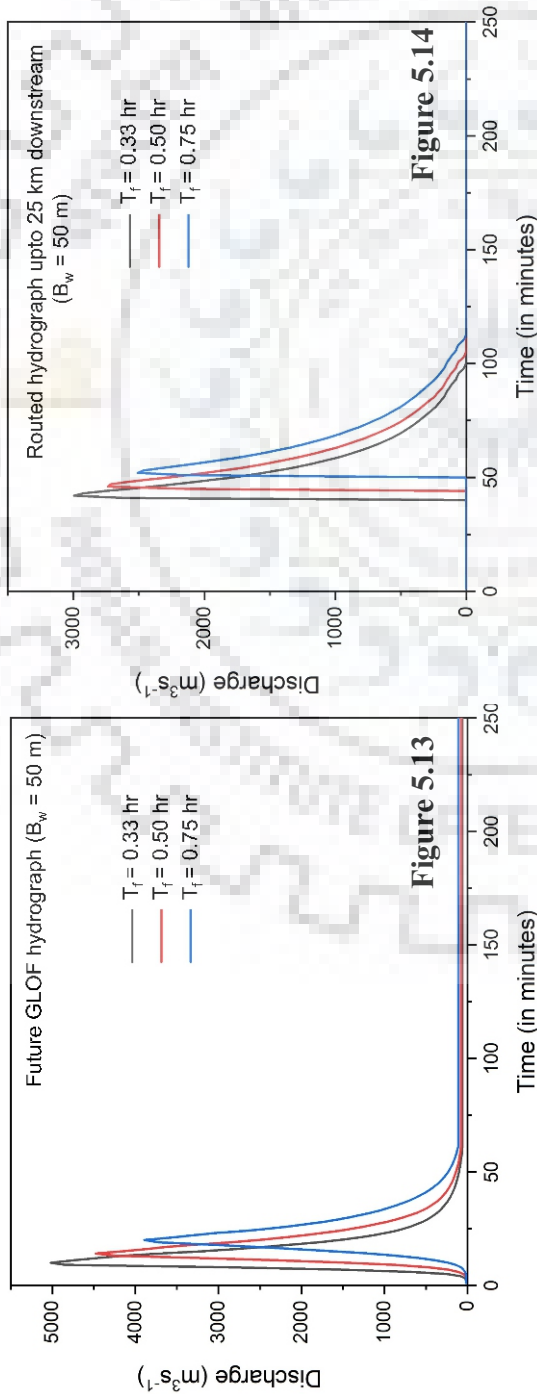
Figure 5.19 Routed hydrograph at different points downstream of the lake for the moraine-failure time of 1 hr (T_f)

Figure 5.20 Routed hydrograph at different points downstream of the lake for the moraine-failure time of 2 hr (T_f)

Figure 5.21 Routed hydrograph at different points downstream of the lake for the moraine-failure time of 3 hr (T_f)
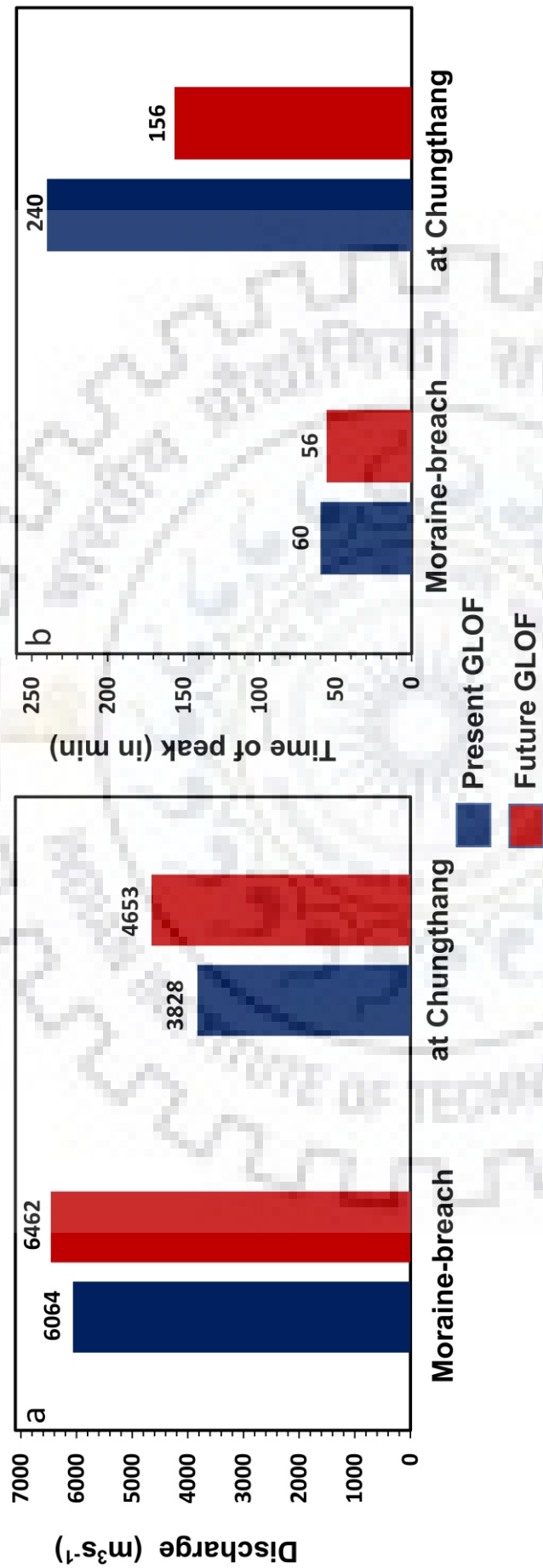
Figure 5.22 Comparison of a present GLOF hazard (Sattar et al., 2019) and future GLOF hazard (present study) of the South Lhonak lake in terms of (a) discharge, (b) time of peak discharge

Table 5.7 Peak discharge (in m^3s^{-1}) and time of peak discharge (in min) for a potential future GLOF of the South Lhonak lake, Sikkim

Moraine-failure time (in hr)	1.0	2.0	3.0
Peak discharge of the breach hydrograph (m^3s^{-1})	8021	7076	6462
Time of peak discharge of the breach hydrograph (in min)	25	40	56

Table 5.8 Peak flood (in m^3s^{-1}) and time of peak discharge (in min) at Chungthang town located 62.35 km downstream from the lake, Sikkim

Moraine-failure time (in hr)	1.0	2.0	3.0
Peak discharge of at Chungthang town (m^3s^{-1})	4801	4677	4653
Time of peak discharge of at Chungthang town (in min)	124 (2.06 hr)	142 (2.4 hr)	156 (2.6 hr)

Table 5.9 Peak discharge (in m^3s^{-1}) and time of peak for a potential GLOF at present (Sattar et al., 2019)

	Peak Flood (m^3s^{-1})	Time of peak (in Hr)
Breach hydrograph	6064.6	1.0
Chungthang Town (62.35 km)	3828.08	4.0

5.11 CONCLUSION

This chapter demonstrates the application of spatially distributed modeled ice thickness to evaluate the overdeepening sites on the glacier bed. These depressions on the glacier bed are the potential sites for future lake formation. The volume of these potential future lakes can be calculated based on the area of the ovedeepening sites. Here, the overdeepenings on the glacier bed were mapped for the 15 larger glaciers of the Dhauliganga basin. A total of 54 overdeepening sites were identified and mapped in the basin that has a volume capacity to hold $15.1 \times 10^7\,m^3$ of water. Further, the method was employed to map the maximum extent of the existing proglacial lakes by investigating the overdeepening on the glacier bed adjacent to the lakes. The future GLOF potential of two glacial lakes (Dhauliganga lake and South Lhonak lake) were evaluated considering their future volume. A series of one-dimensional hydrodynamic simulations were performed with varied breach formation time (T_f) to evaluate its impact of a potential future

GLOF event on hydropower dams located downstream. The results of the hydraulic computation (peak discharge and time of peak) were compared to a potential GLOF at present.

In the case of the Dhauliganga lake, the peak discharge of a potential future GLOF increases by 1267 m^3s^{-1} ($T_f = 0.33$ hr), 1786 m^3s^{-1} ($T_f = 0.50$ hr), 1997 m^3s^{-1} ($T_f = 0.75$ hr) and the time of peak discharge is achieved 4 minutes, 5 minutes and 7 minutes earlier respectively, when compared to the potential present GLOF. The future GLOF hydrographs were routed to evaluate its potential impact on a hydropower dam located 72 km downstream of the lake. At the dam site, a maximum discharge of 1686 m^3s^{-1} is calculated where the peak discharge is reached within 98 min (1.6 hr) after the initiation of the moraine-breach event. Peak discharge of 1595 m^3s^{-1} ($T_f = 0.50$ hr) and 1489 m^3s^{-1} ($T_f = 0.75$ hr) is recorded at the dam site with a time of peak recorded at 103 min (1.7 hr) and 111 min (1.8 hr) respectively.

For the South Lhonak lake, the peak discharge of a potential future GLOF increase by 398m^3s^{-1} ($T_f = 3$ hr) and the time of peak discharge is achieved 4 minutes earlier, when compared to the potential present GLOF ($T_f = 3.09$). The future GLOF hydrograph was routed for a distance of 62.3 km to evaluate its impact on the hydropower dam located at Chungthang town. At Chungthang town there is an increase in the future peak discharge by 825 m^3s^{-1} which arrives the town 84 min (1.4 min) earlier than a potential present GLOF. The method used in the present study proves to be an efficient method to evaluate the future GLOF potential of the existing proglacial lakes.

CHAPTER 6: SENSITIVITY ANALYSIS IN HYDRODYNAMIC MODELING OF GLOF

6.1 INTRODUCTION

Hydrodynamic evaluation of GLOFs involves a series of process-modeling which includes dam breach formation and flood routing. A challenging task is to evaluate the accuracy of the modeled outputs as physically-based hydraulic modeling is sensitive to the various inputs the model demands (Anacona et al., 2015; Worni et al., 2013; Westoby et al., 2014). The process of dam breach is complex and is dependent on many factors like height, width, and slope of the moraine (Worni et al., 2012; Pickret et al., 2011; Wang et al., 2008). The hydrograph obtained during a breaching process determines the flow hydraulics in the downstream region (Anconna et al., 2015; Westoby et al., 2014). Moreover, the channel properties also affect GLOFs and its nature, by influencing its flow over a given terrain. The Manning's roughness coefficient has a significant effect on GLOFs as it directly influences the peak discharge and flow velocity over a given channel (Carrivick, 2006; Bajracharya et al., 2007; Yochum et al., 2012; Carling et al., 2010). Anacona et al. (2015) performed a sensitivity analysis to evaluate the effect of Manning's N and breach hydrograph on GLOF. These parameters were reported to be the main controlling factors for a given GLOF event. Bajracharya et al. (2007) stated the importance of Manning's N for accurate GLOF simulations. A 9 % decrease in the peak discharge was observed as the Manning's N value was increased by 10 % (Carrivick, 2006). Whereas, only 8% variation in the discharge was reported when Manning's N was varied by 30 % (Carling et al., 2010). This was attributed to the dominance of convective acceleration over bed-resistance and also the breach forming process. Similar findings by Yochum et al. (2012) suggests that hydraulic resistance is underestimated in high-gradient channels due to the dominance of flow acceleration in steep slopes. The sensitivity of the hydraulic models to simulate GLOF events varies from case to case depending upon the morphic setting and input parameters. It is therefore elementary to evaluate the sensitivity of these dynamic models and its simulated outputs to various hydraulic inputs and morphic parameters.

In this chapter, the sensitivity of the hydrodynamic model to Manning's N, breach width (B_w) and breach formation time (T_f) is evaluated. In addition, a sensitivity analysis of the modeled hydraulic outputs (flow velocity and flow depth) to various channel characteristics like slope and top-width of the flow channel is evaluated by performing a series of hydrodynamic simulations. As the present thesis evaluates the potential Himalayan GLOFs in the central belt of India, the

sensitivity analysis is based on a study which is performed on the Safed lake system, located in the Goriganga basin, in the state of Uttarakhand. The impact of the potential GLOF on the nearest settlement "Milam" located at a distance of 16.2 km is thereby analyzed for which breach parameters were calculated using empirical models.

6.2 STUDY AREA

The Safed lake (tal) (30°33′46.55″ N and 80°10′19.15″ E) is located in the northern part of the Goriganga basin in the state of Uttarakhand, Central Himalaya. The basin is drained mostly by the Goriganga river, originating from the Milam glacier. The lake has an elevation of 4882 m above sea level (m a.s.l). It is the largest proglacial lake in the basin with a total area of 0.023 km^2. The Milam village is located at a distance of 16.2 km downstream of the lake along the Gonka river which joins the Gori river at Milam. It is a small village in the Pithoragarh district with a population of only 135. It consists of a total of 110 houses spread over an area of 0.25 km^2 at the confluence of the Gonka and the Gori rivers. Figure 6.1 shows the study area, the location of the Safed lake, and the Milam village in the state of Uttarakhand, central Himalaya. The lake is surrounded by several zones of mass wasting, which are potential sources of mass addition to the lake. The cliff located in the left bank of the lake is very steep with slopes varying between 35° to 70°. Also, being a proglacial lake, it is located at the snout of the parent glacier which is marked by a tall ice-wall and a zone of glacier-calving. Figure 6.2 shows the mass wasting zones around the lake, which are potential GLOF triggering sources.

6.3 DATA USED

The present study exploits Corona (KH4), Landsat ETM+ and OLI/TIRS (30 m) to map the lake extent from 1968 to 2018. Terrain data for GLOF modeling was obtained from Advanced Spaceborne Thermal Emission and Reflectance Radiometer (ASTER) global digital elevation model (GDEM). ASTER global DEM is a freely available model (https://earthexplorer.usgs.gov/) that provides elevation information between 83° N and 83° S with a spatial resolution of 30 m. The land use land cover (LULC) classification, to determine Manning's roughness coefficient of the given terrain is obtained using GlobCover (v2) and cross verified using high-resolution geo-referenced CNES/Airbus imagery tiles of google earth. GlobCover is the global product of land cover maps created from the 300 m MERIS sensor onboard of the ENVISAT satellite.

6.4 METHODOLOGY

6.4.1 Growth assessment of the Safed lake

A growth assessment of the Safed lake is performed using multitemporal satellite images. The lake surface is mapped for the year 1968, 1994, 2000, and 2018. The Normalized Difference
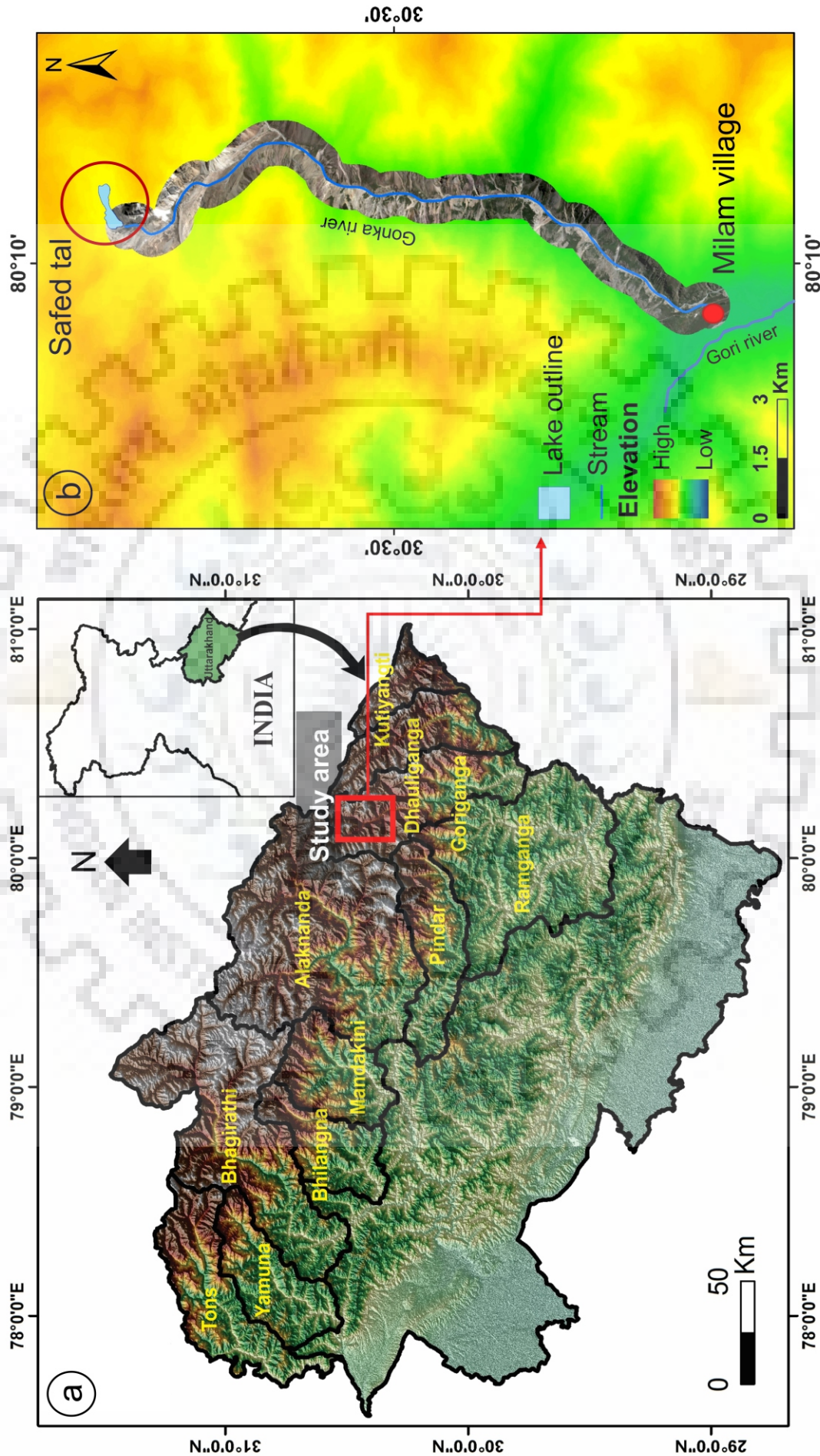
Figure 6.1 (a) The state of Uttarakhand and the location of the study area in the Goriganga basin; (b) the location of the Safed lake (tal) and the Milam village; the village is located at the confluence of the Gorka and the Gori rivers

Water Index (NDWI) method is employed to identify and map the glacial lake surfaces for different years. The lake surface for the year 1968 is mapped by visual interpretation of the high-resolution Corona image. The lake has shown a growth of 0.13 km^2 over a period of 50 years. The lake has doubled its size from 0.10 km^2 in 1968 to 0.23 km^2 in 2018. Figure 6.3 shows the growth of the Safed lake in the last five decades.

6.4.2 Hazard assessment of the Safed lake

The hazard assessment of the Safed lake is performed using hydrodynamic modeling for which the hydraulic parameters were calculated using empirical models. One-dimensional hydrodynamic modeling is employed to calculate the breach hydrograph. The total water volume of the lake is calculated using an empirical relation by Huggel et al. (2002) considering the area of the Safed lake in 2018. The equation is given as:

$$V = 0.104\ A^{1.42} \qquad\qquad eq.\ 1$$

Where V is the total volume of the lake and A is the area of the lake. The total volume of the lake is calculated to be 4.3×10^6 m^3.

One-dimensional modeling (HEC-RAS) is employed to calculate the breach hydrograph. The average breach width and failure time were calculated using the empirical relations given by Froehlich. (1995).

$$B_w = 0.1803 K_o\ (V_w)^{0.32}\ (h_b)^{0.19} \qquad eq.\ 2$$

$$(T_f)\ in\ h = 0.00254\ (V_w)^{0.53}\ (h_b)^{-0.9} \qquad eq.\ 3$$

Where B_w is the breach width, V_w is the volume of the lake, h_b is the height of the breach, and T_f is the time of failure. Here, the volume calculated using equation 1 is considered to derive the breach parameters. The h_b is derived from DEM and is considered to be 60 m assuming that the moraine breach up to this depth (base of the moraine). Based on the above equations the breach width (Equation 1) and breach formation time (Equation 2) is calculated to be 73.13 m and 0.21 hr respectively.

The HEC-RAS 1D model was employed to model a potential GLOF event of the Safed lake. The initial breach hydrograph is calculated based on the parameters calculated above (B_w=73.13 m and T_f = 0.21 hr). Two-dimensional routing of the breach hydrograph is performed for a distance of 16.2 km from the lake up to the Milam village to evaluate its impact on the Milam village. The HEC-RAS 2D (Version 5.0.5) is used to rout the initial breach hydrograph along the main flow channel. The primary input of the model includes terrain data and boundary conditions for simulating an unsteady hydraulic process. ASTER DEM raster is used as a continuous pixel-based terrain input. A flow area is initially defined over the given terrain, containing the area of
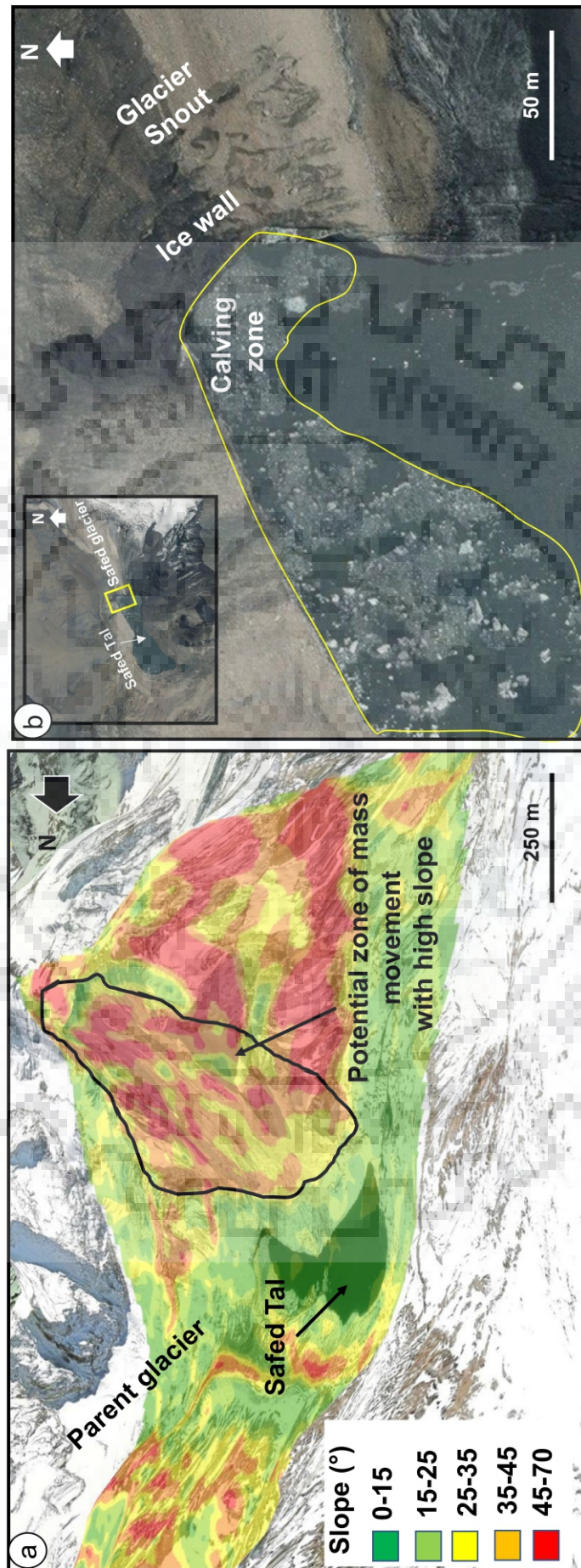
Figure 6.2 (a) The source zones of potential mass wasting; (b) calving zone at the snout of the glacier

interest i.e. the lake to the Milam village. Thereafter, a 2D mesh is constructed within the given flow area, with an individual cell dimension of 30 × 30 m. The land use land cover (LULC) for the flow area is extracted from GlobCover (v2). Each cell has been defined a value of Manning roughness calculated based on the LULC. An average Manning's N based on the LULC within the flow area is calculated to be 0.05, which is considered for routing. The potential GLOF impact of the Safed lake is analyzed by spatial and temporal mapping of the 2D model outputs. Temporal assessment of the hydraulic properties like water depth and velocity have been performed at Milam village.

6.4.3 Sensitivity analysis

a. Model sensitivity to input parameters

A series of hydraulic simulations are performed to evaluate the sensitivity of the hydrodynamic model to the input parameters (Manning's N and breach parameters). Here, we assess the sensitivity of the model to the dam breach parameters in order to evaluate its effect on the breach hydrograph. A total of six hypothetical one-dimensional moraine breach simulations are performed with varied breach width (B_w) and time of failure (T_f). Three scenarios with $T_f = 0.50$ hr, 0.75 hr, and 1.0 hr with a constant $B_w = 100$ m is considered to evaluate the sensitivity of the model to T_f. Similarly, keeping T_f constant, the sensitivity to B_w is evaluated by considering three scenarios with varied B_w (50 m, 75 m, and 100 m). The peak discharge and time of peak are in each scenario is compared to assess the sensitivity to the input parameters. Moreover, to evaluate the two-dimensional sensitivity of the model to the above hypothetical breach hydrographs, the modeled hydrographs are routed along the flow channel from the lake to the Milam village. A Manning's N of 0.05 is considered for routing (Section 3.4.2). The sensitivity is evaluated by assessing the change in the flow depth and flow velocity.

In order to evaluate the sensitivity of the model to Manning's N, a series of two-dimensional routing of the dam-breach hydrograph (modeled in section 6.4.2) is performed. Keeping the dam-breach parameters constant (as section 6.4.2), two-dimensional routing of the potential moraine-breach hydrograph is performed for varied Manning's N (0.03, 0.04, 0.05, 0.06, and 0.07). The sensitivity is evaluated by assessing the change in the flow depth and flow velocity (maximum and mean).

b. Sensitivity to channel characteristics

The sensitivity of the flow hydraulics of a modeled potential GLOF (Section 6.4.2) to the slope and top-width of the channel is evaluated. The slope of the channel is calculated for each 100 m elevation interval along the entire length of the given channel (from the lake to Milam village).
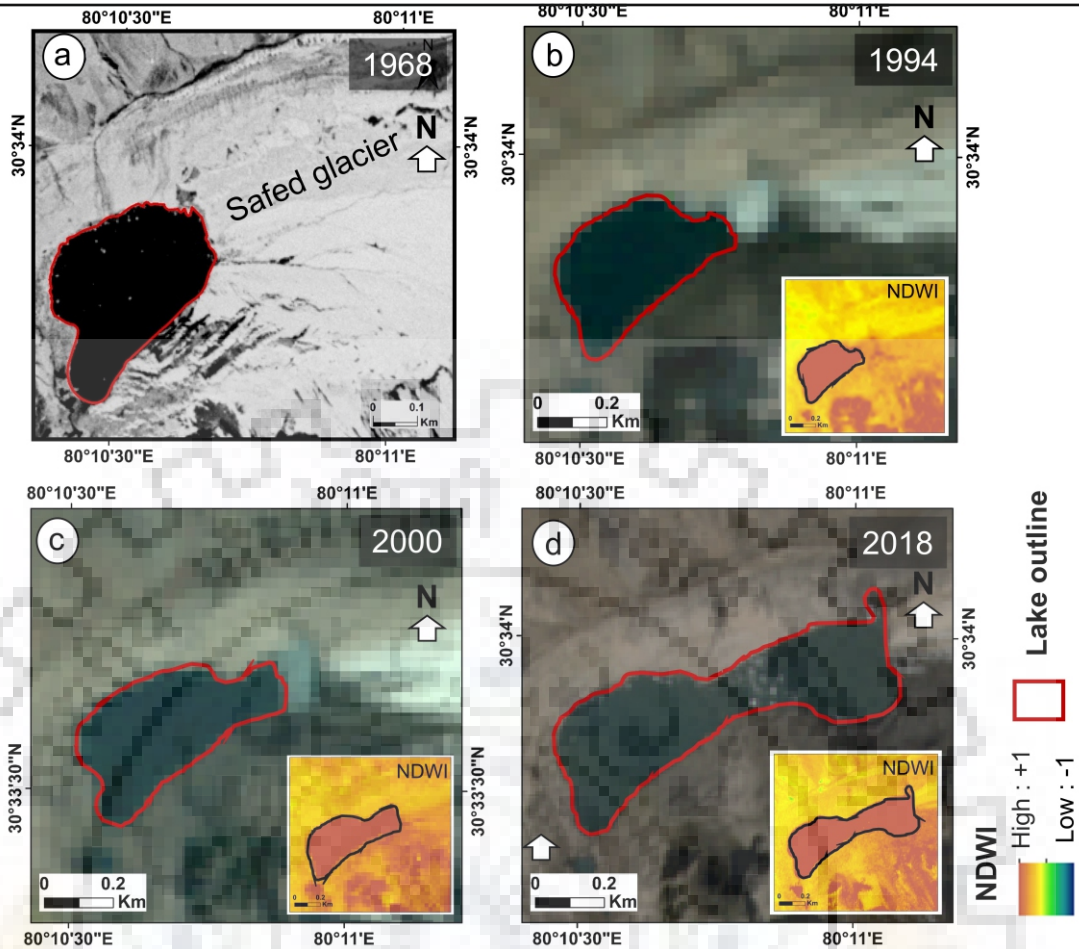
Figure 6.3 The growth of the Safed lake from 1968 to 2018; the subset image shows the NDWI for the respective years
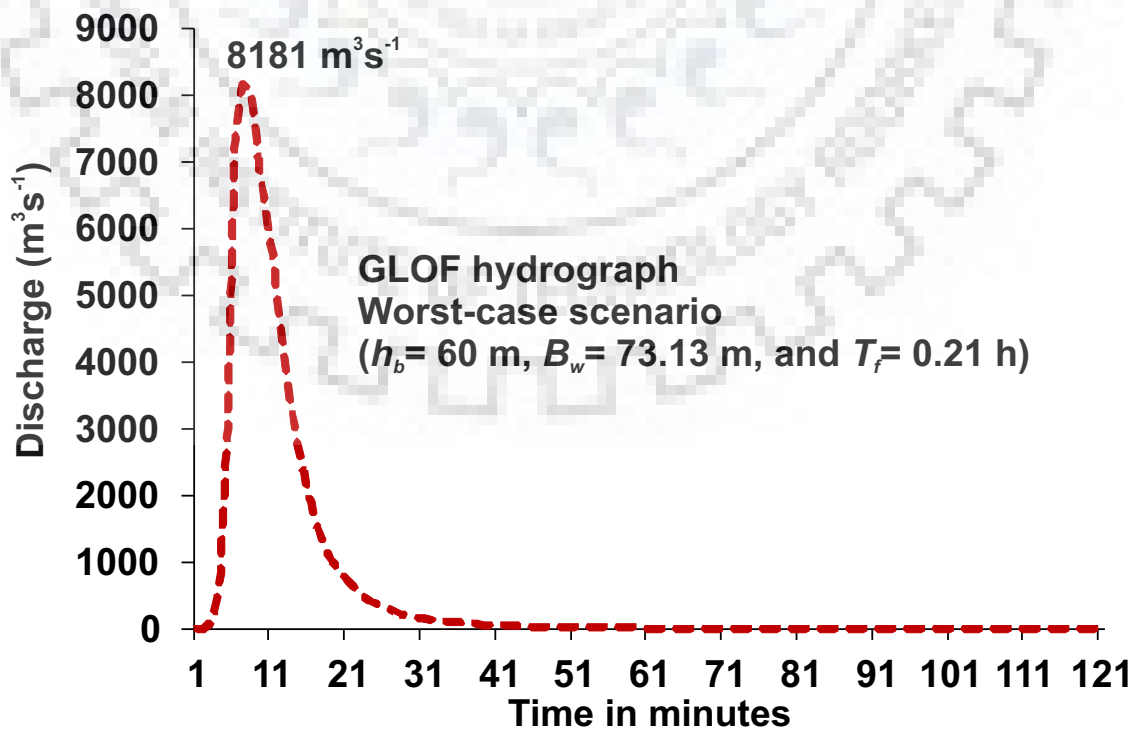
Figure 6.4 The potential moraine-breach hydrograph of the Safed Lake; a peak discharge pf 8868 m³s⁻¹ is reached within 6 minutes after the initiation of the dam breach event

The mean velocity in each 100 m elevation band is calculated from the obtained spatially-distributed 2D modeled results and are plotted against its respective slope values to evaluate its relationship. Similarly, the modeled 2D flow depth is extracted for every elevation band and the mean depth calculated for each band is plotted against the slope of the channel for the sensitivity evaluation.

The sensitivity of the modeled results to the top-width of the flow channel is evaluated using the modeled 2D flow hydraulics. For this, the top-width of the modeled GLOF inundation in the given channel is measured across 20 cross-sections. The top-width (in m) is plotted against the mean flow velocity (ms^{-1}) and inundation depth (m) calculated along the cross-sections. The variation of flow depth and velocity to the top-width of the channel is then evaluated.

6.5 RESULTS AND DISCUSSION

6.5.1 Hazard assessment of the Safed lake

Froehlich. (1995) equations were employed to model a potential GLOF of the Safed lake. The breach event was modeled with a breach width (B$_w$) of 73.13 m and time of failure (T$_f$) of 0.21 hr. The GLOF hydrograph produced a peak discharge of 8181 m^3-s^{-1} that is achieved within 6 minutes after the initial breach event. Figure 6.4 shows the breach hydrograph for which breach parameters were calculated using the Froehlich. (1995) equations. In order to evaluate the impact of the potential GLOF of the Safed lake, two-dimensional hydraulic routing was performed from the lake to the Milam village along the main flow channel. Spatially distributed hydraulic properties (flow velocity and inundation depth) were mapped along the channel for a distance of 16.2 km from the lake to the village (Figure 6.5).

The evaluation of the temporal hydraulics at Milam village revealed flow depths up to a maximum of 5.0 m, that is achieved in 1 hr 15 min after the initial dam breach event. The flow velocities at the village reach up to 3.2 ms^{-1} and the peak occurs at the same time as the maximum flow depth. The potential GLOF inundates a total area of 0.02 km^2 at Milam village. The GLOF potentially inundates four minor settlements consisting of a total of 25 to 30 houses. However, the major part of the village remains unaffected by the GLOF as it located at approximately 200 m towards the west. Figure 6.6 shows the potentially inundated areas at Milam, and the plots shows the change in flow hydraulics (inundation depth and flow velocity) with time.
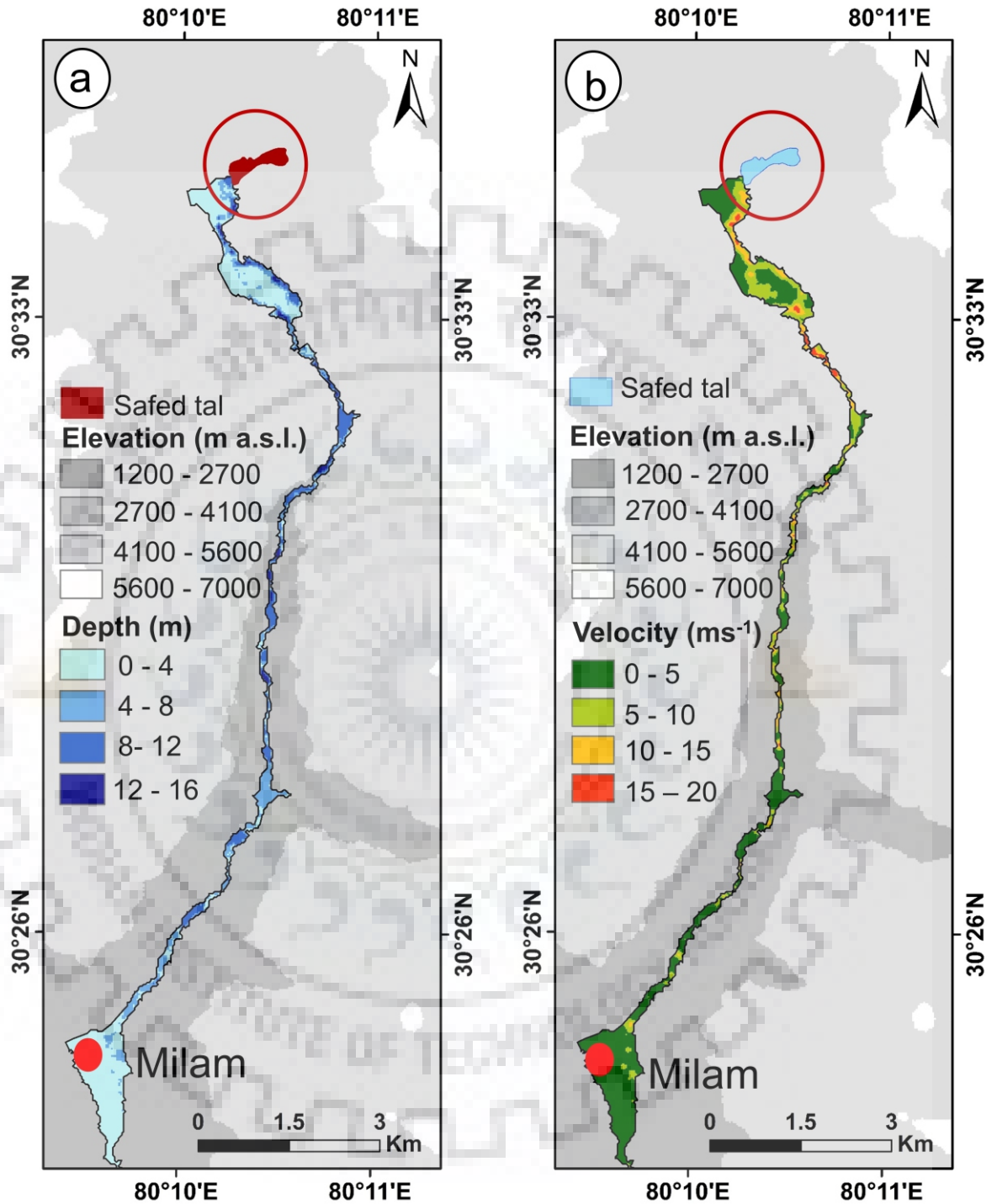
Figure 6.5 Spatially distributed (a) inundation depth (in m) and (b) flow velocity (ms^{-1}) along the flow channel from the lake to Milam village

6.5.2 Sensitivity analysis

a. Model sensitivity to input parameters

The sensitivity of the hydrodynamic model to breach width (B_w), time of failure (T_f) and Manning's N were evaluated by hypothetical scenario modeling (Section 6.4.3). In order to assess the influence of one-dimensional breach parameters on the breach hydrograph, six hypothetical scenarios with varied B_w and T_f were considered.

Three scenarios were considered with varied T_f (0.5 hr, 0.75 hr, and 1.0 hr) and a constant B_w (100 m). The peak discharge changes by ±11.5% when dT_f is 0.25 hrs. The time of peak is delayed by 4 to 5 min when T_f is increased by 0.25 hrs (Figure 6.7a). Similarly, the remaining three scenarios were modeled by keeping T_f (0.5 hr) constant and varying B_w (50 m, 75m, and 100 m). The peak discharge decreased by 2.3 % when B_w was reduced by 25 m, it further decreases by 14.4% when B_w was reduced by 50 m. The time of peak is delayed by 1 min and 4 min when B_w was reduced by 25 m and 50 m respectively (Figure 6.7b). Form the assessment it is evident that GLOF hydrographs are more sensitive to the time of moraine failure as compared to the width of the breach.

To evaluate the two-dimensional sensitivity of the model to the breach hydrographs, the modeled hypothetical GLOF hydrographs with varied T_f were (Figure 6.7a) routed along the flow channel from the lake to the Milam village. The inundation depth and flow velocity of the entire channel were evaluated (Table 6.1). The maximum inundation depth decreases by 3.7% and 5.6% when T_w is increased by 0.25 hr and 0.5 hr respectively. Similarly, the mean depth decreases by 2.9 % and 5.4% when T_f is increased by 0.25 hr and 0.5 hr respectively (Table 6.1). The evaluation of the maximum flow velocity along the given channel reveals a decrease by 2% and 3% when T_f is increased by 0.25 hr and 0.5 hr respectively. Also, the mean velocity shows a decrease by 4 % and 7.4 % when T_f is increased by 0.25 hr and 0.5 hr respectively (Table 6.1). Thus, from the analysis, it is clear that the initial breach hydrograph determines the flow characteristics of a routed GLOF. The hydraulic properties of a GLOF at any point downstream is sensitive to the initial breach hydrograph. The results show that the maximum inundation depth and the mean velocity is slightly more sensitive as compared to the mean depth and maximum velocity respectively.
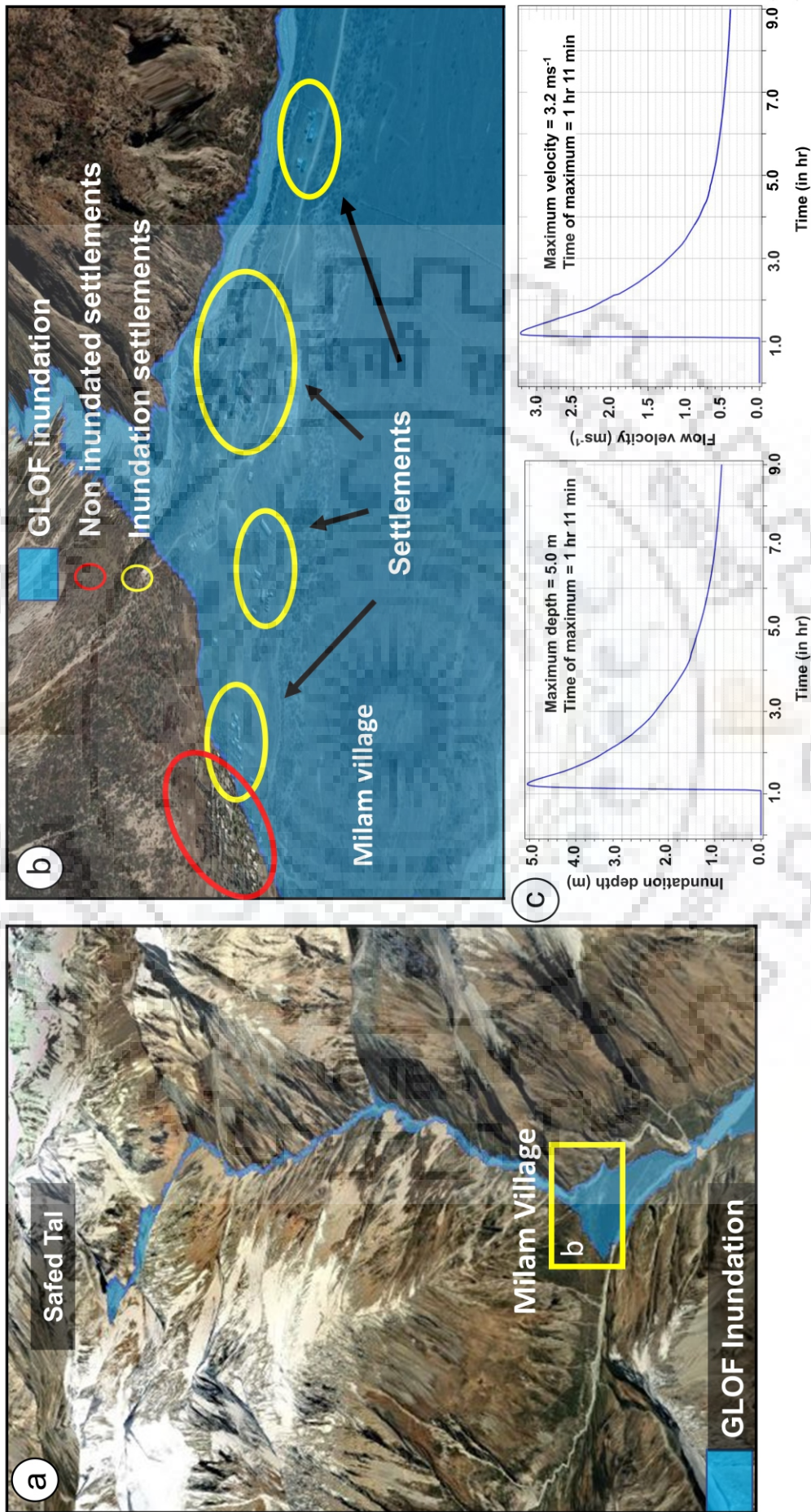
Figure 6.6 (a) GLOF inundation from the Safed lake (tal) to the Milam village; (b) Milam village showing the inundated and non-inundated settlements; (c) plot showing the change of flow depth and velocity with time at Milam

Table 6.1 Hydraulic properties of potential GLOF along the flow channel for varied moraine-failure time.

Along flow channel				
	Inundation depth		Flow velocity	
Time of failure (T_f)	Maximum	Mean	Maximum	Mean
0.5 hr	15.8	4.02	19.8	3.24
0.75 hr	15.2	3.90	19.4	3.11
1.0 hr	14.9	3.80	19.2	3.00

At Milam village, maximum inundation depth decreases by 4.2 % and 8.5 % when T_f is increased by 0.25 hr and 0.5 hr respectively. Likewise, the maximum flow velocity decreases by 4.3 % and 7.5 % when T_f is increased by 0.25 hr and 0.5 hr respectively (Table 6.2). The temporal evaluation of the hydraulic parameters reveals a delay in the peak by 8 minutes and 14 minutes when breach formation is increased by 0.25 hr and 0.5 hr respectively. Form the results it is clear that the timing of GLOF (peak) is sensitive to the initial flow hydrograph, which in turn is a function of the breach width (B_w) and the breach formation time (T_f).

Table 6.2 Hydraulic properties of potential GLOF at Milam village for a varied moraine-failure time.

At Milam village			
Time of failure (T_f)	Maximum depth	Maximum velocity	Time of peak
0.5 hr	4.7	2.77	1 hr 20 min
0.75 hr	4.5	2.65	1 hr 28 min
1.0 hr	4.3	2.56	1 hr 34 min

The sensitivity of the model to Manning's N was tested by performing a series of two-dimensional routing of the dam-breach hydrograph (hydrograph is given in Figure 6.4). Keeping the dam-breach parameters constant (as in section 6.4.2), two-dimensional routing is performed for varied Manning's N (0.03, 0.04, 0.05, 0.06, and 0.07). The results are evaluated by plotting the maximum and the mean flow depth and velocity against the Manning's roughness coefficient (Figure 6.8). The maximum flow velocity decreases with the increase in the channel roughness showing a correlation coefficient of 0.91 (Figure 6.8a). Similarly, the mean velocity vs. Manning's N reveals a similar trend with a correlation coefficient of 0.93 (Figure 6.8b).

The results reveal that flow velocity is more sensitive to the channel roughness as compared to the inundation depth, as both maximum and mean depth do not show significant change with change in the channel roughness. The correlation coefficient for maximum depth vs. Manning's N is calculated to be 0.91 and that of mean depth vs. Manning's N is 0.98 respectively. Figure 6.9 and 6.10 shows the spatial distribution of the maximum depth and flow velocity from the
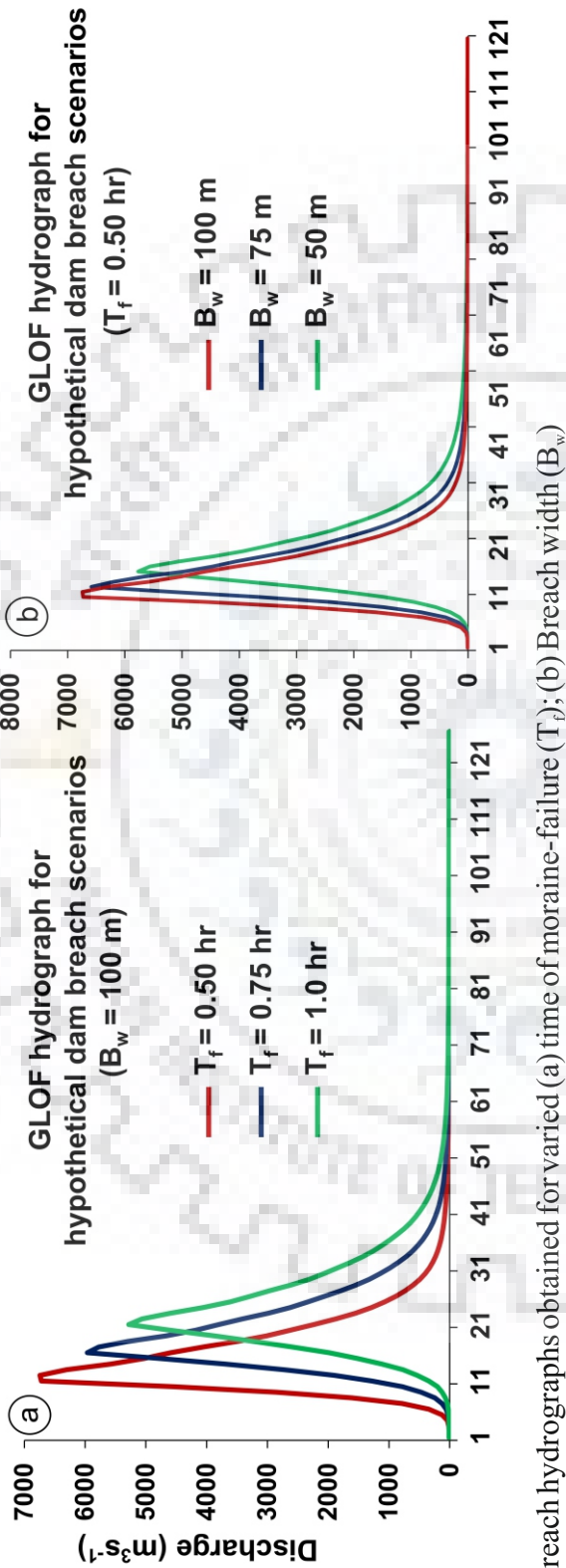
Figure 6.7 Breach hydrographs obtained for varied (a) time of moraine-failure (T_f); (b) Breach width (B_w)
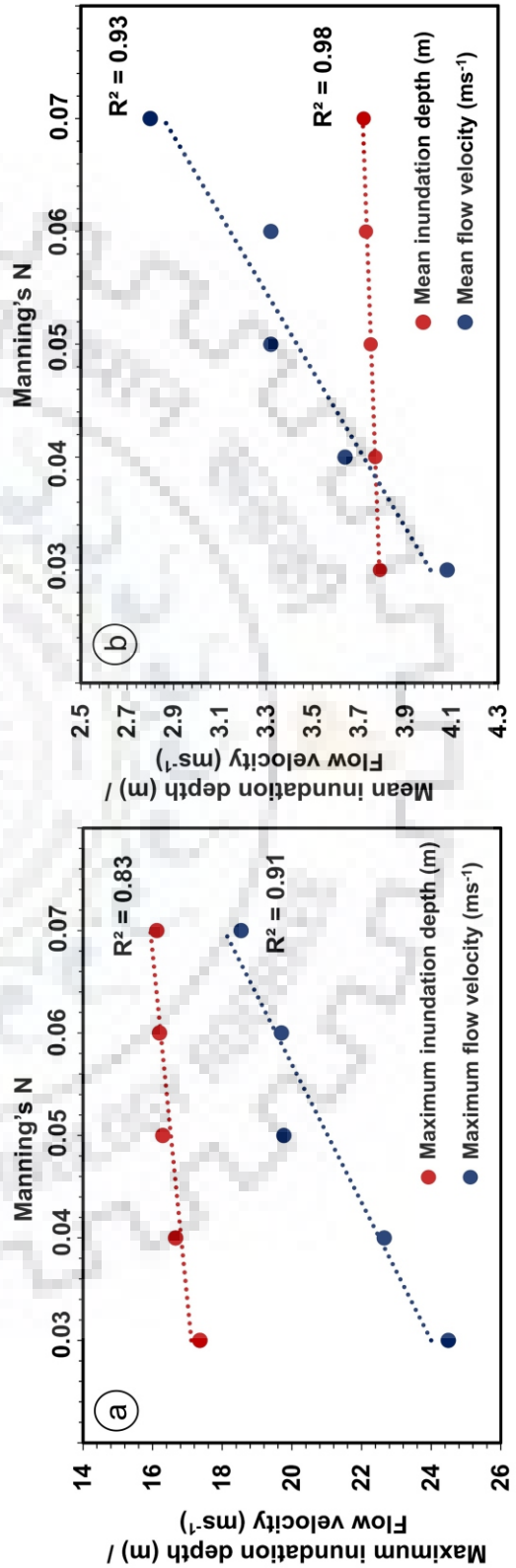
Figure 6.8 Plot of (a) Maximum inundation depth/flow velocity vs. Manning's N; (b) Mean inundation depth/flow velocity vs. Manning's N

Figure 6.10 Spatial distribution of maximum flow velocity along the channel from the Safed lake (tal) to the Milam village for varied Manning's N – (a) N= 0.03; (b) N= 0.05; (c) N=0.07
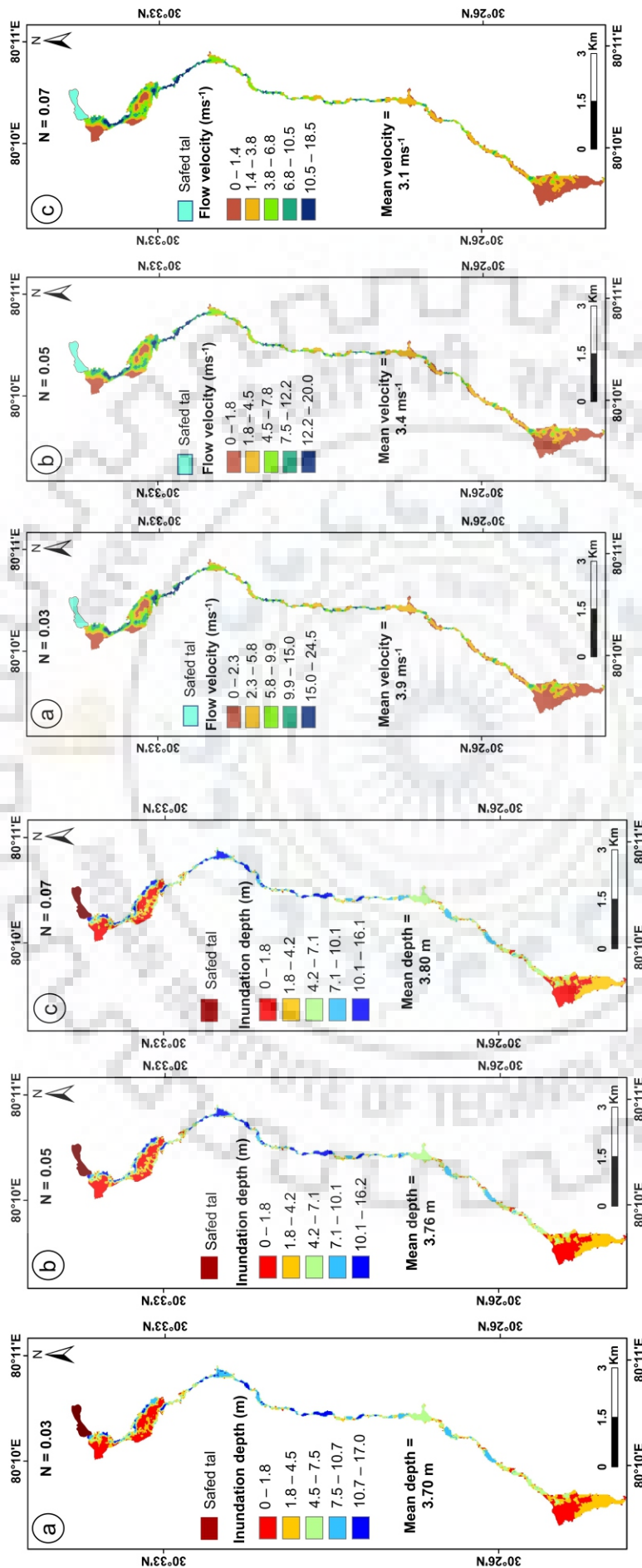
Figure 6.9 Spatial distribution of maximum inundation depth along the channel from the Safed lake (tal) to the Milam village for varied Manning's N – (a) N=0.03; (b) N=0.05; (c) N= 0.07
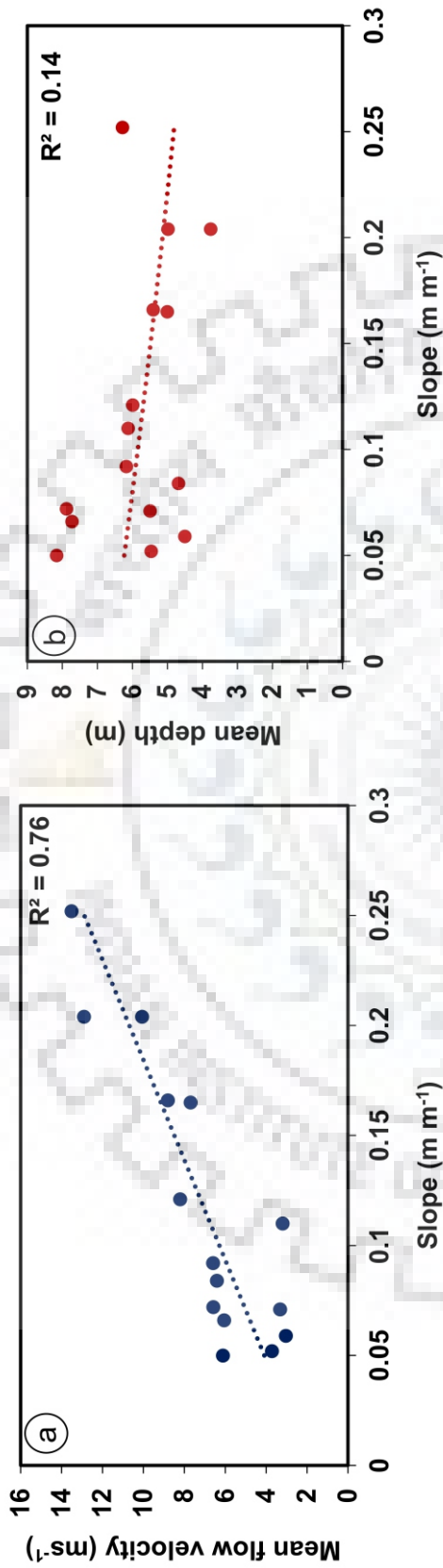
Figure 6.11 Plot showing (a) mean velocity *vs.* slope of the channel; (b) mean depth *vs.* slope of the channel; it is evident that the flow velocity linearly varies with the change in the slope of the given channel; flow depth is not dependent on the slope
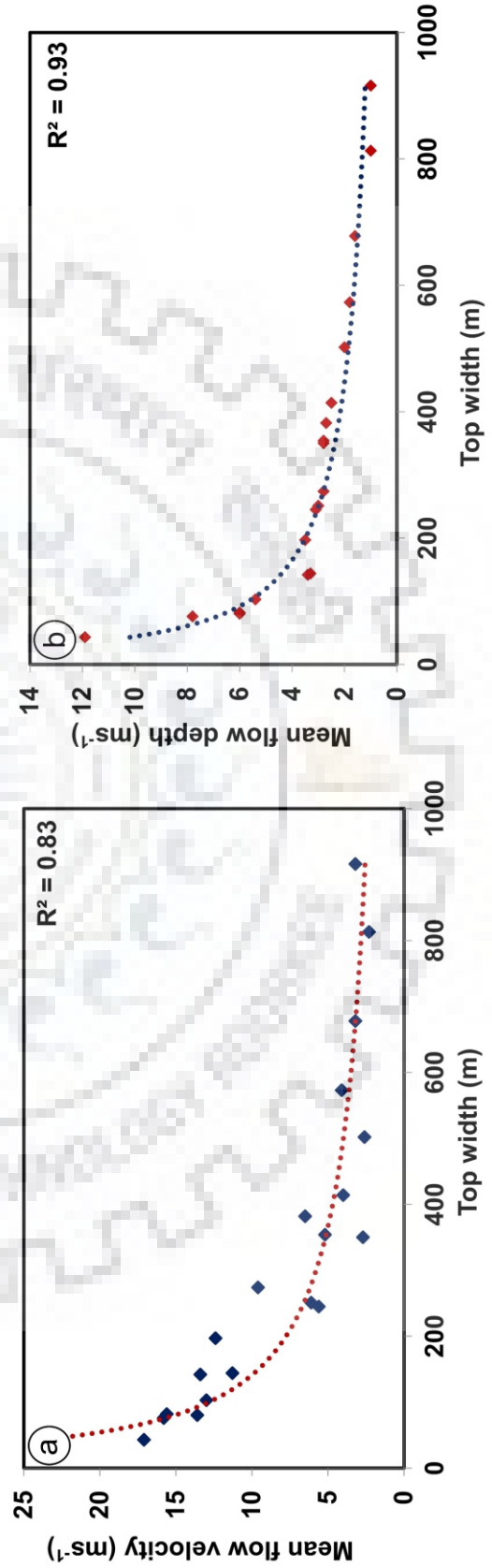
Figure 6.12 Plot showing (a) mean velocity *vs.* top-width of the channel; (b) mean depth *vs.* top-width of the channel; both flow velocity and flow depth vary similarly to the change in the top width of the channel

Safed lake to the Milam village respectively for different Manning's roughness coefficient (N) along the channel.

b. Sensitivity to channel characteristics

The study evaluates the sensitivity of the flow hydraulics (flow velocity and inundation depth) to channel characteristics (slope and top-width). The slope calculated for every 100 m elevation contour is plotted against the mean velocity calculated for each elevation band. A similar analysis is performed by considering the mean depth and the slope of the channel. It is evident that the flow velocity linearly varies with change in the slope of the given channel with a correlation coefficient of 0.76 (Figure 6.11 a). However, flow depth is independent ($R^2 = 0.14$) of the channel slope as it shows a random variation (Figure 6.11 b).

To evaluate the sensitivity of the hydraulic properties of a GLOF to the top-width of the flow channel, the flow velocity and depth is plotted against the top-width of the channel. The top-width is calculated along 20 cross-sections covering the entire flow channel, for which the mean flow depth and velocity are calculated. It is evident that the flow velocity and depth show similar trends when plotted against the respective top-width with correlation coefficients of 0.83 and 0.93 respectively (Figure 6.12). Both the flow velocity and depth tend to decrease as the top width of the channel increases.

6.6 CONCLUSION

The Safed Tal is one of the largest glacial lakes located in the high-altitude regions of Uttarakhand, Central Himalaya. A temporal analysis of the lake using satellite imagery shows enormous growth of the lake. The lake surface has grown from 0.10 km^2 to 0.23 km^2 over the last five decades. In this study we evaluate a potential GLOF of the lake and its impact on the nearest settlement "Milam village", using 1D and 2D dynamic modeling where breach parameters calculated empirically. A moraine -breach event of the lake was modeled for which the breach parameters were calculated empirically. The potential breach event produced a GLOF hydrograph with a peak discharge of $8181 \text{ m}^3\text{s}^{-1}$. Hydrodynamic routing of the potential GLOF hydrograph along the given channel reveals water depth up to a maximum of 5 m and flow velocities up to 3.2 ms^{-1} at Milam village. The GLOF potentially inundates a total area of 0.02 km^2 at the village site thereby affecting a total of 20 to 30 houses located at the site.

Further, the study evaluated the sensitivity of the dynamic hydraulic model and its simulated outputs to various Hydraulic inputs and morphic parameters. For this, a series of hydrodynamic moraine-breach modeling and flood routing was performed to assess the sensitivity of flow

hydraulics to different model input parameters and terrain characteristics. The sensitivity of the initial GLOF hydrograph to the total breach width (B_w) and breach formation time (T_w) was evaluated by considering six hypothetical moraine-breach scenarios with different combinations of B_w and T_f. It was evident that the GLOF hydrograph is more sensitive to the breach formation time (T_f) than that of the breach width (B_w). The peak discharge changed by $\pm11.5\%$ and the time of peak is reached in $\pm$ 4-5 min when T_f was increased or decreased by 0.25 hrs. Whereas the peak discharge decreased by only 2.3 % when B_w was reduced by 25 m, it further decreased by 14.4% when B_w was reduced by 50 m. The time of peak is delayed by 1 min and 4 min when B_w was reduced by 25 m and 50 m respectively. In order to evaluate the two-dimensional sensitivity of the model to the breach hydrographs, the modeled hypothetical GLOF hydrographs with varied T_f were (Figure 6.7a) routed along the flow channel from the lake to the Milam village. The analysis revealed that the initial breach hydrograph determines the flow hydraulics of a routed GLOF. The hydraulic properties of a GLOF at any point downstream is sensitive to the initial breach hydrograph.

The relationship between the flow hydraulics (flow velocity and inundation depth) to channel characteristics were evaluated. The flow velocity is linearly dependent on the slope of the given flow channel. However, the flow depths did not show any relation with the slope of the channel and tend to vary in a random manner. In addition, the flow hydraulics were analyzed with respect to the top-width of the channel. Both, flow velocity and inundation depth reveal a similar trend of decrease with an increase in the top-width of the channel.

CHAPTER 7: SUMMARY AND CONCLUSIONS

Glacial lake outburst floods (GLOF) have been reported catastrophic in the Himalayan terrain, as it led to the destruction of the infrastructure and claimed many human lives in the past. Not all GLOF events that occurred in the Himalaya, have been reported. Moreover, the knowledge of the hazard potential of the existing lakes in the higher reaches of the Himalaya is limited. Over the past few decades, a general trend of glacier retreat is seen in the Himalaya. This has led to the formation of numerous glacial lakes in the high-altitude regions. The existing glacial lakes have been showing an increase in their sizes over time. Therefore, it is fundamental to improve our knowledge of the potential hazard of the existing high-altitude lakes and the risk it presents to the downstream regions. The risk reduction of extreme flood events that occur due to the catastrophic failure of the glacial lakes solely relies on the prior hazard assessment of the pre-existing lakes. Various policy makers seek information on the hazardous lakes prior to the actual implementation of the risk reduction strategies. There are gaps that exist in understanding GLOF processes in the Himalaya and modeling moraine-breach events remain as a challenge.

This thesis is a compilation of hazard assessments of potentially critical lakes in the central part of the Indian Himalaya (Uttarakhand and Sikkim). The study undertaken provides crucial insights into the complex flow phenomenon of the potential GLOF events. This is achieved by the application of field- and modeling-based approaches to simulate the various hydraulic processes and understand the flow phenomenon of GLOFs. The study performs characterization of the potential extreme flood events in terms of its peak discharge (m^3s^{-1}), time of peak (in min), flow velocities (ms^{-1}), flow depth (m), and inundation area (m^2). The impact analysis of the GLOF events to evaluate its potential effect in the downstream regions is achieved by dynamic routing along a given flow channel.

The major findings of the thesis are summarized in the following:

1. Inventory of glacial lakes and temporal growth assessment
An updated glacial lake inventory for central Indian Himalaya (Uttarakhand and Sikkim) has been presented in the thesis. The temporal growth assessment to the individual glacial lakes was carried out by mapping their past surfaces using remote sensing datasets from 1968 to 2018. The state of Uttarakhand has shown a linear growth in the number of glacial lakes from 1968 to 2016. The total number of lakes increased from 61 to 130 in the state within a span of 48 years. The maximum change in the number and area of glacial lakes occurred in the Alaknanda basin located in the central part of the state. The distribution of the lakes with respect to elevation revealed the

existence of maximum lakes in the elevation range of 4500-5000 m a.s.l. In the state of Sikkim, a total of 14 large glacial lakes (>0.05 km^2) were identified in the entire state, the surfaces of which were mapped for 1990, 2000, 2010, and 2018. Their growth assessment indicates that the total area of all the larger lakes increased by 3.5 km^2 over a period of 28 years from 1990 to 2018. Three of the fourteen lakes showed an average percentage increase of 89 % in its total area over a period of 28 years.

The present temporal glacial lake inventory was used to select three potentially critical glacial lakes for the Uttarakhand Himalaya namely, the Satopanth lake, Dhauliganga lake, and the Safed lake for detailed hazard assessment using remote sensing and complex hydrodynamic modeling (Chapter 3, 5, and 6). In the Sikkim Himalaya, a detailed GLOF study is conducted for the South Lhonak lake (Chapter 4 and 5) which is identified to be one of the potentially critical lakes in the state.

2. Field-based 1D and 2D hydrodynamic modeling of potential GLOF

The hazard potential of the Satopanth lake, when combined with a 100-year return period flood event, was evaluated to study its impact on a hydropower station located downstream. Different scenarios of a moraine-breach event of the lake were modeled to calculate the discharge for different moraine failure parameters (Failure time-0.5 hrs, 0.75 hrs, and 1.0 hrs). Further, its impact on the hydropower dam site located at a distance of 28 km downstream, was evaluated using 1D and 2D hydrodynamic routing along the main flow channel. The one-dimensional GLOF modeling coupled with a 100-year return period flood resulted in a peak discharge of 2612 m^3s^{-1} at the dam site. The potential GLOF wave will arrive at the dam site 38 minutes after the initiation of the moraine-breach event. Two-dimensional routing of the GLOF hydrograph was performed from the lake to the dam site to evaluate the spatially distributed hydraulic properties (flow velocity, flow depth, and inundation area) of the potential flood wave. The potential GLOF discharge was combined with the 100-year return period flood discharge at Mana village, resulting in a flood that arrived at the dam site with a maximum velocity of 7.6 ms^{-1}. Assuming that the control gates of the dam remain closed, the water depth at the dam site increases at a rate of 4.5 m per minute. The dam overflows in approximately 4 minutes after the initial arrival of the flood wave (height of the dam=17 m).

3. Bathymetry-based potential GLOF hazard assessment

The risk assessment of the South Lhonak lake, Sikkim has been performed by modeling a potential GLOF event. In order to evaluate its impact in the downstream region, hydraulic routing was carried out along the main flow channel until it reaches the Chungthang town located 62.3 km downstream of the lake. The worst-case GLOF scenario resulted in an overtopping failure

with breach width of 95.78 m. The one-dimensional routed hydrographs were evaluated to determine the peak flood (m^3s^{-1}) and the time of flood wave arrival (hrs) at different locations along the given flow channel. Whereas, two-dimensional routing of flood wave was employed to determine the downstream exposed areas to such a high magnitude GLOF event based on the spatially distributed model outputs of flow depth, velocity, and inundation. A representative modeling of the South Lhonak moraine-breach mechanism was evaluated based on the available field measurements of the damming moraine. In the present study, the worst-case GLOF scenario of the South Lhonak lake yielded an initial flood hydrograph with a peak discharge of 6064.6 m^3s^{-1} releasing 39.05 % of the total lake volume. The flood wave potentially inundates several infrastructures as it propagates through the Latong and Yuigang towns. A peak flood of 3828.08 m^3s^{-1} recorded at the Chungthang town, has a potential to inundate a total area of 55,000 m^2 of the existing settlements, where flow depth and velocity reach up to 8 m and 9 ms^{-1} respectively. Based on the results, the most impacted area in a potential GLOF event of the South Lhonak lake can be identified as the Chungthang town where a major part of the settlement and infrastructure is affected. It may be noted that sudden discharge of such high volumes of water with a peak discharge reaching up to 3828.08 m^3s^{-1} is inferred to cause substantial damage to the hydropower dam site located at Chungthang, which needs further site-specific evaluation. It is also evident from the study that the presence of a paleo-topographic feature cross-cutting the main flow channel significantly minimizes the energy of the South Lhonak lake GLOF wave. Despite being obstructed by such a topographic barrier, the resulting GLOF event can cause significant damage to the downstream regions. The investigation also involved the modeling of a framework to propose a potential flood remediation measure of the South Lhonak lake GLOF by demonstrating the effect of a lateral inline structure along the flow channel, to check the flow of the potential flood wave and thereby reducing the impact of the GLOF wave in the downstream regions. The proposed damage-reduction strategy prevents inundation of two settlements along the given flow area covering a total area of 5836 m^2, five major bridges, and several roads. From the results it is recommended that if an early warning is broadcasted immediately after the initiation of the dam breach event, it would give a response period of 3.75 hours before the flood wave hits the first settlement in the Chungthang town where the peak flood is reached within 15 to 20 min of the flood wave arrival. Moreover, an early warning system, if installed at 21 km downstream of the lake would facilitate forewarnings that can provide an evacuation time of 1.25 hours at Chungthang town.

4. Ice-thickness based mapping of maximum lake extent - impact analysis of potential future GLOF

The application of spatially distributed modeled ice thickness is demonstrated to evaluate the overdeepening sites on the glacier bed. These depressions on the glacier bed are the potential sites for future lake formation. The volume of these potential future lakes can be estimated using area-based scaling of the ovedeepening sites. Here, the overdeepenings on the glacier bed were mapped for the 15 larger glaciers of the Dhauliganga basin. A total of 54 overdeepening sites was identified in the basin with a volume capacity to hold 15.1×10^7 m^3 of water. Further, the methodology was adopted to map the maximum extent of the existing proglacial lakes by investigating the overdeepening on the glacier bed adjacent to the lakes. The future GLOF potential of two glacial lakes (Dhauliganga lake and South Lhonak lake) was evaluated considering their future volume. A series of 1D hydrodynamic simulations were performed with varied breach formation time (T_f) to evaluate the impact of a potential future GLOF event on hydropower dams located downstream. The results of the hydraulic computation (peak discharge and time of peak) were compared to a potential GLOF considering the present lake volume. From the available literature it was observed that no studies were carried on future GLOF assessment considering the future lake volume. Hence, the present study is perhaps the first approach to model future GLOFs and its impact downstream using modeled future lake volume.

In the case of the Dhauliganga lake, the peak discharge of a potential GLOF (considering future lake volume) increases by 1267 m^{3}s^{-1} ($T_f = 0.33$ hr), 1786 m^{3}s^{-1} ($T_f = 0.50$ hr), 1997 m^{3}s^{-1} ($T_f = 0.75$ hr) and the time of peak discharge is achieved 4 minutes, 5 minutes and 7 minutes earlier respectively, when compared to the potential GLOF (considering present lake volume). The future GLOF hydrographs were routed to evaluate its potential impact on a hydropower dam located 72 km downstream of the lake. At the dam site, a maximum discharge of 1686 m^{3}s^{-1}is estimated where the peak discharge is reached within 98 min (1.6 hr) after the initiation of the moraine-breach event. Peak discharge of 1595 m^{3}s^{-1} ($T_f = 0.50$ hr) and 1489 m^{3}s^{-1} ($T_f = 0.75$ hr) is recorded at the dam site with a time of peak recorded at 103 min (1.7 hr) and 111 min (1.8 hr) respectively.

For the South Lhonak lake, the peak discharge of a potential GLOF (considering future lake volume) increase by 398m^{3}s^{-1} ($T_f = 3$ hr) and the time of peak discharge is achieved 4 minutes earlier, when compared to the potential GLOF (considering present lake volume) ($T_f = 3.09$). The future GLOF hydrograph was routed for a distance of 62.3 km to evaluate its impact on the hydropower dam located at Chungthang town. At Chungthang town there will be an increase in the future peak discharge by 825 m^{3}s^{-1} which will arrive at the town 84 min (1.4 hr) earlier than

a potential GLOF (considering present lake volume). The method used in the present study proves to be an efficient method to evaluate the future GLOF potential of the existing proglacial lakes.

5. Sensitivity analysis in hydrodynamic modeling of GLOF

The hazard assessment of the Safed lake located in the Goriganga basin (Uttarakhand) revealed a potential GLOF event with a peak discharge of 8868 m^3s^{-1}. The GLOF potentially inundates the nearest village "Milam" located at a distance of 16.2 km downstream of the lake. The flow velocity and inundation depth at Milam village reach up to a maximum of 5m and 3.2 ms^{-1} respectively. The evaluation of the sensitivity of the hydrodynamic model to different input parameters reveal breach hydrograph to be more sensitive to the time of failure of the moraine when compared to the width of the moraine. Further, two-dimensional model sensitivity in GLOF analysis shows that hydraulic properties of a GLOF at any point downstream is sensitive to the initial breach hydrograph. Also, the sensitivity of Manning roughness is observed more in the flow velocity than that of the inundation depth. The study also shows that the flow hydraulics of GLOF is also dependent on the channel characteristics like slope of the channel and top width of the channel. The flow velocity is directly proportional to the slope of the channel and inversely proportional to top width of the channel.

RECOMMENDATION BASED ON THE FINDINGS OF THE THESIS

Based on the findings of the present study the following recommendations are made:

1. The glacial lake inventory which serves as a preliminary dataset for regional assessment of glacial lake dynamics, should be updated periodically using remote sensing datasets. This will provide an insight on the new lakes forming and the behavior of the existing lakes in terms of their growth over the years.

2. Based on the study presented in chapter 3, it is recommended to regularly monitor the Satopanth lake especially during monsoon and post-monsoon season, due to the potential risk it presents to the downstream region when combined with high-intensity precipitation events.

3. Based on the study presented in chapter 4, it is comprehended that the South Lhonak lake is hazardous as it can cause great damage to the downstream region. It is highly recommended to regularly monitor the lake and its associated moraine using remote sensing and field-based assessments. It is also recommended to investigate the engineering properties and perform

in-situ measurements of the flow barrier present along the GLOF flow channel for more accurate modeling-based assessment.

4. Based on the study presented in chapter 5, it is recommended to investigate the glacier bed to map the future extent of the existing lakes at a regional scale. This would further help in disaster preparedness and planning. As, glacier and GLOF modeling is time and data intensive, the assessment can be restricted to the potentially critical lakes in the Himalaya.

5. Based on the study presented in chapter 6, it is recommended to undertake field investigation of the frontal moraine of the Safed lake for detailed in-situ based GLOF hazard assessment to evaluate its potential impact on the Milam village.

PUBLICATIONS

PUBLICATIONS IN PEER REVIEWED JOURNALS

1. **Ashim Sattar**, Goswami, A., & Kulkarni, A. V. (2019). Hydrodynamic moraine-breach modeling and outburst flood routing-A hazard assessment of the South Lhonak lake, Sikkim. Science of the Total Environment, 668, 362-378. (Impact factor-5.589)

2. **Ashim Sattar**, Goswami, A., & Kulkarni, A. V. (2019). Application of 1D and 2D hydrodynamic modeling to study glacial lake outburst flood (GLOF) and its impact on a hydropower station in Central Himalaya. Natural Hazards, 1-19. (Impact factor-2.319

3. **Ashim Sattar,** Goswami, A., Kulkarni, A., & Das, P. (2019). Glacier-Surface Velocity Derived Ice Volume and Retreat Assessment in the Dhauliganga Basin, Central Himalaya-A Remote Sensing and Modeling Based Approach. Frontiers in Earth Science, 7. (Impact factor-2.89)

4. **Ashim Sattar**, Goswami, A., Kulkarni, A. V. & Emmer, A (2019).Ice-thickness based mapping of maximum lake extent - Hazard assessment of future GLOF. Remote Sensing MDPI (Impact factor-4.4) (Under Review)

5. **Ashim Sattar**, Goswami, A., Kulkarni, A. V. & Emmer, A (2019). Lake evolution, outburst flood modeling and sensitivity analysis of Safed lake, central Himalaya. Journal of Hydrology (Impact factor-4.1) (Under Review)

6. Sadhan Malik; Sudhir K Singh; **Ashim Sattar**; Biswajit Das Rabin Chakrabortty (2019). Analysis of Annual Maximum Extreme Precipitation Events and its Future Trend Analysis with Suitable Global Circulation Model: A case study for Kolkata Metropolitan Area. Urban Climate (Under Review)

PUBLICATIONS IN CONFERENCES *(selected)*

1. **Sattar, A.,** Goswami, A. and Kulkarni, A.V., 2018, April. Hydrodynamic modeling of glacial lake outburst flood (GLOF) and its impact on a Hydropower Station-A case study at the upper Alaknanda Basin, Central Himalaya. In *EGU General Assembly Conference Abstracts* (Vol. 20, p. 1575).

2. **Sattar, A.**, Future projection of GLOF hazard-A 1D and 2D hydrodynamic study of the highest lake in the Dhauliganga Basin, Uttarakhand. In *AGU Fall Meeting Abstracts*.

BIBLIOGRAPHY

Abrams M, Tsu H, Hulley G, et al (2015) The advanced spaceborne thermal emission and reflection radiometer (ASTER) after fifteen years: review of global products. Int. J. Appl. Earth Obs. Geoinf. 38: 292–301.

Ageta Y, Iwata S, Yabuki H, et al (2000) Expansion of glacier lakes in recent decades in the Bhutan Himalayas. IAHS Publ. 264: 165-175.

Aggarwal S, Rai SC, Thakur PK, Emmer A (2017) Inventory and recently increasing GLOF susceptibility of glacial lakes in Sikkim, Eastern Himalaya. Geomorphology. 295: 39–54.

Akhtar M, Ahmad N, Booij MJ (2008) The impact of climate change on the water resources of Hindukush-Karakorum-Himalaya region under different glacier coverage scenarios. J. Hydrol. 355(1-4): 148-163.

Alexander GN (1972) Effect of catchment area on flood magnitude. J. Hydrol. 16: 225–240.

Alho P and Aaltonen J (2008) Comparing a 1D hydraulic model with a 2D hydraulic model for the simulation of extreme glacial outburst floods. Hydrol. Process. 22(10): 1537–1547.

Alho P, Russell AJ, Carrivick JL, Käyhkö J (2005) Reconstruction of the largest Holocene jökulhlaup within Jökulsá á Fjöllum, NE Iceland. Quat. Sci. Rev. 24(22): 2319–2334.

Anacona PI, Norton KP, Mackintosh A (2014) Moraine-dammed lake failures in Patagonia and assessment of outburst susceptibility in the Baker Basin. Nat. Hazards Earth Syst. Sci. 14: 3243.

Anacona, P. I., Mackintosh, A., & Norton, K. (2015): Reconstruction of a glacial lake outburst flood (GLOF) in the Engaño Valley, Chilean Patagonia: Lessons for GLOF risk management. Science of The Total Environment, 527, 1-11.

Anthwal A, Joshi V, Sharma A, Anthwal S (2006) Retreat of Himalayan Glaciers – Indicator of Climate Change. Nat Sci. 4(4): 53-59.

Arcement GJ and Schneider VR (1989) Guide for selecting Manning's roughness coefficients for natural channels and flood plains. US Government Printing Office Washington, DC.

Armstrong RL (2010) The Glaciers of the Hindu Kush-Himalayan Region: A Summary of the Science Regarding Glacier Melt/Retreat in the Himalayan, Hindu Kush, Karakoram, Pamir, and Tien Shan Mountain Ranges. Kathmandu: International Centre for Integrated Mountain Development (ICIMOD).

Azam MF, Wagnon P, Ramanathan A, Vincent C, Sharma P, Arnaud Y, et al (2012) From balance to imbalance: a shift in the dynamic behaviour of Chhota Shigri glacier, western Himalaya, India. J. Glaciol. 58: 315–324.

Bahr B, Meier F, Peckham SD (1997) The physical basis of glacier volume-area scaling perturbations in the ice mass balance rate D (rate of ice accumulation area at relatively high

elevations low elevations (D < 0 on a yearly average), Volume-Size. J. Geophys. Res. 102: 355–362.

Bajracharya S, Shrestha B, Much T (2008) Global climate change and melting of Himalayan glaciers. The Icfai's University Press. 28-46.

Bajracharya SR and Shreshta B (2011) The status of Glaciers in the Hindu Kush-Himalaya Region. ICIMOD. ISBN: 978 92 9115217.

Bajracharya SR, Mool PK, Shrestha BR (2007) Impact of climate change on Himalayan glaciers and glacial lakes: Case studies on GLOF and associated hazards in Nepal and Bhutan. International Centre for Integrated Mountain Development (ICIMOD).

Bandyopadhyay D and Singh G (2018) Response of Himalayan glaciers to climate change, in: 42nd COSPAR Scientific Assembly.

Bandyopadhyay D, Singh G, Birajdar F (2018a) Remote sensing analysis of changes in Chorabari glacier, Central Himalaya, India. Curr. Sci. 00113891 114.

Bandyopadhyay D, Singh G, Kulkarni AV (2018b) Glacier ice mass changes in central himalayas during 2000-2014 using tandem-x data. Int. Arch. Photogramm. Remote Sens. Spat. Inf. Sci.

Barnett TP, Adam JC, Lettenmaier DP (2005) Potential impacts of a warming climate on water availability in snow-dominated regions. Nature. 438(7066): 303-309.

Barros N, Cole JJ, Tranvik LJ, et al (2011) Carbon emission from hydroelectric reservoirs linked to reservoir age and latitude. Nat. Geosci. 4(9): 593-596.

Benn DI, Bolch T, Hands K, Gulley J, Luckman A, Nicholson LI, Quincey D, Thompson S, Toumi R, Wiseman S (2012) Response of debris-covered glaciers in the Mount Everest region to recent warming, and implications for outburst flood hazards. Earth-Sci. Rev. 114: 156–174.

Bennett GL and Evans DJA (2012) Glacier retreat and landform production on an overdeepened glacier foreland: the debris-charged glacial landsystem at Kvíárjökull, Iceland. Earth Surf. Process. Landforms. 37: 1584–1602.

Bernstein L, Bosch P, Canziani O, Chen Z, Christ R, Riahi K (2008) IPCC, 2007: climate change 2007: synthesis report.

Bhambri R, Bolch T, Chaujar RK, Kulshreshtha SC (2011) Glacier changes in the Garhwal Himalaya, India, from 1968 to 2006 based on remote sensing. J. Glaciol. 57: 543–556.

Bhargava ON (1995) Geology, Environmental Hazards and Remedial Measures, Lunana Area, Gasa Dzongkhag: Report of 1995 Indo-Bhutan Expedition. Geological Survey of India, Bhutan Unit, Samtse, India.

Bishop MP, Kargel JS, Kieffer HH, MacKinnon DJ, Raup BH, Shroder JF (2000) Remote-sensing science and technology for studying glacier processes in high Asia. Ann. Glaciol. 31: 164–170.

Bishop MP, Kargel JS, Leonard GJ, Bishop MP (2014) Global Land Ice Measurements from Space. In Global Land Ice Measurements from Space.

Björnsson H (1992) Jökulhlaups in Iceland: prediction, characteristics and simulation. Ann. Glaciol. 16: 95–106.

Björnsson H (2003) Subglacial lakes and jökulhlaups in Iceland. Glob. Planet. Change 35: 255–271.

Bjornsson H (2009) Jokulhlaups in Iceland: sources, release, and drainage. Megaflooding Earth Mars Camb. Univ. Press Camb. 50–64.

Björnsson H and Einarsson P (1990) Volcanoes beneath Vatnajökull, Iceland: Evidence from radio echo-sounding, earthquakes and jökulhlaups. Jökull. 40: 147–168.

Bolch T, Kulkarni A, Kääb A, Huggel C, Paul F, Cogley JG, Frey H, Kargel JS, Fujita K, Scheel M (2012) The state and fate of Himalayan glaciers. Science. 336: 310–314.

Bontemps S, Defourny P, Bogaert EV, Arino O, Kalogirou V, Perez JR (2011) GLOBCOVER 2009-Products description and validation report.

Bookhagen B, Burbank DW (2006) Topography, relief, and TRMM-derived rainfall variations along the Himalaya. Geophys. Res. Lett. 33(8): 1-5.

Brinkerhoff DJ, Aschwanden A, Truffer M (2016) Bayesian inference of subglacial topography using mass conservation. Front. Earth Sci. 4: 8.

Brown PH, Tullos D, Tilt B, Magee D, Wolf AT (2009) Modeling the costs and benefits of dam construction from a multidisciplinary perspective. J. Environ. Manag. 90: S303–S311.

Brunner GW (2002) HEC-RAS River Analysis System: User's Manual. US Army Corps of Engineers. Institute for water resources, Hydrologic Engineering Center.

Bulley HN, Bishop MP, Shroder JF, Haritashya UK (2013) Integration of classification tree analyses and spatial metrics to assess changes in supraglacial lakes in the Karakoram Himalaya. Int. J. Remote Sens. 34: 387–411.

Carey M (2005) Living and dying with glaciers: people's historical vulnerability to avalanches and outburst floods in Peru. Glob. Planet. Change. 47: 122–134.

Carling P, Villanueva I, Herget J, Wright N, Borodavko P, Morvan H (2010) Unsteady 1D and 2D hydraulic models with ice dam break for Quaternary megaflood, Altai Mountains, southern Siberia. Glob. Planet. Chang. 70(1–4): 24–34.

Carrivick LJ (2006) Application of 2D hydrodynamic modeling to high-magnitude outburst floods: An example from Kverkfjöll, Iceland. J. Hydrol. 321: 187–199.

Carter RW, Einstein HA, Hinds J, Powell RW, Silberman E (1963) Friction factors in open channels, progress report of the task force on friction factors in open channels of the Committee on Hydro-mechanics of the Hydraulics Division, in: Proceedings, American Society of Civil Engineers, Journal of the Hydraulics Division. 97–143.

Chandana G and Aggarwal SP (2001) Hydrological modeling using remote sensing and GIS. Centre for Remote Imaging, Sensing and Processing (CRISP), National University of Singapore Institute of Surveyors and Valuers (SISV); Asian Association on Remote Sensing (AARS).

Chanson H (2004) Hydraulics of open channel flow. Elsevier.

Chen D, Stow DA, Gong P (2004) Examining the effect of spatial resolution and texture window size on classification accuracy: an urban environment case. Int. J. Remote Sens. 25: 2177–2192.

Chow VT, Maidment DR, Mays LW (1988) Applied Hydrology, McGraw. Inc N. Y. USA.

Christen M, Kowalski J, Bartelt P (2010) Cold Regions Science and Technology RAMMS: Numerical simulation of dense snow avalanches in three-dimensional terrain. Cold. Reg. Sci. Technol. 63(1-2): 1-14.

Clague JJ and Evans SG (2000) A review of catastrophic drainage of moraine-dammed lakes in British Columbia. Quat. Sci. Rev. 19: 1763–1783.

Clarke GKC, Anslow FS, Jarosch AH, et al (2013) Ice volume and subglacial topography for western Canadian glaciers from mass balance fields, thinning rates, and a bed stress model. J. Clim. 26: 4282–4303.

Coon WF (1998) Estimation of roughness coefficients for natural stream channels with vegetated banks (Vol. 2441). US Geological Survey.

Costa JE and Schuster RL (1988) The formation and failure of natural dams. Geol. Soc. Am. Bull. 100: 1054-1068.

Cuffey KM and Paterson WSB (2010) The Physics of Glaciers. Cambridge, MA: Academic Press.

Das PK (2013) " The Himalayan Tsunami " - Cloudburst , Flash Flood & Death Toll : A " The Himalayan Tsunami " - Cloudburst , Flash Flood & Death Toll : A Geographical Postmortem', (June).

Das S, Kar NS, Bandyopadhyay S (2015) Glacial lake outburst flood at Kedarnath, Indian Himalaya: a study using digital elevation models and satellite images. Nat. Hazard. 77(2): 769-786.

Dashora A, Lohani B, Malik JN (2007) A repository of earth resource information–CORONA satellite programme. Curr. Sci. 926–932.

Dashora A, Sreenivas B, Lohani B, Malik JN, Shah AA (2006) GCP collection for CORONA satellite photographs: Issues and methodology. J. Indian Soc. Remote. 34(2): 153–160.

Davies (2017) Mapping the World's Glaciers. Antarctic glaciers.org.

DHI (1995) DHI MIKE 21 short description, Danish Hydraulic Institute, Hørsholm, Denmark.

DHI (1996) MIKE 21 user guide and reference manual. Horsholm, Denmark.

DHI (2003) Mike-11: a modelling system for rivers and channels, reference manual. DHI–Water and Development, Horsholm, Denmark.

Dobhal DP, Gupta AK, Mehta M, Khandelwal DD (2013) Kedarnath disaster: facts and plausible causes. Curr. Sci. 105: 171–174.

Dyurgerov MB and Meier MF (2000) Twentieth century climate change: Evidence from small glaciers. Proc. Natl. Acad. Sci. 97: 1406–1411.

Dyurgerov MB and Meier MF (2005) Glaciers and the changing Earth system: a 2004 snapshot. Institute of Arctic and Alpine Research, University of Colorado Boulder.

Dyurgerov MB, Meier MF (1997) Year-to-year fluctuations of global mass balance of small glaciers and their contribution to sea-level changes. Arct. Alp. Res. 392–402.

Emmer A (2017) Geomorphologically effective floods from moraine-dammed lakes in the Cordillera Blanca, Peru. Quat. Sci. Rev. 177: 220-234.

Emmer A (2018) GLOFs in the WOS: bibliometrics , geographies and global trends of research on glacial lake outburst floods (Web of Science , 1979 – 2016). Nat. Hazards Earth. Syst. Sci. 18: 813–827.

Emmer A and Cochachin A (2013) The causes and mechanisms of moraine-dammed lake failures in the cordillera blanca, North American Cordillera, and Himalayas. Acta. Univ. Carolinae Geogr. 48(2): 5-15.

Emmer A and Vilímek V (2013) Review article: Lake and breach hazard assessment for moraine-dammed lakes: An example from the Cordillera Blanca. Nat. Hazards Earth Syst. Sci. 13(6): 1551-1565.

Emmer A, Vilímek V, Zapata ML (2018) Hazard mitigation of glacial lake outburst floods in the Cordillera Blanca (Peru): the effectiveness of remedial works. J. Flood Risk Manag. 11: S489–S501.

Evans SG (1986) The maximum discharge of outburst floods caused by the breaching of man-made and natural dams. Can. Geotech. J. 23(3): 385–387.

Evans SG and Clague JJ (1994) Recent climatic change and catastrophic geomorphic processes in mountain environments. Geomorphology. Elsevier. 107–128.

Faeh R, Mueller R, Rousselot P, Veprek R, Vetsch D, Volz C, et al (2012) BASEMENT — Basic Simulation Environment for Computation of Environmental Flow and Natural Hazard Simulation. VAW, ETH Zurich.

Farinotti D, Brinkerhoff DJ, Clarke GKC, Fürst JJ, Frey H, Gantayat P, et al. (2017) How accurate are estimates of glacier ice thickness? Results from ITMIX, the Ice Thickness Models Intercomparison eXperiment. Cryosphere. 11: 949–970.

Farinotti D, Huss M, Bauder A, Funk M (2009b) An estimate of the glacier ice volume in the Swiss Alps. Glob. Planet. Chang. 68: 225–231.

Farinotti D, Huss M, Bauder A, Funk M, Truffer M (2009a) A method to estimate the ice volume and ice-thickness distribution of alpine glaciers. J. Glaciol. 55: 422–430.

Farinotti D, Huss M, Fürst JJ, Landmann J, Machguth H, Maussion F, et al (2019) A consensus estimate for the ice thickness distribution of all glaciers on Earth. Nat. Geosci. 12: 168–173.

Frey H, Machguth H, Huss M, Huggel C, Bajracharya S, Bolch T, et al (2014) Estimating the volume of glaciers in the Himalayan–Karakoram region using different methods. Cryosphere. 8: 2313–2333.

Froehlich DC (1995) Peak outflow from breached embankment dam. J. Water Resour. Plan. Manag. 121(1): 90–97.

Fujita K, Sakai A, Nuimura T, Yamaguchi S, Sharma RR (2009) Recent changes in Imja Glacial Lake and its damming moraine in the Nepal Himalaya revealed by in situ surveys and multi-temporal ASTER imagery. Environ. Res. Lett. 4(4): 045205.

Fujita K, Suzuki R, Nuimura T, Sakai A (2008) Performance of ASTER and SRTM DEMs, and their potential for assessing glacial lakes in the Lunana region, Bhutan Himalaya. J. Glaciol. 54: 220–228.

Gantayat P, Kulkarni AV, Srinivasan J (2014) Estimation of ice thickness using surface velocities and slope: case study at Gangotri Glacier, India. J. Glaciol. 60: 277–282.

Gantayat P, Kulkarni AV, Srinivasan J, Schmeits MJ (2017) Numerical modelling of past retreat and future evolution of Chhota Shigri glacier in Western Indian Himalaya. Ann. Glaciol. 58: 136–144.

Gardelle J, Arnaud Y, Berthier E (2011) Contrasted evolution of glacial lakes along the Hindu Kush Himalaya mountain range between 1990 and 2009. Glob. Planet. Change. 75: 47–55.

Ghosh S, Luniya V, Gupta A (2009) Trend analysis of Indian summer monsoon rainfall at different spatial scales. Atmospheric Sci. Lett. 10: 285–290.

Gudmundsson MT, Sigmundsson F, Björnsson H (1997) Ice–volcano interaction of the 1996 Gjálp subglacial eruption, Vatnajökull, Iceland. Nature. 389: 954.

Haakeem KA, Abirami S, Rao VV, Diwakar PG, Dadhwal VK (2018) Updated inventory of Glacial Lakes in Teesta Basin using remote sensing data for use in GLOF risk assessment. J. Indian Soc. Remote Sens. 46: 463–470.

Haeberli W (1983) Frequency characteristics of glacier floods in The Swiss Alps. Ann. Glaciol. 4: 89-90.

Haeberli W and Hoelzle M (1995) Application of inventory data for estimating characteristics of and regional climate-change effects on mountain glaciers: a pilot study with the European Alps. Ann. Glaciol. 21: 206–212.

Haeberli W, Frauenfelder R, Hoelzle M, Maisch M (1999) On rates and acceleration trends of global glacier mass changes. Phy. Geo. 81(4): 585-591.

Haritashya UK (2018) Evolution and controls of large lakes in the Himalaya. Remote Sens. 1–11.

Haritashya UK, Bishop MP, Shroder JF, Bush ABG, Bulley HNN (2009) Space-based assessment of glacier fluctuations in the Wakhan Pamir, Afghanistan. Climatic Change. 94(1–2): 5–18.

Haritashya UK, Kargel JS, Shugar DH, Leonard GJ, Strattman K, Watson CS, Shean D, Harrison S, Mandli KT, Regmi D (2018) Evolution and Controls of Large Glacial Lakes in the Nepal Himalaya. Remote Sens. 10: 798.

Haritashya UK, Pleasants MS, Copland L (2015) Assessment of the evolution in velocity of two debris-covered valley glaciers in nepal and new zealand. Geografiska Annaler: Series A. Phys. Geogr. 97(4): 737-751.

Haritashya UK, Singh P, Kumar N, Singh Y (2006) Hydrological importance of an unusual hazard in a mountainous basin: Flood and landslide. Hydrol. Process. 20: 3147–3154.

Harrison S, Kargel JS, Huggel C, et al (2018) Climate change and the global pattern of moraine-dammed glacial lake outburst floods. Cryosphere. 12(4): 1195-1209.

Heeswijk BM Van, Kimball JS, Marks D (1996) Simulation of Water Available for Runoff in Clearcut Forest Openings During Rain-On-Snow Events in the Western Cascade Range of Oregon and Washington. U.S. Geological Survey: Water-Resources Investigations Report 95-4219.

Heeswijk BM, Kimball JS, Marks D (1996) Simulation of Water Available for Runoff in Clearcut Forest Openings During Rain-On-Snow Events in the Western Cascade Range of Oregon and Washington. U.S. Geological Survey: Water-Resources Investigations Report. 95-4219.

Heid T and Kääb A (2012) Evaluation of existing image matching methods for deriving glacier surface displacements globally from optical satellite imagery. Remote Sens. Environ. 118: 339–355.

Hervouet JM (2007) Hydrodynamics of Free Surface Flows: Modeling with the Finite Element Method. John Wiley & Sons.

Hewitt K (1982) Natural dams and outburst floods of the Karakoram Himalaya. International Association of Hydrological Sciences Publication 138 (Symposium at Exeter 1982 - Hydrological Aspects of Alpine and High-Mountain Areas). 259-269.

Hewitt K (2005) The Karakoram Anomaly? Glacier Expansion and the 'Elevation Effect,' Karakoram Himalaya. Mt. Res. Dev. 25(4): 332-340.

Hoelzle M, Haeberli W, Dischl M, Peschke W (2003) Secular glacier mass balances derived from cumulative glacier length changes. Glob. Planet. Change. 36(4): 295-306.

Huggel C, Haeberli W, Kääb A, Bieri D, Richardson S (2004) An assessment procedure for glacial hazards in the Swiss Alps. Can. Geotech. J. 41(6): 1068–1083.

Huggel C, Kääb A, Haeberli W, Teysseire P, Paul F (2002) Remote sensing based assessment of hazards from glacier lake outbursts: a case study in the Swiss Alps. Can. Geotech. J. 39: 316–330.

Huggel MJ, Glasser NF, Brasington J, Hambrey MJ, Quincey DJ, Reynolds JM (2014) Modelling outburst floods from moraine-dammed glacial lakes. Earth-Sci. Rev. 134: 137–159.

Huss M and Farinotti D (2012) Distributed ice thickness and volume of all glaciers around the globe. J. Geophys. Res. Earth Surf. 117: 1–10.

Huss M, Farinotti D, Bauder A, Funk M (2008) Modelling runoff from highly glacierized alpine drainage basins in a changing climate. Hydrol. Process. 22: 3888–3902.

ICIMOD (2010) Formation of glacial lakes in the Hindu Kush-Himalayas and GLOF risk assessment. In: Ives JD, Shrestha RB, Mool PK. International Centre for Integrated Mountain Development, Kathmandu, May 2010.

Immerzeel WW, van Beek LPH, Bierkens MFP (2010) Climate Change Will Affect the Asian Water Towers. Science. 328: 1382-1385.

Iverson RM, Schilling SP, Vallance JW (1998) Objective delineation of lahar-inundation hazard zones. Geol. Soc. Am. Bull. 110(8): 972–984.

Ives JD (1986) Glacial lake outburst floods and risk engineering in the Himalaya. Kathmandu: ICIMOD.

Ives JD, Shrestha RB, Mool PK (2010) Formation of glacial lakes in the Hindu Kush-Himalayas and GLOF risk assessment. ICIMOD Kathmandu.

Iwata S (2002) Glacier lakes and their outburst flood assessment in the Bhutan Himalaya. Glob. Env. Res. 6: 3–17.

Jain SK, Lohani AK, Singh RD, Chaudhary A, Thakural LN (2012) Glacial lakes and glacial lake outburst flood in a Himalayan basin using remote sensing and GIS. Nat. Hazards. 62: 887–899.

Jha LK and Khare D (2016) Glacial lake outburst flood (GLOF) study of Dhauliganga basin in the Himalaya. Cogent. Environ. Sci. 2: 1249107.

Jha LK and Khare D (2017) Detection and delineation of glacial lakes and identification of potentially dangerous lakes of Dhauliganga basin in the Himalaya by remote sensing techniques. Nat. Haz. 85(1): 301-327.

Johannesson H, Saemundsson K (1989) Geological Map of Iceland. 1:500000. Bedrock Geology. Icelandic Museum of Natural History and Iceland Geodetic Survey. Reykjavik.

Kääb A, Berthier E, Nuth C, Gardelle J, Arnaud Y (2012) Contrasting patterns of early twenty-first-century glacier mass change in the Himalayas. Nature. 488(7412): 495-498.

Kääb A, Huggel C, Paul F, Wessels R, Raup B, Kieffer H, Kargel J (2002) Glacier monitoring from ASTER imagery: accuracy and applications, in: Proceedings of EARSeL-LISSIG-Workshop Observing Our Cryosphere from Space. 43–53.

Kääb A, Wessels R, Haeberli W, Huggel C, Kargel JS, Khalsa SJS (2003) Rapid ASTER imaging facilitates timely assessment of glacier hazards and disasters. EOS Trans. Am. Geophys. Union. 84: 117–121.

Kargel JS, Beedle MJ, Bush AB, Carreño F, Castellanos E, Haritashya UK, Leonard GJ, Lillo J, Lopez I, Pleasants M (2014) Multispectral image analysis of glaciers and glacier lakes in the Chugach Mountains, Alaska, in: Global Land Ice Measurements from Space. Springer. 297–332.

Kargel JS, Cogley JG, Leonard GJ, Haritashya U, Byers A (2011) Himalayan glaciers: The big picture is a montage. P. Natl. A. Sci. 108(36): 14709–14710.

Kargel JS, Leonard G, Crippen RE, Delaney KB, Evans SG, Schneider J (2010) Satellite Monitoring of Pakistan's Rockslide-Dammed Lake Gojal. Eos Trans. Am. Geophys. Union. 91: 394–395.

Kaser G, Großhauser M, Marzeion B (2010) Contribution potential of glaciers to water availability in different climate regimes. Proc. Natl. Acad. Sci.

Kattelmann R (2003) Glacial Lake Outburst Floods in the Nepal Himalaya: A Manageable Hazard?

Keunza K, Dorji Y, Wangda D (2004) Landslides in Bhutan. Country Report, Department of Geology and Mines, Royal Government of Bhutan, Thimpu.

Klimeš J, Benešová M, Vilímek V, Bouška P, Rapre AC (2014) The reconstruction of a glacial lake outburst flood using HEC-RAS and its significance for future hazard assessments: an example from Lake 513 in the Cordillera Blanca, Peru. Nat. Hazards. 71(3): 1617–1638.

Komori J (2007) Recent expansions of glacial lakes in the Bhutan Himalayas. Quat. Int. 184(1): 177–186.

Komori J (2008) Recent expansions of glacial lakes in the Bhutan Himalayas. Quat. Int. 184: 177–186.

Korup O, Tweed F (2007) Ice, moraine, and landslide dams inmountainous terrain. Quat. Sci. Rev. 26: 3406–3422.

Kulkarni AV and Karyakarte Y (2014) Observed changes in Himalayan glaciers. Curr. Sci. 237–244.

Kulkarni AV, Bahuguna IM, Rathore BP, Singh SK, Randhawa SS, Sood RK, Dhar S (2007) Glacial retreat in Himalaya using Indian remote sensing satellite data. Curr. Sci. 69–74.

Kulkarni AV, Dhar S, Rathore BP, Babu Govindha Raj K, Kalia R (2006) Recession of samudra tapu glacier, Chandra river basin, Himachal Pradesh. J. Indian Soc. Remote Sens. 34: 39–46.

Kumar A and Sharma MP (2016a) Assessment of risk of GHG emissions from Tehri hydro-power reservoir, India. Hum. Ecol. Risk Assess. 22: 71–85.

Kumar A and Sharma MP (2016b) A modeling approach to assess the greenhouse gas risk inKoteshwar hydropower reservoir, India. Hum. Ecol. Risk Assess. 22: 1651–1664.

Kumar A and Sharma MP (2016c) Carbon stock estimation in the catchment of Kotli Bhel 1Ahydroelectric reservoir, Uttarakhand, India. Ecotoxicol. Environ. Saf. 134: 365–369.

Kumar A, Negi HS, Kumar K, Kanda N, Singh KK, Pandit A, Ramsankaran RAAJ (2018) Estimation of recent changes in thickness and mass balance of the Patsio glacier in the Great Himalayan region using geodetic technique and ancillary data. Geocarto Int. 1–17.

Kumar A, Sharma MP, Yang T (2018) Estimation of carbon stock for greenhouse gasemissions from hydropower reservoirs. Stoch. Environ. Res. Risk Assess. 32: 3183–3193.

Kumar A, Yang T, Sharma MP (2019) Long-term prediction of greenhouse gas risk to the Chinese hydropower reservoirs. Sci. Total Environ. 646: 300–308.

Kumar B, Murugesh Prabhu TS (2012) Impacts of Climate Change: glacial lake outburst floods (GLOFs). Clim. Chang. Sikk. Patterns, Impacts Initiat. Inf. Public Relations Dep. Gov. Sikk. Gangtok. 81–101.

Kumar V, Mehta M, Mishra A, Trivedi A (2017) Temporal fluctuations and frontal area change of Bangni and Dunagiri glaciers from 1962 to 2013, Dhauliganga Basin, central Himalaya, India. Geomorphology. 284: 88–98.

Lemke P, Ren J, Alley RB, Allison I, Carrasco J, Flato G, Fujii Y, Kaser G, Mote P, Thomas RH, Zhang, T (2007) Observations: changes in snow, ice and frozen ground.

Linsbauer A, Frey H, Haeberli W, Machguth H, Azam MF, Allen S (2016) Modelling glacier-bed overdeepenings and possible future lakes for the glaciers in the Himalaya-Karakoram region Ann. Glaciol. 57: 119-130.

Linsbauer A, Paul F, Haeberli W (2012) Modeling glacier thickness distribution and bed topography over entire mountain ranges with glabtop: application of a fast and robust approach. J. Geophys. Res. Earth Surf. 117: 1–17.

Linsbauer A, Paul F, Hoelzle M, Frey H, Haeberli W (2009) The swiss alps without glaciers - a GIS-based modelling approach for reconstruction of glacier beds. Proc. Geomorphometry. 243–247.

Lliboutry L, Arnao MB, Pautre A, Schneider B (1977) Glaciological Problems Set by the Control of Dangerous Lakes in Cordillera Blanca, Peru. I. Historical Failures of Morainic Dams, their Causes and Prevention. J Glaciol. 18(79): 239-254.

Maanya US, Kulkarni AV, Tiwari A, Bhar ED, Srinivasan J (2016) Identification of potential glacial lake sites and mapping maximum extent of existing glacier lakes in Drang Drung and Samudra Tapu glaciers, Indian Himalaya. Curr. Sci. 111: 553–560.

Maharjan SB, Mool PK, Lizong W, Xiao G, Shrestha F, Shrestha RB, Khanal NR, Bajracharya SR, Joshi S, Shai S, Baral P (2018) The status of glacial lakes in the Hindu Kush Himalaya. ICIMOD Research Report 2018/1. Kathmandu: ICIMOD.

Maidment DR (2002) ArcHydro: GIS for Water Resources. ESRI Inc., Redlands, CA.

McNabb RW, Hock R, O'Neel S, Rasmussen LA, Ahn Y, Braun M (2012) Using surface velocities to calculate ice thickness and bed topography: a case study at Columbia Glacier, Alaska, USA. J. Glaciol. 58: 1151–1164.

Mergili M and Schneider JF (2011) Regional-scale analysis of lake outburst hazards in the south western Pamir, Tajikistan, based on remote sensing and GIS. Nat. Hazards Earth Syst. Sci. 11: 1447–1462.

Mergili M, Emmer A, Juřicová A, et al (2018) How well can we simulate complex hydro-geomorphic process chains? The 2012 multi-lake outburst flood in the Santa Cruz Valley (Cordillera Blanca, Perú). Earth Surf. Process. Landforms. 43(7): 1373-1389.

Miller JD, Immerzeel WW, Rees G (2012) Climate change impacts on glacier hydrology and river discharge in the Hindu Kush–Himalayas. Mountain Res. Dev. 32(4): 461-468.

Mishra A, Negi BDS, Banerjee A, Nainwal HC, Shankar R (2018) Estimation of ice thickness of the Satopanth Glacier, Central Himalaya using ground penetrating radar. Curr. Sci. 114: 785–791.

Mool PK (1995) GIS and remote sensing application in slope instability study. Paper presented at the Regional Workshop on Landslide Hazard Management and Control in the Hindu Kush Himalayas, 12–14 July, Kathmandu, Nepal.

Mool PK and Bajracharya SR (2003) Tista Basin, Sikkim Himalaya: Inventory of Glaciers and Glacial Lakes and the Identification of Potential Glacial Lake Outburst Floods (GLOFs) Affected by Global Warming in the Mountains of Himalayan Region. International Center for Integrated Mountain Development, Kathmandu, Nepal.

Mool PK, Wangda D, Bajracharya SR, Kunzang K, Gurung DR, Joshi SP (2001) Inventory of glaciers, glacial lakes and glacial lake outburst floods. Monitoring and early warning systems in the Hindu Kush-Himalayan Region: Bhutan. Inventory Glaciers Glacial Lakes Glacial Lake Outburst Floods Monit. Early Warn. Syst. Hindu Kush-Himal. Reg. Bhutan.

Morlighem M, Rignot E, Seroussi H, Larour E, Ben Dhia H, Aubry D (2011) A mass conservation approach for mapping glacier ice thickness. Geophys. Res. Lett. 38: 1–6.

Nagabhatla N, Sahu SK, Gaetaniello A, Wen L, Lee W (2015) Understanding Impacts of Climate Variation in Varied Socio-ecological Domains: A Prerequisite for Climate Change Adaptation and Management. Handb. Clim. Change Adapt. 589–617.

Nagai H, Ukita J, Narama C, Fujita K, Sakai A, Tadono T, Yamanokuchi T, Tomiyama N (2017) Evaluating the Scale and Potential of GLOF in the Bhutan Himalayas Using a Satellite-Based Integral Glacier–Glacial Lake Inventory. Geosciences. 7(3): 77.

Nela BR, Singh G, Kulkarni AV, Malik K (2018) Optimum Conditions for Differential SAR Interferometry Technique to Estimate Himalayan Glacier Velocity. ISPRS Ann. Photogramm. Remote Sens. Spat. Inf. Sci. 45: 137–140.

Nie Y, Liu Q, Liu S (2013) Glacial lake expansion in the Central Himalayas by landsat images, 1990-2010. PLoS One. 8(12): 1-8.

Nie Y, Sheng Y, Liu Q, Liu L, Liu S, Zhang Y, Song C (2017) A regional-scale assessment of Himalayan glacial lake changes using satellite observations from 1990 to 2015. Remote Sens. Environ. 189: 1–13.

Nuimura T, Sakai A, Taniguchi K, et al (2015) The GAMDAM glacier inventory: A quality-controlled inventory of Asian glaciers. Cryosphere. 9(3): 849-864.

O'Brien JS (2001) FLO-2D Users Manual. Nutrioso, Arizona. 83 pp. and appendices.

O'Connor JE, Hardison JH, Costa JE (2001) Debris flows from failures of Neoglacial-Age moraine dams in the Three Sisters and Mount Jefferson wilderness areas, Oregon (No. 1606). US Department of the Interior, US Geological Survey.

Osti R and Egashira S (2009) Hydrodynamic characteristics of the Tam Pokhari Glacial Lake outburst flood in the Mt. Everest region, Nepal. Hydrol. Process. Int. J. 23: 2943–2955.

Pandit MK and Grumbine RE (2012) Potential Effects of Ongoing and Proposed Hydropower Development on Terrestrial Biological Diversity in the Indian Himalaya. Conserv. Biol. 26(6): 1061-1071.

Pattanaik DR, Pai DS, Mukhopadhyay B (2015) Rapid northward progress of monsoon over India and associated heavy rainfall over Uttarakhand: a diagnostic study and real time extended range forecast. Mausam. 66: 551–568.

Paul F (2000) Evaluation of different methods for glacier mapping using landsat tm. EARSeL eProceedings. 1: 239–245.

Paul F, Huggel C, Kääb A (2004) Combining satellite multispectral image data and a digital elevation model for mapping debris-covered glaciers. Remote Sens. Environ. 89: 510–518.

Pfeffer WT, Arendt AA, Bliss A, et al (2014) The Randolph Glacier Inventory: a globally complete inventory of glaciers. J. Glaciol. 60(221): 537-552.

Pickert G, Weitbrecht V, Bieberstein A (2011) Breaching of overtopped river embankments controlled by apparent cohesion J. Hydraul. Res. 49(2): 143-156.

Quincey DJ, Richardson SD, Luckman A, et al (2007) Early recognition of glacial lake hazards in the Himalaya using remote sensing datasets. Glob. Planet. Change. 56(1-2): 137-152.

Radić V and Hock R (2011) Regionally differentiated contribution of mountain glaciers and ice caps to future sea-level rise. Nat. Geosci. 4: 91.

Raj G, Babu K, Kumar VK, SN, R (2013) Remote sensing-based inventory of glacial lakes in Sikkim Himalaya: semi-automated approach using satellite data. Geomatics, Nat. Haz. Risk. 4(3): 241-253.

Raj KBG and Kumar KV (2016) Inventory of glacial lakes and its evolution in Uttarakhand Himalaya using time series satellite data. J. Indian Soc. Remote Sens. 44: 959–976.

Raj KBG, Remya SN, Kumar KV (2013) Remote sensing-based hazard assessment of glacial lakes in Sikkim Himalaya. Curr. Sci. 359–364.

Ramsankaran RAAJ, Pandit A, Azam MF (2018) Spatially distributed ice-thickness modelling for Chhota Shigri Glacier in western Himalayas, India. Int. J. Remote Sens. 39(10): 3320–3343.

Rana B, Shrestha BA, Reynolds JM, Aryal R, Pokhrel AP, Budhatoki KP (2000) Hazard assessment of the Tsho Rolpa Glacier Lake and ongoing remediation measures. J. Nepal Geological Soc. 22: 573–570.

Ray PC, Chattoraj SL, Bisht MPS, Kannaujiya S, Pandey K, Goswami A (2016) Kedarnath disaster 2013: causes and consequences using remote sensing inputs. Nat. Hazards 81: 227–243.

Remya SN, Kulkarni AV, Pradeep S, Shrestha DG (2019) Volume estimation of existing and potential glacier lakes, Sikkim Himalaya, India. Curr. Sci. 116(4): 1-8.

Reynolds JM (1998) High-altitude glacial lake hazard assessment and mitigation: a Himalayan perspective. Geol. Soc. Lond. Eng. Geol. Spec. Publ. 15: 25–34.

Reynolds JM (1999) Glacial hazard assessment at Tsho Rolpa, Rohwaling, Central Nepal. Q. J. Eng. Geol. 32: 209–214.

Reynolds JM, Dolecki A, Portocarrero C (1998) The construction of a drainage tunnel as part of glacial lake hazard mitigation at Hualcán, Cordillera Blanca, Peru. Geological Society, London. Eng. Geol. Spec. Publ. 15 (1): 41–48.

RGI Consortium (2017). Randolph Glacier Inventory (RGI) – A Dataset of Global Glacier Outlines: Version 6.0. Technical Report, Global Land Ice Measurements from Space, Boulder, CO: Digital Media.

Richardson SD (2010) Remote sensing approaches for early warning of GLOF hazard in the Hindu Kush–Himalayan region. Final report-ver, 1.

Richardson SD and Reynolds JM (2000) An overview of glacial hazards in the Himalayas. Quat. Int. 65: 31-47.

Rounce DR, Watson CS, McKinney DC (2017) Identification of hazard and risk for glacial lakes in the Nepal Himalaya using satellite imagery from 2000–2015. Remote Sens. 9.

SAC (2016) Monitoring Snow and Glaciers of Himalayan Region, Space Applications Centre, ISRO, Ahmedabad, India, 413 pages, ISBN: 978 – 93 – 82760 – 24 – 5.

Sattar A, Goswami A, Kulkarni AV (2019) Hydrodynamic moraine-breach modeling and outburst flood routing-A hazard assessment of the South Lhonak lake, Sikkim. Sci. Total Environ. 668: 362-378.

Scherler D, Bookhagen B, Strecker MR (2011) Spatially variable response of Himalayan glaciers to climate change affected by debris cover. Nat. Geosci. 4: 156.

Scherler D, Leprince S, Strecker MR (2008) Glacier-surface velocities in alpine terrain from optical satellite imagery-Accuracy improvement and quality assessment. Remote Sens. Environ. 112: 3806–3819.

Sharma RK, Pradhan P, Sharma NP, Shrestha DG (2018) Remote sensing and in situ-based assessment of rapidly growing South Lhonak glacial lake in eastern Himalaya, India. Natural Hazards. 1-17.

Shreve RL (1966) Statistical law of stream numbers. J. Geol. 74: 17–37.

Shukla A, Garg PK, Srivastava S (2018) Evolution of glacial and high-altitude lakes in the Sikkim, Eastern Himalaya over the past four decades (1975-2017). Front. Environ. Sci. 6: 81.

Sophie B, Pierre D, Eric VB (2010) GlobCOVER 2009 Products Description and Validation Report (UCLouvain and ESA).

Stocker TF, Qin D, Plattner GK, Tignor M, Allen SK, Boschung J, Nauels A, Xia Y, Bex V, Midgley PM (2013) Climate change 2013: The physical science basis.

Stoffel M and Huggel C (2012) Effects of climate change on mass movements in mountain environments. Prog. Phys. Geogr. 36: 421–439.

Swaroop S, Raina VK, Sangeswar CV (2003) "Ice flow of gangotri glacier," in Proceedings of the Workshop on Gangotri glacier. 26–28.

Tachikawa T, Kaku M, Iwasaki A, Gesch D, Oimoen M, Zhang Z, et al (2011) ASTER global digital elevation model version 2. Summ. Valid. Results. 7: 1–27.

Tashi T (1994) Preliminary report on the investigation of glacial lakes at Pho Chhu source and the assessment of food affected areas in Lunana. Thimphu, Royal Bhutanese Government.

Thakur PK, Aggarwal S, Aggarwal SP, Jain SK (2016) One-dimensional hydrodynamic modeling of GLOF and impact on hydropower projects in Dhauliganga River using remote sensing and GIS applications. Nat. Hazards. 83: 1057–1075.

Tiwari RK, Gupta RP, Gens R, Prakash A (2012) Use of optical, thermal and microwave imagery for debris characterization in Bara-Shigri glacier, Himalayas, India, in: Geoscience and Remote Sensing Symposium (IGARSS), 2012 IEEE International. IEEE. 4422–4425.

United States Army Corps of Engineers, Hydrologic Engineering Center USACE-HEC. (2006). Hydrologic modeling system HEC-HMS user's manual, Davis, Calif.

Vilímek V, Emmer A, Huggel C, Schaub Y, Würmli S (2014) Database of glacial lake outburst floods (GLOFs)-IPL project No. 179. Landslides. 11: 161–165.

Vuichard D and Zimmermann M (1986) The Langmoche flash-flood, Khumbu Himal, Nepal. Mt. Res. Dev. 90-94.

Wang W, Xiang Y, Gao Y, Lu A, Yao T (2015) Rapid expansion of glacial lakes caused by climate and glacier retreat in the Central Himalayas. Hydrol. Process. 29(6): 859-874.

Wang X, Ding Y, Liu S, Jiang L, Wu K, Jiang Z, Guo W (2013) Changes of glacial lakes and implications in Tian Shan, central Asia, based on remote sensing data from 1990 to 2010. Environ. Res. Lett. 8(4): 044052.

Wang X, Liu S, Guo W, Xu J (2008) Assessment and simulation of glacier lake outburst floods for Longbasaba and Pida lakes, China. Mt. Res. Dev. 28: 310–317.

Wang X, Siegert F, Zhou AG, Franke J (2013) Glacier and glacial lake changes and their relationship in the context of climate change, Central Tibetan Plateau 1972–2010. Glob. Planet. Change. 111: 246-257.

Watanabe T, Ives JD, Hammond JE (1994) Rapid growth of a glacial lake in Khumbu Himal, Himalaya: prospects for a catastrophic flood. Mt. Res. Dev. 329–340.

Watanbe T and Rothacher D (1996) The 1994 Lugge Tsho glacial lake outburst flood, Bhutan Himalaya. Mt. Res. Dev. 16: 77–81.

Westoby M, Brasington J, Glasser N, Hambrey M, Reynolds J, Hassan M, Lowe A (2015) Numerical modelling of glacial lake outburst floods using physically based dam-breach models. Earth Surf. Dynam. 3 (1): 171–199.

Westoby MJ, Glasser NF, Brasington J, Hambrey MJ, Quincey DJ, Reynolds JM (2014) Modelling outburst floods from moraine-dammed glacial lakes. Earth-Sci. Rev. 134: 137–159.

WGMS (2016) Glacier Thickness Database 2.0, eds I. Gärtner-Roer, L. M. Andreassen, E. Bjerre, D. Farinotti, A. Fischer, M. Fischer, et al., Zurich: World Glacier Monitoring Service.

Worni R, Huggel C, Clague JJ, Schaub Y, Stoffel M (2014) Coupling glacial lake impact, dam breach, and flood processes: A modeling perspective. Geomorphology. 224: 161–176.

Worni R, Huggel C, Stoffel M (2013) Glacial lakes in the Indian Himalayas—From an area-wide glacial lake inventory to on-site and modeling based risk assessment of critical glacial lakes. Sci. Total Environ. 468: S71–S84.

Worni R, Stoffel M, Huggel C, Volz C, Luckman B (2012) Analysis and dynamic modeling of a moraine failure and glacier lake. J. Hydrol. 445: 134–145.

Yamada T (1998) Glacier lake and its outburst flood in the Nepal Himalaya. Data Center for Glacier Research. Jpn. Soc. Snow Ice Monogr. 1: 96.

Yamada T and Sharma CK (1993) Glacier lakes and outburst floods in the Nepal Himalaya. IAHS Publ.-Publ. Int. Assoc. Hydrol. Sci. 218: 319–330.

Yochum SE, Bledsoe BP, David GCL, Wohl E (2012) Velocity prediction in high-gradient channels. J. Hydrol. 424–425: 84–98.

Zemp M and van Woerden j (2008) Global Glacier Changes: facts and figures. UNEP - World Glacier Monitoring Service. 88.

Zemp M, Frauenfelder R, Haeberli W, Hoelzle M (2005) World-wide glacier mass balance measurements: General trends and first results of the extraordinary year 2003 in Central Europe. Data Glaciol. Stud. 99: 3–12.